Universitat Autònoma de Barcelona

3D PRINTING OF CERAMIC-BASED SOLID STATE ENERGY CONVERSION DEVICES

Arianna Pesce

Universitat Autònoma de Barcelona

3D PRINTING OF CERAMIC-BASED SOLID STATE ENERGY CONVERSION DEVICES

Arianna Pesce

Tesi Doctoral
Programa de Doctorat en Ciencía de Materiales

Dr. Albert Tarancón Rubio (Director)
Dr. Alex Morata García (Director)
Dr. Eva Maria Pellicier Vilà (Tutora)

Departament de Fisíca
Facultat De Ciencíes
2021

Universitat Autònoma de Barcelona

Institut de Recerca en Energia de Catalunya
Catalonia Institute for Energy Research

PhD thesis

3D PRINTING OF CERAMIC-BASED SOLID STATE ENERGY CONVERSION DEVICES

Candidate:
Arianna Pesce

Supervisor:
Dr. Albert Tarancón Rubio
Dr. Alex Morata García
Dr. Eva Maria Pellicier Vilà

eit InnoEnergy
Knowledge Innovation Community

Material Science PhD school
January 2021

Institut de Recerca en Energia de Catalunya
Catalonia Institute for Energy Research

El **Dr. Albert Tarancón Rubio**, profesor ICREA del Departament de Materials avancado par la enegia del Instituto de Reserca de Energia de Catalunya,

i el **Dr. Alejandro Morata García**, investigador del Departament de Materials avancado par la enegia del Instituto de Reserca de Energia de Catalunya,

CERTIFIQUEN:

Que **Arianna Pesce** ha realizat sota la seva direcció el treball d'investigació que s'exposa a la memòria titulada "3D printing of ceramic-based solid state energy conversion devices" per optar al grau de Doctor per la Universitat Autònoma de Barcelona.

Que el disseny dels experiments, sintesi de mostres, llur caracterització, l'anàlisi dels resultats, i la redacció dels articles i d'aquesta memòria son fruit del treball d'investigació realizat per Arianna Pesce.

I perquè així consti, signen el present certificat,

Dr. Alber Tarancón Rubio

Dr. Alejandro Morata García

Barcelona, 31 d'agost de 2020

Preface

This thesis collects the work and the results achieved between 8th March 2017 and 31st August 2020 and it is submitted to an evaluation committee and the PhD School of the Autonomous University of Barcelona (UAB), Spain for a Philosofiae Doctor degree in Material Science. The work here presented was performed in the laboratories of the Catalonia Institute for Energy Research (IREC), Spain under the supervision of Dr. Albert Tarancon and Dr. Alex Morata with the collaboration of the Nanoionics and Solid State Energy Devices Group (reference number: 2017 SGR 1421). Part of the results were achieved during an abroad period at the Fraunhofer Institute for Microengineering and Microsystems (FhG-IMM), Mainz, Germany, under the supervision of Dr. Gunther Kolb. The project has partially received funding from the 3D-MADE project (ENE2016-74889-C4-1-R) and the Cell3Ditor project (project reference: 700266). The Innoenergy PhD School Programme and the European Institute of Technology (EIT) have partially funded the mobility program.

Abstract

In the last decades, additive manufacturing technologies (AM) have obtained a wider spreading, moving from the prototyping scale to the commercial distribution for some types of materials. The ceramic materials are well known for their high stiffness, brittleness and toughness, which make their processing limited in shape and extremely expensive (high consumption of tools or moulds for individual use). Additive manufacturing can reduce the cost of manufacturing and open new designs, near-free to shape, not realizable with subtracting manufacturing. Next step of the research in this field is the application of additive manufacturing to the field of functional materials, where the requirements of structural, microstructural, optical and electric properties are higher than for commercial applications. In particular the near-free design opportunity is particularly interesting for applications in which the area plays an important role on the final performance, such as in catalysis and for electrochemical devices. In these cases, often more than a ceramic material is necessary arising the interest of the scientific community to the multi-material possibility of 3D printing, to enable the production of such devices with reduced manufacturing steps and on consequence, reducing the cost. This thesis focuses on the printing of complex geometries devices to prove the unfair advantage of additive manufacturing, as in the catalysis field, as for fuel cells and electrolysis application. For this purpose, the work addresses on developing of printable media and hybridization of two different printing technologies to produce the entire device in a single step: stereolithography and robocasting. Stereo-lithography (SLA) offers the possibility of obtaining high-density structures (>90%) with high spatial resolution, in the order of 25 µm in the three directions. Electrolytes for Solid Oxide Cells (SOCs) have been produced in 3mol% and 8mol% yttria stabilized zirconia. Button cells were realized with state-of-the-art materials to characterize the electrochemical performance. At first, it was demonstrated that SLA technology is suitable to produce electrolytes with properties comparable with the ones produced by traditional manufacturing. The freedom of design, characteristic of the 3D printing, enables the increase of the performance according with the implement of the area. As a further step, the possibility of implementing multi-material options, necessary to print a commercial

device based on SOCs technology, was explored in this thesis. Using SLA as a base, a robocasting system was added to the machine. In this way, a five-material 3D printer could be achieved. The required pastes for robocasting were integrally produced, mixing the ceramic commercial powders with organic materials in appropriate proportions and evaluating their rheology performance and curability. In this way, cathode, anode and interconnect layers were produced. The hybridization of SLA with robocasting was satisfactory achieved, demonstrating the possibility of printing stacks of layers of the different components. The co-sintering of such systems was conducted, facing the challenge of the simultaneous annealing of layers of different materials. The first cells using this procedure were obtained and tested. While still requiring optimization to improve their performances, these cells are the first-time demonstration of the feasibility of SOC devices by multi-material 3D printing. Micro-channel plates, used as bed for CO_2 methanation reaction were produced with SLA, proving their efficiency compared with stainless steel ones in terms of CO_2 conversion. A heat exchange reactor with integrated manifolds was produced by 3D printing for the first time.

Resumen

En las últimas décadas, las tecnologías de fabricación aditiva han logrado una amplia difusión, evolucionando desde los primeros prototipos hasta conseguir una extensa distribución comercial. Los materiales cerámicos son bien conocidos por su alta rigidez, fragilidad y tenacidad, que dificultan la consecución de formas complejas y hace extremadamente costosa su mecanización (gran consumo de herramientas o moldes para uso individual). La fabricación aditiva puede reducir el coste de fabricación y abrir nuevos diseños, con libertad de forma prácticamente total, no realizables mediante técnicas tradicionales. El primer paso de la investigación en este campo es la aplicación de la fabricación aditiva al campo de los materiales funcionales, donde los requisitos de propiedades estructurales, microestructurales, ópticas y eléctricas son superiores a los de las aplicaciones comerciales. En particular, la oportunidad de diseños complejos es interesante para aplicaciones en las que el área activa juega un papel importante en el rendimiento final, como en catálisis o en dispositivos electroquímicos. En estos casos, a menudo es necesario más de un material cerámico. Por este motivo es de un gran interés la impresión 3D de múltiples materiales, que permitiría la producción de dichos dispositivos con pasos de fabricación reducidos y, en consecuencia, reduciendo el coste. Esta tesis se centra en la impresión de dispositivos de geometrías complejas para probar las ventajas exclusivas de la fabricación aditiva, tanto en el campo de la catálisis como en la aplicación de pilas de combustible y electrolizadores. Para ello, el trabajo aborda el desarrollo de soportes imprimibles y la hibridación de dos tecnologías de impresión diferentes para producir todo el dispositivo en un solo paso: estereolitografía y robocasting. La estereolitografía (SLA) se caracteriza por obtener estructuras de alta densidad ($> 90\%$) con gran resolución espacial, del orden de 25 µm en las tres direcciones. Se han producido electrolitos para celdas de óxido sólido (SOC) en zirconia estabilizada con itria al 3% y al 8% molar. Se produjeron pilas de botón incorporando materiales estándar de cátodo y ánodo sobre los electrolitos imprimidos, para caracterizar el rendimiento electroquímico. Después de haber demostrado que la tecnología SLA produce electrolitos adecuados con propiedades comparables a las producidas por la fabricación tradicional, se ha medido un incremento de rendimiento, coherente con el

incremento de área activa, realizado mediante la corrugación del electrolito. Seguidamente, en esta tesis se exploró la posibilidad de implementar opciones multimaterial, necesarias para imprimir un dispositivo comercial basado en tecnología SOCs. Utilizando SLA como tecnología base, se agregó a la máquina un sistema de robocasting, logrando imprimir cinco materiales. Las pastas necesarias para la impresión por robocasting se han desarrollado íntegramente en el marco de esta tesis a partir de polvos cerámicos comerciales y componentes orgánicos, evaluando su reología y capacidad de curado; produciendo materiales de cátodo, ánodo e interconector. La hibridación de SLA con robocasting fue alcanzada satisfactoriamente, demostrando la posibilidad de imprimir apilamientos de capas de los diferentes componentes. El sinterizado conjunto de tales sistemas fue llevado a cabo, afrontando los retos de la calcinación conjunta de capas compuestas por distintos materiales. Las primeras celdas obtenidas utilizando este procedimiento fueron testadas. Aunque será necesaria una optimización para mejorar los rendimientos, estas celdas son la demostración de la posibilidad de fabricar dispositivos SOC mediante impresión 3D multimaterial. Finalmente, usando técnica de SLA se produjeron placas de microcanales, utilizadas como lecho para la reacción de metanización de CO_2, demostrando su eficacia frente a la tecnología tradicional basada en acero inoxidable en términos de conversión de CO_2. También se fabricó por primera vez un reactor de intercambio de calor con colectores integrados mediante impresión 3D.

Contents

Chapter 1

Introduction

This chapter covers the necessary background and theoretical aspects for this thesis.
Starting from Section 1.1, which presents a general overview of the nowadays energy economy, the reasons for an energy transition to a renewable resources based one and the main issues to accomplish this transition.
Section 1.2 presents the technology of Solid Oxide Cells explaining its working principles, materials and manufacturing technologies involved, as well on the materials point of view as on the manufacturing itself.
Following the same scheme, the principles of methanation reactors are explained in Section 1.3, focusing on the design, current fabrication and catalyst development.
Section 1.4 presents the core elements of this thesis, here the different 3D printing technologies are introduced with their implementation to work with ceramic materials. A deeper analysis of the 3D printing technologies employed in this work such as stereolithography and robocasting, is presented in Section 1.4.1 and 1.4.2, focusing on the working principles and the printable feedstock.
The use of additive manufacturing in the energy field is reviewed, with a focus on Solid Oxide Cells and catalytic reactors (Section 1.5).
Finally, last section is devoted to explain the motivation of this thesis, focusing on the possibilities of the 3D printing technologies and a brief introduction to the Cell3Ditor project, in which frame this thesis has been partially developed.

1.1 Role of hydrogen and solid oxide energy devices in the current energy scenario

Nowadays the production of energy is mainly based on combustion of fossil fuel, whether it is for industrial or residential applications or for the automotive sector. Over more than one hundred years, since the Industrial Revolution, humankind has become more and more dependent and used to energy. Our society is based on an energy system suffering immediate electricity supply thanks to power plants which convert fossil fuels into power and a grid that completely covers the territory in the developed countries. Similarly, gas supply allows cooking or warming the vast majority of houses and the distribution of gas stations is spread over the whole territory, which enable the intensive use of cars [1].
This availability of energy supports a fast development of the humankind and a continuous improvement of life expectancy and quality of life. However, on the other side, the production and intensive use of fossil fuels is strongly affecting the health of the people due to air pollution, especially of the ones living in cities. The World Health Organization (WHO) estimates that in 2018 more than six million people prematurely died worldwide due to a poor air quality [2]. For many years, the major concern of most governments was the search for possible solutions to match the energy requirements of the economy. Nowadays, the investment in alternative sources of energy is driven by the unsustainability of the previous energy economy, seeing the only possible solution to maintain the increase of temperature below 2°C in declining on the use of fossil fuels, as established in 2015 by the Paris Agreement [3]. However, the desirable growth of Renewable Energy Sources (RES) is still limited by its intermittent production over space and time. It becomes critical the possibility to store the produced energy during the high productive hours, to reuse it during high demanding periods [1].
The use of several storage strategies are currently under debate based on different technologies and it is far from the intention of the author establishing a unique solution that cover all the demands. As clearly presented in Figure 1.1, different strategies present advantages and disadvantages becoming more suitable than the others within a certain range of applications (discharge time and capacity). Among these different ways to store energy, hydrogen production by electrolysis with renewable electricity is a promising solution. Moreover, it can be used in fuel cells to produce electricity without emissions (see Figure 1.2).
However, due to expected issues in transport and storage of hydrogen, the production of other easy-to-handle renewable gases based on H_2 are also considered. In particular, the co-electrolysis of steam and CO_2 is an electrolysis process able to directly produce syngas (a mixture of hydrogen and carbon monoxide), that can be used to produce high added-value products such as

methane or methanol (Figure 1.3). Methane can be straightforwardly injected in the already existing natural gas grid and used to run domestic or industrial applications [4]–[6].

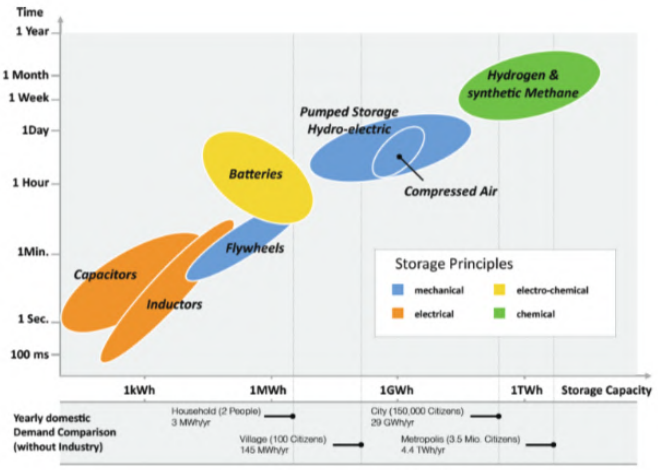

Figure 1.1: *Comparison between the different storage technologies, reporting discharge time and storage capacity [7].*

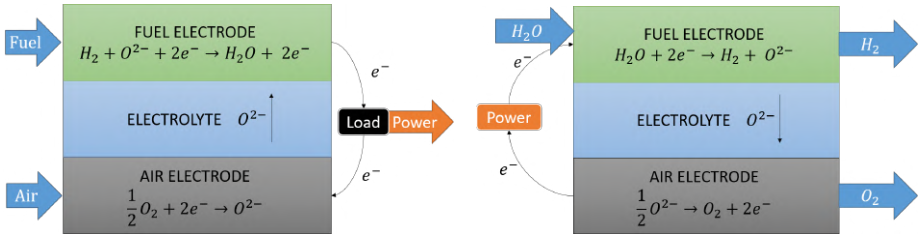

(a) SOFC *(b) SOEC*

Figure 1.2: *Principles of Solid Oxide Cells.*

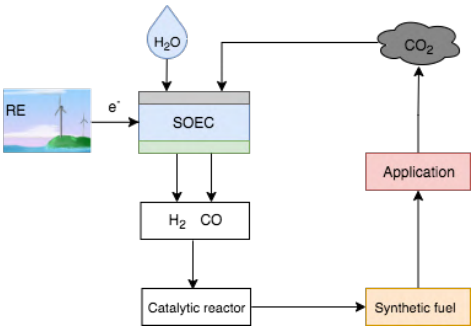

Figure 1.3: *Power-to-Gas cycle in carbon neutral regime.*

1.2 Solid Oxide Cells

Fuel cells are electrochemical devices capable to convert the chemical energy stored in the hydrogen bond into electrical energy with water as by-product. Historically, they have been classified based on the nature of the electrolyte materials:

- **AFC** (Alkaline Fuel Cell) uses a liquid solution of potassium hydroxide (KOH) as electrolyte that carries OH^- ions moving from the cathode side to the anode side, where their recombine with hydrogen to produce water [8]. They have been used by NASA in the Apollo space program [9]. Among their advantages, this class of fuel cell works at low temperature (50°-200°C), present low starting time and use non-expensive catalysts (Ni and Ag in anode and cathode, respectively) [8], [10]. However, they present a short life time since the electrolyte is corrosive and extremely sensitive to CO_2 contamination, which requires purification of gases before the supplying to the cell [8], [11].

- **PEMFC** (Proton Exchange Membrane Fuel Cell) uses a polymer membrane as electrolyte that transports protons when it is saturated with water, but does not allow the electron to pass [11]. The requirement of water limits the maximum operating temperature below 100°C. Electrodes require Pt catalyst loading, which increases the cost of the cell [12]. PEMFCs present high power density (around 350 mW/cm^2) quick start and lightweight, making them suitable for the transportation sector [10].

- **MCFC** (Molten Carbonate Fuel Cell) presents an electrolyte usually made of lithium and potassium carbonate, through which carbonate ions (CO^{3-}) can pass [13]. This type of cells requires temperatures above 600°C to obtain a molten conductive salt [11]. This temperature makes possible to feed the cell with natural gas instead of pure hydrogen [14], thanks to the spontaneous steam reforming taking place inside the cell [10]. MCFCs present an efficiency up to 60% [15] using materials such nickel compounds and stainless steel. Due to the relative high temperature and viscous nature of the electrolyte, the time to reach operation and to respond to power change is pretty long. Their application is related to stationary power generation [10], [11].

- **PAFC** (Phosphoric Acid Fuel Cells) presents an electrolyte based on phosphoric acid (H_3PO_4) dispersed in a ceramic matrix (usually silicon carbide) [16], working in the temperature range between 150°C and 200°C [17]. In this type of cell, the charge carrier is the hydrogen ion obtained from the splitting of molecular hydrogen at the anode. The proton is then recombined with oxygen to form water. CO_2 does not

affect the performance of the components allowing the use of reformed fossil fuels [11]. PAFCs present an efficiency around 40% and can tolerate some amount of carbon monoxide (not more than 1.5%, due to the platinum electrodes) [18]. On the other hand, sulfur poisons the electrodes [13]. They were the first cells to be developed, in the middle of 1960s, presenting a configuration really close to the original fuel cells proposed by *William Robert Grove* in 1839 [13]. Among their disadvantages, there is the cost of the platinum necessary in the electrodes, a significant weight of the device due to the requirement of heavier material for the bipolar plates, the harsh corrosive conditions that the materials have to stand and a relatively low power density compared with other technologies [16].

- The term *Solid Oxide Cell* (**SOC**) indicates the family of fuel cells and electrolysers which electrolytes are based on ceramic materials, i.e. solid oxides. Solid Oxide Fuel Cells work at higher temperatures (T=600°-900°C) compared with the other technologies listed before. This involves particular challenges due to the choice of materials for fulfilling the need of standing at such temperatures and for ensuring good thermal matching that avoids cracking during the heating up and down of the device. Related stability issues over time represents the main issue of this technology [19]. Finally, the requirement of operation at high temperature increases the starting up time, which makes difficult to cover expectations of portable applications. Opposite, their high efficiency makes this class of fuel cell the leading technology for the stationary application [20]. Also interestingly, SOFCs are able to work with a wide range of fuels, not only pure hydrogen, since the hydrocarbons have the potential to experience the internal reformation above 600°C, following the reaction:

$$CH_4 + H_2O \longrightarrow CO + 3\,H_2 \tag{1.1}$$

Since water is produced during operation at the fuel electrode, no additional water needs to be supplied. The steam reforming of hydrocarbons allows to use liquid fuels which have a higher energy storage capacity around a factor 6 compared with hydrogen [19], [21]. However, it is important to mention that the use of alternative fuels involves several issues that are still not solved. The efficiency of these devices using H_2 is above 60% and, considering the high quality of the heat produced during the operation, this efficiency can increase above 90% in Combined Heat and Power systems (CHP) [22]–[25]. Industrial developments are taking this technology to the market with major players as *Solidpower* and *Ceres Power* for residential CHP in the scale of kWs, *Bloom Energy* for security supply generators (hundreds of kW) or *LG*

Fuel Cell System for gas hybrids turbine (ca. 1 MW) [22].
Solid Oxide Fuel Cells are especially suitable for working as electrolysers in "reverse" mode due to the benefits of operating at high temperature, eventually, showing excellent efficiencies over 90% [26].

1.2.1 Working principles of SOCs

A Solid Oxide Cell is made of two porous electrodes with two different atmospheres, separated by a dense electrolyte, which is a ceramic material (a detailed overview of the material is reported in the Section (1.2.2). In fuel cell mode, air or oxygen are supplied to the air electrode (or cathode) and hydrogen (or other type of fuel) to the fuel electrode (or anode). In the fuel electrode, the hydrogen is oxidized to form water and two electrons, following the reaction expressed in Equation 1.3. This requires oxide ions to meet the hydrogen molecule releasing elctrons, which can only be reached in the so-called Triple Phase Boundary (TPB) where the electrolyte, the electrode and the gas phase are in contact. The reaction region can be extended beyond the TPBs near the electrolyte by using a material that shows Mixed Electronic Ionic Conduction (MIEC). Alternatively, composites mixing two materials, one with good ionic conductivity and another with good electronic conductivity, also enable this TPB extension. This is actually the most used solution, using as ionic conductor the same material of the electrolyte to improve the compatibility among the two layers. Moreover the fuel electrode has to be a good catalyst for the fuel oxidation. Due to the high working temperature, the kinetics of the reaction is favoured and metals like nickel can be used instead of expensive catalyst required in low-temperature fuel cells such as Pt, Pd, etc. [27] As previously mentioned, hydrogen reacts with the oxide ions coming from the electrolyte to produce water as by-product. The oxygen ions are driven across the electrolyte by the difference in oxygen chemical potential between fuel and air compartments of the cell following the Nernst equation:

$$E_{OCV} = E_0 + \frac{RT}{2F} ln \frac{p_{\mathrm{H_2}} p_{\mathrm{O_2}}^{1/2}}{p_{\mathrm{H_2O}}} \tag{1.2}$$

where E_0 is the difference of the equilibrium potential of the two reduction/oxidation reactions under standard condition, R is the universal gas constant, T is the temperature, F is the Faraday constant and p is the normalized partial pressure of each species.
The state-of-the-art (SoA) electrolyte material is 8mol% yttria-stabilized zirconia, which is a substituted fluorite with aliovalent cations [28]. The oxide ions flowing across the electrolyte are produced at the air electrode, where the oxygen is reduced to oxygen ions using additional electrons (Equation

1.4). As well as in the fuel electrode, the reaction takes place at the TPBs. If the air electrode material is a pure electronic conductor, the suitable conditions are only present at the interface with the electrolyte, while, if a MIEC is employed the active area can be enlarged. SoA cathode materials are based on the perovskite structure (ABO_3) which allows a large amount of oxygen vacancies to be formed, determined by the B-side cations [29], [30]. Externally closing the circuit between the anode and the cathode results in an overall reaction as presented in Equation 1.5 and a continuous flow of current.

$$\text{Hydrogen oxidation: } H_2 + O^{2-} \longrightarrow H_2O + 2\,e^- \tag{1.3}$$

$$\text{Oxygen reduction: } \frac{1}{2}\,O_2 + 2\,e^- \longrightarrow O^{2-} \tag{1.4}$$

$$\text{Overall cell: } H_2 + \frac{1}{2}\,O_2 \longrightarrow H_2O \tag{1.5}$$

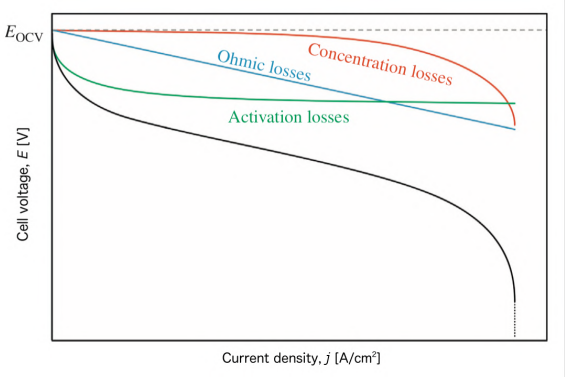

Figure 1.4: *In black, typical V-j curve of a SOFC, in green, V-j curve considering only activation losses, in blue, considering only the ohmic losses and in red the concentration ones [22].*

A typical polarization curve which characterizes a fuel cell is presented in Figure 1.4. In an ideal case, the Open Circuit Voltage (OCV) is determined from the Nernst equation (Equation 1.2). The deviation from the ideal value of OCV typically indicates gas leakages due to poor sealing or partially porous electrolytes. The experimental V-j curve can be divided in three parts according to the major overpotential contributions. The beginning of the curve is dominated by the activation losses, i.e. the potential required to drive the reaction at the desired rate. The middle corresponds to ohmic losses at the electrolyte or the electrodes. At high current densities, the so-called concentration losses are related to a gas diffusion-limited behaviour. High consumption of reactants at high current densities involves a poor gas supply to the TPBs generating an overpotential **Cooper2017.**

The same cell can work as an electrolyser, to produce hydrogen and oxygen from steam, when the cell polarisation is forced opposite. In electrolysis mode the role of the electrodes is exchanged, namely, the cathode become the anode, and vice versa, reason why the preferred use of the terms "fuel" and "air" electrodes. In electrolysis mode, the steam is provided to the fuel electrode, where the reduction of water takes place. The steam is electrochemically reduced with electrons provided by an external source of electricity. Hydrogen and oxide ions are formed (Equation 1.6). Oxide ions are transported through the electrolyte to the air electrode where they recombine and release oxygen molecules (Equation 1.7). The reactions taking place in a SOEC are presented in Equation 1.8:

$$\text{Fuel electrode: } H_2O + 2\,e^- \longrightarrow H_2 + O^{2-} \tag{1.6}$$

$$\text{Air electrode: } O^{2-} \longrightarrow \frac{1}{2}\,O_2 + 2\,e^- \tag{1.7}$$

$$\text{Overall reaction: } H_2O \longrightarrow H_2 + \frac{1}{2}\,O_2 \tag{1.8}$$

Compared with other electrolysis technologies, SOECs exhibit higher rate of hydrogen production, due to the higher working temperature, since the reactions which take part are thermally activated [31].
Finally, as previously stated, it is worth remarking that providing the cell a mixture of water and carbon dioxide it is possible to directly obtain syngas (mixture of hydrogen and carbon monoxide) as product, that can be further employed to produce valuable hydrocarbons, such as in the Fisher-Tropsch process [32]. In this case the reactions taking place are the following:

$$\text{Fuel electrode: } CO_2 + 2\,e^- \longrightarrow CO + O^{2-} \tag{1.9}$$

$$\text{Air electrode: } O^{2-} \longrightarrow \frac{1}{2}\,O_2 + 2\,e^- \tag{1.10}$$

$$\text{Overall reaction: } H_2O + CO_2 \longrightarrow H_2 + CO + O_2 \tag{1.11}$$

1.2.2 Materials for SOCs

In the next sections, the state of the art materials used in SOCs manufacturing are presented. The review has been divided based on the function of the components: electrolytes, fuel and air electrodes and interconnects.

1.2.2.1 Electrolytes

One of the key components in SOCs is the electrolyte. It is made of a ceramic material that becomes a fast ionic conductor at high temperature. This imposes a working temperature above 600°C. At the same time, the electrolyte needs to prevent the conduction of electrons to avoid the short-circuit of the cell. By definition, the electrolyte needs to be thermally stable at high temperature and chemical inactive in oxidant and reductive atmosphere and it has to be gas-tight to avoid the mixing of fuel and air, which is detrimental not only for the performance of the cell but also for potential safety issues due to the high exothermic reactions taking place when hydrogen and oxygen meet together. Moreover, reasonable strength and mechanical properties are necessary, especially when the electrolyte is the support layer of the cell.
Oxides with fluorite and perovskite structures have been the first choice of materials for this kind of application. In particular, the 8mol% yttria stabilized zirconia (8YSZ) is the state-of-the-art material for electrolytes due to its good ionic conductivity (although not the highest, as seen in comparison with other fast conductors in Figure 1.5), cost, stability and chemical and mechanical compatibility [28], [33].

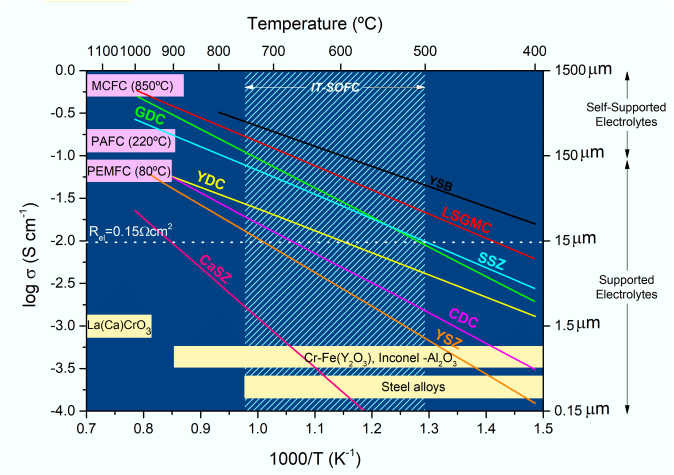

Figure 1.5: *Ionic conductivity as a function of the temperature for different electrolyte materials. The value $log\sigma = -2$, marked with a dot line, represent and ASR of the cell of $0.15\,\Omega\,cm^2$ in an electrolyte of $15\,\mu m$. In this conditions GDC can operate around 500° C, while YSZ requires 700° C.*

Figure 1.5 is a valid guide to follow the latest trend in material choice for SOC electrolytes, the left axis reports the values of ionic conductivity, while the right axis indicates the thickness of the electrolyte, in order to facilitate the chose of appropriate thickness, working temperature and material. In

fact, the ionic conductivity decreases with temperature with different slopes depending on the material. At a fixed temperature minimizing the ohmic resistance can be achieved by using materials with higher ionic conductivity or decreasing the thickness of the layer itself, according to the Second Ohm's Law:

$$R = \rho \frac{L}{A} \tag{1.12}$$

The state of the art strategy is to produce the thinnest electrolyte as possible in yttria stabilized zirconia (YSZ) [34], since it shows good chemical and mechanical stability and it can be produced with high quality [35]. Researches have been dedicated to explore new combination of materials, starting from zirconia based compounds, like scandia-stabilized-zirconia (SSZ), which is characterized by higher ionic conductivity compared with YSZ, but it presents some disadvantage: a phase transition between 600°and 700°C, that can be suppressed with the addition of Gd_2O_3, Y_2O_3, CeO_2 and Al_2O_3; aging issues over time and higher cost compared to YSZ due to the high cost of scandium [36]–[38].
As an alternative, ceria shows high ionic conductivity when doped with gadolinia, samaria, yttria or calcium, but at high temperatures, it becomes unstable at low oxygen partial pressure. Despite the issue, it is typically used as an interlayer to avoid unfavourable reactions with the electrodes. In particular, gadolinia doped ceria (GDC) has been used in SoA cells as a diffusion barrier layer to avoid the formation of strontium and lanthanum zirconate, typically occurring for YSZ in contact with SoA lanthanum-based air electrode side [36], [39]–[41].
Except from the fluorite structure electrolyte, such zirconia and ceria based ones, material based on perovskite structure, such as lanthanum gallate electrolytes provide an alternative to the state-of-the-art materials. The most commonly reported is LSGM (Lanthanum Strontium Gallate Magnesite, $La_{0.8}Sr_{0.2}Ga_{0.8}Mg_{0.2}O_3$) with or without the addition of other elements such as cobalt or iron, which can increase its ionic conductivity [42]. Although undesired reactions with the fuel electrode are possible, LSGM is considered a possibility to decrease the working temperature of SOFCs [28], [43]. Pursuing lowering the operation temperature other materials based on lanthanum and bismuth have been proposed such as LAMOX, BICUVOX, ESB and DWSB. These materials, studied in the last years, have not matched yet the overall performance of zirconia based electrolytes, therefore remaining restricted to research uses [44]–[47].

1.2.2.2 Fuel electrodes

The fuel electrode is usually a cermet, i.e. a ceramic-metal composite to match the thermal expansion coefficient of the other components of the cell,

especially the electrolyte. Its requirements are to be electrically conductive, to show a high electro-catalytic activity and, if applicable, to provide direct internal reforming. It should be stable in reducing environment, present a large number of triple phase boundaries and be abundantly available and at low cost. Moreover, it has to avoid coke deposition (internal reforming) and sulphur poisoning. The stat-of-the-art materials are nickel-based cermets that work in all the temperature range and are available at low cost. Lately perovskite oxides like titanates or chromites have been studied to avoid oxidation and agglomeration issues present in metal-based composites [27], [48]. Alternatively, some research efforts have been dedicated to materials able to direct reforming of hydrocarbons fuels without finding ultimate solutions [36].
Nickel is introduced in the layer as nickel oxide (NiO), since its sintering temperature is suitable with the production of the following ceramic layers. Then the oxide is easily reduced as first step of the operation of the cell, while introducing the fuel in the chamber [49]. The change in volume resulting from the reduction of the nickel oxide generates an increase in the porosity of the fuel electrode that allows the diffusion of the gases, but can cause the cracking of the anode as well. For this reason and to match the stress with the electrolyte interface and avoid the coarsening of the nickel particles at the working temperature, ceramics are added to the nickel oxide. Usually the choice is to use the same material of the electrolyte, to increase the chemical stability and reduce the stresses. The nickel oxide reduces easily to metallic nickel, but since the coarsening at operating temperature, which never disappear even with the addition of ceramics, a oxidation process after operating leads to cracks in the fuel electrode that can affect the integrity of all the cell, especially when the nickel plays the role of support layer [50]. Research has been devoted mainly to infiltration solution to improve the tolerance to carbon and sulphur, respectively with barium compounds and ceria [51]. Some other studies focused in changes in the ceramic part of the cermet, trying scandia stabilized zirconia [52] and ceria doped with gadolinia [53], samaria [54] and yttria [55]. With the same purpose some studies tried to substitute nickel with copper, which is cheaper [56].

1.2.2.3 Air electrode

The choice of material for the air electrode is strictly dependent on the sintering and working temperature of the cell. In fact, most of them react with zirconia at the manufacturing temperature and the conductivity and catalytis activity strongly depend on the operating temperature (thermally activated). The state-of-the-art perovskites are the lanthanum based compounds. The SoA at high temperatures is the lanthanum strontium manganite (LSM) mainly due to its good chemical compatibility with YSZ, the

most common electrolyte material. As it is a purely electronic conductor, it is often mixed to extend the TPB region [57]. LSM reacts with YSZ above 1200°C [58], for this reason it has been coupled with ceria-based diffusion barrier layer, such as samaria [57] or gadolinia doped ceria [59].
LSM conductivity presents reasonable electronic conductivities at intermediate to high temperature (800°-1000°C), showing a polarization resistance around $1\,\Omega\,cm^{-2}$ at 1000°, but it increases to $2000\,\Omega\,cm^{-2}$ at 500°C [60]. In this intermediate range of temperatures, other perovskites are preferred [61]. For instance, LSC (Lanthanum Strontium Cobaltite, $La_{0.6}Sr_{0.4}CoO_{3-\delta}$) is a mixed conductor, used for its high electrochemical activity. However, it shows thermal mismatch with the electrolyte. Because of this, other alternatives based on ferrites such as LSCF (Lanthanum Strontium Cobalt Ferrite, $(La_{0.6}Sr_{0.4})_{0.95}Co_{0.2}Fe_{0.8}O_{3-\delta}$), which matches the expansion of the electrolyte are often used. Both materials react with zirconia-based electrolytes, reason why a ceria interlayer is added to prevent the formation of detrimental phases mentioned above [29].
The next generation of low temperature air electrodes is pursued by using new compounds such as layered perovskite structure in $Ba_{0.5}Sr_{0.5}Co_{0.8}Fe_{0.2}O_3$ [62], $PrBaCo_2O_{5+\delta}$ [63] or Ruddlesden-Popper phases in nickelates (K_2NiF_4-type) [64]–[66].

1.2.2.4 Stack components

The outcome of a single cell cannot meet the requirements of power or hydrogen production. The cells are therefore assembled in a stack to increase the outputs. To connect the cells, interconnects are required. Their purpose is to separate the two atmospheres, distribute the gases and collect the electrons to the external circuit. Recent research has been devoted to produce stable and performing interconnects with an affordable cost. In a full ceramic concept, the most used option was lanthanum chromite ($LaCrO_3$) doped with cobalt, iron, nickel, magnesium, copper, strontium, calcium, and vanadium [67]. In the last years, chromites based on yttrium, neodymium or strontium have been developed. Due to the high cost of rare earth-based perovskites, their use is limited [68]. Owing to the generally high cost of ceramic materials, the application of ceramic interconnects is exploited only in entirely ceramic stacks, as the one presented by *Saint Gobain* [69].
To limit the cost of the interconnect, metals have been proposed instead of ceramics, especially after the operation temperature of SOCs was lowered below 800°C. Precious metals have been discarded due to the inconvenience of their price and the possibility of dissolving in oxygen and hydrogen atmosphere, e.g. silver [70]. Since the interconnect has to resist reducing and oxidising atmospheres at high temperatures, some metals, such as aluminium, silicon and chromium are able to produce an oxide layer to protect the layers

below from corrosion. These materials were used to develop alloys. The ones based on aluminium (NiCrAl, CoCrAl and FeCrAl) show excellent corrosion resistance, but present low electronic conductivity, hindering their use as an interconnect [68]. Chromia provides less resistance to corrosion, but its conductivity is higher than the other oxides, so alloys based on the system NiCr, NiCrFe or CrFe were investigated (with preference for the Cr-Fe one for the possibility of matching the TEC with the one of the cell components). Commercial solutions are largely based on ferritic steels and chromium based alloys, austenitic steels and nickel alloys are a possible solution when high creep resistance is required, but their cost and the thermal expansion limit their use.
One of the critical issues of metallic interconnects is the chromium evaporation under operative conditions, which causes the reduction of performance of the cell itself, poisoning the cathode and the cathode/electrolyte interface [71]–[74]. In detail, LSCF electrodes suffer less from chromium poisoning compared with LSM ones, result proven in a working stack over two years [71], [75]. In the case of LSCF electrode, coatings are applied on the steel to reduce the contact resistance, using rare-earth oxides [76], [77] or perovskites [78]–[80]. In the case of LSM, protective coatings are required, usually based on binary oxides such as MnO_2, Co_3O_4 and CuO, which are favourable regarding the cost but cannot stop completely the poisoning [81]. In long term applications, stability over thousands of hours is required. Only few examples of stacks have been reported. One from Jülich, which interconnect is coated with manganese oxide and a layer of perovskite from the system $LaMnO_3$–$LaCoO_3$–$LaCuO_3$ has been operated over 63000 hours with reasonable results [82]–[84].
The interconnect is in contact with the fuel electrode as well, which is usually made by a Ni cermet. At the operating temperature diffusion of chromium into nickel and Ni into the steel can cause different problems. In the first case, changing the contact properties between materials and eventually reducing the catalytic activity of the electrode [68] and in the second case, promoting the local formation of austenitic steel, which behaves different in terms of conductivity and thermal expansion, opening the possibility of dramatic mechanical stresses during cycling of the device [85].
In planar designs of stacks, sealing are applied to separate the two atmospheres. Since the high working temperature the materials applied are glasses, brazing alloys and mica [86], [87]. Actually the state-of-art is directed to the use of barium-calcium-aluminosilicate glasses [88], this class of materials suffer from chromium poisoning as well, with the formation of $BaCrO_4$ [89], to prevent it aluminization [90] and spinel coating [91] have been applied.

1.2.3 Solid Oxide Cells and stack configurations

Solid Oxide Cells have been studied for decades and they are already available in the market in different configurations and designs. Tubular and flat geometries are the main configuration and, for each of them, different solutions have been explored. For the tubular cells the most common architectures are close-end-tube (Figure 1.6a), open micro-tubular cells (Figure 1.6b) or flattened tubular cells (Figure 1.6c).

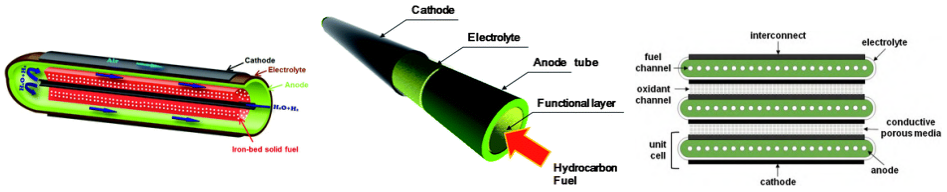

(a) Close end tubular cell [92] *(b) Micro-tubular cell [93]* *(c) Flattened tubular cell [94]*

(d) Design solutions for tubular cells.

For the flat ones, square and rectangular shapes have been adopted (Figure 1.7a and 1.7b), with the gas channel shaped in the cell or not. Large areas have been reached such as the one presented by *NextTech* in 2011 (Figure 1.8c) [95].

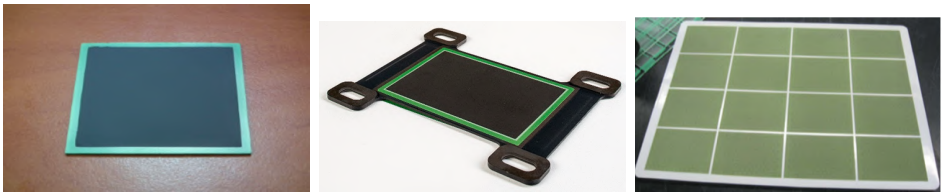

(a) Square cell [96] *(b) Rectangular cell [40]* *(c) Flat cell of 1200 cm^2 [97]*

Figure 1.7: *Design solutions for flat cells.*

For both shapes the cells are divided based on the support layer, which can be a layer of the cell itself, usually thicker to provide the mechanical properties or an external layer, that may be the interconnect or another support, as sketched in Figure 1.8

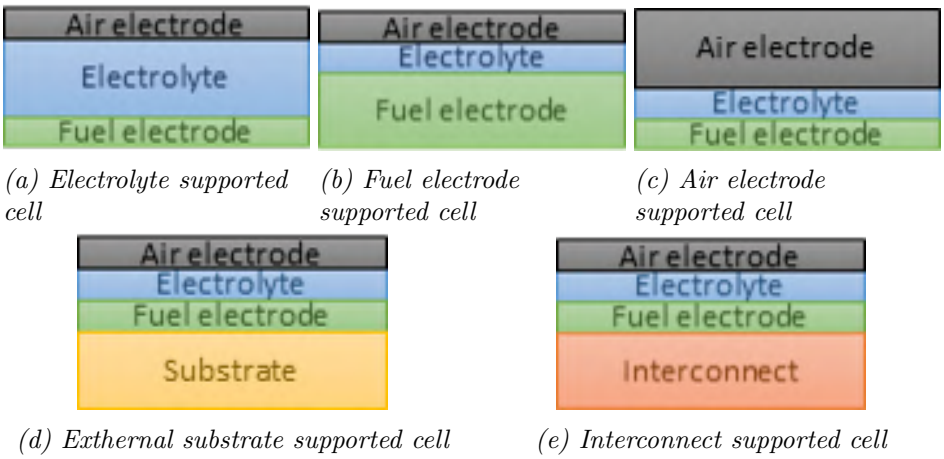

(a) Electrolyte supported cell

(b) Fuel electrode supported cell

(c) Air electrode supported cell

(d) Exthernal substrate supported cell

(e) Interconnect supported cell

Figure 1.8: *Different types of supported cells, represent in flat configuration.*

Depending on the supporting layer there are different advantages and disadvantages. Electrolyte supported cells suffer less from anode re-oxidation and offer strong mechanical properties, but they require to work at high temperature to reduce the ohmic losses of the electrolyte. On the other hand, on fuel electrode supported cells, the ohmic losses are reduced, but the probability of cracking of the support increases in case of re-oxidation of the nickel. Moreover, the air electrode does not suffer of oxidation issues, but its thickness can reduce the conductivity and limit the mass transport. In the case of supporting from external layers, they offer the possibility of reducing the ohmic losses decreasing the thickness of the different layers. However, if using the interconnect as support, its structuration for flow distribution has to be reduced to enable the production of the cell. The use of an independent support (beyond the necessary components of the stack) adds complexity during the manufacturing [95]. The choice of a specific configuration clearly fixes the manufacturing techniques to be employed and the design of the cell. As an uttermost example, micro-SOFCs based on silicon substrates use mainstream microelectronics and thin film manufacturing techniques since their active parts are in the nano and micro-scale, which allows working at very low temperatures [98].

Once the cell is produced, various cells has to be connected to obtain the necessary power or hydrogen output, the obtained stack can present different designs depending on the shape of the initial cells. The most used configurations are reported in Figure 1.9. The planar design, shown in Figure 1.9a, is currently the most common. In this planar stacks, the cells and interconnects are in the shape of plates that are stacked in series, giving great flexibility

in the design of the manifolds and in the fabrication of components, which need to be extremely flat to avoid mechanical failure during the assembly.

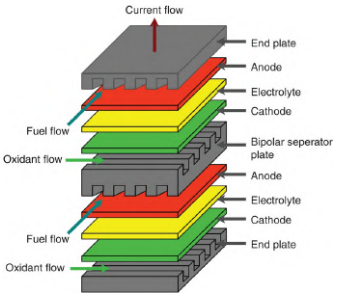

(a) Planar stacking [99]

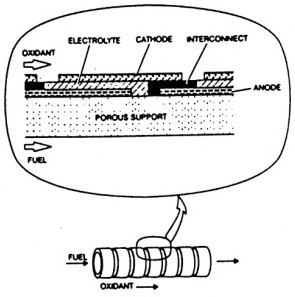

(b) Segmented cells in series design [100]

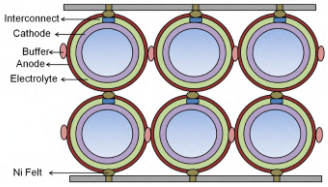

(c) Tubular stacking [101]

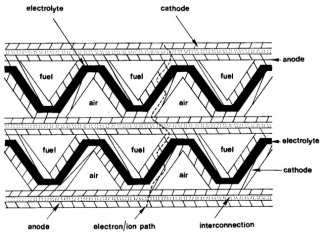

(d) Monolith stack [102]

Figure 1.9: *Different stacking configuration.*

The segmented-cells-in-series-design consists of cells connected in electrical and gas flow series. This solution is valid both for planar and tubular cells (Figure 1.9b). The configuration improves the gas distribution and consequently the performance of the device. However, sealing issues arise due to the number of connections required [22]. Tubular stack is the connection of tubular cells as reported in Figure 1.9c, this option reduces the issues of thermal stress and sealing, which can be completely avoided. On the other hand, it imposes long current collection paths, which could reduce the power density [103]. The monolithic design, Figure 1.9d, is characterized by thin cells connected by corrugated plates to minimize the volume and the flow. This solution involves issues as the difficulties of producing stack components and the limitation of fabrication techniques [100].

1.2.4 State-of-the-art Solid Oxide Cells manufacturing

One of the most popular techniques to produce ceramic materials for SOC is tape casting. This is used for the production of porous electrodes or dense electrolyte supporting layers. The ceramic material is supplied by a slip or slurry made of the ceramic powders, solvents, binders, dispersants and plasticizers to optimize the rheological properties and the quality of the final tape [104]. The formulated slip is deposited on a polymeric substrate and here spread by one or two blades (doctor blade) to homogenize the thickness (Figure 1.10). The tape is dried under controlled atmosphere and, eventually, cut and sintered [105]. Two tapes can be connected by co-lamination and calendaring. In this case, the original tapes are joint passing between two or more rollers and sequentially fired together to guarantee the adhesion [95].

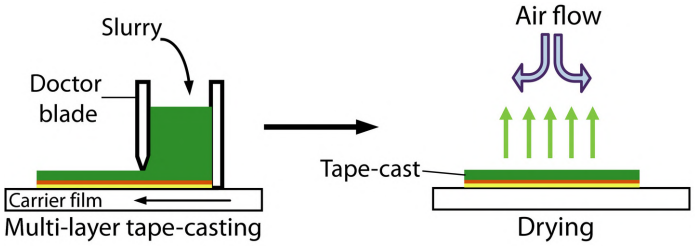

Figure 1.10: *Tape casting [106]*

When a thickness higher than 800 µm is required, pressing of the powder is preferred (cold, warm, hot pressing or cold, hot-isostatic pressing), due to the long drying time if such component is produced by tape casting, this technique is longer and more expensive than the previous due to the necessity to produce the pieces unit-by-unit, so it is used for small pieces or complex shapes [107].
For tubular designs, the most advantageous method is the extrusion. In this case, the powders are mixed with water and binders obtaining a viscous slip compared with the one for tape casting. Afterwards, the tubes are dried, cut and sintered [108].
Once obtained the support layer, the others need to be deposited on top. The choice of the deposition technique is related to the thickness, microstructure, substrate geometry and cost. For planar design the most widely used technique is screen printing. The slip is in the same order of viscosity of the ones used for tape casting, but with a pseudo-plastic behaviour due to the application methodology shown in Figure 1.11. The material is squeeze through a mesh and the shape has to be kept until the end of the drying process. The thickness can vary between 5 and 100 µm for each deposition, depending on the mesh and the slip used; the sintering temperature and the

composition influence the density of the final layer [109].

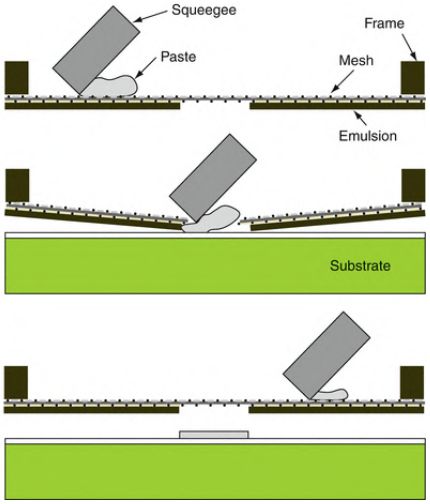

Figure 1.11: *Screen printing methodology [110].*

For obvious reasons the screen printing cannot be applied on tubular design. In this case, a valid technique, used for planar cells as well, is spray coating. Suspensions of ceramic powder with binders and solvents are nebulized using compressed air and deposit on the substrate. Overspray and not-homogeneous deposition are among the main disadvantage of this technique, which is still the most used for complex geometries.[95]
When thin layers are pursued, dip and spin coating are valid solution, used respectively for tubular and planar designs. In the first case the substrate is immersed in the slurry of the desired material, process that can be repeated different times if major thickness is desired [111]; in the second approach the deposition occurs during the rotation at high speed of the substrate [112]. For both techniques the viscosity of the slurry plays an important role in the homogeneity of the layer.
Among the industrial techniques, roller and curtain coating are implemented to deposit layers on flat cells in a production line, without the handling of the operator. In the first case, shown in Figure 1.12a, the material is spread by rollers, while the substrate is moving below, the thickness of the layer can be adjusted by tuning the gap between substrate and rollers, obtaining final values between 5 and 50 µm. In the curtain coating, Figure 1.12b, the material falls continuously from a tank as in a waterfall and the substrate is moving below; the unused suspension can be recovered and in contrast to the roller one, not planar substrate can be coated [113].

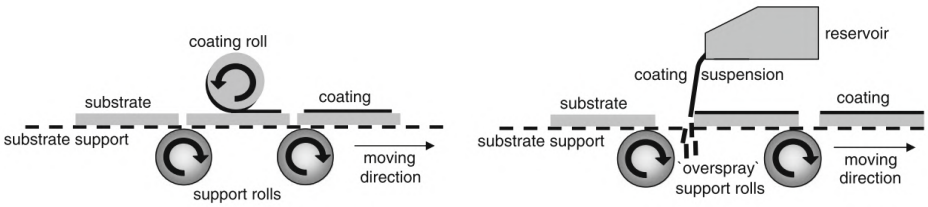

(a) Roller coating *(b) Curtain coating*

Figure 1.12: *Industrial coating techniques [88].*

Alternative techniques used in the laboratory scale are: atmospheric and vacuum plasma spraying [114], [115], physical vapour deposition (evaporation, sputtering, pulsed laser deposition) [116], [117] and chemical vapour deposition [118], those techniques although proven valid to manufacture thin layers are sometimes difficult and expensive to scale in big production lines.

1.3 Catalytic reactors for methanation reactions

Methanation reactions of CO and CO_2 are known for more than a century. They were discovered by *Sabatier* and *Senderens* in 1902, and gained more interest in the last decades. Originally CO methanation was used to purify syngas, mainly in ammonia production and later to purify hydrogen steam for PEMFC. In the oil crisis of 1970s, CO methanation was used to produce synthetic natural gas (SNG) from coal [119]. At the beginning of 21^{st} century, with the increasing awareness of climate change and greenhouse gases impact, the methanation of carbon dioxide gained interest, for the opportunity of reducing CO_2 emission and storing the electricity produced by renewable resources in the form of methane (Power-to-Gas), as presented in Section 1.1. The production of methane from hydrogen requires a carbon source, usually carbon monoxide or dioxide, enable the gathering of carbon based emission and the use to produce valuable products [6].

1.3.1 Working principles of Sabatier reactors

Methanation processes convert carbon oxides and hydrogen into methane. In case of carbon mono-oxide, the reaction is described by Equation 1.13, in case of carbon dioxide by Equation 1.14.

$$CO + 3\,H_2 \rightleftharpoons CH_4 + H_2O\,(g) \tag{1.13}$$

$$CO_2 + 4\,H_2 \rightleftharpoons CH_4 + 2\,H_2O\,(g) \tag{1.14}$$

Although the thermodynamic favours the methanation reaction ($\Delta G_{298K} = -130.8 kJ/mol$), a catalyst is required to maintain high conversion rates and selectivity [120]. The possible catalyst suitable for methanation reactions were completely identified by *Fischer, Tropsch* and *Dilthey* in 1925 [121] and are here reported in decreasing order of activity: Ru, Ir, Rh, Ni, Co, Os, Pt, Fe, Mo, Pd, Ag. Taking into account cost, activity and selectivity, *Mills* [122] reduced the list and highlighted the suitability depending on the activity: Ru > Fe > Ni > Co > Mo and selectivity: Ni > Co > Fe > Ru.
The term catalyst is usually referred to a complex system of materials. The most important is the active metal, the material described until here, which is usually dispersed on metal oxide supports. These supports present a high surface area to disperse the active metal, good surface properties to allow a good attachment between the phases and stability at the working temperatures. Eventually promoters can be added to improve the electron mobility of the catalyst and/or enhance the dispersion and thermal stability, changing the chemical composition and the microstructure of the catalyst [123].
Ru-based catalysts show high activity even at low temperature [124]. *Abe et al.* obtained the maximum yield of methane at 160°C on Ru nanoparticles

on TiO_2 support, proving that the size of the particles determines the hydrogenation activity while the selectivity toward methane improves with the increase of the particle size [125], [126]. Generally, Ru is characterized by long stability over time and high activity. Moreover, only small amounts are necessary to achieve high performances. It can be used in combination with nickel to form a bimetallic compound with enhanced performance. When Ru segregates on the surface of the catalyst, it offers more Ru active sites, improving the resistance to sulphur poisoning, a critical issue in the nickel based catalyst [127], [128]. The main disadvantage of the Ru is its cost, as well for other noble materials, such as Ir, Rh, Os, Pt and Pd, which are valid option as well. In particular, Pd conversion is strongly influenced by the support, being the best combination Pd/TiO_2, showing a strong selectivity towards methane in carbon monoxide hydrogenation, while for carbon dioxide, mesopourous silica is preferred [129], [130]. Similarly, Pt shows high activity on TiO_2 nanotubes and Rh on CeO_2 [131]. It is worth to mention that Mo as active metal tend to produce other hydrocarbons, but it is a sulphur-resistance catalyst in form of metal, oxide or sulphur [132]. In the same direction, combining Co and Mo on Al_2O_3 supports improves the catalytic activity of the system and enhances its resistance to sulphur contamination [133]. Co can be added to Ni and Pt as well to increase the methane yield compared with the single-metal counterparts [134], [135]. A similar behaviour is shown by iron, which has a low methanation activity when pure, but forming the bimetallic Fe/Ni the performance bypass the ones of pure Ni [124], [136].
Nickel is the widest used catalyst due to the fulfilling of high activity, selectivity and low cost, although the performance vary depending on the size of the particles [137], the amount of metal in the catalyst [136], and the composition of the support [138].

1.3.2 State-of-the-art manufacturing of methanation reactors

Different solutions in the design of current methanation reactors have been proposed, reaching different level of maturity (see Figure 1.13).

The simplest configuration of a reactor is the fixed-bed one: the solid catalyst is loaded into the bed, which may consists of a high number of narrow tubes or structures to support the powder [139], [140]. Fixed-bed reactors present high reaction rate and the possibility to produce steam at high temperature to be re-used. However, issues related to the formation of hot-spots, which requires a cooling system and results in a complex set-up, are occurring. Fluidized reactors, in two or three phases, use a liquid or gas phase as carried medium to suspend the solid and behave as a fluid. They have high heating rate and good heat management and mass transfer, but they

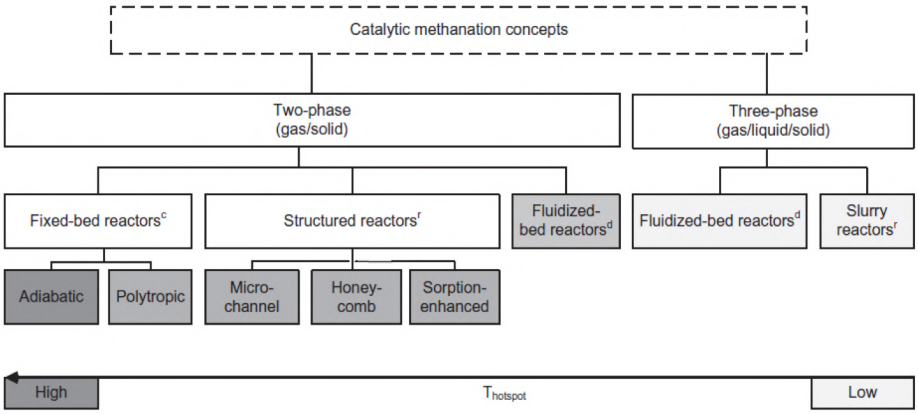

Figure 1.13: *Different solutions for Sabatier reactors, in superscript the level of development: c – commercial, d – demonstration scale, r – research [119].*

present lower reaction rates and higher catalyst consumptions due to friction [141], [142]. The advantages of these two classes of reactors have been combined in the so-called structured reactors, which show a moderate number of hot-spots reaching the reaction rate limits due to the thermodynamic of the process. Despite this advantage, this class of reactors is the most expensive one, which limits its deployment [119].
Micro-reactors, which possess characteristic sizes in the micro-scale, present many advantages, since it is possible a fast mixing of the substance and a better control and transfer of temperature and consequently better control of the reaction, less degradation of the catalyst, energy saving, and higher ratio surface to volume [143]–[145]. Lately, efforts have been devoted to introduce micro-reactors at an industrial plant scale [146].
Many companies focus their interest in the fixed-bed solution, for instance, *Air Liquid* still produces reactors developed in the 70s based on two adiabatic fixed-bed reactors, with intermediate cooling system and gas recycling, these reactors have been applied in oil refineries and coal gasification plants respectively [147], [148]. *Haldor Topsøe* produces a similar reactor to the one of *Air Liquid*, but with 3-4 reactors instead of two [149]. Other commercial products were proposed by *Ralph M. Parsons (RMP), Imperial Chemical Industries (ICI), Koppers Clariant* and *Foster Wheeler*, based on different adiabatic fixed-bed reactors connected in series. Although the commercial availability of these products for many years, research in the fixed-bed reactors is still taking place devoted to the reduction of cost and increase of the flexibility [119].
Since the formation of hot-spots is a critical disadvantage in the fixed-bed reactors, *Linde* developed a reactor cooled by a heat exchanger and a second

adiabatic reactor. To overcome the issue of the hot-spots, the fluidized-bed reactors were realized with internal heat exchange by two companies, *Bituminous Coal Research Inc.* and *Thyssengas. Chem Systems Inc.* developed a triple-phase reactor, in which the catalyst was suspended in an inert fluid (mineral oil) to improve the heat removal and the temperature control [119]. The interest in these two approaches increased over the years and pilot plants have been developed by *Paul Scherrer Institute (PSI)* and *Engie gas company* based on two phases fluidized-bed reactors, while *Gotz et al.* focused on the three phase reactor, even if the addition of a third phase complicate the mass and heat transfer [150]–[152].
Regarding the application for methanation processes, it has been proved that the heat management in micro-channels reactors, obtained by the stacking of etched stainless steel foils as shown in Figure 1.14, was improved compared to conventional reactors, in which the maximum peak of conversion can be missed due to temperature gradients [153], [154].

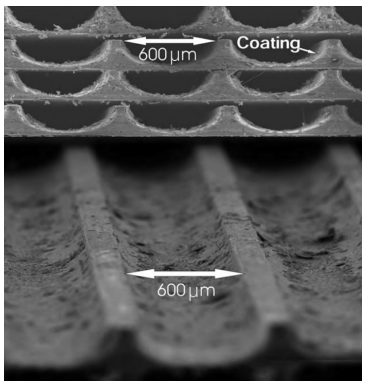

Figure 1.14: *Stacked micro-channels plates to realize a reactor, detail of a channel [154].*

Brooks et al. designed a micro-reactor with cooling channel in order to improve the heat management, found that the reaction starts easier at above 350°C, due to the higher kinetics and performance increase around 10% with a decreasing gradient of temperature with respect to an isothermal profile [155].
In general plates with micro-channels, later assembled in a reactor are produced by etching [156], [157], milling [158]–[160] or hot pressing [161]. Few studies reported the production of monolith bed by extrusion based on metals, such as aluminium [162] and copper [163]. The material choice is oriented to stainless steel [154], [164], metals resisting to corrosion [146] such as reported cases of Fecralloy (Al-alloyed ferritic stainless steel) [159], [160] and aluminum [161].

The preparation of the catalyst influence as well the conversion, affecting the dispersion of the active material in the support [164] and their interaction [165].
The traditional production methods are: impregnation [166]–[168], precipitation [169]–[171] and sol-gel [172], [173]. Other methods, less employed, are: deposition-precipitation [174], hydrothermal synthesis [175], ion exchange method [176], mechanical mixing [177], solution combustion method [178] and microwave heating [179]. In particular co-precipitation and co-impregnation offer higher dispersion, stability and conversion compared to the catalyst produced by the respective sequential method [180], [181].

1.4 3D printing technologies

Additive manufacturing, also known as 3D printing, is a shaping technology consisting on adding material layer by layer until the manufacture is finished. This is opposite to conventional fabrication of three-dimensional pieces from a bulky mass by subtraction (milling, drilling, cutting, etc.). The user designs the piece with a CAD (Computer-aided design) software and provides it to the 3D printing machine, which automatically produce the piece. This addittive approach enables a better use of raw materials, reducing the wastes, compared with traditional manufacturing techniques based on removal of material (Figure 1.15) [136].

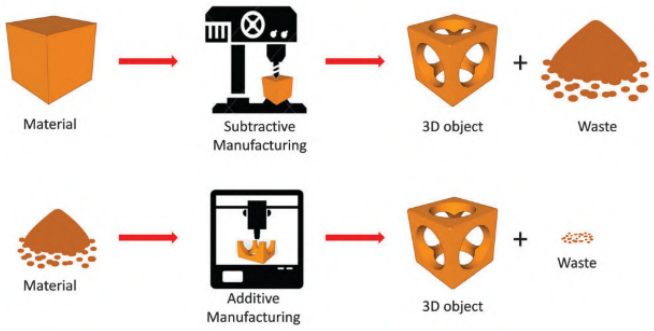

Figure 1.15: *Comparison between subtracting and additive manufacturing [182].*

3D printing is of special interest for highly valuable materials such as ceramics difficult to shape with conventional techniques. To conventionally produce ceramic pieces, the powder of the material are mixed with a binder, shaped in the desired form, by injection moulding, die pressing and tape casting, and follow by a sintering step at high temperature. These manufacturing techniques limit the possible designs, often limited to flat and tubular geometries. Moreover, further processing is extremely expensive due to the stiffness and brittleness of the ceramics, giving rise to problems such expensive tooling, high cracking probability and final low resolution. In case of additive manufacturing, toolless processing is possible and currently unfeasible designs are allowed.
A possible classification of the 3D printing techniques relies on the form in which the printable material is supplied to the printing stage. Many authors have divided the techniques according to Figure 1.16.

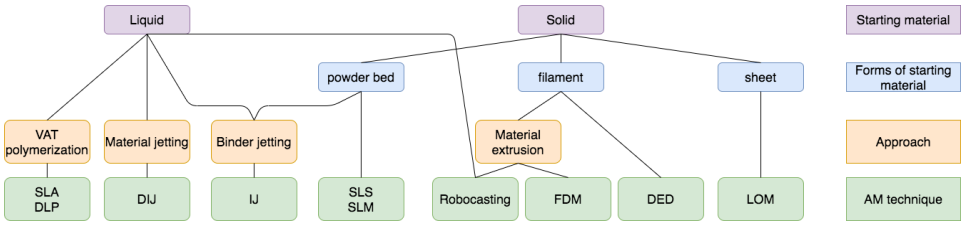

Figure 1.16: *Categorization of 3D printing technologies.*

The VAT polymerization systems, in which the feedstock is in a liquid form, includes the **SLA** (sterolithography) and **DLP** (Direct Light Processing). The origin of 3D printing is placed in 1986, when Charles Hull realized the first plastic stereolithography system [183]. SLA can work with plastic materials and metallic or ceramic ones [184], [185].

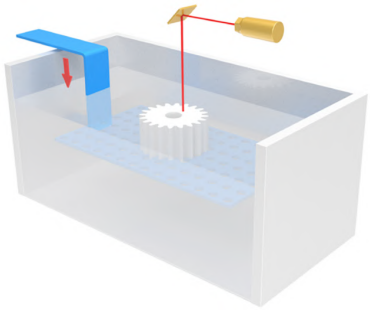

Figure 1.17: *SLA [186]*

Figure 1.17 shows the printing process by SLA. The printing platform, the base where the piece will grow, is covered with a thin layer of photocurable paste. The laser hits the surface according to the design, causing the polymerization of the medium. At this point the printing platform moves down to enable the recoation of the surface with fresh slurry. The process continues repeating the previous sequences until the piece is finished. This technique enables the production of pieces with high resolution. On the other hand, the process is slower compared with other technologies. This technique has been used to produce casting moulds [187], [188], microelectronic components [189], [190] and especially bio engineering, such as bone scaffolds, bone implants and dental components [191], [192].
The difference between SLA and DLP is the illumination of the material. In SLA the source is usually a laser which raster the surface a high speed reproducing the CAD design, while in the DLP technology, the light irradiates the surface in a single shot rotating between on and off position thousands of mirrors, this make the process quicker compared with SLA [193], [194]. As in

the case of SLA, mixing the photo-curable system with solid load makes possible to print structures of carbon nanotubes [195] or ceramic materials [196].

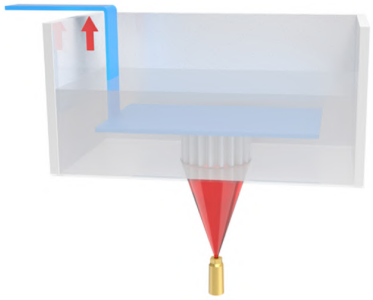

Figure 1.18: *DLP [186]*

Direct inkjet printing (DIJ) deposit a low viscous suspension of binder and material, entering in the class of material jetting, known as well with other names (PolyJet, Drop-on-Demand). The working principles are similar to the desktop printer on paper, only the repetition of many layers give the three dimensional feature at the piece. The suspension is deposited by droplets on the substrate. The high number of noodles enables the formation of a continuous layer (Figure 1.19). The technique is famous for its speed and the capability of covering big surfaces with thin layers, but it has poor growing rate in the z direction, tens of layer to reach some micron thickness [197], [198]. The incapability of produce thick layer and the coarsening of the particles and the consequently clogging of the nozzles are the main problems of this technique [197].

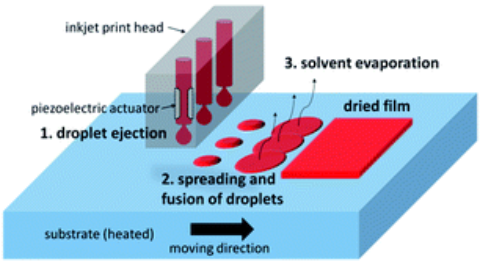

Figure 1.19: *Scheme of inkjet printing process [199].*

The definition of powder bed includes the techniques in which the feedstock material is supplied to the printing platform in powder form and there melted, **SLM** (Select Laser Melting) or sintered **SLS** (Select Laser Sintering).

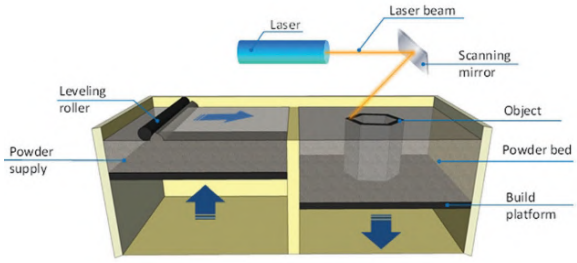

Figure 1.20: *Scheme of SLM/SLS process [182].*

The printing steps are similar to SLA. The printing material, in the form of powder is supplied in a thin layer, it is solidified into the desired shape to reproduce the design by laser melting or sintering, then the platform moves down and the process restart, in the following layer the heat affects the previous layer merging them together (Figure 1.20). After the printing step, the cleaning process to remove the powder is easier compared with SLA and can be automatized with air blowing. The excess powder can be re-use entirely. Metals and thermoplastic polymers can be printed by SLS, with different laser power, but SLM works only with metals. In case of ceramics, the power required to reach the sintering is too high for pure compound such as alumina, so organics [200] or inorganics [201] binders, including eutetic materials [44], with lower melting point are added to achieve almost full densification. An isotactic step before sintering is often used. SLM does not need post-processing, but the thermal gradient generating inside the material causes cracks, porosity and low quality [202], [203].
Similar to this technology is the **Binder jetting**, in which the shaping of the material does not happen for the local phase change of the powder, but to the deposition of a binder which reproduce the CAD file (Figure 1.21). The layer is heated up to guarantee the binding of the powder to maintain the shape until the thermal treatment that gives the final properties to the piece [204], [205].

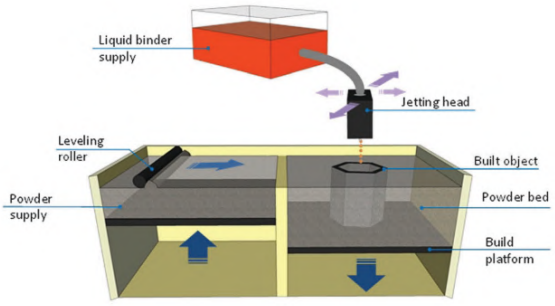

Figure 1.21: *Scheme of the binder jetting process [182].*

For the material extrusion processes, the main difference between technique is the form of the printing materials, in **FDM** (Fused Deposition Modelling) a continuous filament is heated in the nozzle to reach a semi-liquid state and then extruded on top of the previously deposited layers to form a three dimensional object (Figure 1.22). This technique has higher production speed compared with the previous ones, but at the same time, the pieces present poor surface quality and low mechanical properties, in particular between each layer [206]. The elevated speed makes FDM useful for rapid prototyping and for the commercial distribution, nevertheless it is used to print nanocomposites as well [207].

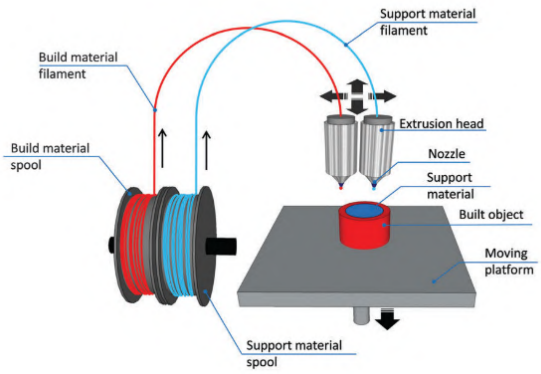

Figure 1.22: *Scheme of FDM printing process [182].*

In the case of **Robocasting printing** (or Direct Ink Writing, DIW) the working principles are similar to the ones of FDM, while the feeding material is in the form of high viscous paste, used mainly for ceramic materials in which the powders are added to the organic compounds in percentage higher than 40vol%, in order to obtain the proper rheological properties to keep the

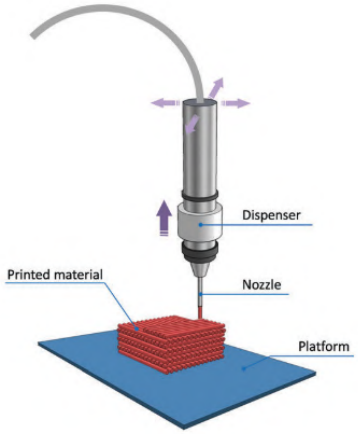

Figure 1.23: *Scheme of robocasting printing process [182].*

shape of the green piece (Figure 2.26). A further step of drying, heating or sintering is often required [182].

Direct Energy Deposition (DED) covers a series of metal additive manufacturing techniques in which the material is supplied through a wired and sintered by a laser, an electron beam or a wire arc welding (Figure 1.24) [182].

In **LOM** (Laminated Object Manufacturing) the material is supplied in the

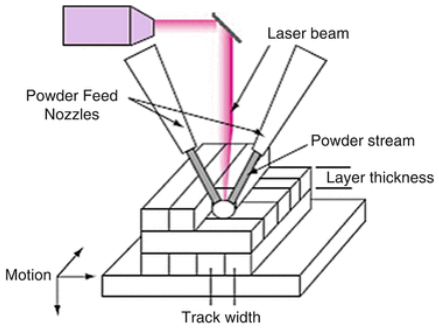

Figure 1.24: *Direct Energy Deposition [208].*

form of tape, continuously rolling over the building platform, a laser cut it to reproduce the slice of the 3D object and the adhesion is carried by the laser and adhesive previously deposited on the tapes (Figure 1.25). The pieces are characterized by few thermal stresses, however delamination, porosity and anisotropic properties are the main issues, causing the losing of interest over the years and nowadays it is used for simple structures, as gears [186].

A scenographic technology, part of the material extrusion class, used for huge deposition is the **Contour Crafting**, big nozzle and high pressure make possible the extrusion of concrete paste or soil, to realize entire build-

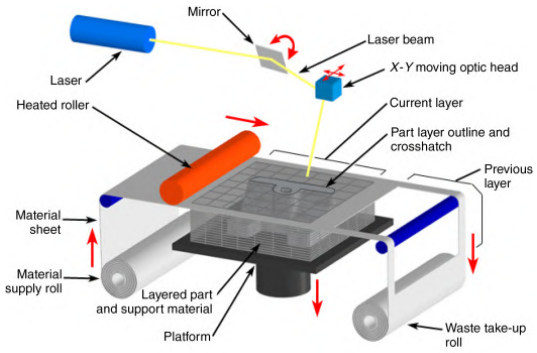

Figure 1.25: *Laminated Object Manufacturing [209].*

ings (Figure 1.26).

Figure 1.26: *3D printed Villa by WinSun [210].*

In this work the efforts have been dedicated to two technologies: stereolithography and robocasting. The choice of these two techniques is driven by i) the high resolution of the SLA and its capability of producing dense ceramic layers and ii) the possibility of easily printing multiple materials by robocasting. Considering the importance of these printing systems for this thesis, we present a deeper analysis of their working principles and properties of the slurries.

1.4.1 SLA printing

Stereolithography technique was first developed by *Hull* in 1986 and later commercialized by *3D System Inc.* Initially working with plastic materials, in the years it has been modified to work with different kind of materials, such as metal and ceramic powder mixed with monomeric precursors which react with the source of light.

Compared with other 3D printing technologies it offers high surface finishing, with resolution up to 10 µm [211]. On the other hand the process is relatively slow, as the printable slurries, the recoating system and penetration of light for curing need to be developed carefully. Even for plastics a post processing step of cleaning of the uncured material is necessary, often followed by a final curing step [183].

1.4.1.1 Principles of operation of SLA

The stereolithography process is based on the selective photo-polymerization of a monomeric medium by a source of light, usually in the UV range, which rasters the surface of the slurry reproducing layer-by-layer the design of the desired piece. The system is constituted by a building or printing platform where the desired piece is going to grow, a reservoir or tank containing the feedstock material and a source of light (a recoating system may be present as well). Under illumination, a thin layer of the deposited material is cured, i.e. the monomers react thanks to a photoinitiator forming longer chains which are solid. Afterwards, the platform is moved down a fixed gap (lower than the penetration of the light) and the process is repeated once again. Since the reaction is not complete, in the following layer the monomers react with part of the radicals of the previous one, enabling the adhesion between layers. When the printable material is a polymeric one, the building platform is placed inside the tank and it moves down in the slurry, as in the machines from *3D System*, (top-down approach) shown in Figure 1.27a, or out from it such in the *Formlabs* ones, (bottom-up approach) shown in Figure 1.27b [212].

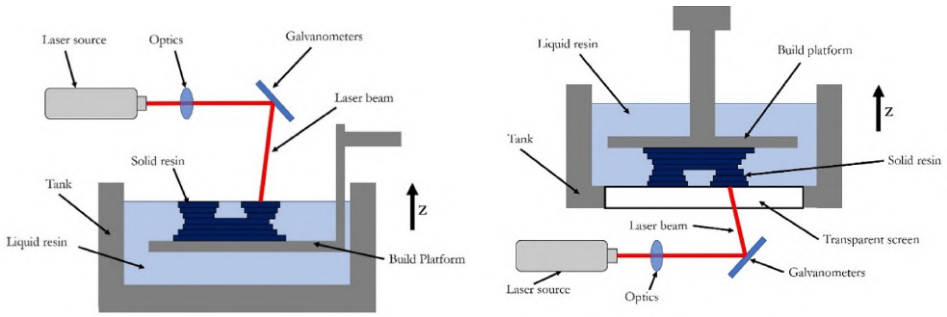

(a) Top-down approach *(b) Bottom-up approach*

Figure 1.27: *Different approach of stereolithography [212].*

When powders are added to the polymeric slurry to produce metallic or ceramic parts, new challenges arise. The first is the development of a suitable printing material, taking into account the scattering phenomena due to

the addition of a second phase, becoming the curing process more difficult.
Griffith et al. first developed a ceramic stereolithography system in 1996. They employed the top-down approach using silica and alumina as starting materials. The printing step, which defines the resolution, was of 150 µm and the final pieces were curled. Anyway the pieces were sintered up to 1550°C, being the first reported ceramic pieces manufactured by SLA [213].
Hinczewski et al. studied the properties of a printable slurry and reported pieces produced by SLA and sintered them with an optimized cycle to avoid the bending of the piece [214], [215].
Doreau et al. were the first to present and patent [216], [217] a system with the tank separated from the building platform. The material is supplied by a piston and spread by a two blades scraper. The approach was still top-down, but the building platform was not moving inside the VAT. A visual representation is given by the comparison between Figure 1.27a and 1.28a. The advantage of this configuration is the use of a high viscous paste, i.e. higher ceramic loads, resulting in better quality of the final pieces [218]. The use of a separate tank allows high spreading speeds and no requirements for a relaxation period, so the shooting with the laser can start immediately after the deposition resulting in less dead time [219].

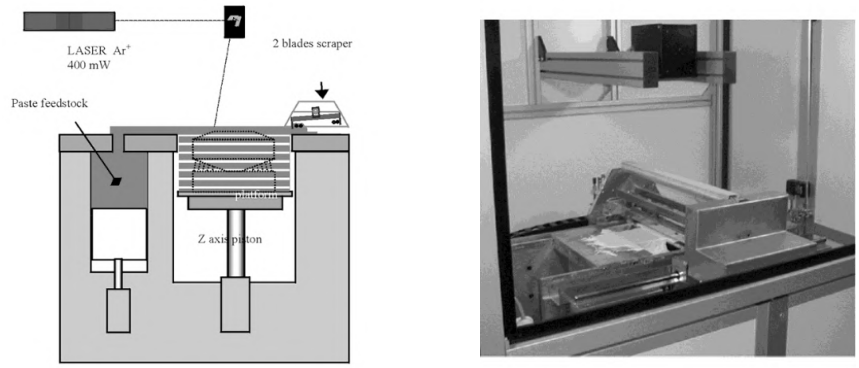

(a) Scheme of the stereolithography printing method.

(b) Picture of the apparatus developed by Optoform.

Figure 1.28: *Scheme and view of the apparatus used by Doreau et al. [219].*

This approach was implemented with the use of a doctor blade system instead of a scraper and used by the company *3DCERAM* (actually *3DCERAM-Sinto*) which developed the machine used in this work, as is reported in Figure 1.29.

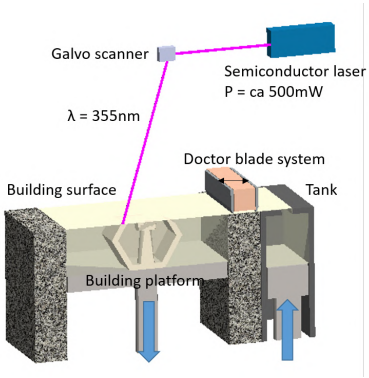

Figure 1.29: *Scheme of the stereolithography machine used in this work [220].*

It is interesting to mention the first reported application of the prototype described above, consisting in a biomedical application to produce part of skull bones costumed on patients suffering from severe head accidents [221], [222].

1.4.1.2 Feedstock materials for SLA

The SLA printable material is usually referred as "*slurry*" or "*paste*" when is loaded with ceramic particles and "*resin*" referring only to the organic compounds. In this case, the organic part is not made of a single compound, but by a mixture of different chemicals with different functionality. At minimum, it consists on the reactive monomer to form the polymeric chain and the photo-initiator to start the reaction, but it usually includes diluents, stabilizers, plasticisers and flexibilisers (among these, the first is an additive blended physically and not reacting, while the ladder reacts chemically with the monomer and become part of the polymer) [223]. In the case of ceramic slurries, dispersant and surfactants are also required to avoid the agglomeration of the particles.
The process of photo-polymerization is presented in Table 1.1. It starts with the light breaking one of the bonds of the photo-initiator, creating a radical. This phase is called *free radical formation*. The active radical reacts with a monomer generating a system radical-monomer (*initiation*), the active radical bonded to the monomer reacts with other monomers and the radical moves over the last monomer added to the chain. In this way, the chain grown increasing its molecular weight up to thousand of units, turning into a solid (phase called *propagation*).

Free radical formation	$PI \xrightarrow{h\nu} I^{\bullet}$
Initiation	$I^{\bullet} + M \longrightarrow I{-}M^{\bullet}$
Propagation	$I{-}M^{\bullet} + M \longrightarrow I{-}M{-}M{-}M{-}M{-}...{-}M^{\bullet}$
Termination	$I{-}M{-}M{-}M{-}...{-}M{-}I$

Table 1.1: *Reactions of photo-polymerization process*

A single radical can easily lead to the polymerization of over a thousand of monomers, the propagation may end for three different causes:

1. **Recombination**, when two chains merge joining the radicals.

2. **Disproportion**, in case that a radical inhibits another, but without merging the two chains.

3. **Occlusion** is the case when the free radicals remain trapped in the solid polymer, without the possibility to access to other monomers, but still active.

For photo-lithography processes most of the monomers are usually multi-functional monomers, since they generate crosslinked polymers which show higher stiffness and mechanically toughness compared with linear ones. Two types of monomers are commercial available, namely: i) the acrylates, characterized by the anion $CH_2{=}CHCOO^{-}$ and ii) the epoxies, characterized by a cyclic ether with a three-atom ring. Due to the reaction speed rate, acrylates monomers are preferred to epoxy ones [184], [224].
The addition of ceramic particles increases formulation complexity problems arising from the dramatic increase of viscosity, which has to be tuned in an optimal range. It has to be as high as possible to generate a dense body, able to be sintered, but with a proper rheology for the recoating process. The machine used in this work offers the possibility to work with high viscosity pastes, i.e. high ceramic loads, to obtain higher density and keeping the shape after the sintering without curling and bending.
The ceramic loading changes the interaction with the light, which can be dominated by the scattering. The cure depth, i.e. how deep a beam can cause the curing of the slurry, can be modelled with the following equation [184], [225]:

$$C_d = D_p ln\left(\frac{E}{E_c}\right) \tag{1.15}$$

where C_d indicate the cure depth, D_p the resin sensitivity, E the energy dose and E_c the critical energy dose to cause the polymerization or gellation of the resin. In case of polymeric resin, the resin sensitivity depends only on the material, while in case of a ceramic loading it is a function of the

particle size, the amount of ceramic and the refractive index of monomer and ceramics:

$$D_p = \frac{2}{3}\frac{d}{Q}\frac{1}{\phi}\left(\frac{n_0}{\Delta n}\right)^2 \tag{1.16}$$

where d is the particle diameter, Q is the scattering efficiency term, ϕ is the volume fraction and Δn is the difference between the refractive index of the ceramic and the monomer (n_0). Several studies confirmed these empirical equations indicating that the cure depth increases with exposure [213] and decreases with the ceramic load [225]. This model is valid when absorption does not play a major role, otherwise the particles absorb the light and less of it will be available to the photo-initiator to form radicals. An example of this issue is the developing of SiC and Si_3N_4 stereolithography, merely reported if compared with the accomplishment cases of zirconia e alumina [226]–[229].

1.4.2 Robocasting printing

Robocasting, which is similar to FDM process, consists in the extrusion of a liquid slurry through a narrow needle controlled by a robotic system which doses the deposition according to a CAD design, reproducing a desired shape layer-by-layer. Contrary to other extrusion technologies such as FDM, the retains of shape is due to rheological properties of the ink more than on the drying and solidification [230]. Particular attention was devoted to this technique in the case of ceramic materials due to the capability of producing dense near-net shape pieces. Although the technique is of easier and faster use compared with others like selective laser sintering, the green pieces need to be fired at high temperature to obtain the final mechanical properties typical of ceramic pieces [231], [232].

1.4.2.1 Principles of operation of robocasting

Figure 1.30 represents how a printing process by robocasting is carried out. The printing system is made of a substrate moving in the z direction and the head of the deposition system, finishing with the needle, moving in x and y. The material is stored into cartridges and supplied to the head with a system of tubes or, in case of small volumes, a syringe is directly connected to the head. Before the needle, a valve regulates the flow of the material. During the printing, the dispenser move laterally, the valve opens when the deposition is required to form a layer according to the design. At the end of each layer the substrate, which may be part or not of the final pieces, is lowered of a fixed printing step, namely the height of the deposition, and the process starts again until the design is completed [233].

The solidification step is a critical stage for the adhesion of layers. If it hap-

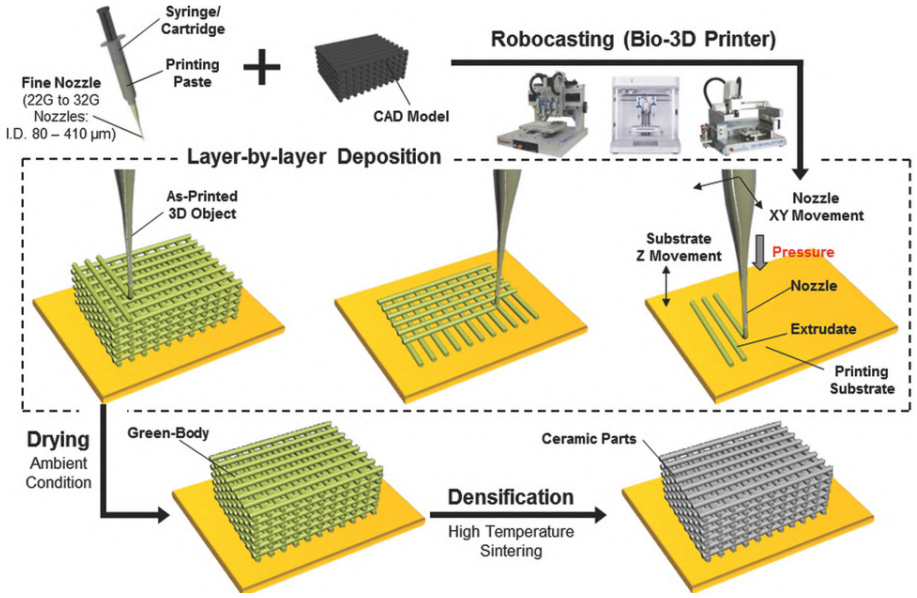

Figure 1.30: *Scheme of the robocasting printing process [231].*

pens during printing of the layers, it results in a poor attachment or clogging of the needle. Therefore, the efforts are devoted to postpone it until the end of the printing. Examples of this are printing in oil to delay the drying of the colloidal suspension [234] or the use of an additional polymerization process after the deposition (to actively control the solidification process) [235].
The quality and the accuracy that characterize this printing process, are determined by the co-existence and interaction of different parameters. The size of the nozzle and the speed of the movements affect the resolution, which ultimately affects the quality. This is also influenced by the particle size, the solvent, the type of ink (that has to be optimized for the type of needle) and the motion system. These parameters affect one each other to give rise to the final pieces [236].
Robocasting systems can easily be improved to deposit more than one material at a time, implementing two different solutions, namely: i) assembling different valves and nozzles on the same moving head [237] or ii) feeding different material inside the same nozzle [238]. The first solution is the most interesting one, especially for keeping purity avoiding cross contamination. Moreover, it is easier to automatize the interchange of materials. This approach is used in the hybridization of the printing system used in this work, which combines SLA and robocasting. In our system, four different nozzles were assembled on the same robotic arm that was coupled to a SLA printing machine. This approach enables the alternative printing of five materials in the same machine (one by SLA and four by robocasting).

1.4.2.2 Feedstock materials for robocasting

The robocasting system is fed with a mixture of organics compound, called "*resin*" and ceramic powders, referred as "*slurry*" for its nature or to differentiate it from the SLA one, "*ink*". The ink properties are critical for the success of the printing. For the nature of the process the ink should be well dispersed and the particles size congruent to avoid the clogging of the nozzle. A reversible shear thinning at high shear rate is necessary to allow the ink to flow through the needle and keep the shape when printed. For the very same reason, a high elastic module is required to keep the self-sustaining structures and print high aspect ratio designs [230], [231], [238]. According to the literature, inks can be based on water [239], non-aqueous solvents [240] and aqueous hydro-gel forming inks [241]. Aqueous inks are nontoxic and cheap, but the evaporation process requires longer times. On the other hand, fast drying could be a problem for solvent based inks. Moreover, some of the employed solvents such as toluene and methyl ethyl ketone are toxic and expensive. Pursuing a fast and cheap controlled solidification, without the formation of toxic vapour, inks based on photo-curable compounds such as the one developed for SLA have been investigated [242]. After the deposition, the material is illuminated with UV light causing the solidification of the piece, which can easily be handled for further processing (adhesion on flexible substrate) or sintered at high temperature [243].

It is important to remark that, in this work, the parts produced by robocasting do not only need to solidify but also to adhere and be implemented in the stereolithography printed layers. Accordingly, a good compatibility and proper adhesion are required between the two type of printable materials.

1.5 Additive manufacturing for energy applications

3D printing has revolutionized the word of rapid prototyping and the custom applications. Since its entrance in the market, applications in different fields have been investigated and exploited. One of them is the use for energy application, where AM is used to overpass some limitations and improve energy devices, which help moving forward a more sustainable future. Additive manufacturing can produce small quantities at low cost [244] since there is no necessity of fabricate new moulds for each design [245], enabling the optimization and the validation of innovative ideas and reducing the time for product development [246]. Moreover it reduces the handling of the pieces, the length of the supply chain since only the starting materials need to be purchased. Regarding this point the saving of materials with respect to subtracting manufacturing was evaluated to be up to the 40% [244], [247].
These advantages rose the interest of researchers which applies 3D printing technologies to the energy field, such as in photo-voltaic applications [248], [249], for Li-ion batteries [250], [251] and supercapacitors [252].
Applications in the field of solid oxide cells, in fuel and electrolysis are presented in detail in the following sections (1.5.1 and 1.5.2), as well as for the use in the catalysis field (Section 1.5.3), since these are the application on which this work is focused on.

1.5.1 AM for SOFCs

One of the main challenges to produce SOFCs by AM is the achievement of an electrolyte with the appropriate properties. As explained previously, the electrolyte of SOFCs needs to hold high ionic conductivity with the purpose of minimizing the ohmic losses, it must be fully dense to separate the hydrogen and oxygen atmospheres while as thin as possible to reduce the ohmic contribution to the total resistance of the cell (which should be ideally below $0.5\,\Omega\mathrm{cm}^2$ at the operating temperature). The former requirement restricts the number of additive manufacturing techniques that can be used for the fabrication of an ideal electrolyte, since full density is not easy to achieve by most of the available 3D printing techniques. 3D printing technologies mainly used for this purpose so far are direct inkjet printing (DIJ), selective laser sintering (SLS), robocasting and stereolithography (SLA).
Most of the reported trials to 3D print electrolytes has been carried out by employing direct inkjet printing (DIJ). The reason is the suitability of this technique to create very thin layers. A couple of pioneering works, published ten years ago by *Sukeshini et al.* [253], [254] used inkjet printing to fabricate electrolytes, as well as electrodes. The cells exhibited a maximum power densities of $430/460\,\mathrm{mW/cm}^2$ at 850°C using hydrogen as a

fuel. More recently, *Esposito et al* [255] deposited by DIJ 1.2 µm-thick YSZ electrolytes on NiO-8YSZ tape casted anode supports. This, together with screen printed LSM-YSZ cathodes resulted in ASR values below 0.5 Ωcm^2 at 750°C and open circuit voltages (OCV) of 1.15 V, which led to measure maximum power densities of 1500 mW/cm^2 at 800°C. One year later, the same group presented YSZ structures obtained by hydrothermal synthesis of zirconia nano-colloid by the same technique. In this work, the possibility of implementing honeycomb patterns was demonstrated and, while not yet implemented in a measurable cell, the potential to enlarge the active area without thinness losses of the electrolyte was demonstrated [256]. *Chao Li et al.* were also able to obtain YSZ electrolytes by using inkjet printing technology. They printed YSZ membranes of $\sim$ 6 µm in thickness onto anode supports of NiO-YSZ [257]. This thickness is obtained by four material deposition steps. Finally, they measured the performance of a full cell with a LSM cathode, producing a maximum power of density of 860 mW/cm^2 and 1.05 V of OCV at 800°C. *Wang et al.* focused on GDC as electrolyte material [258]. They developed stable GDC inks that were printed onto NiO-YSZ cermet substrate finally achieving 8 µm of thickness with ten layer depositions. In the same direction, *Mosiadz et al.* inkjetted CGO nanoparticles on highly textured Ni-5wt.% by using two types of techniques, namely, electromagnetic and piezoelectric inkjet printing. The piezoelectric actuator approach was able to produce layers free of cracks suitable for future implementation on SOFCs [259]. *El-Toni et al.* used the same inkjet technique to print GDC electrolytes onto honeycomb LSM substrates, which were also fabricated with inkjet printing [257], [260]. Similarly, *Young et al.* used inkjet to print both components, the electrolyte and the anode [261]. In addition to the reduction of the thickness of the electrolyte, some works on this technology were addressed to improve the cell performance by structuration of the electrolyte/electrode interface [262], [263]. Following this strategy, *Farandos et al.* used for the first time DIJ to produce 3D scaffolds of YSZ after previous simulation of the expected behaviour of different patterns [264], [265]. In these works, they successfully printed YSZ micro-pillars (shown in Figure 1.31) and square lattices on a NiO-YSZ anode substrates. Interestingly, the same group have dedicated efforts to avoid high-temperature and long-times requirements for the densification of the electrolyte to reduce the risk of reactivity with the electrodes in future co-sintering approaches [266].

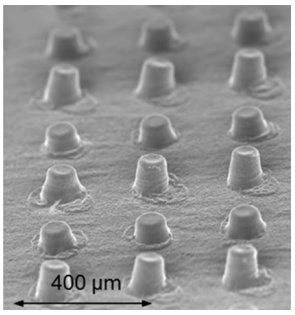

Figure 1.31: *Micro-pillars produced by inkjet printing [265].*

Beyond inkjet printing of thin layers, 3D printing is able to produce advantageous high-aspect ratio pieces with almost no shape restriction (free-form design). Using this approach, *Masciandaro et al.* [267] recently presented a seminal work focused on printing electrolytes using a commercial SLA printer. While SLA technology has long been subject of study for many years to produce zirconia parts [268], it was used for the first time for the fabrication of self-supported dense 3YSZ layers. Moreover, the high spatial resolution of this technique was exploited for structuring electrolytes with honeycomb conformation which were compared with a flat printed structure. Thickness values were 260 µm for the hexagonal cells with an active area of 1 mm^2 each, forming a network connected by 530 µm thick beams of 220 µm in width; the thickness for the flat cell was 340 µm with an active area of 1.54 cm^2. Complete fuel cells were made by brush painting electrode materials until complete cells were obtained with the structure: NiO-YSZ|YSZ(3D printed)|LSM-YSZ. Ionic conductivity values of 0.022 S/cm were obtained at 900°C in good agreement with previous works reported in the literature. Under fuel cell operation conditions, open circuit voltages of 1.14 V at 800°C were measured, perfectly matching the theoretical ones, indicating the gas-tightness of the 3D printed membrane. Power peak densities of 100 mW/cm^2 were obtained at 900°C for the flat cell, being compatible with the values expected for SOFCs based on 3YSZ electrolytes of the current thickness. In case of honeycomb cells, slightly higher values were found (115 mW/cm^2) at the same temperature, attributed to an improvement of the active area. *L. Wei et al.* [196] worked in the same direction, using DLP-stereolithography for the electrolyte production, manufacturing a 500 µm thick electrolytes based on 8YSZ and achieving 1.04 V of OCV and a maximum power density of 176 mW/cm^2 at 850°C. Finally, it is worth mentioning that some activity in the fabrication of electrolyte materials has been recently reported using other techniques such as robocasting [269], Digital Light Processing (DLP) stereolithography [270], Ceramic On-Demand Extrusion (CODE) [271], [272] or Thermal Ink-Jet (TIJ) printing [273]. However, due to the previously mentioned specific features required for SOFC electrolytes, inkjet and SLA

continue dominating this field of application.

Due to the porous structure requirement of the electrodes, techniques such as robocasting, laser sintering or powder bed are the preferred for the fabrication of self-supported cathodes and anodes. Alternatively, inkjet is employed to deposit functional layers or infiltrate already existing porous scaffolds fabricated by other means. In these cases, 3D printing is used to carry out a functionalization more than a proper shaping step. This type of functionalization steps are considered a promising solution since latest results using functional layers and infiltrated composites in the field of SOFCs yielded excellent performances increasing the durability of the cells. Complementary, the current and future development of multi-material printing capabilities can be of major importance since graded compositions, especially in these functional layers, represent a reduction in the polarization resistances and, therefore, a great enhancement of the final device. This section summarizes the last advances including a comprehensive list of the technical parameters, cell designs and performances recently reported in the literature for SOFC printed cells.
As mentioned in previous sections, Ni-YSZ cermets are the standard material for SOFC anodes. In this particular case, although a certain control of the microstructure is preferred, porosity can be eventually reached after NiO reduction of dense NiO-YSZ layers. Therefore, it is interesting to study the possibility of controlling the microstructure of the layer by simply tuning 3D printing parameters. As an example, *Yi. et al.* [274] obtained dense parts of NiO-YSZ (60-40wt.%) by SLS and SLM when using a CO2 lasers while porous structures when employing a fibre laser. This tunability is interesting for the fabrication of anode supports. However, most of the existing works are focused on the deposition of anode functional layers on top of standard anode supports fabricated by other means (e.g. tape casting). In this other approach, the control of the porosity becomes less important while a gradation of the composition or a multi-material deposition turns out to be a key factor. Regarding graded layers, *Sukeshini et al.* [275] reported functionally graded SOFC anode interlayers printed using Aerosol Jet Printing (AJP) achieving a power density of 235 mW/cm^2 at 850°C in anode-supported cells. Regarding the infiltration of existing porous scaffolds with complementary materials to increase the electrochemical performance, *Wang et al.* [276] detailed the successful use of inkjet printing for the infiltration of NiO-$Gd_{0.1}Ce_{0.9}O_{2-x}$ on NiO-8YSZ substrates for obtaining a maximum power of density of 380 mW/cm^2 and an OCV of 0.9 V at 600°C in NiO-8YSZ|NiO-GDC|GDC|LSCF-GDC cells. More recently, *Mitchell-Williams et al.* infiltrated CGO by DIJ on a porous NiO-YSZ anode to increase the oxidation capability of the anode [277] while *Dudek et al.* fabricated multi-component cermet anodes of Cu-Ni-YSZ for direct carbon

fuel cells with solid oxide electrolyte (DC-SOFCs), combining Cu and Ni yielded an increase of 25% in the performance of the DC-SOFC cells [278], [279]. Finally, other studies used the inkjet technology to produce interlayers that improve the compatibility with the electrolyte (avoiding undesired reactions). This compatibility layers have been deposited over dense electrolytes [253], [254] or infiltrated on porous electrodes [275], [276]. As a particular example, *Shimada et al.* impregnated an electrolyte-supported cell of Ceria-doped Scandia-stabilized Zirconia with $BaZr_{0.9}Y_{0.1}O_{3\text{-}\delta}$ (BZY) by DIJ. BZY impregnation showed an elevated performance of $790\,mW/cm^2$ [280].

Similar to anodes, most studies on 3D printing of cathodes were focused on the use of inkjet printing, covering the optimization of the necessary inks and the printing process. Since the cathode is typically the last layer in the fabrication flow of SOFCs, one have less restrictions regarding compatibility with the electrolyte or undesired densification during subsequent thermal treatments. Likely due to this advantage, there is an abundant collection of works on 3D printing of cathodes in the literature. Regarding the printing process itself, *Chen et al.* [281] were able to print LSCF using environmentally friendly aqueous suspension and *Hill et al.* [282] reached enough resolution to print arrays consisting of microdots of $60/90\,\mu m$ in diameter. Still working on LSCF, *Han et al.* [283] optimized different parameters, such as deposition rate, viscosity and porosity of the sintered layer to obtain the condition at which the power density of the corresponding cells is maximized, reaching the value of $377\,mW/cm^2$ at 600°C. More specifically, *Yashiro et al.* [284] studied the advantages of using inkjet printing technology by comparing the performance of cells based on standalone air-brushed cathodes and cathodes combining inkjet printed and air-brushed layers. The material was again the state-of-the-art LSCF, this time in combination with GDC (LSCF-GDC), deposited on GDC dense electrolytes. The cells including the printed layers presented enhanced performances with maximum power densities of $710\,mW/cm^2$ at 600°C (compared to $540\,mW/cm^2$ measured for the conventional cell). This work claims that the improvement is due to an induced higher number of Triple Phase Boundaries (TPBs) available for the electrochemical reaction.
As mentioned for anodes, the infiltration of existing scaffolds is a common strategy that involves inkjet printing. For instance, *Venezia et al.* [285] infiltrated LSCF cathode layers with different materials such as $La_{0.6}Sr_{0.4}CoO_{3\text{-}\delta}$ (LSC) and GDC. The aim was to prove the beneficial effects of a higher electrochemical activity of LSC compared with the pure LSCF, together with a raising in the stability at the cathode-electrolyte interface due to the addition of GDC. Electrochemical measurement showed an improvement attributed to the implementation of these materials compared to a not infiltrated reference sample. The cell manufactured with the cathode infiltrated with LSC

presented a power density of 350 mW/cm^2 at 700°C, while the sample with GDC offered 310 mW/cm^2 at 700°C, both of them remarkably higher than the reference not-infiltrated sample holding 250 mW/cm^2 at 700°C. Similarly, *Tomov et al.* used the inkjet printing to infiltrate LSCF/GDC cathodes with GDC [286] and GDC-cobalt oxide [287] nanoparticles reaching an improvement of the electrochemical properties and the stability of the cathode. Due to the excellent results obtained for infiltrated cells, 3D printing is also considered a promising candidate to scale up such type of functionalization processes giving them the required level of homogeneity, reproducibility and velocity [288]. The optimization of the electrode porosity is one of the most important factors to increase the performance and durability of the cells. Different works were therefore devoted to study the capability of 3D printing to control this important parameter in SOFCs. *Yu et al.* [289] showed unique porous structures based on silver nanoparticles deposited by inkjet printing while *Li et al.* [290] introduced pore formers to produce cathode layers, the final microstructure is presented in Figure 1.32. Although the use of pore formers yielded in an improved performance of the cells fabricated by *Li et al.* (maximum power of 950 mW/cm^2 vs. 550 mW/cm^2 at 750°C in NiO-8YSZ|YSZ|SDC|SSC-SDC configuration), even higher performances were obtained when using conventional techniques, which stresses the need for improving the current strategies to generate porosity by inkjet printing.

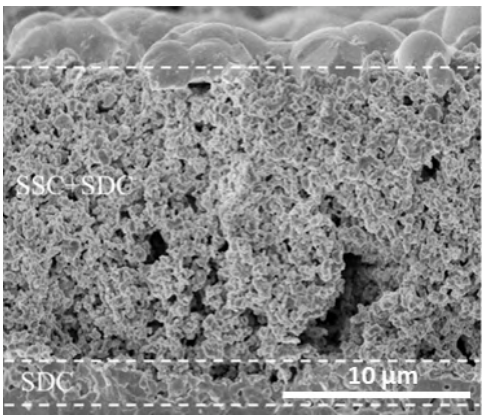

Figure 1.32: *SSC-SDC cathode produced by inkjet printing [290].*

To end up with this section, it is important to remark that more complex multi-layered systems were also inkjet printed and tested by some authors. *Farandos et al.* [291] used the inkjet technique to deposit LSM-YSZ|LSM bilayers over 3D printed YSZ electrolytes building up cells that reached a maximum power density of 690 mW/cm^2 at 788°C. Even one step beyond, in the already mentioned works of *Sukeshini* [253], [254], anode|electrolyte|cathode layers were all deposited by 3D printing giving rise

to the first generation of fully printed cells (although supported on commercial anodes). With no doubt, this high value-added full-device concept becomes the most interesting approach when thinking about mass production of SOFCs by 3D printing since a single-step fabrication strategy can represent a competitive advantage compared to traditional manufacturing techniques.

Support/ printing method	**Multilayer SOFC printed structure**	**OCV (V); MPD (mW/cm^2)**	**T (°C)**	**Ref.**
Anode/inkjet	NiO-YSZ|**NiO-YSZ**|**YSZ**|**LSM-YSZ**|**LSM**	1.1; 460	850	[254]
Anode/inkjet	NiO-YSZ|**NiO-YSZ**|**YSZ**|LSM-YSZ|LSM	1.1; 300	800	[253]
Anode/inkjet	NiO-YSZ|**NiO-YSZ**|**YSZ**|**LSM-YSZ**|**LSM**	1.1; 210	800	[253]
Anode/inkjet	NiO-YSZ|**YSZ**| LSM-YSZ	1.15; 1500	800	[255]
Anode/inkjet	NiO-YSZ|**YSZ**| LSM-YSZ	1.05; 860	800	[257]
Anode interlayer/inkjet	**NiO**|**NiO-YSZ**| **YSZ**|LSM	0.3; 1750	750	[261]
Anode/AJP	NiO-YSZ|**YSZ**| **LSM-YSZ**|**LSM**	1.05; 400	850	[292]
Anode/AJP	NiO-YSZ|**YSZ**| **GDC**|**LSCF**	1.15; 600	800	[292]
Electrolyte/SLA	NiO-YSZ|**3YSZ**| LSM-YSZ (flat)	1.14; 100	900	[267]
Electrolyte/SLA	NiO-YSZ|**3YSZ**|LSM-YSZ (honeycomb)	1.14; 115	900	[267]
Electrolyte/DLP	Ag-GDC|**8YSZ**| Ag-GDC	1.04; 176	850	[196]
Electrolyte/ Robocasting	NCAL|**SDC**|NCAL	0.78; 448	550	[269]
Electrolyte/AJP	NiO-YSZ|**NiO-8YSZ**|**8YSZ**|YSZ-LSM	1.2; 235	850	[293]

Anode/inkjet	NiO-8YSZ|**NiO-GDC+GDC**|GDC|LSCF-GDC	0.9; 380	600	[276]
Electrolyte/inkjet	NiO-YSZ-**BZY**|$ScCeZrO_2$|LSM	∼1.1; 790	900	[280]
Electrolyte/inkjet	**CGO**-NiO-8YSZ|8YSZ|LSCF	∼0.95; ∼145	800	[277]
Electrolyte/inkjet	**Ni-YSZ**|8YSZ|LSM-GDC|LSM	∼1.02; 96	800	[278]
Electrolyte/inkjet	**Cu-Ni-YSZ**|8YSZ|LSM-GDC|LSM	∼1.02; 118	800	[278]
Electrolyte/inkjet	**Ni-YSZ+Cu**|8YSZ|LSM-GDC|LSM	∼1.02; 80	780	[294]
Anode/inkjet	NiO-YSZ|**8YSZ**|**LSM-YSZ**|**LSM**	0.77; 690	788	[291]
Anode/inkjet	NiO-GDC|GDC|**LSCF-GDC**	0.43; 110	600	[284]
Anode/inkjet	NiO-GDC/GDC/**LSCF-GDC**|LSCF-GDC	0.94; 710	600	[284]
Electrolyte/inkjet	NiO-GDC|3YSZ|LSCF|**LSC**	1.04; 350	700	[285]
Electrolyte/inkjet	NiO-GDC|3YSZ|LSCF|**GDC**	1.04; 310	700	[285]
Anode/inkjet	NiO-8YSZ|YSZ|SDC|**SSC-SDC**	1.10; 950	750	[290]

Table 1.2: *List of Solid Oxide Fuel Cells reported in the literature including at least one 3D printed layer. Details on the support part of the cell, the printing method, the materials of the different layers, the OCV and maximum power density (MPD) and the operating temperature were included. The bold text indicates the layer manufactured by 3D printing*

1.5.2 AM for SOECs

As previously mentioned, Solid Oxide Electrolysis Cells are electrochemical devices able to convert water into hydrogen and oxygen by injecting electricity. In other words, SOECs are SOFCs operated in reverse mode. Due to this analogy, the materials and configurations described above for SOFCs are also used in the state-of-the-art SOEC technology and, therefore, most of the developments on 3D printing of this type of fuel cells can be extra-

polated to SOECs [295]. Despite these similarities and due to the relevance of the SOEC technology for future energy scenarios, it is worth mentioning some works specifically devoted to develop 3D printing for SOECs. *Farandos et al.* [264], [265] proposed the formulation of inks for inkjet printing of functional layers for SOFC and SOEC devices reporting for the first time an electrolysis measurements upon 3D printed manufactured electrolytes. The cells were made by inkjet printing $\sim 20\,\mu$m-thick 8YSZ layers over NiO-8YSZ substrates while painted LSM-YSZ and LSM were employed as an oxygen electrode. OCV values of 0.84 V at 800°C in CO_2-CO/air atmospheres were obtained while a current density injection of $-0.78\,A/cm^2$ was applicable at 1.5 V in SOEC mode (Figure 1.33). Further studies of the same group show results on SOEC cells with printed electrolyte and cathode. Dense layers of 8YSZ with $9\,\mu$m in thickness were obtained after inkjet printing and sintering them on top of NiO-8YSZ substrates. On the oxygen electrode side, LSM-YSZ interlayers combined with LSM cathodes (with a thickness of 9 and $20\,\mu$m, respectively) were deposited to complete the cells. The performance of such cells increased, in comparison with their previous study, obtaining an astonishing current density injection of $-3.33\,A/cm^2$ at 1.5 V at 788°C. These values clearly exceed the ones for cells produced by traditional manufacturing techniques proving the potential of inkjet printing for the fabrication of highly performing SOECs [291].

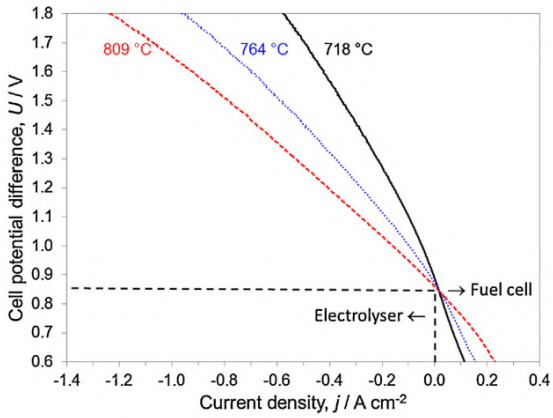

Figure 1.33: *V-j curve in electrolyser and fuel cell mode of a cell with inkjet printed electrolyte [265].*

Among other interesting advantages, 3D printing can be used to easily optimize the manifolds and flow distribution in the channels of the interconnects or to improve the specific energy/power density by modifying the structural elements of the stacks. In these regards, *Linne et al.* [296] studied how to reduce the weight and homogenize the flow of SOEC stacks by 3D

printing advanced manifolds to be used in spatial missions to Mars, where robustness, efficiency and power density per unit mass and volume are key factors.

1.5.3 AM for reactors

In parallel with the research devoted to the optimization of the catalyst and performance, with the development of additive manufacturing technologies their use in the catalysis field has been investigated as well. The application of AM can be classified in base of the used technology, the type of reactor, or the material. Here we review the solution presented in the literature based on the part of the reactor which is printed. So we are going to identify three parts:

- The bed, being it considered the entire reactor or an inert phase on which one or more layers, including the active metal, are deposited.
- The catalyst, supported or not on a substrate, i.e. the active phase of the reaction is produce by a 3D printing technology.
- Rapid prototyping, in this case the additive manufacturing technology is used to produce a mould afterwards used to obtain a desired structure.

1.5.3.1 3D printing of beds

Starting from the support production, different materials and technology have been used, as well as different catalytic application.
Lefevere et al. demonstrated the effect of the design of the bed, produced by robocasting technology, in the conversion of methanol to light olefins. The substrate was produced in stainless steel and infiltrated with the active catalyst. They used ZSM-5, a medium- pore zeolite composed of intersecting straight and sinusoidal 10-ring pores, proved as a valid catalyst for the reaction under study. Samples are printed by robocasting of stainless steel slurry in a 1-1 and 1-3 stacking (see Figure 1.34), a commercial honeycomb structure of corderite and powder were used as reference for comparison. The monolith structures were infiltrated with the catalyst suspension and placed in a quartz tube or in a fixed bed reactor in case of powder to run the characterization at 350°C and atmospheric pressure, under a methanol and nitrogen flow at different space velocities. Obtaining better performance for the monolith structure compared to the powder bed one over all the range of space velocity, in particular at higher value, the printed structure alternated 1-3 showed better performance due to the higher tortuosity of the path, which enhanced the mass and heat transfer [297].
Danaci et al. devoted their efforts to the production of 3D printed metal beds for the CO_2 methanation by robocasting. At the beginning they produced porous structures based on stainless steel 316L, different designs and nozzle parameters were tried. The printed structures (designs are shown in

Figure 1.34) were infiltrated with a water based slurry for dip-coating of Ni/Al_2O_3, in which the Ni-loading was 12%. An optimization process of the slurry formulation, regarding the viscosity and the attachment was carried out previous to the study. The conversion was evaluated by gas chromatography analysis under a flow of CO_2 H_2 and He in ratio 1:4:15, at atmospheric pressure, over a range of temperature from 250°to 450°C, after the initial reduction of the catalyst *in situ*. The higher conversion was obtained for an alternate structure (Figure 1.34b), showing an increment of around 40% at 300°C compared with the not alternate structure (Figure 1.34a). This behaviour was ascribed to the different contact time between reactant gases and catalyst surface, to the heat and mass transfer properties [298].

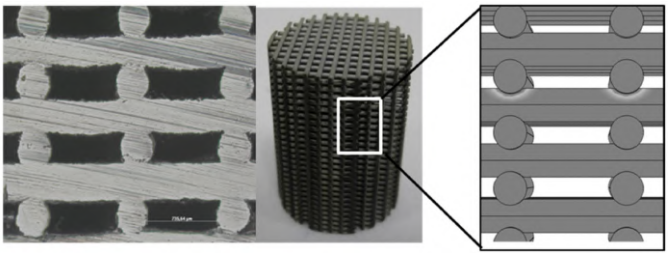

(a) Not alternated deposition, 1-1 stacking

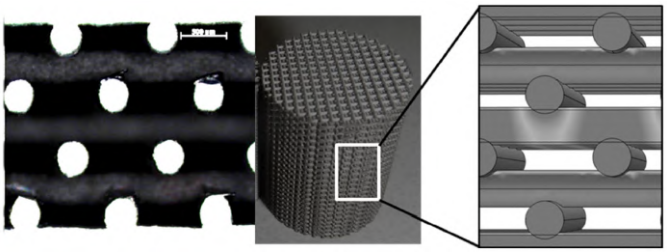

(b) Alternated deposition, 1-3 stacking

Figure 1.34: *Catalyst support deposited by robocasting by Danaci et al. [298]*

Based on this first promising result, the same group proposed a support for CO_2 methanation reaction based on copper, using the same preparation technique developed in the previous study and with the alternate geometry, due to the higher conversion rate. The sintering atmosphere and temperature were optimized, Ni/Al_2O_3 catalyst was deposited by wash-coating on an optimized copper substrate and a stainless steel one as comparison. The conversion was evaluated in a similar set-up as described in the previous work, with a gas flow of CO_2, H_2 and N_2 in ratio 1:4:5 and in the range between 280°and 500°C. The performance was compared with the one obtained by the same geometry produced in stainless steel and powder catalyst. The res-

ults show comparable performance between the two printed materials and slightly higher than in powder form [299].
Following this line of research, a mini pilot plant was set-up, scaling the dimension of the reactors up to 15 times. Although further optimization and homogenization of the parameters look necessary, the study presents a successful scaling up from the lab scale to the pilot plant scale [300].
Pérez et al. at *Tecnalia R&I* (Spain) developed and patented a multichannel reactor for Sabatier reaction using SLM of stainless steel 316L. They successfully scaled it up in a waste water treatment plant in Spain, in the frame of the RENOVAGAS Spanish project, keeping similar performance to the ones obtained in the lab scale. At first they compared the performance of a reactor made of 16 channels of 1.75 mm with a fixed bed reactor of 9 mm of diameter, both of them loaded with Ni/Al_2O_3 catalyst and tested under CO_2 and H_2 flow in ratio 1:4, in the temperature range between 200°and 400°C, showing an improvement of the conversion rate around 20% all over the temperature range. The synthetic natural gas (SNG) produced fulfilled the requirement for the direct injection in Spanish gas grid ($\geq$ 95mol% CH_4, $\leq$ 5mol% H_2 and $\leq$ 2.5mol%CO_2). The tested reactor was scaled up to 97 channels and, thanks to its modularity, four units were assembled to obtain 388 channels in the pilot plant [301].
Similar materials and technologies have been used in different application, such as methanol steam reforming and Fisher Tropsch reaction.
Liu et al. printed by SLM different geometries, i.e. continuous curve, stacking 1-1 and 1-3 and stagger, this last one changing the porosity changing the radius of the row. Not coated stainless steel, copper and aluminium alloy coating were tested to study the influence of materials on hydrogen production. All the samples were coated with alumina and the precursors of the catalyst itself, i.e. Cu/Zn/Al/Zr. Results showed a 20-40% higher conversion of methanol for staggered structure. Among the set of samples with change in porosity, the one with decreasing porosity from the inlet to the outlet revealed better performance, due to the higher residence time inside the reactor. The most performing plate was produced with different coating to evaluate the effect of the materials, showing a better conversion for the copper coated structure, since the layer avoided the reaction between catalyst and stainless steel, while the aluminium one caused the deactivation of the catalyst [302].
Stiegler et al. proposed the realization of porous structures based on a diamond cell by SLM of stainless steel 630. Al_2O_3/MgO was electrodeposited on it and Ru catalyst was deposited on top, choice made on previous optimization of the catalyst for CO_2 methanation. The reactor was tested over a wide range of conditions, pressure from 1 to 20 bar, and temperature, from 200°to 400°C and different load of catalyst, proving the suitability of this kind of design. It was possible to reach high conversion of CO_2, close to the equilibrium up to 375°C without the detection of critical hot-spots [303].

Based on a similar design, *Fratalocchi et al.* realized a support structure to be used in Fisher Tropsch reaction, with the purpose to enhance the heat transfer of a fixed bed reactor thanks to the increased porosity obtained by the repetition of a diamond cell of $AlSi_7Mg_{0.6}$. The system was filled with $Co/Pt/Al_2O_3$ as catalyst and pellet of α-Al_2O_3 to keep the catalyst in place. The reactor was tested in an automatic test rig, under H_2/CO flow, ratio 2:1, pressure of 25 bar and in the temperature range 190°-230°, over 600 hours, proving isothermal conditions were kept even under high CO conversions [304].
Using SLS of stainless steel instead of SLM, *Mohammad et al.* produced micro-channels plates infiltrated with different catalyst, namely Co, CoNi, CoRu and CoFe, over a mesoporous silica support for catalyst (MCM-41) to be used in Fisher Tropsch synthesis. The reactor was fed with a mixture of syngas (H_2/CO 3:1) and the conversion was evaluated over the temperature range between 180°C and 300°C at atmospheric pressure. The results showed a beneficial effect of Ru with Co, increasing the CO conversion, while the addition of a second metal to the Co affect mainly the selectivity to hydrocarbons [305].

1.5.3.2 3D printing of catalyst system

Some studies reported the use of additive manufacturing to manufacture directly the catalyst in three-dimensional shape to control the porosity and its increase compared to a fixed-bed reactor. To pursue this goal, robocasting was the preferred choice for its capability to produce open structures and to tune the slurry composition.
Couck et al. formulated a slurry based on an aluminosilicate zeolite (ZSM-5), to produce monolith structure to be used for CO_2 absorption and N_2 and CH_4 separation. Zeolites are a common material for this process, but in the form of pellet they show a high pressure drop and slow diffusion of molecules and consequently low mass transfer properties. In this preliminary study, the proposed design is similar to the one shown in Figure 1.34a and it is compared with the powder material. It showed lower capacity, ascribed to the use of binder in the slurry. However, the separation potential of CO_2 in N_2 and CH_4 is excellent, promising new opportunities for the absorbent materials [306].
The same group investigated the effect of the printing stacking (as the one proposed by *Danaci et al.* and reported in Figure 1.34) and type of binder (bentonite, SiO_2, $AlPO_4$ and their combination) in a printed structure of zeolite ZSM-5. At first the best combination of materials to achieve high conversion of methanol to olefin was pursued and, using this best combination, the effect of architecture was investigated, comparing the printed structure

with a bulk sample. The printed catalysts were placed in a fixed bed alumina reactor to be introduced in the furnace to test the conversion over the range 300°– 450°C. In the case of single binder catalyst, bentonite and silica performed better in the conversion. A linear combination of these two materials worked better up to 375°C, after which all the combinations achieved the 80% of conversion, due to an higher stability over time (TOS > 40h). The binder system constituted by silica and $AlPO_4$ was chosen to study the effect of architecture. Smaller fibre diameter (400 µm) improved the conversion and the stability. The reason was ascribed to a shorter diffusion path inside the structure, with a reduced use of the catalyst with the increase of the deposited fibre. Different levels of porosity were tested. The lower the porosity, the higher the conversion, but lower the stability, affecting the heat and mass transfer properties of the system. As found in other studies, an alternate stacking improved the performance, and in this case the stability, increasing the turbulence of the flow, which affect the mass and heat transfer [307].
Different design patterns have been tested as well for Fisher Tropsch reactions. The sample was produced by robocasting of a PVA based paste with precursors to obtain NiMo catalyst, activated by KOH, with two different designs: one based on honeycomb patterns and another on square ones. After the removal of the binders, the honeycomb structure presented cracks and not-uniform shrinkage, reason why the further evaluation of CO conversion was performed on the square design under a flow of CO and H_2 in ratio 2:1. A pellet of activated carbon impregnated with NiMo was used as reference of traditional manufacturing. Results showed an improvement in the 3D printed structure, ascribed to the fast transport compared with the pellet [308].
Middelkoop et al. performed a comparative study between in-house and commercial Ni/Al_2O_3 catalyst in pellet form and produced by robocasting, to be used in CO_2 methanation. Tests between 350°and 450°C, under H_2/CO_2 flow, ratio 4:1, showed a higher productivity for 3D printed structure, slightly higher for the commercial precursors, due to the more homogeneous distribution of Ni species detected by XRD-CT [309].
The optimization of catalyst is a critical point, barely being a single component, but a mixture of elements. The best ratio between each component has to be investigated. Inkjet printing can reduce the synthesis time, being able to produce quickly and automatically various compositions, using at the same time cartridges loaded with the different precursors. This approach have been used for photoelectrical water splitting [310], solar fuel devices[311], electrocatalysis [312], [313], photocatalysis [314] and water photoelectrolysis [315], [316].

1.5.3.3 3D printing for casting of reactors

As mentioned before 3D printing is often used to validation of new designs and solution. In the catalysis field, some studies report the use of polymeric compounds, which manufacturing is cheaper, to realize then the counterpart in metal or ceramic. *Kramer et al.* used a FDM printer to produce monolith in ABS to optimize the design of a monolithic reactor in function of temperature profile and time to reach the desired temperature [317].
Working with the same technology, *Li et al.* developed a hard template in PLA to be filled with phenol–formaldehyde (PF) paste and deposit on top Al_2O_3 and Ni as catalyst for syngas methanation. The obtained structures were placed in a fixed bed reactor to run the characterization under $H_2/CO/N_2$ flow at 375°C, showing higher or lower conversion compared to powder catalyst depending on the design [318].
An interesting application was implemented by *Knitter et al.* for gas phase reaction and tested on two different reaction: oxidative coupling of methane and isoprene selective oxidation to citraconic anhydride. Stereolithography was used to produce polymeric replica of housing and test plates with different designs. These were used to produce a silicone moulds to shape Al_2O_3 (Figure 1.35 shows the resulting alumina structure), which offer high resistance to elevate temperature and corrosive environments. This approach enabled the rapid substitution of test plates (Figure 1.35a), with the consequence of a wider screening of catalyst and the possibility of trying different structuration of the plates (Figure 1.35b) and the corresponding effect on the performance. The different plates were placed face to face in an appropriate housing (Figure 1.35c) to be sealed and placed into a furnace, up to 1000°C, proving to be gas tight up to 1.2 bar without any sealant [319].

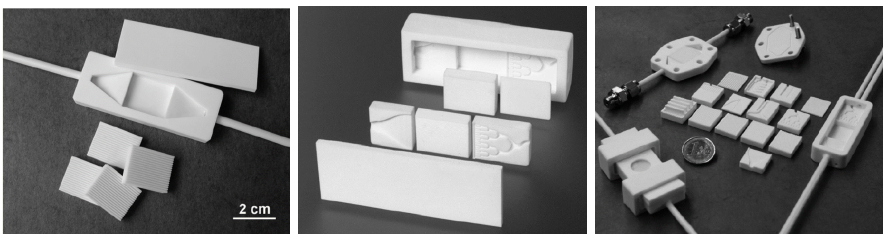

(a) Different micro-channel test plates to be exchanged

(b) Structuration of the test plates

(c) Housing and test plates in comparison

Figure 1.35: *Substrate and housing for micro channels reactors [319].*

1.6 Aim and scope of the thesis

The purpose of this thesis is to prove the suitability of ceramic 3D printing to manufacture valuable ceramic-based devices for energy applications. The approach intends to take currently existing energy technologies such as Solid Oxide Cells and Methanation Reactors beyond the state of the art by taking advantage of specific features of 3D printing. The added value aimed in this thesis is related to an improvement of the performance by design, an easier assembly of the parts or a straightforward automation of the complex manufacturing procedure.
This work covers different aspect from the development of printable feedstock, the optimization of printing and processing parameters, the structural and functional characterization of the printed parts (compared with the ones produced by conventional techniques) and the discussion of the enhanced performance by 3D printing.
More specifically, the thesis covers the following aspects (here presented chapter by chapter):
Chapter 2 describes the experimental technologies used in this work. In particular, Section 2.1 introduces the overall printing process, starting from the Computer Aided Design (CAD) and the critical aspects and features to pursue or avoid to obtain quality pieces. The printing step itself is described, first the SLA printing of commercial slurries is presented and secondly its hybridization with the robocasting technology to enable the multi-material printing. The post-processing, i.e. the cleaning and the thermal treatment, concludes this section and the manufacturing process. Section 2.2 reports the fabrication of the energy devices, describing the design approach and their functionalization, namely the used electrodes in case of SOCs and the catalyst for the methanation supports. In the case of the hybrid cells, the challenges of the process are presented, review the components for the formulation of printable slurries. For this purpose, state-of-art materials have been used as components of the cell, namely, 8YSZ as electrolyte and LSM-YSZ and NiO-YSZ mixtures as air and fuel electrodes, respectively. The choice of these materials is due to their co-sintering compatibility and resistance and performance at operating temperatures above 800°C. As interconnect, a ceramic material was chosen, with the mail aim to face a single-step sintering challenge for the whole stack. Among the other possibilities, LCTM ($La_{0.4}Ca_{0.6}Ti_{0.4}Mn_{0.6}O_{3-\delta}$) has been used for its compatibility with the cell components, as highlighted by *Hosseini et al.* proposing its use for the co-sintering of SOFCs [320].
At last the characterization techniques used during this work are described, as the for the structural point of view as for the electrochemical and catalytic ones.
Chapter 3 is dedicated to the optimization step prior to the achievement

of significant samples. The work is here presented following the production steps: at first all the components of the slurries are characterized and their suitability proof. Based on this reagents, the printable feedstocks are developed and optimized to achieve the best printability, due to the polymerization rate and flowing through the needle of the robocasting. During the development of the hybrid prototype, some efforts have been dedicated to the correct tuning of the different steps, the removal of the SLA material and the technology used to do so, the deposition of the inks and their polymerization. The final step in the printing process of ceramic is the thermal treatment, including the removal of organics and the sintering. This is the last step presented, concerning the monomaterial printing an optimization of the phases in the final pieces has been carried out. For the multimaterial printing a wider sweep of parameters was necessary in order to enable the co-sintering of the different layers, characterized by different TECs and requiring different porosity level. To conclude the chapter, the properties of the printed pieces are determined to be established as characteristic of the printed pieces.
In **Chapter 4** the performance of solid oxide cells based on printed electrolytes with a design comparable with the ones produced by pressing or tape casting are evaluated, to confirm the production of dense pieces, gas tightness and with suitable output. Designs prohibit for the traditional manufacturing techniques have been optimized based on the output power. An improvement of the performance was achieved coherent with the increase of the active area by unit of volume reached only thanks to the additive manufacturing technology. Such produced cells were tested in fuel cell, electrolysis and co-electrolysis mode, confirming the expected improvement. The electrochemical characterizations of cells realized by hybrid printing is then reported. The section is divided into symmetrical cells of fuel and air electrodes materials, the latter evaluating different sintering temperature and the gas diffusion depending on it. The results on a single-step manufacturing, co-sintered cell are reported and discussed, compared with cell based on printed electrolyte.
Chapter 5 presents the work done in the catalysis field, in which 3D printing reduces the limitations of manufacturing cost and possible achieving designs, making ceramics a competitor for various application, as in the Sabatier reactors. The effects on CO_2 conversion due to support material (alumina and state-of-the-art stainless steel) and design have been carried out.

Chapter 2

Experimental method

This chapter describes the experimental techniques used in this work, introducing their working principles, general purposes and their specific application in this thesis.
In Section 2.1, the 3D printing process is presented and explained, starting from all the software aid procedures, i.e. the design, rescaling and placing of the desired pieces, focusing on the limitations and precautions to assume at the moment of drawing the parts. Further on, the 3D printer system itself is presented in detail. Based on the nature of the printable material: ceramic particles dispersed in a polymeric matrix, and the working structure of the process, the obtained pieces need additional post processing, here reviewed.
Section 2.2 enters into detail on the devices realized in this work, Solid Oxide Cells based on printed electrolyte, cells produced in a single step (SLA+robocasting) and supports for methanation reaction, detailing the manufacturing process and their functionalization.
The following section is devoted to present the analysis techniques used to characterized printable materials and the printed pieces.
Section 2.4 discusses the set-up and techniques to evaluate the electrochemical performance of the Solid Oxide Cells.
Finally the experimental set-up for the evaluation of carbon dioxide conversion is described in Section 2.5. This part refers to the equipment at the Fraunhofer Institute for Microengineering and Microsystems, located in Mainz, Germany.

2.1 3D printing process

Additive manufacturing techniques have the capability of producing a three-dimensional piece from CAD designs. Although the printing process can be considered restricted to the parts production step using the 3D printer, the success of this process depends on a previous design step, and, in the case of ceramics on a subsequent post-processing step.
The base technology in this work is stereolithography (SLA). The definition of this printing approach is presented in Section 1.4.1. The system used is a commercial equipment from 3DCERAM (France) presented in Figure 2.1. Robocasting is also used for multi-material deposition, through a prototype arm incorporated in the SLA system (further details in the relative section 2.1.2).

Figure 2.1: *Picture of Ceramaker*

2.1.1 CAD design

The design of the pieces and the programming of the actions to perform during the printing, can be divided in three different stages. The first key step is a careful design of the desired piece. Once the design is stablished, a slicing of the pieces is required. The third dimension of the printing is given by the repetition and adhesion of a pile of two dimensional layers (the so-called slice). Their size depend on the resolution of the machine and the polymerization behaviour of the slurries. A dedicated software converts the 3D design in an assembly of slices, that can be read by the software controlling the machine, which allows to define the working parameters and control the

movement of axis and illumination of the laser. A detailed description of all the steps, the key factors and the limitations to take into account before production are here reviewed. As the drawing dedicate softwares, called Computer Aided Design (CAD), we used and tested different options during this work: Solidworks, Fusion 360 and PTC Creo 5.0. Each of them presents advantages and disadvantages. The preferred option, in general, was the use Solidworks. This application consists on a parametric design software based on operations, which enables the design of three dimensional pieces starting from a two dimensional sketch, and its extrusion in the third dimension.
Independently on the used software, some constrains have to be kept in mind during the design process, these limitations come from the working principles of stereolithography (see Section 1.4.1.1).

The printing process works slice by slice, features smaller than the resolution, i.e. the slicing step, will not be reproduced (see Figure 2.2).

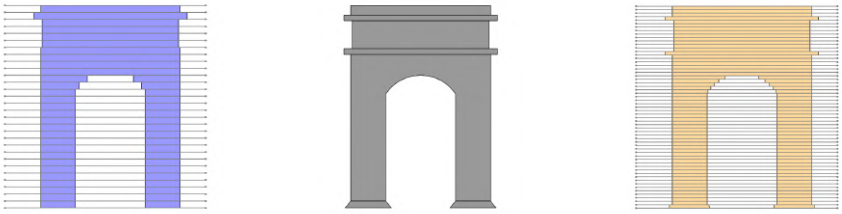

(a) Slicing of 5 mm *(b) Original design* *(c) Slicing of 2.5 mm*

Figure 2.2: *During the printing process the features smaller than the resolution of the machine are not reproduced, as it can see in Figure 2.2a compared with the original design (Figure 2.2b), while lower resolution even if not reproduce perfectly the design, allows to appreciate more details (Figure 2.2c).*

Also at the end of the printing, the desired pieces will be embedded into uncured paste that the user has to remove before the thermal treatment, otherwise applying temperature the uncured paste will turn solid, losing the designed features. For this reason it is necessary that, in the design process step, the removal of uncured pasted is foreseen, and adequate structures are projected. For example, it is important to avoid empty shell, while open channels for the mechanical access of the operator, giving preference to wider and straight paths rather than thin and curves ones etc. (Figure 2.37a).
It is also a factor to be considered that the parts in contact with the printing platform should have the maximum possible area to avoid movement of the pieces during the manufacturing process. Figure 2.4 illustrates this fact: a structure with reduced contact (Figure 2.4a) is more prone to lead to subsequent printing errors.

(a) Curve access to the channels *(b) Straight access to the channel*

Figure 2.3: *Channels are easier to clean when the access is through a straight path instead a curved one, in the case reported, design proposed in Figure 2.3b has to be preferred to design in Figure 2.3a.*

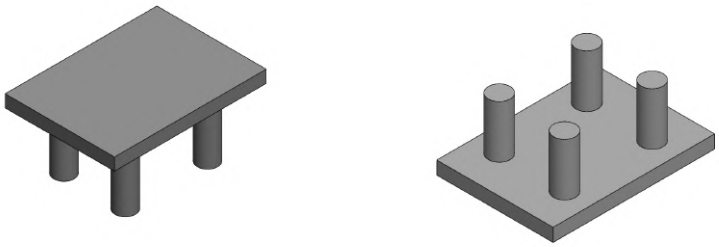

(a) Minor area touching the platform (b) Major area touching the platform

Figure 2.4: *Although controintuitive, the orientation in Figure 2.4b has to be preferred because offered major area to resist to the scraping of following layer.*

For this same reason, cylinders and round surfaces cannot be printed with the curve surface touching the platform. If necessary, a design modification is required, adding a rectangular part in contact with the platform that can eventually be be removed during the post processing (Figure 2.5).

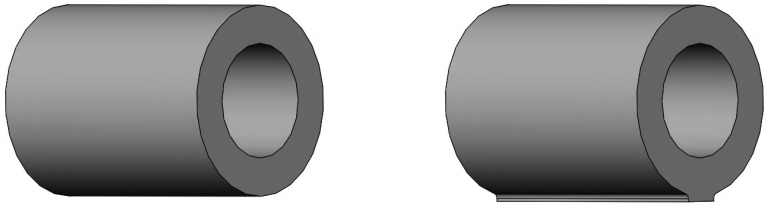

(a) Cylinder touching the platform *(b) Cylinder flatted to offer major resistance to the scraping*

Figure 2.5: *Cylinder and round surface should not be printed with the round surface touching the platform, if it cannot be avoided a flat surface has to be added.*

In the same line, suspended structures cannot be printed unless supports are introduced, to be removed after the printing, a thin layer of uncured paste needs to be present between the piece and the support. The distance between the two cured surfaces has to be chosen adequately. If it is too thin, the user will not be able to separate them during the cleaning process, if too board the support will move under the pressure of the tape casting system resulting in defects or fractures of the parts (Figure 2.6).

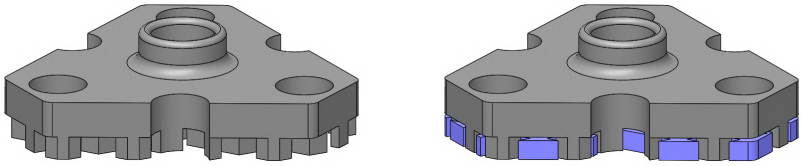

(a) Piece with suspended structure *(b) Piece with suspended structure and supports (highlighted in blue)*

Figure 2.6: *Suspended structures cannot be printed without supports, otherwise the structure will collapse.*

In line with the previous constrain, the direction of printing has to be taken into account at the moment of the design. All the parts of each piece have to present some mechanical strength to stand. For this reason, floating points and layers are impossible to print and lead to defects in the pieces around. A typical example is given in Figure 2.7. In the first case, the printing of the arms starts by floating points, which will lead to defective printing, whereas in the second case the arms are attached to the body leading to a successful printing.
Summed to the printing direction, the direction of scraping need to be considered as well. The blades will apply a stress on the paste and cured parts

during the spreading of new material. For long structures, such as tubes, it is preferable to orientate them parallel to the scraping direction (Figure 2.8).

(a) Man with arms along his body

(b) Cut to show the layer steps during the printing, floating points

(c) Man raising his arms

(d) Cut during the printing, no floating point

Figure 2.7: *Paradigmatic example of what it is possible to print by SLA (2.7c) and what would be not possible (2.7a). If the printing of the arms starts without supporting structure, mainly as two points floating in the printing platform, a movement will take place during the printing.*

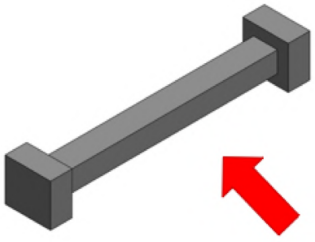

(a) Tube oriented perpendicular to the scraping direction

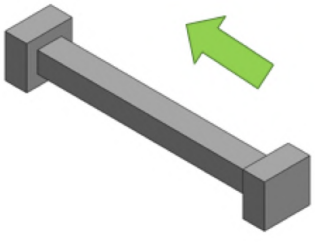

(b) Tube oriented parallel to the scraping direction

Figure 2.8: *2.8a) wrong orientation of tubes, suffering the stress of the scraping, probably resulting in a bending of the tube, 2.8b) correct orientation to reduce the strain on the printed layers during the scraping.*

Also, for the same reason, when thin vertical walls are printing, the use of supports to increase the resistance to the movement of the blades is recommended (Figure 2.9).

(a) Piece with thin walls

(b) Piece with thin walls and supports

Figure 2.9: *Piece with thin walls, vertical supports (highlighted in blue) are recommended to improve the resistance to scraping.*

Some restrictions from post processing also impose limitations to the designs. For instance, during the sintering process stresses are released. The presence of sharp edges may lead to the formation of cracks, so fillets should be added on sharp edges (Figure 2.10).

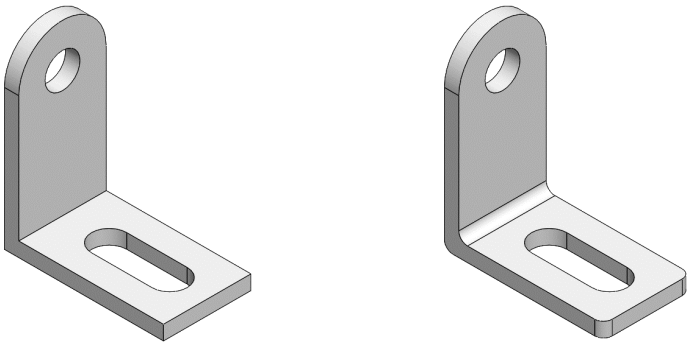

(a) Sharp edges

(b) Rounded edges

Figure 2.10: *Rounding of the edges helps to release the stress during the sintering and prevents cracking.*

A second example is the removal of organics during the debinding process as explained in detail in Section 2.1.3.2). The gas molecules have to reach a surface to be release in the environment. This limits the walls thickness to not more than 3 mm, or eventually 5 mm if a protective atmosphere is

used during the thermal cycle. Also from the materials usage point of view, thinner walls are preferable with supporting nerves to provide structural resistance comparable to a bulky part (Figure 2.11).

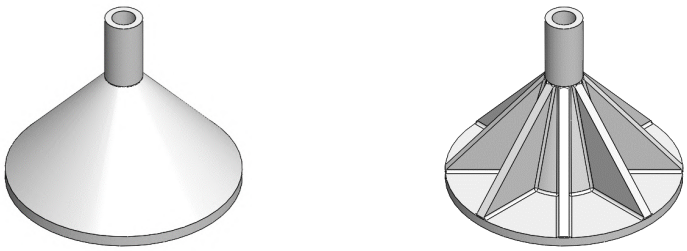

(a) Bulk piece *(b) Bulk part substituted with nerves*

Figure 2.11: *To help the releasing of organics and prevents cracks and furthermore reduce the consumption of material, it is preferred to avoid bulk part that are not functional and try to substitute them with nerves and thinner walls.*

A second software is necessary to prepare the "*platform*", i.e. the file which the printer software is capable to read, with the relative position of the parts. In this work we use *Magics*, in which the printing area can be defined, and the pieces placed to take the maximum advantage of the available space. In long printing processes, i.e. with pieces higher than 1 cm, these parts should be placed in the centre of the platform, to contrast the possible flow of the paste at the edges, that will result in a poor and bent printed piece (example in Figure 2.12).

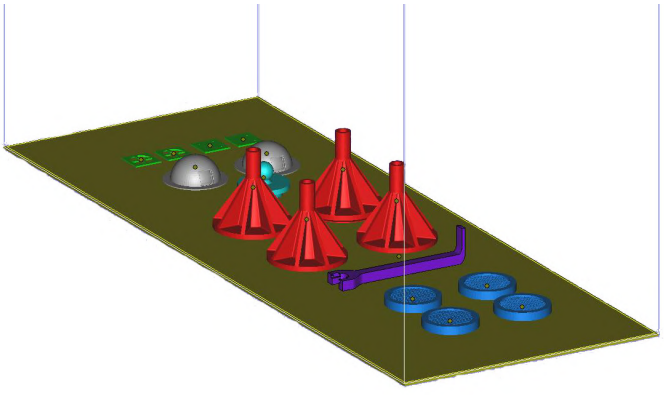

Figure 2.12: *Example of printing platform in Magics, the green square represents the printing area, the purple lines indicate the maximum height (not reported in the picture).*

The piece will face different shrinkage in different directions due to the removal of the organics and the sintering of the ceramic particles [321]. To account with this fact, the software allows the different rescaling in different directions. Figure 2.13 shows the desired dimension on the left side and the rescaled one, in perspective view and top view to better appreciate the changing in dimension.

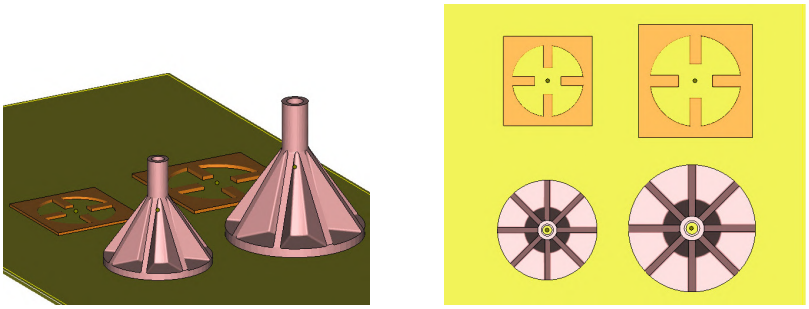

(a) Perspective view of the rescaling *(b) Top view of the rescaling*

Figure 2.13: *On the left of each picture the design pieces, on the right the piece as it has to be printed to obtain the original design.*

The values for rescaling are given from the producer for each type of material and at a recommended sintering temperature. When the sintering conditions are different from the ones provided by the supplier, it is necessary to establish new values. For this purpose, a batch of test pieces can be produced and measured after the sintering, which leads to new shrinkage values calculated using Equation 2.1:

$$s_x = 1 + \frac{x_d - x_m}{x_d} \tag{2.1}$$

where s_x is the shrinkage factor to be applied in x direction, x_d is the desired value and x_m is the measured value. This calculation has to be repeated for the three direction (i.e., x, y and z). Table 2.1 reports the values for the three different materials used in this work, for alumina, the values for 1700°C and 1550°C are reported.

axis	**3YSZ**	**8YSZ**	**Al_2O_3 1700°C**	**Al_2O_3 1550°C**
x	1.239	1.276	1.159	1.086
y	1.235	1.273	1.146	1.081
z	1.257	1.289	1.187	1.069

Table 2.1: *Shrinkage in the three direction for the different materials.*

Furthermore, *Magics* program implement the so called *z compensation*. Basing on the working principles of the machine, each time a layer is irradiated by the laser and cured, the three layers below are exposed as well and the residual radicals react. This is the key for achieving a good adhesion between each layer of the piece. In case a layer has no cured paste below, as in suspended or bridge points, the three layers below are exposed and cured as well. To avoid this over-curing problem, the software corrects automatically the design based on the cure depth of the laser, introduced by the user. In this way the first laser curing will occur with the over-cure of the forth layer above (Figure 2.14).

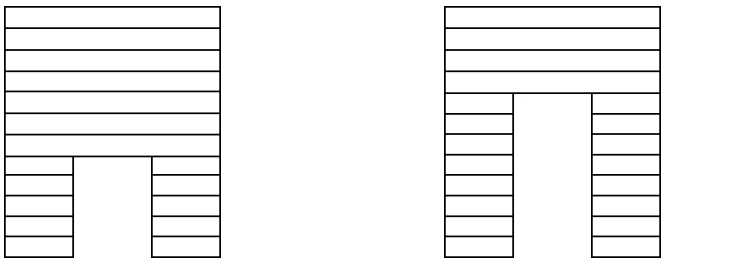

(a) Piece without z-compensation *(b) Piece with z-compensation*

Figure 2.14: *Each slice represents a layer during the printing, clearly the piece obtained in 2.14a is deformed and not corresponding to the original desire, as it is the one reproduce in 2.15b*

Other practical feature of *Magics* used in this work is the possibility of labelling the pieces, changing the last layers of the piece (in this work 200 µm have been mainly used), as shown in Figure 2.15.

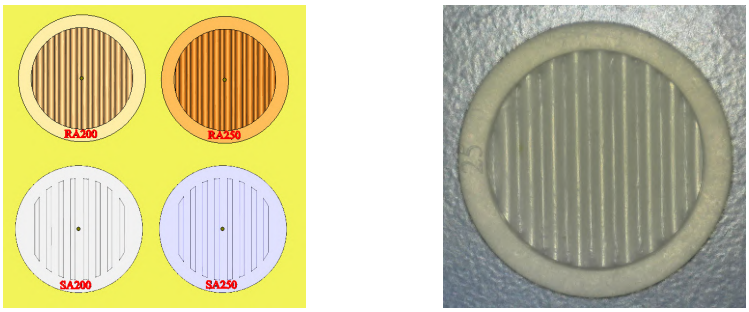

(a) CAD fiel with the engraving of the samples' names *(b) Printed piece with engraved written*

Figure 2.15: *Examples of writing feature to distinguish the samples after the printing.*

The 3D printer is controlled from a third software, *DMC* (*Direct Machine Composer*),which controls all the orders the machine has to perform during the printing and the movement of the mechanical parts and the laser. The relevant parameters are referred below, reporting their range and the typical values used.

- **Scraping speed**: with the term "*scraping*" is indicated the process of recoating the platform with a fresh layer of paste by the doctor blade system, the numerical values of speed and distance are optimized by the different materials and reported in Table 2.2.
- **Lowering step**: it is the step of which the platform moves after each curing of the laser and determines the resolution of the printing, its value is fixed at one fourth of the cure depth (a detailed description of this parameter is reported in the next section) of the paste to ensure the attachment between the layers, reported in Table 2.2.
- **Laser power**: As detailed further on in Section 2.1.2.1 the used laser shows a power between 100 mW to 1.2 W depending on the diode current and the frequency of use. At higher power corresponds higher cure depth, up to a saturation of the active radicals that can be activated.
- **Laser frequency**: it ranges from 30 kHz t0 160 kHz, depending on the application. 120.5 kHz is the optimized value to cure, while the outside marking of the piece is carried out at 160 kHz. In hybrid printing, different frequencies have been applied, to maximise the cure depth of the high absorbance slurries. During the laser ablation, the frequency is set at 30kHz to obtain the higher power required to remove the material.
- **Laser speed**: it ranges from 10 mm/s to 5000 mm/s. Lower speeds correspond to higher exposure, i.e. higher cure depth. Typical values change depending on the purpose. For the curing of the SLA, the speed of the rastering is 5000 mm/s, while for the marking it is 2500 mm/s. In case of the robocasting slurries values have be chosen depending on the absorbance in the range 10-1250 mm/s, while for the laser ablation of the cured paste the speed can vary from 10 mm/s to 120 mm/s depending on the desired depth of the ablation.
- **Hatch type**: this parameter defines the pattern with which the laser rasters the surface. The very same concept is used for defining the way the dispenser deposits the robocasted material. The available possibilities are presented in Figure 2.16. In case of curing, the preferred option in the lines profile, while for the deposition of the robocasting materials the contours one has been proved to be the most suitable

one.

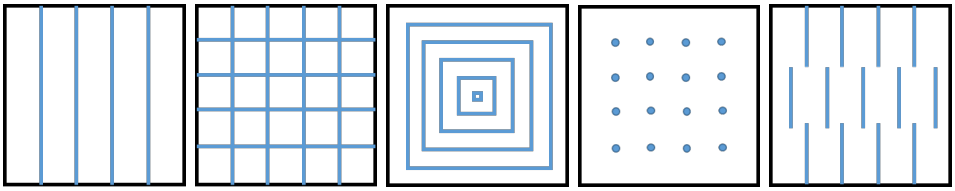

(a) Lines pattern *(b) Cross pattern* *(c) Contour pattern* *(d) Dots pattern* *(e) Stripes pattern*

Figure 2.16: *Hatch type*

- **Hatch angle**: in each layer defines the angle of the hatching referred to an axis. During the printing such value changes of 90°in each layer, this solution, already known for polymeric stereolithography has been applied from the 90s in the WEAVE and STAR-WEAVE scan patterns [224], [322].

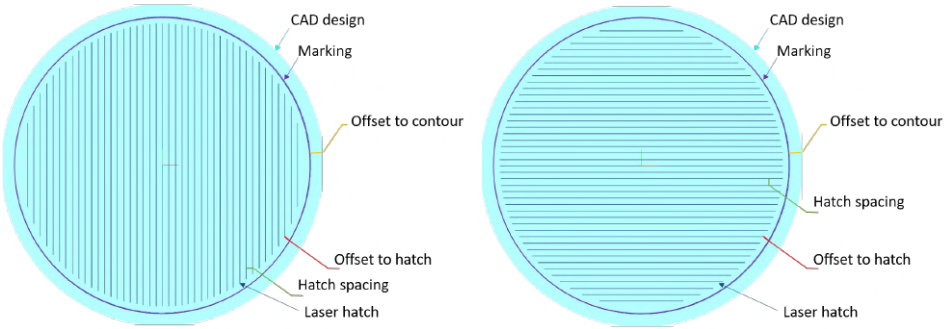

(a) Slice n *(b) Slice n+1*

Figure 2.17: *Identification of the different hatching parameters described in the text. The two figures represent the slice n and n+1. The hatching patter is turned 90° to improve the attachment of the layer and reduce the amount of uncured paste.*

- **Hatch spacing**: it defines the space between two different pattering lines of the laser/dispenser. For a better understanding, the hatching parameters are identified in Figure 2.17. For the curing of SLA pastes the distance is fixed at 40 µm. For the robocasting we screen possibility in the range from 10 to 100 µm. For the laser milling a wider range (10 µm - 5 mm) has been used to reproduce different features in the printed pieces. The distance between passages is a critical parameter in the deposition of the robocasting slurries, since such distance affects

the amount of material deposited and the possible failures during the printing.

- **Offset to contour**: this parameter defines the distance between the border of the CAD design and the marking of the laser or dispenser, the purpose of this parameter is in the first case, to compensate the lateral curing of the laser to optimize the x and y resolution. In the second case it is to compensate for the physical dimension of the needle and the deposited material.

- **Offset to hatch**: it defines a distance between the marking line and the hatch pattern. It is applied to avoid the overcuring and overdeposition, in case of curing and depositing, respectively. This solution has been integrated in the polymeric stereolithography with the STARWEAVE pattern since 1991 [224], [322].

To summarize the parameters we used in this work the optimal value for each one, in case of the monomaterial printing are reported in the Table 2.2 for the different slurries, 3YSZ, 8YSZ and alumina.

Parameter	**3YSZ**	**8YSZ**	**Al_2O_3**
Scraping speed	20 mm/s	20 mm/s	30 mm/s
Lowering step	25 µm	25 µm	50 µm
Laser power	550 mW	600 mW	300 mW
Laser frequency hatching	120.5 kHz	120.5 kHz	120.5 kHz
Laser frequency marking	160 kHz	160 kHz	160 kHz
Laser speed hatching	5000 mm/s	5000 mm/s	5000 mm/s
Laser speed marking	2500 mm/s	2500 mm/s	2500 mm/s
Hatch type	Lines	Lines	Lines
Hatch angle	0°-90°	0°-90°	0°-90°
Hatch spacing	40 µm	40 µm	40 µm
Offset to contour	100 µm	100 µm	100 µm
Offset to hatch	80 µm	80 µm	80 µm

Table 2.2: *Printing parameters for stereo-lithography.*

Moreover, the selection can change in base of the desired results. For example, when the laser ablation was used to increase the roughness of the surfaces and in this case different parameters have been applied. Table 2.3 reports the range studied and the most used values in two application, the removal of material to build the "*pool*" to deposit the robocasting material and to increase the roughness.
Each robocasting dispenser is controlled with the same parameters, changing the passing of the laser with the deposition of the material. A similar

Parameter	**Range**	**"*Pool*" ablation**	**Roughness improvement**
Slice step	25 µm - 1 mm	200 µm	500 µm
Laser power	200 mW - 1.5 W	1.4 W	1.2 W
Laser frequency	30-60 kHz	30 kHz	30 kHz
Laser speed	10-300 mm/s	60 mm/s	40 mm/s
Hatch type	Any type	Cross	Cross
Hatching distance	25 µm - 1 mm	25 µm	500 µm
Offset to contour	Anyone	No external marking	No external marking
Offset to hatch	Anyone	100 µm	500 µm

Table 2.3: *Laser parameters for milling of cured paste.*

list of parameters is reported in Table 2.4. In this case a range of value for each parameter is reported, but Section 3.2.2 analyse the influence of each parameter and presents a deeper analysis.

Parameter	**Range**	**Typical value**
Slice step	25 µm - 1 mm	200 µm
Gap platform - needle	100 µm - 1.5 mm	400 µm
Pressure	0.2 - 3 bar	0.8 bar
Deposition speed	10-120 mm/s	40 mm/s
Hatch type	Any type	Contour
Hatch spacing	25 µm - 5 mm	1.2 mm
Offset to contour	Anyone	No external marking
Offset to hatch	Anyone	1 mm

Table 2.4: *Software parameters for robocasting deposition.*

After the deposition of the robocasting slurries, a cure step is required, due to the high absorbance of the powder used in their development, the conditions in this case are different from the ones proposed for the SLA. Such step has been optimized as well. As in the previous case the range of values and the most typical ones are reported in Table 2.5, and compared with an ink made of the organic compounds without the ceramic load used to produce the channels, the so called "*sacrificial*" ink.

To summarize the steps of the CAD design, a flow chart of the different operation described in this section is here presented:

Parameter	Range	Ceramic slurries	Sacrificial
Laser power	200 mW - 1 W	800 mW	200 mW
Laser speed	10-5500 mm/s	10 mm/s	1250 mm/s
Hatch type	Any type	Lines	Lines
Hatch spacing	25 µm - 5 mm	1.5 mm	100 µm
Offset to contour	Anyone	100 µm	100 µm
Offset to hatch	Anyone	80 µm	80 µm

Table 2.5: *Software parameters for curing the robocasting slurries.*

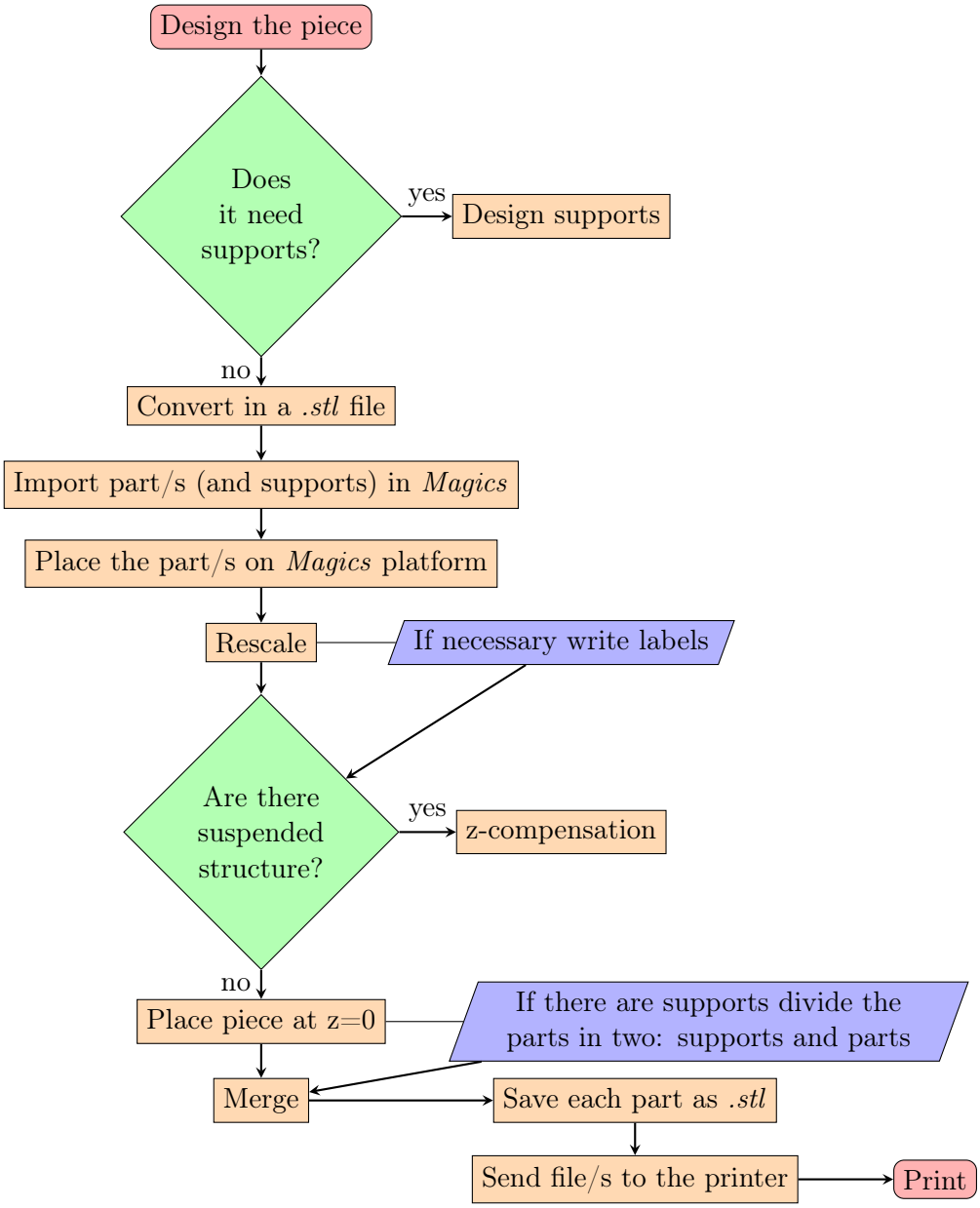

2.1.2 Printing step

For the printing process we used a commercial Ceramaker (3DCERAM, France), the machine is based on stereo-lithography of ceramic slurries. The slurries are made of ceramic powders and organic compounds: monomers, photo-initiator, diluent and dispersant. The commercial system at the moment of writing this thesis included only the SLA, being able to print only one material at the time. For this reason, it will be referred as monomaterial printing, presented in Figure 2.18.

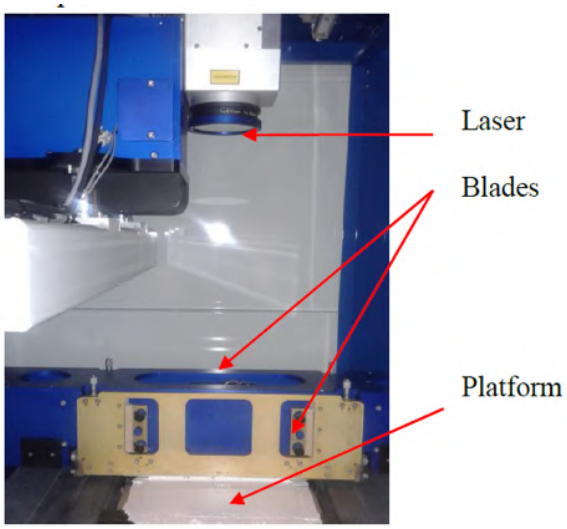

Figure 2.18: *Monomaterial configuration of the Ceramaker, the main parts are highlighted, the blades for the recoating after each printing step, the laser and the printing platform cover with the printing material.*

A prototype robocasting system was integrated in the machine in the frame of the Cell3Ditor project (Figure 2.19). This integration enables the production of up to five material at time (one from the SLA, which is giving the structure, and four with the robocasting). The use of this solution will be referred as hybrid or multimaterial printing. It is important to notice that although the robocasting system can work independently, depositing the feedstock material directly on the printing platform, the goal of this work is the hybridization of this two systems to produce a SOFC device, so the robocasting was used as standalone technology only for test and calibration. In the scheme below, the sequence of actions occurring during the printing steps are listed (Figure 2.20).

Figure 2.19: *Robocasting arm in position over the printing platform.*

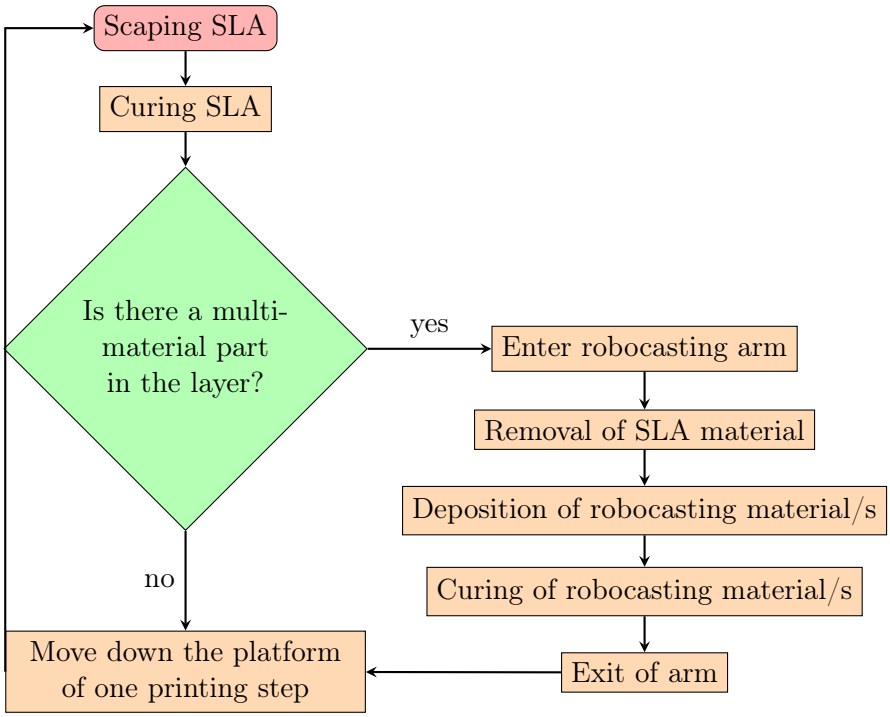

Figure 2.20: *Actions during printing*

In additive manufacturing process driven by light polymerization the cure depth is a critical parameter, giving information about the effectiveness of the reaction and establishing the thickness of the layer of each printing step in order to guarantee a good adhesion between the layers and consequently good properties of the final piece.
The interaction of light with turbid suspension have been studied widely, since the development of photo-curable slurries suitable for 3D printing [221], [323]; obtaining an empirical correlation between the energy of the light source, dimension of the ceramic particles and, a component due to the light interaction with the medium and the particles, in case of not absorbing particles:

$$C_d = D_p ln\left(\frac{E}{E_c}\right) \tag{2.2}$$

where C_d indicate the cure depth, E the energy dose and E_c the critical energy dose, D_p is the resin sensitivity, which is a function of the particle size, the ceramic load and the refractive index of monomer and ceramics:

$$D_p = \frac{2}{3}\frac{d}{Q}\frac{1}{\phi}\left(\frac{n_0}{\Delta n}\right)^2 \tag{2.3}$$

where d is the particle diameter, Q is the scattering efficiency term, ϕ is the volume fraction and Δn is the difference between the refractive index of the ceramic and the monomer (n_0). The profile of polymerization is presented in Figure 2.21. The laser cannot be considered adimensional and consequentially the polymerized material has a parabolic shape, if the laser is scanning in the x direction, the figure is elongated in the same direction. To optimized the resolution of the piece, an offset to the contour of the CAD is considered for the curing process (See Figure 2.17).

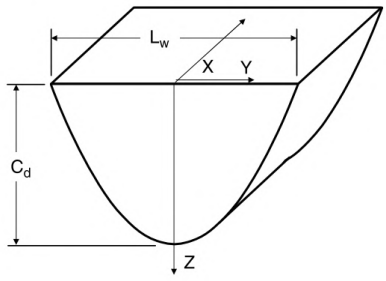

Figure 2.21: *Cured line showing the parabolic shape of the profile, C_d indicate the cure depth and L_w, the cure width [224].*

This cured width is proportional to the beam size and it increase with the cure depth, following the equation:

$$L_w = W_0\sqrt{\frac{2C_d}{D_p}} \tag{2.4}$$

where L_w, C_d and D_p have been defined before and W_0 is the $1/e^2$ Gaussian half-width of the beam spot.
To evaluate the real cure depth of the developed paste, and to adjust the power of the laser before each printing, a test about the real value of the cure depth was performed, a square sample was cured with a single laser shot out of the printing platform with abundance of paste, so the polymerization would not be stopped by the limited amount of slurry. Each sample was realized at a different laser power and its thickness was measured over eight points. For commercial slurries, the cure depth had to match fixed values (four times the slicing distance), meaning 100 µm for zirconia paste and 200 µm for alumina one. Due to high viscosity of 8YSZ paste a value of 115/125 µm had been proved to be more efficient. For the robocasting slurries, due to a general high absorption of the particles, which leads to low cure depth values, the maximum possible value has been pursued.

2.1.2.1 Monomaterial printing process (SLA) of commercial slurries

As explained in Section 1.4 ceramic stereolithography requires highly viscous slurry (as show in Figure 2.22) made of a high ceramic powder load (above 45vol%) [324], dispersed in a organic mixture.

Figure 2.22: *Commercial SLA paste*

The components of the organic mixture are:

- Monomers and oligomers, which are the basis of the polymeric chain that will develop under light exposure. Two different types are suitable for SLA printing, linear monomers or branched one, this are preferred since can generate cross-linked structures able to trap the ceramic particles.
- The photo-initiator is a compound sensible to UV or visible light that generates a radical under exposure and this radical starts the polymerization of the monomers.
- The diluent is a low viscosity compound that fluidizes the slurry, it is usually reactive as well in the polymerization process.
- The dispersant and surfactant improve the dispersion of ceramic particles in the monomer to avoid the agglomeration [215].

In the case of the machine used in this work, the light source is a semiconductor laser (NANIO AIr 355-3-V, from InnoLas Photonics, Germany) with a fix wavelength of 355 nm and a nominal maximum power of 1.2 W at 100 kHz. The real profile of power in function of the percentage of current through the diode is reported in Figure 2.23 at the working frequency (120.5 kHz), measured with a powermeter Fieldmate equipped with a sensor PM-10 from Coherent, USA.

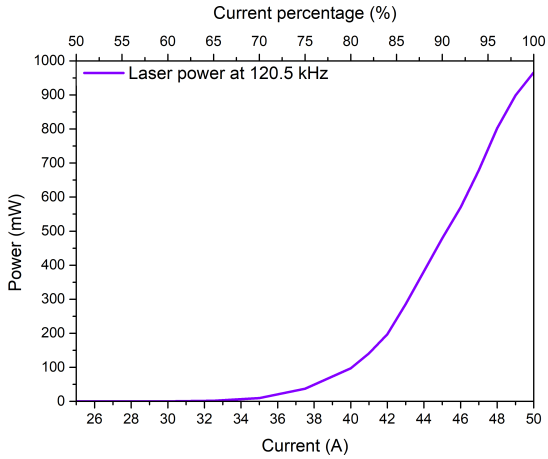

Figure 2.23: *Power curve of the UV laser in function of the current passing through the diode*

Under UV exposure, the photo-initiator forms a radical which reacts with the monomers/oligomers to form long polymeric chain. During this

process the ceramic particles, which were fine dispersed in the liquid slurry, get trapped inside the solid [214].
The ceramic slurry has to fulfil several requirements to be printable:

- A good dispersion of the particles is necessary to obtain a good final piece with homogeneous properties.
- The viscosity and the rheological behaviour have to be suitable for the recoating of each layer.
- The cure depth has to be satisfactory to guarantee the adhesion between layers [214], [215], [324].

In case of failure of the first requirement, not only the properties of the final piece will not be uniform, but if the agglomeration is sever enough to be comparable with the layer thickness, the blades will move this agglomerate over the printing platform, resulting in a not flat layer or a damage of the layers printed before.
The viscosity has to be suitable to be spread by the doctor blade to ensure the recoating of the platform, but high enough to sustain itself and the printed pieces. For that to be possible, a shear thinning behaviour is required, meaning that the viscosity is reduced with the applied deformation. In this way, the paste will oppose less resistance to the spreading [325], but it will not flow from the platform, giving sustaining to the pieces during printing. When a high ceramic load is added to a liquid, a shear thickening behaviour may appear [326]. This behaviour is characterized by the viscosity increasing applying a force (see Figure 2.24) and this will prohibit a proper recoating of the layers. To avoid this phenomena, a Newtonian low viscosity of the organic mixture is required, often with the addition of diluents and dispersants [214], [238], [327].

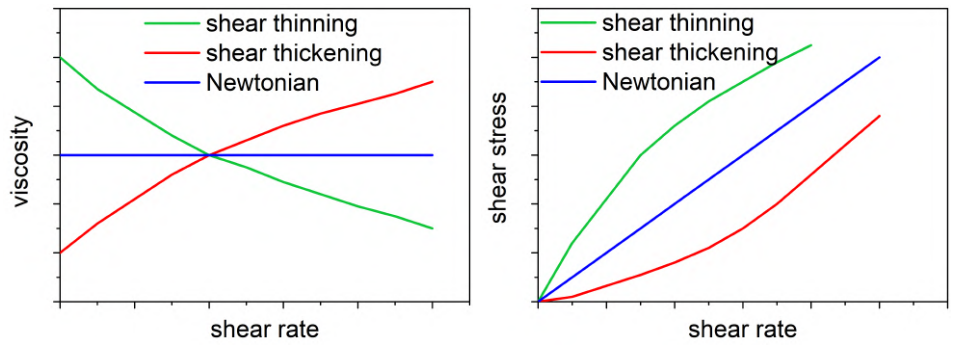

(a) Viscosity behaviour *(b) Shear stress behaviour*

Figure 2.24: *Different rheological behaviour in function of the shear stress.*

A critical aspect for the printing process is the cure depth of the slurry, this value indicate how deep the laser penetrate and cure the paste. Over this parameter the entire printing process is calibrate [328]. The layer thickness is set to a fourth of the cure depth, in this way after each recoating the light can penetrate and cure the layers below obtaining the adhesion between them [208]. In fact, a critical point in the exposure is not to connect all the active sites of the polymeric chain, in order to have a second polymerization with the following layers. While low curing depth will prohibit a proper adhesion between layers (examples of this kind of failures are reported in Figure 2.25), since in the following layer a scraping step is required, this usually leads to a shifted piece. The layer thickness is chosen a priori, defining the printing material from the software and the power of the laser is tuned to match this value.

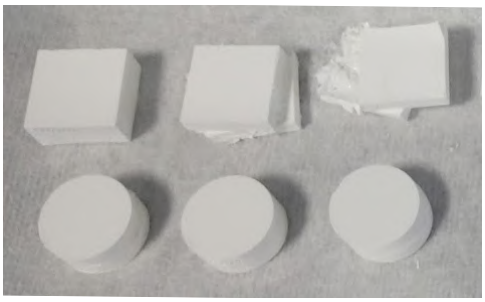

Figure 2.25: *Example of printing fail, in which the layers present bad attachment and consequently shift in the scraping direction.*

2.1.2.2 Robocasting of in house developed slurries for multimaterial printing

The nature of SLA technology makes it difficult to hybridize it to obtain multi-material option. For this reason, as explained above, multiple materials are supplied by a robocasting system. The printable slurries are stored in different cartridges. A pressure-controlled piston is used to regulate the flow. The cartages are connected to a robotic arm where four electric valves control the start of deposition of material through needles.

The valves xQR41V by Nordson Corporation, USA, which control the flowing of the robocasting inks work with Optimum general purpose dispense tips, from the same company. These stainless steel tips present the disadvantage of bending at the minimum collision, often achieve during the calibration with the spacers, resulting in a deposition shifted respect to the design, as shown in Figure 2.27. To overcome this issues Optimum Smooth-Flow tapered dispensing tips have been purchase from the same provider and tested in the machine. These ones are recommended from medium to high

(a) Cartridges *(b) Pressure regulators* *(c) Valves and needles on the robotic arm*

Figure 2.26: *Robocasting system integrated in the commercial Ceramaker.*

viscosity fluid and due to their conical shape are less prone to bending.
The SmoothFlow tips are produced in poly-ethylene, showing higher flexibility and in poly-propylene, more rigid, both have light-blocking additive to protect UV-sensible materials. The poly-ethylene ones are preferred since a minor shift is observed in case of collision with the platform.

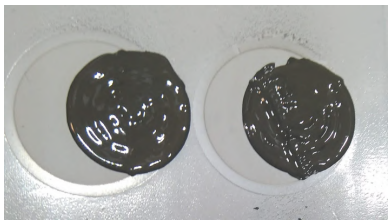

Figure 2.27: *Effect of tip bending, the deposition is shifted with respect to the milled "pool", the alignment between laser and tip was calibrate previously*

The robocasting slurries need a much lower viscosity compared with the SLA ones (comparing Figure 2.22 and 2.28) since the flow through tubes and needles is required.
The rest of their requirements are however shared with the SLA pastes: good dispersion of particles, suitable rheology and proper cure depth. The failure in meeting these requirements, on the other hand, manifests in immediate issues. The agglomeration of particles may clog the valve and the needle during the printing, resulting in no material deposited. An unappropriated viscosity may hinder the flow through the system or generate an excessive flow and spreading of the paste. The poor cure depth will lead to uncured (liquid) paste, that will be dispersed by the blade scraping of the following SLA layer, contaminating the whole platform (see Figure 2.29). Details on the optimization of the rheology of the robocasting slurries are presented in

Section 3.1.3.

(a) NiO-YSZ slurry *(b) LSM-YSZ slurry* *(c) Sacrificial slurry*

Figure 2.28: *Robocasting slurries of fuel (2.28a) and air electrode material (2.28b) and a slurry made only of organics to print embedded channels (2.28c)*

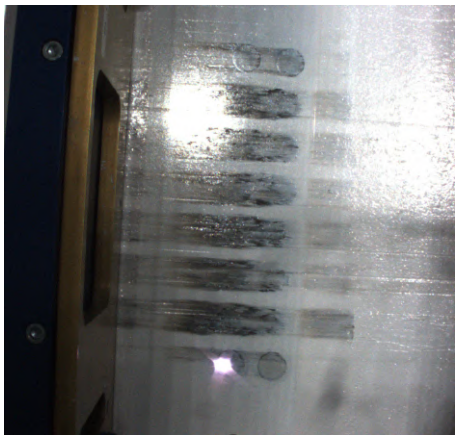

Figure 2.29: *Picture during the process, the NiO-YSZ was not cured completely and the blades spread it over the entire platform.*

2.1.3 Post-processing

At the end of the printing process, the piece is in green state, meaning that it shows poor mechanical properties more comparable with plastic than with ceramics. The pieces are embedded in uncured paste that, once the hardened pieces are removed, can be reused for other printings. Figure 2.30 shows the printing platform at the end of a mono-material printing. The formation of this kind of "*brick*" of high viscous paste helps to keep the position of the

pieces during the printing process under the scraping stress from the blades.

Figure 2.30: *Picture of the printing platform as removed from the printer*

2.1.3.1 Cleaning

After the printing process, it is necessary to clean the parts before the final thermal treatment, to recover the uncured paste for further printing and to obtain a high quality of the final pieces, in fact, if any remaining uncured paste suffers the thermal treatment it will turn in hard ceramic and defects from the original design. These defects can be removed only by mechanical abrasion (not always possible in complex designs).
The first step of cleaning consists in saving the uncured paste and has to be done without any solvent, as the contact of the paste with solvent will banish any further use (Figure 2.31). Later the piece can be cleaned with the help

Figure 2.31: *Picture of the printing platform after removing the uncured paste*

of solvents. A commercial solvent, Ceracleaner (3DMIX, France) was mainly used. While this cleaner mildly removes the uncured paste and solvent is not so aggressive to damage the pieces, but as well is not so fast to remove the uncured paste. For simple pieces, without support and with wide, open channels the use of brushes and Ceracleaner is sufficient. Different combination of solvent and methodologies were tested to find other cleaning options more appropriate for complex pieces: the best one was found to be a mix-

ture of 80vol% heptane and 20vol% toluene under stirring. In case of narrow channels the use of ultrasound for 15-30 minutes can be useful. Longer time causes the heating of the system and the paste can cure by thermal effect. In any case, the mixture heptane-toluene is volatile and the piece dries in around one minute, which generates cracks. For this reason a final step in Ceracleaner is necessary to prevent the formation of defects. Another critical point is the time between printing and thermal treatment, that should be as short as possible, in fact, since the piece is still made of ceramic powder and polymers, they can be affected by light and humidity.

2.1.3.2 Thermal treatment

As already explained, at the end of the printing process the properties of the pieces are given by the polymeric matrix which trapped the ceramic particles in shape (Figure 2.32a). Further thermal treatments are necessary to obtain the final ceramic pieces. The first step is the **debinding**, which is a long treatment, comprising ramps with slopes below 0.5 K/min, under gas flow, air or nitrogen, to remove the organic compounds, without burning them. The debinding itself stops at 800°C, but a **pre-sintering** step above 1000°C is added to make possible the handling of the piece, which shape is not kept anymore by the organic matrix. As represented in Figure 2.32b, this step is fundamental to ensure a minimum mechanical stability of the pieces in case a change of the furnace is required. The following step is the **sintering** itself, depending on the material the final temperature and time of dwell. In this step, a controlled atmosphere is not required, but oxidant or slightly oxidant conditions are preferred. In the sintering step the ceramic particles get closer and the diffusion begins, generating a solid final piece (Figure 2.32c).

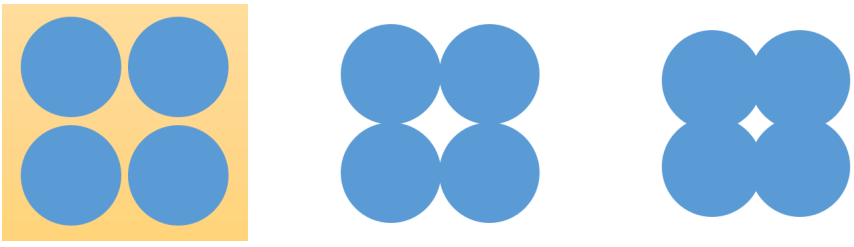

(a) Green part *(b) Part after debinding* *(c) Part after sintering*

Figure 2.32: *Different steps of a printed piece during the thermal treatment, the following shrinkage is easy understandable.*

As explained, this treatment requires a continuous gas flow, often with a change of gases, so tubular furnaces were used (Lenton, UK and Hobersal,

Spain), equipped with dedicated gas control system (Bronkhorst, Netherlands).

2.2 Fabrication of energy devices

During this work, we applied 3D printing technologies to the production of high temperature ceramic-based storage devices.
The selection of materials is a key issue. For the application in SOCs, purely ionic conductive materials are required for the electrolyte, and electrochemically active electrical or mixed ionic-electronic conductive materials are needed for the electrodes (as reviewed in Section 1.2.2).
Moreover, all the materials must present similar thermal expansion coefficient and present chemical compatibility at the high manufacturing temperatures. The selected set of materials are well known in the SOC field: 8YSZ, Ni-YSZ as fuel electrode, and LSM-YSZ as oxygen electrode. Two different types of cells were produced: electrolyte supported ones, in which only the electrolyte was printed by SLA and the electrodes were deposited in a second step, and the hybrid cells, entirely produced in a single 3D printing process. In both cases, the electrolyte is made of commercial paste provided by 3DCERAM (France) based on 3mol% or 8mol% yttria stabilized zirconia. For the hybrid cells, the electrode slurries were developed in the laboratory (further description of the process is presented in Section 2.2.2.2).
While the final objective is to produce an entire functional cell (Figure 2.33a), symmetrical cells have also been produced to allow the performance evaluation of every single component, i.e. electrolyte, anode and cathode (Figures 2.33b, 2.33c and 2.33d).

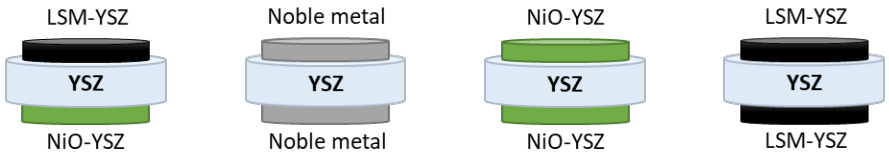

(a) Scheme entire cell

(b) Symmetrical cell with noble metals as electrodes

(c) Symmetrical cell with fuel electrodes

(d) Symmetrical cell with air electrodes

Figure 2.33: *Configuration of electrochemical cells*

2.2.1 Electrolyte Supported Cells

The great contribution that 3D printing can provide to fuel cell technology is the suppression of the constrain to planar and tubular designs. In this thesis, YSZ electrolyte has been chosen as supporting element. There are several reasons for this choice, among which the low light absorbance (which

facilitates the SLA printing step), and the high required sintering temperature are the most important ones. The fabrication of electrolyte supported cells requires a certain thickness to sustain the structure, the minimum value is assumed to be 150 µm [329].
The resistance of a layer presenting an ohmic behaviour is depending on the resistivity of the material (ρ), and geometrical factors, area (A) and thickness (L) following the Second Ohm's Law:

$$R = \rho \frac{L}{A} \tag{2.5}$$

To improve the performance of a cell, i.e. reduce its resistance, it is possible reduce the resistivity, using a material with higher ionic conductivity or changing the geometrical factors of the electrolyte. The state-of-art solution is, as mentioned before, to reduce as much as possible the thickness of the electrolyte, moving from electrolyte to anode supported cells. In this work the SLA has been used to produce electrolytes and enhance their area through complex designs.

2.2.1.1 Printed electrolyte for SOCs

While current design of SOCs are constrained mainly in two shapes: the planar and the tubular ones, the use of 3D printing technologies can provide complex shapes. In this work the purpose of using additive manufacturing is to enable the production of electrolyte supported cells, in which the active area is higher than the one of a planar cell with the same projected area (reference for the cell produced by state-of-the-art manufacturing). As it is shown in Figure 2.34a, all the printed electrolytes are made of a thin membrane (250 µm), which is the active electrolyte and consequently as thin as possible, and a thick ring (2 mm thick and 3 mm high). This ring has a double role, in first place it is necessary to handle the thin membrane and remove it from the printing platform at the end of the printing, and in second place, it is design on the measurement station, in order to facilitate the sealing between the housing and the electrolyte (Figure 2.34b). Moreover, being the sealing the weakest point and source of leakages in the set-up of electrochemical measurements, this solution enables to put the possible leakages away from the components of the cell [267].
Different studies proposed the enhancement of the performance tuning the shape of the interface between electrodes and electrolytes. Most of them [262], [263], [330], [331] are based on simulations, proposing different geometries and optimizing the dimensions of such structures. *Cebollero et al.* used laser machining to locally reduce the thickness of the electrolyte fol-

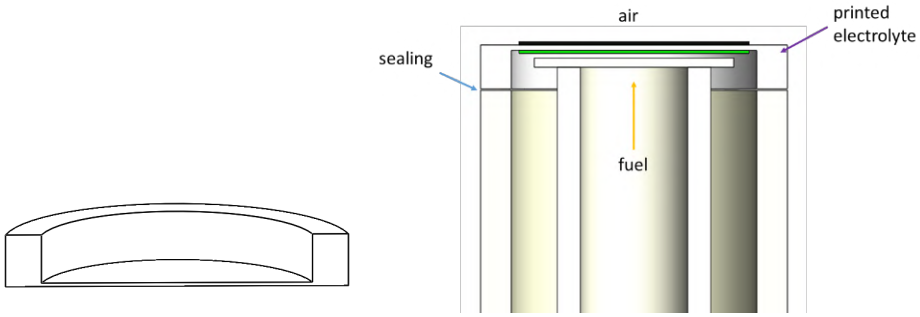

(a) Cross section of the printed electrolyte

(b) Scheme of the set up and the use of the ring in the sealing

Figure 2.34: *Scheme of the integration of the ring in the design of the electrolyte membrane and its use for the sealing in the set up*

lowing a path of dots, obtaining a reduction of the ASR of symmetrical cells [332], [333]. Other works on micro-SOFC proposed the structuration of the electrolyte layer by nanopattern transfer technique [334], [335].
Figure 2.35 shows the proposed design to be manufactured by mean of stereolithography. These designs have faced a previous step of optimization regarding the direction of printing, the use of supports, the use and thickness of the external ring. These designs are produced, cleaned and sintered with high success ratio, ensuring a good replication of the design. Table 2.6 reports the values of the active areas of the different designs and the improvement compared with the planar reference electrolyte, which has an area of 2.00 cm^2.

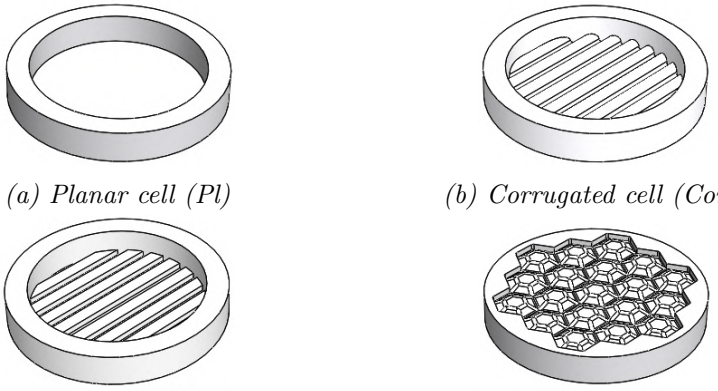

(a) Planar cell (Pl)

(b) Corrugated cell (Corr)

(c) Square aligned cell (SA)

(d) Hexagonal cell (Hex)

Figure 2.35: *CAD designs of the proposed cells in this work.*

The manufacturing of the mentioned cells was made with commercial paste of 8mol% yttria-stabilized zirconia from 3DMIX (France), the laser power

Cell	Active area [cm^2]	Increase [%]
Pl	2.00	–
Corr	3.15	+ 57%
SA	3.12	+ 56%
Hex	2.40	+ 20%

Table 2.6: *Active area of the cells based on different design of the electrolytes*

was set around 400 mW, tuned in order to obtain a cure depth above 100 µm, the printing step in z direction was set at 25 µm, one fourth of the polymerization test.
Once the printing process is over, the pieces were removed from the platform and cleaned (see Section 2.1.3.1) and, as described in Section 2.1.3.2, placed in a tubular furnace under flowing atmosphere to remove the organics and then sintered. The recommended cycle for is up to 1300ºC for 4 hours.

2.2.1.2 Functionalization

To obtain a Solid Oxide Cells, the electrodes are painted on the 3D printed electrolytes. State-of-the-art materials were used [34], [36], namely Ni-YSZ as fuel electrode (introduced as NiO and reduced *in situ*) and LSM-YSZ as oxygen electrode. Commercial inks were used (Fuelcell materials, USA), brush painted on the electrolyte following the specification of the producer. The nominal composition of each ink is reported in Table 2.7.

Compound	Percentage by weight [%]
NiO-YSZ	
NiO	66
$(Y_2O_3)_{0.08}(ZrO_2)_{0.92}$	34
solid load	73-77
LSM-YSZ	
$(La_{0.80}Sr_{0.20})_{0,95}MnO_{3-x}$	50
$(Y_2O_3)_{0.08}(ZrO_2)_{0.92}$	50
solid load	60-70

Table 2.7: *Composition electrodes inks*

To overcome the adhesion problems reported from *Cebollero et al.* [332], [333], an attachment layer of 8YSZ is deposited by powder wet deposition with an air brushing system (see Figure 2.36). The ink used is based on ethanol and 8YSZ powder of $\sim$ 200 nm of diameter (Kceracell, South Korea) and PVP (polyvinyl pyrrolidine) used as dispersant, the solution is stirred

overnight until it reaches a proper mixing.
The bed is heated up to 50°C to allow the ethanol to evaporate when touch the sample. A thermal treatment at 1150°C for 1 hour is applied to attach the powder to the sample while keeping an appropriate roughness for the attachment. The effectiveness of this process is reviewed and proved in Section 4.1.1.2

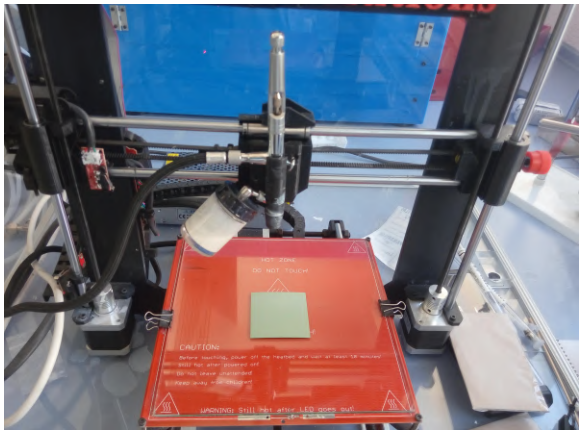

Figure 2.36: *Airbrush set-up*

2.2.2 Hybrid Self-Supported Cells

To manufacture hybrid self-supported cells, we used the combination of two systems: SLA and robocasting. The SLA provides the electrolyte, acting also as backbone structure that provides mechanical properties and shape to the cells. The robocasting is used to produce the electrodes, interconnectors, and embedded channels. For the last elements a slurry without ceramic load is used, that, after the thermal treatment, will result in an empty space. In Figure 2.37 channels embedded in the printed piece are presented).

2.2.2.1 Multi-material printing process

The hybridization of SLA and robocasting presents some difficulties that have to be overcome. For example, the resolution of SLA and robocasting are different (25 µm in the first case and between 150 µm and 400 µm in the second one, depending on the tuning of parameters. This means different designs in the drawing phase and different slicing in the *DMC* software. One of the requirements for a good SLA printing is to have a flat surface after each layer, including a proper recoating of the previous one. This finish is obtained in the Ceramaker by depositing the layers by tape casting. If the

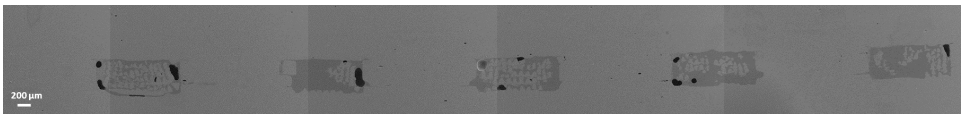

(a) Embedded channels obtained by robocasting of sacrificial material

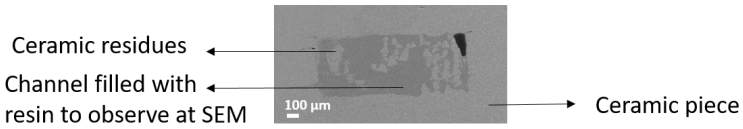

(b) Detail of a channel

Figure 2.37: *2.37a rendering of SEM images of channels embedded in alumina piece, 2.37b detail of a channel, to enable the observation with SEM the piece is embedded in epoxy resin which fills the voids, and covered with gold.*

robocasting materials would be deposited directly on the final layer of SLA they will result in domes over a flat surface, which would be removed by the friction of the following scraping by the blades. For this reason, it is necessary to ensure that the robocasting material is embedded in the SLA, as presented in the sketch in Figure 2.38.

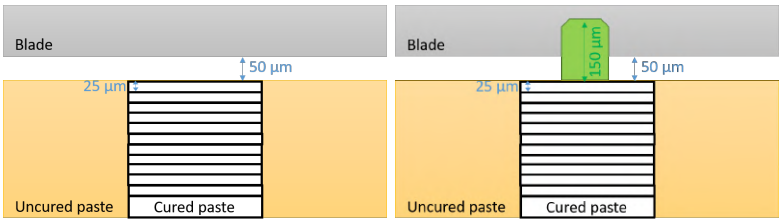

(a) Gap before scraping in mono-material condition

(b) Deposition of robocasting on final layer of SLA

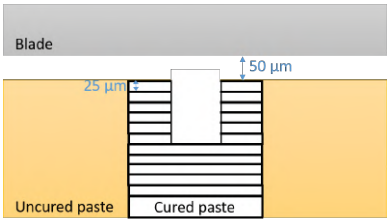

(c) Forming of the "pool" before robocasting deposition

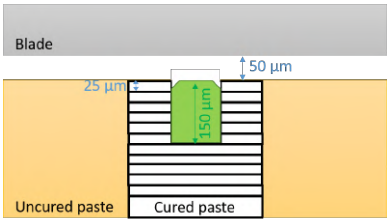

(d) Deposition of the robocasting in the "pool"

Figure 2.38: *2.38a and 2.38b present the situation before and after the robocasting deposition without the removal of SLA material, 2.38c and 2.38d present the same moments with the removal of the SLA material.*

We tried two different solutions to remove the SLA material, as first, a milling

of the cured paste performed by the laser at a different power, secondly a blowing by compressed air of the uncured paste. A combination of the two solutions has been applying to take advantage from the speed and the cleanliness of the air blowing and the increasing roughness to help the attachment achievable by the laser machining.

2.2.2.2 Slurries formulation

In the case of the robocasting slurries, we developed the printable feedstock, based on the compatibility with the SLA material, in order to enable the attachment of the robocasting layer to the SLA layer and viceversa. Moreover it is important to ensure the slurry need flow through the needle (or tip) and to get spread it in the "*pool*".
As mentioned in Section 1.4.1.2, the components of SLA paste, are monomer, diluent, photo-initiator and dispersant. On this basis we carried out the development of the robocasting inks. The best results have been obtained using a combination of TMPTA and DMPA (Sigma-Aldrich, USA) as photo-initiator. Trimethylolpropane triacrylate (TMPTA), shown in Figure 2.39 is a branched monomer with three active sites, used to produce ceramic-based slurries for stereolithography [336], [337].

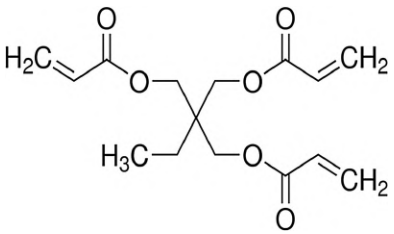

Figure 2.39: *TMPTA*

1,6 hexandiol diacrylate (HDDA) is a linear acrylate with two active sites, which takes part in the polymerization process. It is suitable to be used as diluent, as it exhibits lower viscosity than TMPTA [336], but higher shrinkage due to polymerization [215], [338], [339].

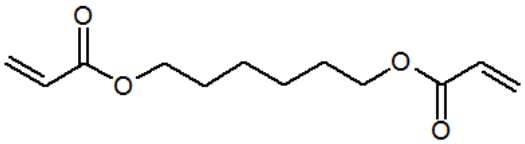

Figure 2.40: *HDDA*

2,2-Dimethoxy-2-phenylacetophenone (DMPA) is used as photo-initiator due to the absorption in the UV range of the laser [214], [215], [338], [340].

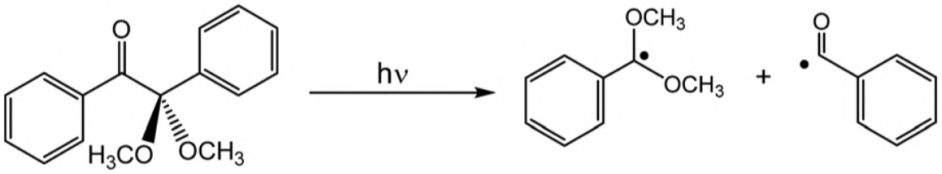

Figure 2.41: *DMPA and its formation of radicals [341].*

To prepare the slurries the starting powder was dried overnight at 120°C, to remove any trace of humidity. To mix and homogenize the ingredients, a planetary centrifugal mixer, Thinky ARE-250 (Polydispensing, France), was used. At first we mix the liquid components and degas them to remove eventual bubbles, then we add the powder and mix it in different steps to avoid the over heating and the consequent polymerization of the slurry (details are reported in Table 2.8).

Material	Mixing	Degassing
Liquid compounds	6 min 1000 rpm	6 min 1200 rpm
Slurry components	6 min 1000 rpm	
	6 min 1500 rpm	
	2 min 2000 rpm	
	(2 min 2000 rpm)	(2 min 2000 rpm)

Table 2.8: *Mixing steps for the in-house developed slurries*

2.2.2.3 Designs for single-step processing of SOFC cells

In the case of the multimaterial printing, different designs have been tried to obtain good pieces, from the point of view of the printability, the removal from the platform and the co-sintering.
The shape of the produced button cells is in general an electrolyte of 25 mm in diameter with two electrodes of the same size. With this architecture, the robocasting step is parametrized with three parameters: the diameter of the region in which the material will be removed, the diameter of the deposition, and the region exposed to the laser curing (Figure 2.42).

An important issue to take into account is that, if equal dimensions are imposed for the removal and deposition diameter, this will cause problems of over deposition on the edge, and consequently uncured robocasting ink

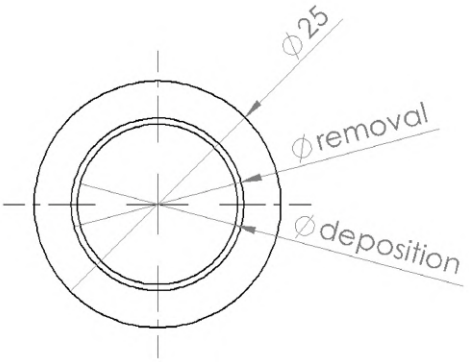

Figure 2.42: *CAD design used for the multi-material cells.*

in the SLA paste after the first scraping of the blades. To overcome this, according with the deposition sizes, a difference of 0.7 mm is applied. To ensure the complete polymerization of the material, the diameter for the curing is set equal to the one for the material removal. Thicker 8YSZ rings of 3.5 mm are used in this case, compared with the 2.5 mm (before sintering) chosen in the 3D printing electrolytes presented in Figure 2.34a. This choice responds to a necessity of a higher robustness to sustain the entire structure at the time of detaching and cleaning.
SRUs are under study regarding the printability and the co-sintering to achieve fully printed devices.

2.2.3 Supports for methanation reaction

For application on CO_2 methanation, the catalyst is packed in a fixed bed reactor or deposited on an inert support, which can be made of micro-channels to obtain a better control of the heat management than in a compact reactor. Plates with micro-channels were produced with different material and different technologies to evaluate the suitability of using ceramic additive manufacturing of alumina materials to produce the bed for the reactor. Moreover, the use of additive manufacturing enables the structuration of the channels to further improve the conversion of the carbon dioxide.
Testplates were designed with trenches defined in position to allow forming channels when assembled face to face. Stacks of four plates are placed in a stainless steel housing (Figure 2.43) designed to ensure the gas tightness of the system (further description is presented in Section 2.5.1).

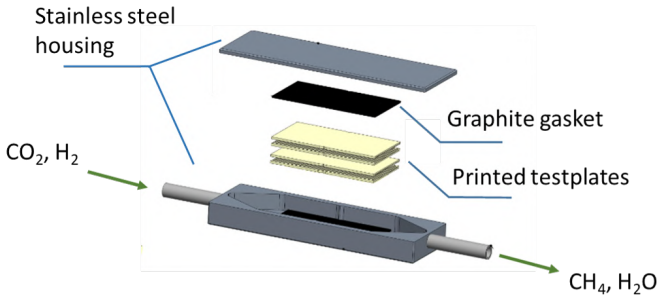

Figure 2.43: *Stainless steel housing for the printed testplates, the welding of the lid can be open after the test to examine the substrates.*

2.2.3.1 Design testplates

A first set of plates was produced with two different materials: alumina and stainless steel 316L, both generally used as support materials [342], [343]. Two different manufacturing techniques where used to produce the stainless steel plates: mechanical milling of commercial tapes, and Selective Laser Sintering. For this test, the design and size of the samples are reported in Figure 2.44.
A second batch of plates was produced in alumina by SLA to investigate the effect of the geometry on the performance. A flat-channel design, as the one used in the material study, was compared with the one with a herringbone engrave. Figure 2.45 shows the two designs with their dimensions, the width of the channels is maintained constant, while an the increase of the area of c.a. 20%, is obtained with an engraved structure (Figure 2.45d). To compare the results, the depth of the flat design used in this study is lower, to keep the same volume between the two sets of samples (Figure 2.45b).

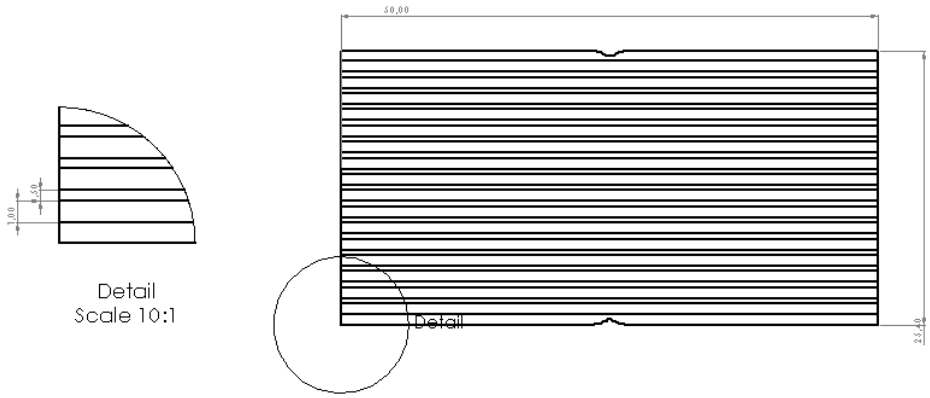

(a) Top view of the design with detail of the channel

(b) Side view of the design

Figure 2.44: *Design, with relative dimensions, of the plates used in the study on the influence of different materials.*

2.2.3.2 Catalyst production

The plates described in the previous section, play the role of support for the catalyst, which needs to be deposited and attach to the substrates. The chosen catalyst for this study is Ni/CeO_2, that presents high conversion efficiency towards the CO_2 reduction to CH_4 [344]. As explained in Section 1.3.1, the ceria is used as support element, to improve the dispersion and the compatibility of the active phase, i.e. the Ni, and the substrate. The precursors, $Ni(NO_3)_2\,H_2O$ (Fisher Scientific, USA) and CeO_2 (SigmaALdrich) were mixed in order to obtain 20% of metallic Ni in the final mixture. The powder were calcined at 450°C for six hours to complete the impregnation process. A binder, polyvinylalcohol (PVA, Mowiol 40-88, Sigma Aldrich, USA) is dissolved in water, in a 5wt% of the final weight, after 3 hours stirring at 65°C, 10wt% of catalyst is added with 1wt% of acetic acid and stirred at room temperature overnight to ensure a good mixture of the components. The final ratio of the components of the suspension is binder:water:catalyst:acetic acid = 5:84:10:1. The catalyst is wash coated in the channel and the excess is removed by mean of a sharp blade. After the deposition, the samples dry for one hour to allow the removal of eventually bubbles and fired at 450°C for six hours to attach the catalyst to the substrate. This procedure is usually repeated twice to obtain the desired amount of catalyst [343].

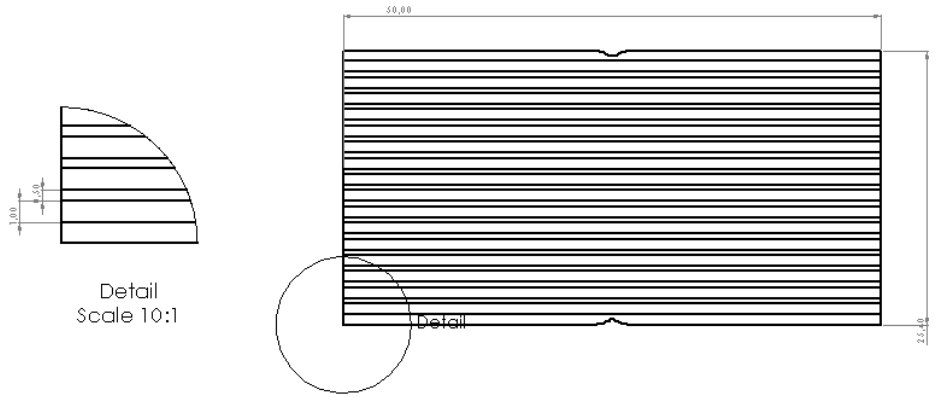

(a) Top view of the flat design with detail of the channel

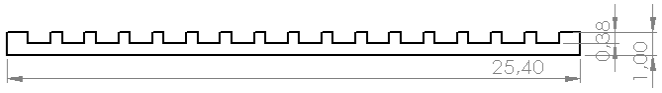

(b) Side view of the flat design

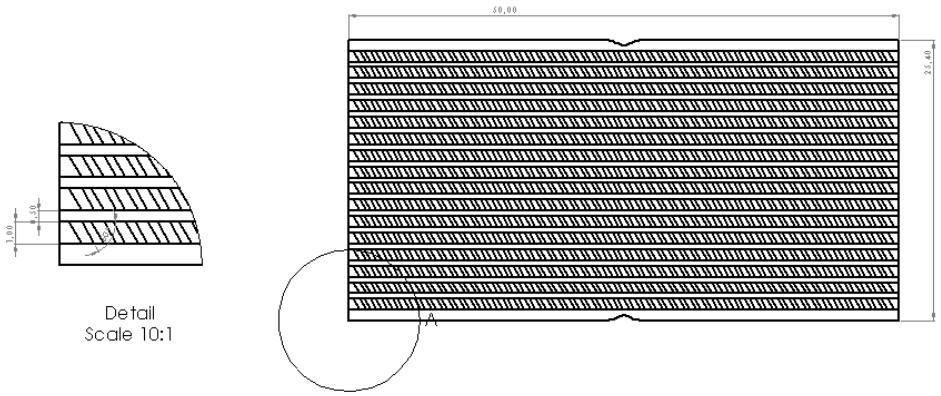

(c) Top view of the herringbone design with detail of the channel

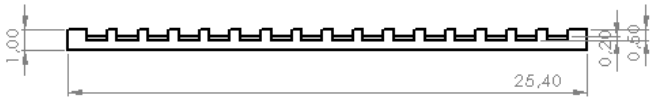

(d) Side view of the herringbone design

Figure 2.45: *Design, with relative dimensions, of the plates used in the study on the influence of different designs.*

2.3 Structural characterization techniques

This section describes the techniques used in this work to characterize the printable slurries and the compounds used to generate them (i.e. both organic reagents and ceramic powders). It also presents the characterization procedures and techniques for the study of the printed pieces and electrochemical devices.

2.3.1 X-ray diffraction (XRD)

X-Rays Diffraction is a wide use, not destructive technique to identifies compounds and the crystallographic phase in which they are crystalized. For their characteristic wavelength (in the order of Ångstrom), comparable with the reticular lattice, x-rays diffraction is suitable to detect the crystallographic planes of the sample. X-rays are produced accelerating ions against a metal electrode, usually copper. These photons have a characteristic wavelength from the target material and high intensity. When the produced x-rays hit the sample, the atom of the specimen scatters the beam (Figure 2.46). If these atoms are in a regular crystal lattice a constructive interference may occur, i.e. the different path ($2dsin\theta$) is equal to an integer time the wavelength, following the Bragg's equation (2.6) [345].

$$n\lambda = 2dsin(\theta) \tag{2.6}$$

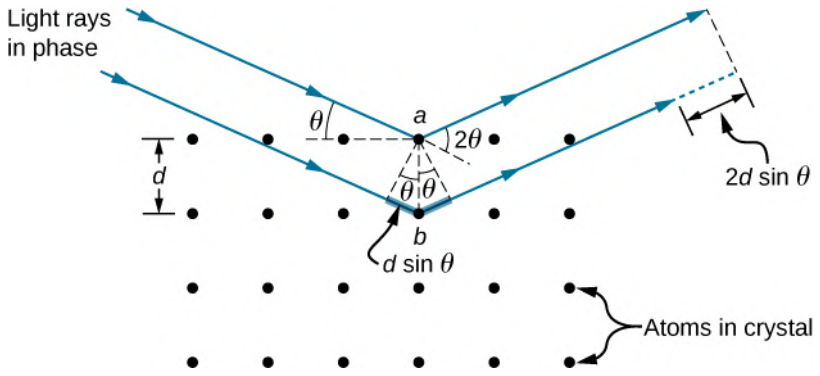

Figure 2.46: *Scheme of the diffraction in a crystal lattice, the incident rays are scattered from an atom, when the different phase is an integer number the interference is constructive and reveals a peak in the pattern.*

In this work, XRD has been used to study the composition of the powder used as starting compounds for the printing feedstock, to identify the printed layers, determine the crystalline phase of the printed pieces and eventual secondary phase of the catalyst generated during operation. The

equipment is a a Bruker-D8 Advance using copper Kα radiation (1.5418 Å) with a nickel filter and Lynxeye 1D detector (Figure 2.47). The analysis was performed in a range of 2θ from 20°to 80°, imposing sample rotation for the printed pieces and no rotation for the powders [346].

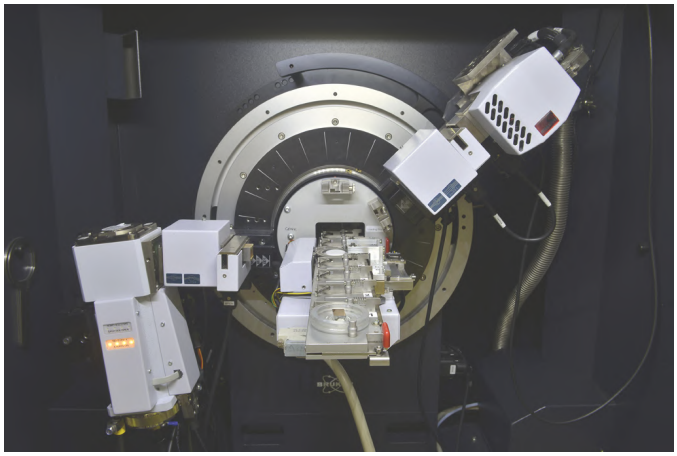

Figure 2.47: *XRD equipment at IREC facility*

2.3.2 UV-Vis Spectroscopy

Since the printing process is based on UV light, UV-Vis spectroscopy has been adopted to evaluate the response of the different compound that constituted the printable slurries, i.e. the photoinitiator, the monomers, the dispersant and the powder to the light beam.
The scheme in Figure 2.48 representss the set-up. During the UV-Vis spectroscopy, a beam is produced by a tungsten-halogen visible lamp and a deuterium ultraviolet lamp to cover the spectrum from 185 nm and 3300 nm. In this work we restricted to the range from 200 nm to 800nm. The beam is directed to a monocromator and a system of mirrors splits it into two different paths. One of the paths goes through the sample and reacts with the specimen. The intensity of the remaining light is measured by a photomultiplier detector (UV/Vis range) and a Peltier controlled PbS (NIR range), and it is correlated with the incident intensity. The reference is obtained from the second beam, that crosses a blank sample consisting on an empty sample holder.
In this study the absorption of light was studied for monomers, diluents, dispersants, photo-initiators and powders, to predict the behaviour under laser exposure and to optimize the development of the paste. Figure 2.49 shows the equipment used, a LAMBDA 950 UV/Vis/NIR Spectrophotometer by Perkin Elmer (USA), equipped with two modules: one for liquid specimen with quartz cuvettes (transparent in the UV region), and a Praying

Mantis Diffuse Reflection Accessory (Harrick Scientific Products Inc., USA) to measure samples in powders form.

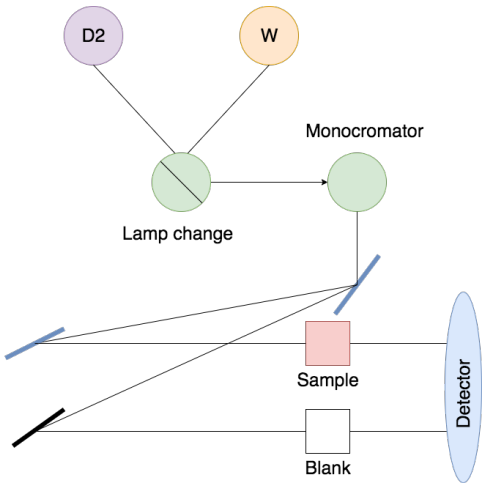

Figure 2.48: *Scheme of the working principles and set-up of the UV-Vis spectroscopy.*

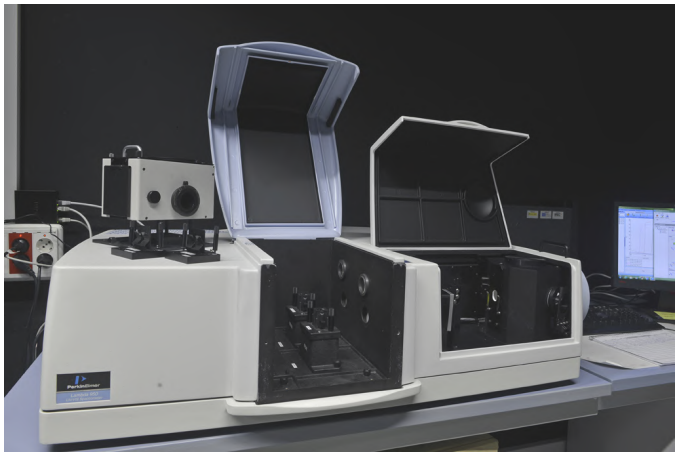

Figure 2.49: *UV-Vis spectroscopy equipment*

2.3.3 Thermal-gravimetric analysis (TGA)

The TGA monitors the change of weight of a sample during a thermal cycle, optionally under particular gas flows. **In this study** we used this technique on pastes to determine the debinding temperature, detecting the loss of the organic compounds. This helped the optimization of the debinding cycles, giving time to the organic compounds to release in the atmosphere. The

equipment used is a TGA4000 by Perkin Elmer (USA), used in the range from 30°C to 800°C, heating ramp of 1 K/min and a dwell in temperature of one hour.
To analyse the sintering behaviour of the different materials to develop a suitable co-sintering cycle, the study is carried out by optical dilatometry (Expert System Solutions, Spain) at FAE S.A.U. (Spain).

2.3.4 Rheological measurements

The rheological behaviour is an important aspect of the development of printable slurries. These need to show a shear thinning behaviour to be printable, as explained in Section 1.4.1.2 and 1.4.2.2. Adding a ceramic load to a resin, the obtained slurry can show a shear thickening behaviour, which has to be avoided, as it is detrimental both for SLA [214], [347] and robocasting application [243].
For this reason, **in this thesis** the evaluation of the rheological properties of the different formulations of printable feedstocks developed has been carried out. The characterization was conducted with a Brookfield DV2T Viscometer by Brookfield Engineering Laboratories Inc. (USA), shown in Figure 2.50. This equipment is made of a fixed external cylinder and a concentric one, which spin at different speed, measuring the torque at different angular velocity and applying geometrical factor of the system the system it is possible to obtain the viscosity [348].

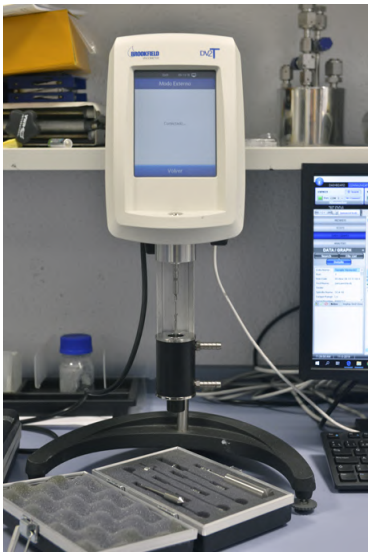

Figure 2.50: *Viscosimeter at IREC facility*

2.3.5 Raman spectroscopy

Raman spectroscopy is a non-destructive technique to analyse, identify and quantify chemical compounds, working with a monocromatic light focused on the sample through the objective lens of an optical microscope. Photons are inelastically scattered by the sample, i.e. they are absorbed and re-emitted at higher or lower frequencies compared with the incident one. This shift, called Raman shift, is characteristic of the vibrational and rotational bond of molecule and permits the identification of the sample composition [349]–[351].
In this work Raman spectroscopy has been used to identify the crystal phase of 8 mol% yttria-stabilized-zirconia, depending on the thermal treatment. It is well known in literature that the XRD peaks of cubic and tetragonal phase of zirconia are close to make its identification difficult [352], while *Hemberger* [353] and *Yashima* [354] suggested the use of Raman spectroscopy to unequivocally identify the phase of zirconia by the shift of the 645 cm^{-1} Raman band with the content of Y_2O_3. The used equipment is Horiba superhead Raman with Horiba syncerity CCD (Horiba, Japan) used with the 532 nm excitation line and 100x objective (Figure 2.51).

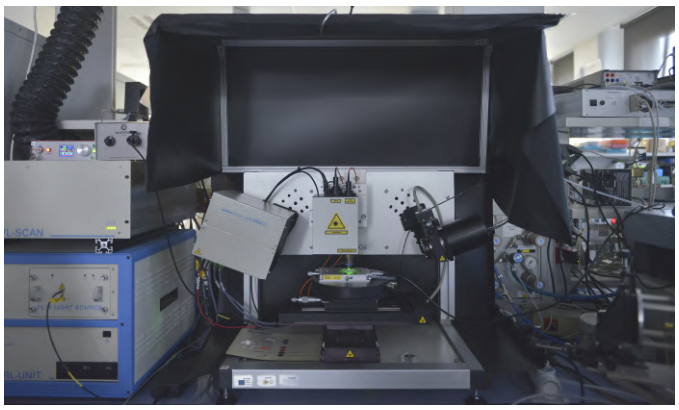

Figure 2.51: *Raman equipment at IREC facility*

2.3.6 Confocal optical profilometry

Confocal optical profilometry is used to measure the surface height of the different regions of a sample by detecting the focused regions at different z point. In this way, 3D images are obtained. **In this work** this technique is used to obtain a closer view of the samples, highlighting microscopic details otherwise not detected, moreover the capability of realizing 3D topography of extended areas has been used to map and represent the surface of the printed pieces and evaluate the reproduction of the CAD design.

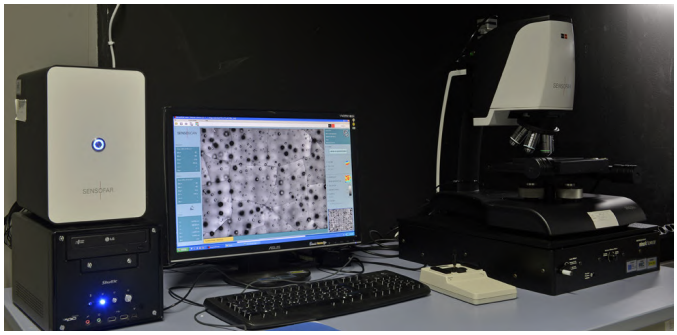

Figure 2.52: *Confocal/optical microscope at IREC facility*

The equipment used, reported in Figure 2.52, is a PLu Neox (Sensofar, Spain), an optical profiler, combining confocal scanning, phase shift interferometry, vertical scanning interferometry, and spectroscopic reflectometry.

2.3.7 Scanning Electron Microscopy (SEM) and Energy- Dispersive X-ray spectroscopy (EDX)

Scanning Electron Microscopy (SEM) is a microscopy technique in which an electron beam is used to scan a sample to recreate the image of its surface (Figure 2.53).
The interaction of the primary electrons (beam) with the specimen generates different types of electrons, which give a series of information of the sample, due to their different penetration and interaction with the matter (Figure 2.54) [355]. Secondary electrons penetrate few nanometres in the specimen and they are sensitive to the tilting of the surface, this makes them particular adapt to reproduce the surface topography of the sample. On the other hand, back-scattered electron, although they are also sensitive to the surface topography, their main characteristic is their capability of giving information about to the atomic number, enabling to distinguish different phase of different materials in the sample [356]. When the electron bean excites the specimen with an energy higher than the ionization energy of the target atom, it scatters inelastically with an atomic electron causing its ejection from the atom, generating a vacancy. When this vacancy is replaced from an electron from an outer shell there is the emission of a characteristic x-ray photon to balance the energy [357]. If the equipment is equipped with the appropriate detector, the emitted photons can be spotted, providing information about the presence of different species. This technique is called Energy-dispersive X-ray spectroscopy (EDX).

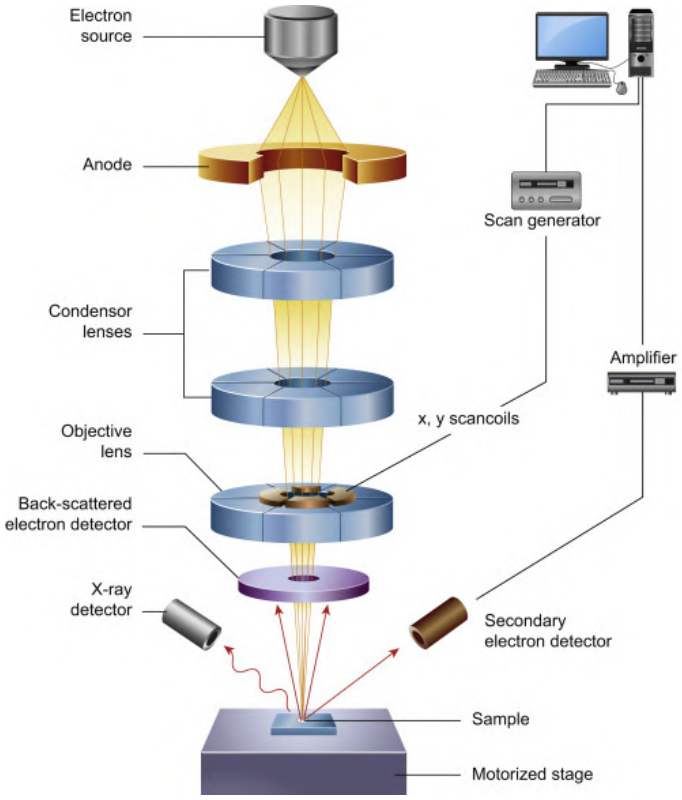

Figure 2.53: *Scheme of Scanning Electron Microscope [358].*

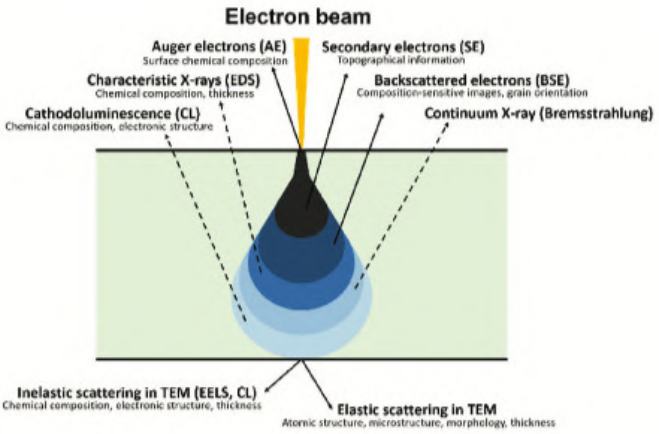

Figure 2.54: *Electron penetration and scattering in the specimen [359].*

In this work, we applied secondary electrons (SE) to analyse the topology of the samples, attachment, thickness of different layers, micro-structure and porosity. While the composition of layers and diffusion of elements after

Figure 2.55: *SEM at IREC facility*

high temperature thermal treatment have been studied by EDX. Most of the SEM investigations of this thesis were performed using a field emission system from Zeiss Auriga (Figure 2.55) The system is equipped with the Oxford Inca Pentafet X3 Energy Dispersive X-ray Analyser.
The SEM analysis, presented in Chapter 5, were performed with a microscope Leo 1550 VP with a Gemini column (Zeiss, Germany) provided with a hot-cathode emission with LaB_6-cristal.

2.3.8 Gas-chromatography

Gas chromatography is a physical separation method in which a mobile phase is separated and resolved by the different retention times through a stationary phase. The sample, consisting on a mixture of compounds in the gas phase, is injected in the column with a inert carrier gas (i.e. here Helium). Each gas has a characteristic retention time in the column, enabling the identification from the chromatogram, the integration of the area of the peaks, allows the quantification of each gas (Figure 2.56) [360].
In this work we used the gas-chromatography to evaluate the CO_2 conversion in the Sabatier reaction. The proper ratio of CO_2 and H_2 was confirmed before the test and the products have been identified at the exit of the reactor. The conversion is evaluated over a range of temperature and each value has been averaged over at least three measurements (see section 2.9). The used equipment is an Agilent 7890A (Agilent, USA, Figure 2.57) multi-dimensional process chromatograph with two thermal conductivity detectors and one flame ionization detector. The method acquisition as well as the quantitative and qualitative analysis was supported by the Agilent OpenLAB CDS ChemStation Workstation software M8301AA.

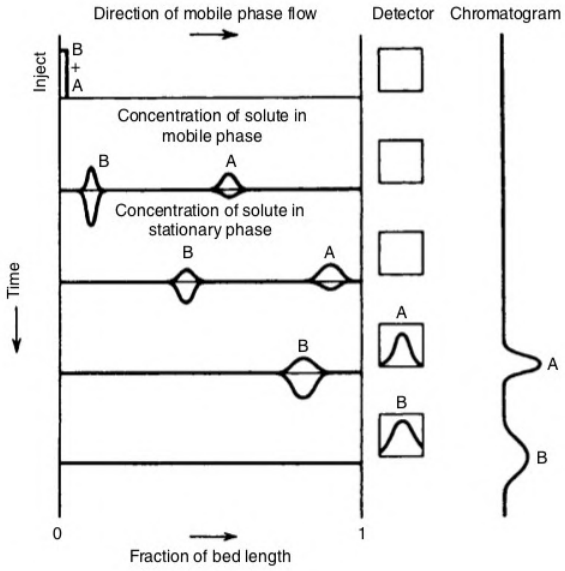

Figure 2.56: *Scheme of the working principle of gas-chromatography [360].*

Figure 2.57: *Agilent 7890A*

2.4 Electrochemical characterization procedures

As mentioned before, fuel cells are devices able to convert chemical energy from a fuel directly into electrical energy [103]. Solid Oxide Fuel Cells require high working temperatures to activate the different involved processes. For this reason, the tests have been carried out using high temperature furnaces, in set-ups able to stand temperature up to 1000°C and capable to sustain tight atmospheres under gas flows (H_2, air, CO_2 and H_2O).The choice of inert materials is critical not only for the components of the cell itself but for all the electrical contacts and gas connections. This section describes the necessary set-ups and the characterization techniques used to evaluate the performance of the cells.

2.4.1 Test station

During the test the cells need to stay at high temperature under continuous flow of gases, to withstand this hard condition, Norecs (Norway) developed a sample holder, called Probostat, widely used for electrochemical testing [267], [285], [332], [361]. The Probostat presents a metal base with BNC connections for multimeter and impedance spectrometer, four 1/8" gas connection (two inlet and two outlet) in order to obtain two chamber with different atmosphere and thermocouple connections to control the temperature near the cell (Figure 2.58). The base is kept outside the furnace and heated at maximum at 120°C.

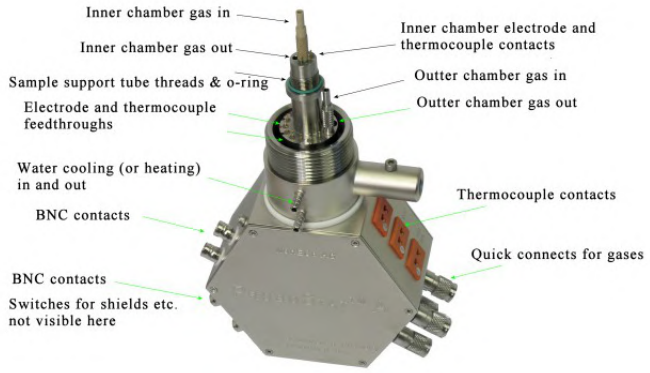

Figure 2.58: *Probostat base, highlighting the different connections.*

Three concentric tubes are connected to the base, the first one supply the inlet gas to the internal chamber and contains a gold mesh to contact the bottom electrode, connected with wires to the base. The second tube separates the two chambers. The cell is sealed to this tube, typically with Ceram-

abond 552 (Aremco, USA). The upper electrode is connected as well with gold mesh and wires to the base and an alumina holder is placed on top and connected to the base with springs to keep the cell in place. A quartz tube sends the inlet gas of the external chamber directly to the outer electrode. A type S thermocouple is placed next to the cell and connected to the base. The third tube closes the external chamber. For a better understanding of the connection, a scheme of the cell assembly is presented in Figure 2.59.

The upper part of the tube (zoom of Figure 2.59), containing the sample, is

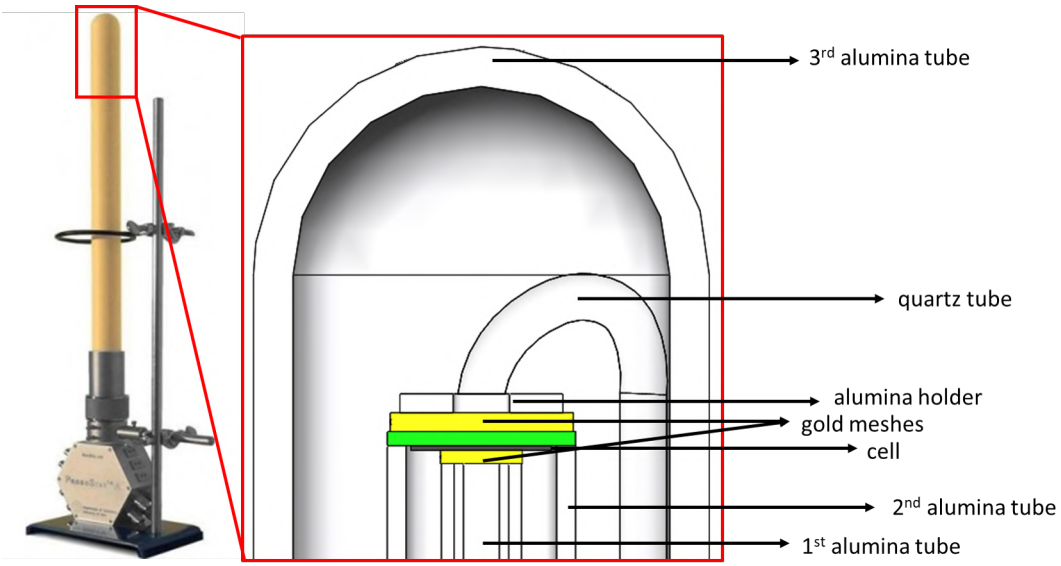

Figure 2.59: *Probostat set-up, zoom of the placing of the cell.*

placed in a vertical furnace, a system of mass flows connected in parallel supplies the gases (air, H_2, CO_2) and high amount of water vapour (EL-FLOW and CEM, Bronkhorst, Netherlands). The flows in the different modes are reported in Table 2.9, normalized by the area of the sample.

	H_2O [mg h^{-1} cm^{-2}]	**CO_2** [ml min^{-1} cm^{-2}]	**H_2** [ml min^{-1} cm^{-2}]	**Air** [ml min^{-1} cm^{-2}]
SOFC	-	-	22.22	55
SOEC	963	-	2.22	45
co-SOEC	696	5.52	2.22	45

Table 2.9: *Gases distribution in different modes*

Electrodes painted with gold are connected throughout the meshes and the wires to different apparatus depending on the target phenomena. In case of symmetrical cells, the Electrchemical Impedance is measured using a

galvanostat frequency response analyser (Alpha-A, Novacontrol, Germany), while for entire cell the values are measured with a Parstat 2273 (PAR, USA). The same equipment has been used to record polarization curve in SOFC mode, while in electrolysis and co-electrolysis mode a multi-meter Keithley 2400 (Keithley, USA) and a power supply (LABPS3005D, Velleman, Belgium) were used. An overview of the entire set-up is presented in Figure 2.60.

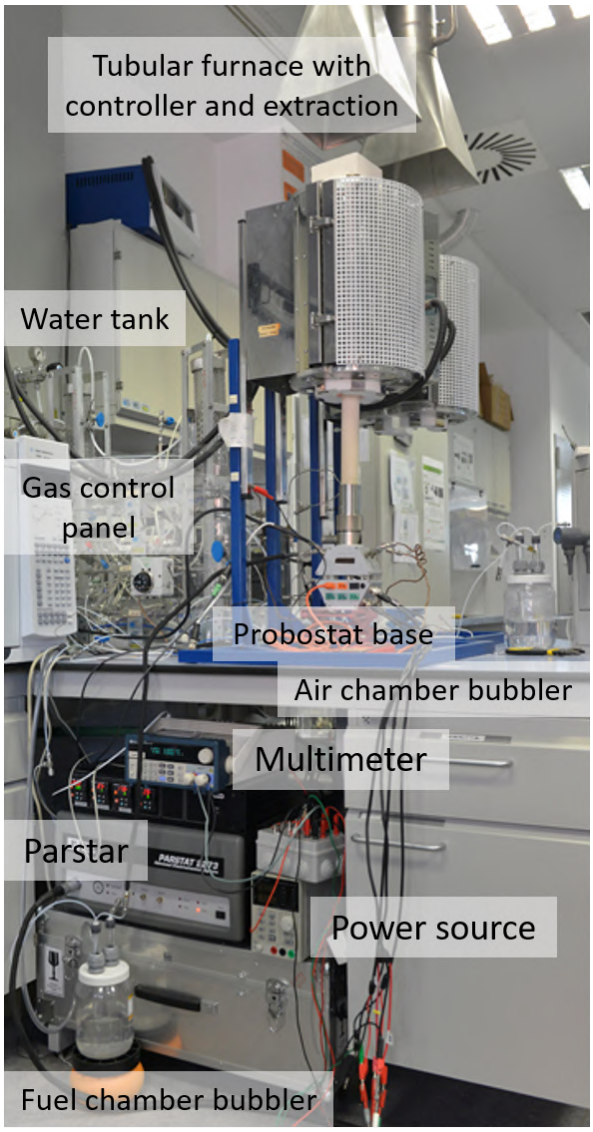

Figure 2.60: *Electrochemical test station.*

2.4.2 Electrochemical Impedance Spectroscopy (EIS)

Knowing the electrical properties and contributions to the overall resistance from each layer composing a SOC cell is crucial for the determination of bottlenecks in performance and the optimization of the materials and components [362].
Applying a potential difference, the different layers respond in a unique way to the change in the applying voltage. The rate of this change is depending to the type of interface: slow for chemical reactions in contact with the atmosphere and faster for conduction inside a polycrystalline electrolyte. Electrochemical Impedance Spectroscopy (EIS) is the study based on the response of a system to a perturbation with an AC signal. Some working assumptions have to be fulfilled during the test to keep the validity of the measurement [363], [364]:

- Linearity: the system should be linear along the potential applied in all the frequency range, small perturbation has to be pursued.
- Causality: the change in the output should be caused only from the signal applied.
- Stability: the system should not evolve during the test.

The obtained values of impedance can be represented in different ways:

- Argand diagram or complex plane, which shows the relationships between complex impedance, magnitude and phase angle.
- Nyquist plot, the most used representation of the EIS for SOCs, it plots the imaginary part of the impedance versus the real part, showing a general arc behaviour.
- Bode plots highlight the dependence of the functionality with the frequency, the representation can present in the y axis: the real or imaginary part of the impedance or the phase angle.

The parameters used in this study (summarized in Table 2.10) have been chosen to obtain the maximum ratio between signal and noise depending on the performance of the cells.

Type of cell	Frequency range	Amplitude	Voltage
Symmetrical cell	20 MHz - 100 mHz	50 mV	–
SOFC	500 kHz - 100 mHz	20 mV	OCV
	500 kHz - 100 mHz	20 mV	0.7 V
SOEC	500 kHz - 100 mHz	20 mV	OCV
	500 kHz - 100 mHz	20 mV	1.3 V
co-SOEC	500 kHz - 100 mHz	20 mV	OCV
	500 kHz - 100 mHz	20 mV	1.3 V

Table 2.10: *EIS parameters applied for this study*

The EIS of symmetrical cells (same electrodes on both sides Figure 2.33b, 2.33c and 2.33d) is recorded without applying any voltage or current bias. From the Nyquist plot it is possible to highlight the contributions of the different players of the cell, i.e. (i) the serial resistance (R_e in the Figure 2.61), which value is due of the ohmic processes in the cell, the electrical connection, the wires and the electrolyte itself, and (ii) the polarization resistance, often formed by two arcs, including the polarization losses, ascribed to the electrodes (R_1 and R_2 in Figure 2.61). For the entire cell (electrolyte with air

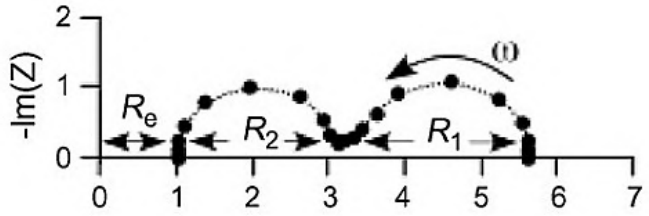

Figure 2.61: *Example of Nyquist plot with the contribution highlighted [365].*

and fuel electrode, Figure 2.33a) the EIS is recorded at OCV (Open Circuit Voltage), to determine the pristine condition of the cell and at operating condition, i.e. the when the cell shows an ohmic behaviour, distinguish by a linear part in the polarization curve (see next section), fixed at 0.7 V for SOFC mode and 1.3 V for electrolysis and co-electrolysis.

2.4.3 Polarization curves (V-j curves)

Polarization curves give information about the output power in SOFC mode and the injected current in SOEC mode, giving immediate information about the performance of the cell and the overall internal resistance. When working as fuel cell, the voltage is measured at different current values originating the characteristic shape presented in Figure 2.62.

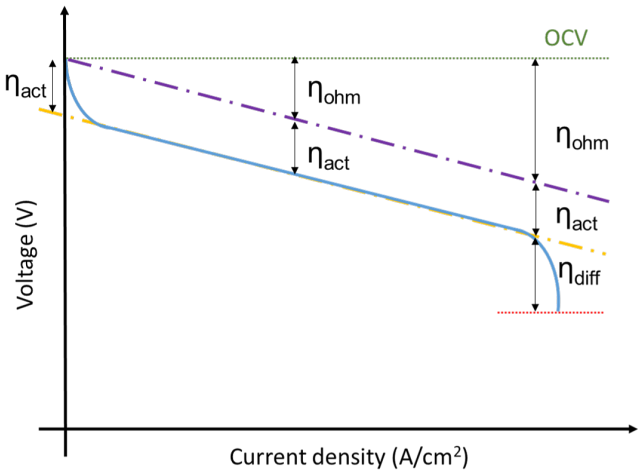

Figure 2.62: *Polarization curve for SOFC*

The curve starts from the Open Circuit Voltage (OCV), point in which no current load is applied. This value depends only on the two different atmospheres at each side of the cell. It can be compared with the theoretical one, calculated by the Nernst equation (Equation 2.7). Any discrepancy from the expected value indicates a problem with the tightness of the system, like the sealing of the cell, or in general a crack, a pinhole or some porosity in the electrolyte.

$$E = E_0 + \frac{RT}{2F} ln \frac{p_{H_2} p_{O_2}^{1/2}}{p_{H_2O}} \tag{2.7}$$

Increasing the current, an initial drop correlated with the activation of the electrodes appears, followed by the linear or ohmic behaviour, in which the resistance of the cell is given by the slope of the curve (this is the linear area in which the EIS at operative condition is recorded), at lower voltage values diffusion phenomena start to appear. It is not recommended to inject current after reaching too low voltages, since the cell is degradating more and following tests may be compromised. In this work, the recording of the polarization curves stops at 0.6 V and it is extrapolated by mathematical model to 0.4 V, to highlight the maximum power density. When the cell works in electrolysis or co-electrolysis mode, the applied current change sign. Since the cell is working in "reverse" mode compared to the previous situation, hydrogen is produced by the cell. The direction of the polarization curve changes and the OCV value changes as well, since products and reagents change (Equation 2.8).

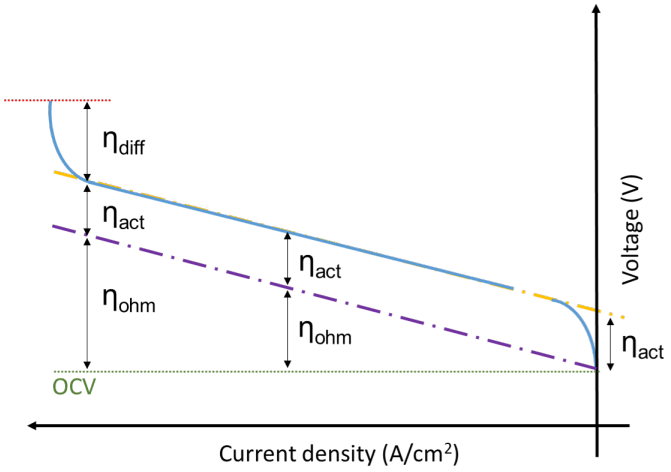

Figure 2.63: *Polarization curve for SOEC and co-SOEC*

$$E = E_0 + \frac{RT}{2F} ln \frac{p_{H_2O}}{p_{H_2} p_{O_2}^{1/2}} \tag{2.8}$$

The same parts of the curve can be recognized: the activation of the electrodes, the linear behaviour, where EIS is recorded and diffusion step. Independently on the working mode of the cell, the polarization curves are always normalized by the area, presenting not the current but the current density, in order to compare samples of different dimensions.

2.4.4 Degradation study

In the same test station, (i.e. same gases flows, contacts and instruments), degradation studies have been carried out. After an initial electrochemical characterization of the cell to determine the original performance, a current corresponding to the one initially providing 0.7 V is applied and the voltage is recorded periodically. An ideal zero degradation cell present a flat line at 0.7 V, while, in reality, it is well known that an initial drop is present in the first hundreds of hours, corresponding to stabilization of the cell, and a subsequent more stable operation follows [366]. Since degradation studies run for hundreds of hours, a common phenomena is the presence of spikes and noise over the recorded measurement, this usually correspond to heat management issues, supply of the gases or water condensation.

2.5 CO_2 conversion

This section is dedicated to the description of the procedures for measuring Sabatier reactions. The work on this field was performed at the Fraunhofer Institute for Microengineering and Microsystems (IMM, Mainz, Germany). The performance of a catalytic process is evaluated based on the conversion of the reagents into the products and the selectivity toward the desired specimen [128], [180], [367]. In case of the Sabatier reaction, the reactor is fed with CO_2 and H_2 and the obtained output is methane and water, according to the reaction:

$$CO_2 + 4\,H_2 \rightleftharpoons CH_4 + 2\,H_2O\,(g) \tag{2.9}$$

being the methane the valuable product and the water the secondary one. Apart of them, it is possible to obtain CO, ethane and other carbon based compounds as byproducts. A good catalyst is sensitive to methane and not to CO, which is the most probable byproduct. The reaction take place at high temperature (above 200°C) and it is favoured by the pressure (Figure 2.64).

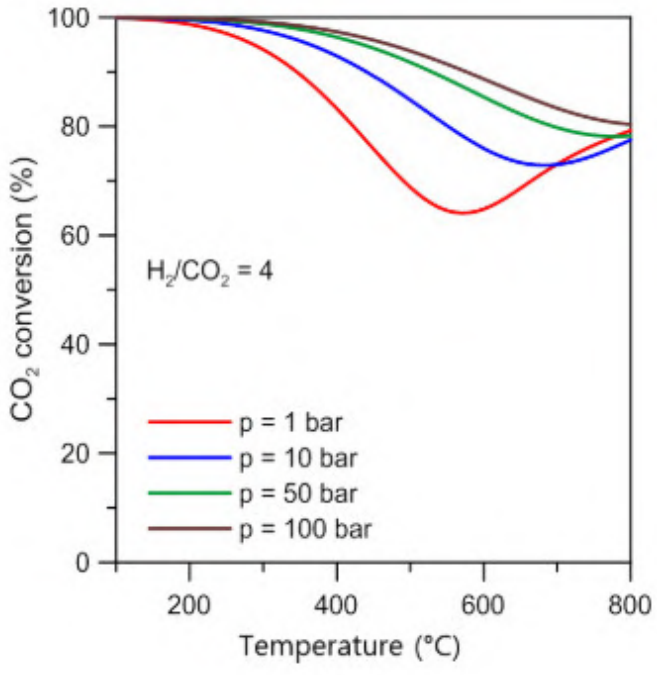

Figure 2.64: *CO_2 conversion depending on temperature and pressure, calculated by simulation with Gibbs free energy minimization method [343].*

2.5.1 Set-up

In this study the effect of the substrate on the conversion of CO_2 is analysed, the catalyst composition is kept constant over the tests. The different substrate are produced as plates, as described in Section 2.2.3, and assembled face to face in order to form channels. The stacks are placed in a stainless steel holder, tightly closed by welding and assembled in the test-rig. Figure 2.65 reports a picture of the open housing with testplates placed inside. The

Figure 2.65: *Testplates placed in the steel housing*

welded housing, called as well reactor, is placed in the test rig described in Figure 2.66.

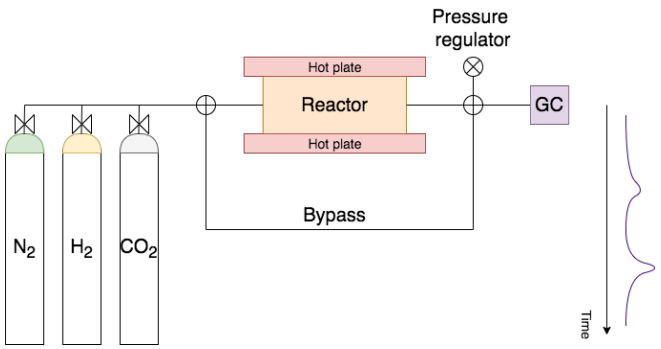

Figure 2.66: *Set-up for the analysis of the CO_2 conversion*

The reactor is placed between two hot plates to control the temperature and connected to the gas lines, to provide the necessary reactants, and to the gas-chromatography to analyse the conversion. All the lines and connections are heated above 200°C to avoid water condensation.
The system is designed to allow two separate measurements: i) the reaction one, in which the gases pass through the reactor, and ii) the bypass, in which

no reaction occurs. This configuration is used to measure the gas composition before running the tests. As first step, the sealing and gas-tightness of the system is checked. For that purpose, the system is pressurized at 10 bar of nitrogen, and the pressure drop is monitored at least for four hours, considering the test passed if the drop is lower of 0.5 bar. Proved the safety of the set-up, pure hydrogen at 1 bar flows in the sample heated up at 400°C for one hour to reduce completely the catalyst. So the system is exposed to a mixture of hydrogen and CO_2 in ratio 4:1 and small amount of nitrogen at 6 bar, and heated up to 280 °C. The real ratio of gases is measured by gas-chromatography on an average of four samples, this step is repeated before each change in composition through an independent line from the reaction site (bypass mode). Defined the exact ratio between the different gas input, the reaction starts and the composition at the exit of the reactor is measured by gas-chromatography, evaluating the conversion in the range of temperature between 280°C and 340 °C at a space velocity of 45 l/h g_{cat}. The gas supply was calculated on the WHSV (weight hourly space velocity), the flow is normalized on the weight of catalyst present in the reactor, in order to compare devices presenting different amount of catalyst.

Chapter 3

Optimization of the 3D printing process for ceramics

3D printing of functional materials, particularly ceramics, is still in its infancy and there is only a limited number of works devoted to this topic, especially in comparison to plastics and metals. The printer employed in this work is one of the few commercially available machines for ceramic printing. The original machine is a SLA industrial printer that has been hybridized with a robocasting multi-nozzle arm within the frame of the European "Cell3Ditor" project (coordinated by IREC) to enable the manufacturing of enhanced SOC parts and, eventually, SOCs stack in a single production step. With these ambitious goals in mind, the possibilities of the commercial printer have been explored and optimized for this particular application as well as new concepts has been implemented to accomplish the printing of five different materials at a time. In this frame, we developed and optimized printable feedstocks which were not available in the market, we optimized the whole set of printing parameters (especially to combine SLA and robocasting techniques) and we faced the problem of the co-sintering of materials with different TECs and different densification requirement.
The chapter is divided into different parts following the necessary steps of the printing process: i) Section 3.1 is devoted to the development of printable feedstock; ii) Section 3.2 focuses on the optimization of the printing parameters to improve the quality of the printing; iii) Section 3.3 is devoted to the thermal treatments for the debinding and sintering of the pieces; iv) Section 3.4 deals with the characterization of the obtained pieces, regarding the composition and microstructure of the printed parts and the electrochemical properties (if applicable).

As previously mentioned, we decided to divide this chapter according to the printing steps. However, another alternative way could be accord-

ing to the type of printing, namely, mono-material (SLA) or multi-material (SLA+robocasting). While the first one is based on commercial slurries (some of them developed by the company 3DCERAM for the Cell3Ditor project) and methods (our focus was in the designs and characterization), the hybrid one required a deeper development of printable materials, printing technologies and (co-)sintering. Following this division the results of mono-material studies are mainly reported in Section 3.3.1, 3.4.1 and 3.4.2, while the rest are on hybrid printing (development of printable feedstocks in Section 3.1, optimization of the printing parameters in Section 3.2 and the challenge of the co-sintering step in Section 3.3.2).

3.1 Development of printable materials for robocasting

Due to the high sintering temperature, which prevents the direct sintering or melting of most of the ceramics with laser, in the SLA 3D printing process the printable material is not just ceramic powder but a slurry made of this powder and an organic vehicle. The organic components react with light, polymerizing and trapping the ceramic powder inside a hardened structure. During the following thermal treatment, the organics are removed by slow evaporation under gas flow, step called debinding, and the remaining particles are sintered in the final shape by high temperature steps.
In this section, we present the development of robocasting slurries of NiO-YSZ, LSM-YSZ and LCTM (the stereolithography feedstock was developed by 3DCERAM). The study covers the characterization of commercial ceramic powders and the organic compounds, the optimization of their ratio to obtain the best printable slurries. In the last part, the slurry itself is analyzed, being the curing and printing attempts the last validation step.

3.1.1 Characterization of ceramic powders

Ceramic powders are a key aspect in the 3D printing process, as explained in Section 1.4.1.2. Solid powders are the only components of the slurry that remain in the final piece at the end of the fabrication process, giving the part its ultimate properties. Unlike polymeric printers, in which the light interact only with the organic compounds, in the ceramic ones a big role is played by the absorbance and scattering of radiation by the solid particles. For this reason, the characterization of the powder is the first step to develop a suitable printable slurry.

3.1.1.1 Compositional and structural analysis

Although most of the powders used were commercial, we performed XRD characterization of them to confirm the composition and to further compare with the printed pieces.
As mentioned previously in this thesis, the combination of nickel oxide with 8mol% yttria stabilized zirconia has been used for the fuel electrode, due to the good electrochemical properties and the compatibility with the electrolyte material. Figure 3.1 presents the spectra of the powder for the fuel electrode. The quantification analysis obtained by the software *X'Pert HighScore Plus* reveals a ratio between NiO and YSZ of 63:37, in good accordance with the desired mixture 60:40, percentage required to ensure a proper con-

ductivity of the cermet obtained after reduction [368].

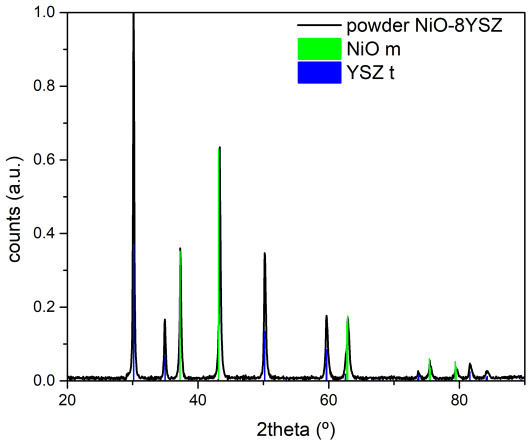

Figure 3.1: *XRD pattern of the NiO-YSZ commercial powder employed for the fuel electrode. NiO reference pattern num.: ICDD-03-065-6920, YSZ reference pattern num.: ICDD-01-070-4431.*

Figure 3.2 presents the pattern of the powder of Lanthanum Strontium Manganese Oxide (LSM) and 8YSZ. Pure phases in a ratio of LSM:YSZ=57:43 (close to the desired 50:50) were confirmed. According to literature, value of LSM higher than 30vol% in the composite LSM-YSZ show electrical conductivity close to the pure LSM [369], [370] while the resistance increases when the YSZ content overcome the 50% [371].

Keeping in mind the goal of producing an entire stack in a single printing and sintering steps, a ceramic interconnect is necessary to enable the co-sintering of all the cell components. *Hosseini et al.* proposed a manganese-doped lanthanum calcium titanate (LCTM) interconnect for flat-tubular SOFCs. The material corresponds to a perovskite structure in which different amounts of manganese substitute the titanium in the lattice ($La_{0.4}Ca_{0.6}Ti_{1-x}Mn_xO_{3-\delta}$, with x=0.0, 0.2, 0.4, 0.6) [320]. According to the conductivity measurements reported, a custom mixture of $La_{0.4}Ca_{0.6}Ti_{0.4}Mn_{0.6}O_{3-\delta}$ with an average particle size of d_{50} between 0.5 µm and 5 µm and a BET around $6\,m^2/g$ has been ordered to Kceracell, Korea. Figure 3.3 reports the comparison between the received powder and the one synthesized by *Hosseini et al.*, confirming the proper crystallography structure of the commercial material.

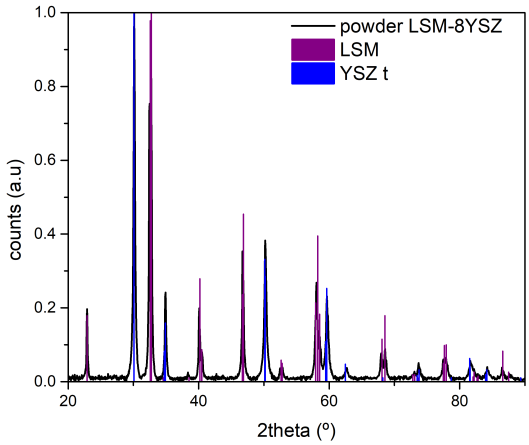

Figure 3.2: *XRD pattern of the LSM-YSZ commercial powders for the oxygen electrode. LSM reference pattern num.: ICDD-01-089-0649, YSZ reference pattern num.: ICDD-01-070-4431.*

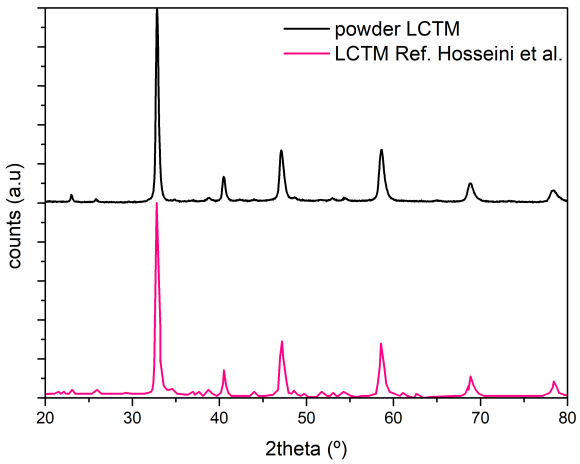

Figure 3.3: *XRD pattern of $La_{0.4}Ca_{0.6}Ti_{0.4}Mn_{0.6}O_{3-\delta}$ commercial powder for the interconnect compared with a pattern reported in the literature [320].*

3.1.1.2 UV-Vis light absorbance of the ceramic powder

The amount of UV-radiation absorbed by the powder is a critical aspect for the polymerization step, because, if the light is absorbed by the powder, less photons would be available to break the bond of the photo-initiator and form

the radicals.
In this regard, the starting materials for the fuel electrode have been optically characterized (Figure 3.4). At the wavelength of the UV-laser of the printer, the nickel oxide presents a high absorbance (96%), compared with the 8YSZ, while its mixture with YSZ shows a lower value (92%). The value of the mixture is in the limit for a proper UV-curing, according to previous experience from 3DCERAM.

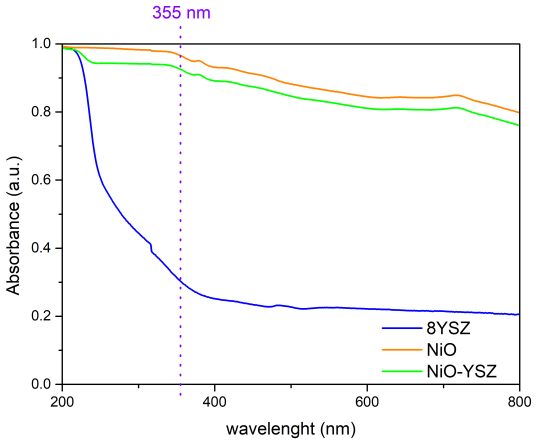

Figure 3.4: *UV-Vis absorbance spectra of for the fuel electrode ceramic materials, the operation wavelength of the laser used in this work is represented by a dotted line.*

For the air electrode, LSM and the composite LSM-YSZ were optically characterized as presented in Figure 3.5. LSM shows an absorbance of 98% at the UV-laser wavelength. The addition of YSZ decreases the absorbance to a value of 96%, which is very high. Indeed this level of absorbance generates issues in the photo-polymerization process since the photons are absorbed by the ceramic powder and cannot react with the photo-initiator [226].

Finally, Figure 3.6 presents the absorbance of the interconnect material, LCTM, which is similar to the LSM, in comparison with the other components of the cell. From this graph, it is possible to advance polymerization issues in the behaviour of the slurries based on these electrode and interconnect materials (as it will be reported in Section 3.1.3 and 3.2.3).

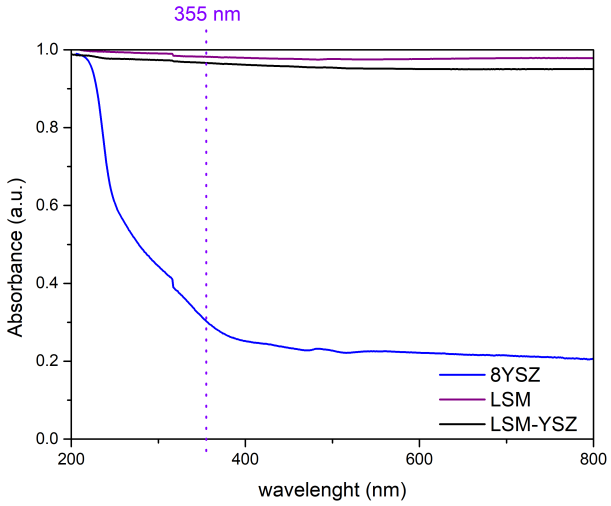

Figure 3.5: *UV-Vis absorbance spectra of for the air electrode ceramic materials, the operation wavelength of the laser used in this work is represented by a dotted line.*

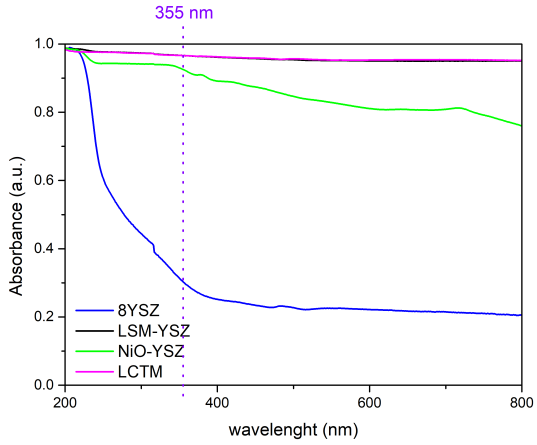

Figure 3.6: *UV-Vis absorbance spectra of for the ceramic materials used in this work, the operation wavelength of the laser used in this work is represented by a dotted line.*

3.1.2 Characterization of organic compounds for the robocasting slurries

The organic compounds form the structure of the printed piece after polymerization, giving the desired shape. The photo-initiator reacts with the UV

light to form radicals. When it is mixed with a proper monomer, the radicals attach to the active site of the monomer and a chain starts to grow. The increasing in the molecular weight of the chains turns the compound into a solid (Section 1.4.1.2). They eventually include components to improve the printability, such as a diluent and a dispersant.
We developed our mixtures starting from reagents, TMPTA, the monomer, and DMPA, the photo-initiator. A deeper description of these components, including their chemical formula, is reported in Section 2.2.2.2. The reactants and their mixture at different ratio have been characterized regarding both their interaction with light and their rheological properties.

3.1.2.1 Absorbance of the organic vehicles under light irradiation

Most of the polymers employed in the slurries are light sensitive. In the case of the photo-initiator, this is a desired property since it absorbs photons to form active radicals that initiate the photopolymerization. For the monomers, this is a detrimental effect that can inhibit the reaction sites, or degrade the polymeric piece. For this reason, knowing the light interaction of the organics, especially at the wavelength of the laser (355 nm, marked in the figures), is an important step previous to the slurry formulation.
Figure 3.7 reports the absorbance of the different liquid reagents employed in this work, two different acrylates monomers, TMPTA and HDDA, compared with a commercial ready mixture, Spot-LV. TMPTA, which is a trifunctional acrylate, was used as the main monomer while HDDA, which is a bifunctional acrylate, was employed as reactive diluent. Its active sites are the same as for the TMPTA [184], but it presents a lower viscosity, reason why it is employed as diluent. Neither of them absorbed light at the laser wavelength, indicating that the reaction with light happens only through the photo-initiator. A commercial resin, Spot-LV, is reported to indicate the abosorbance of a working mixture of the monomer, aliphatic acrylates in this case, and photo-initiator, phosphine oxide, showing high absorbance due to the presence of the photo-initiator. We chose DMPA as photo-initiator, according to the literature [214], [215], [338] and the high absorbance values in the UV region (Figure 3.8), which prove the suitability of this compound as a photo-initiator for the desired application.
Different amounts of DMPA were added to the TMPTA monomer, in order to find an optimal ratio (in terms of light absorbance). This is determined by UV-Vis spectroscopy, reported in Figure 3.9, and the "cure depth" of the different mixture under laser illumination (Figure 3.10). In additive manufacturing process driven by light polymerization, the cure depth is a critical parameter, giving information about the effectiveness of the reaction. On this parameter is established the thickness of the layer of each printing step

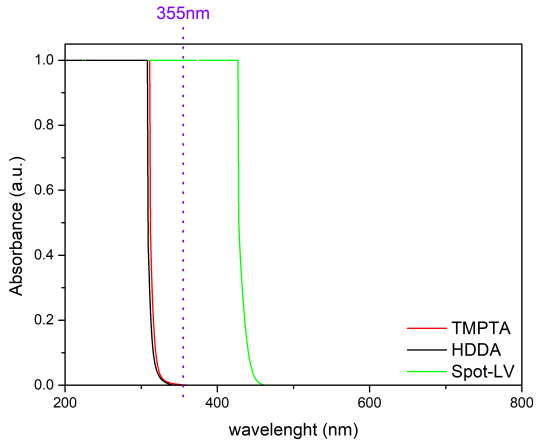

Figure 3.7: *UV-Vis absorbance spectra of for the liquid organic compounds used in this work, the operation wavelength of the laser used in this work is represented by a dotted line.*

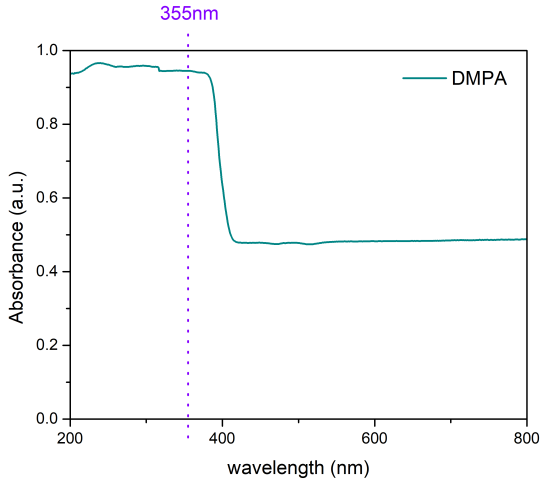

Figure 3.8: *UV-Vis absorbance spectra of for the DMPA photo-initiator, the operation wavelength of the laser used in this work is represented by a dotted line.*

in order to guarantee a good adhesion between the layers and consequently good properties of the final piece.

UV-Vis analysis shows complete absorption of light with sample with photo-initiator in the range between 0.5wt.% to 5wt.% (Figure 3.9). The trend of the curing depth shows a maximum at 0.5wt.% of DMPA to decrease to poor conversion for values higher than 2wt.% (Figure 3.10). This behaviour

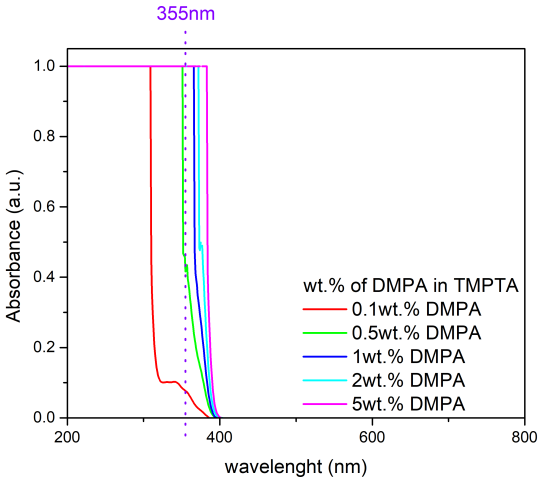

Figure 3.9: *UV-Vis absorbance spectra of TMPTA with different amount of DMPA, the operation wavelength of the laser used in this work is represented by a dotted line.*

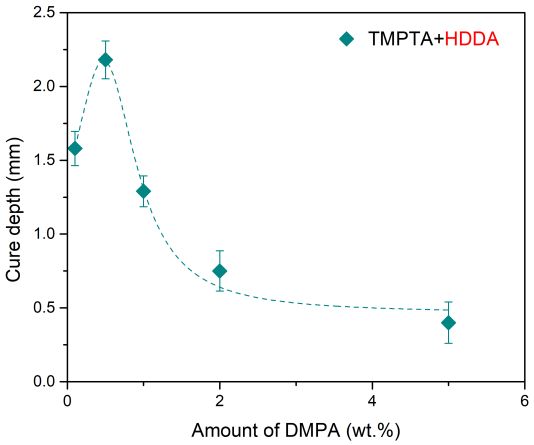

Figure 3.10: *Polymerization thickness as function of the photo-initiator concentration. Dashed line as a guide for the reader.*

is also reported in literature as the"inner filter effect" namely, the blocking on the penetration of the light in a high-absorbing media [372].

Overall, the light absorbances for different scenarios are reported here and are considered guidelines in the formulation of the final printable feedstocks. The ultimate amounts of each compound were then adjusted by taking into consideration more practical issues like the values of the polymerization tests

when adding the specific ceramic particles in the slurries (numerical values are reported in Section 3.1.3) or their rheology and printability (same section).

3.1.2.2 Rheological behaviour

In literature, it is well reported that at the time of developing a ceramic slurry, the mixture of organic compounds should show Newtonian behaviour, i.e. the viscosity is constant independently on the speed of the applied force [214], [238], [327]. This is necessary to obtain a shear-thinning behaviour after the adding of the ceramic load. A shear-thinning fluid shows a decrease in the viscosity at the increase of the shear rate, i.e. the speed at which the force is applied. Both stereolithography and robocasting systems require this type of behaviour since the slurry flows under strain, whatever it comes from a doctor blade system or the extrusion through a needle, but to keep the shape when no force is applied. The analysis here reported are dedicated to the development of robocasting formulation (since the SLA slurries employed in this work are developed by 3DCERAM, as previously mentioned).
Figure 3.11 reports the viscosity and shear stress as a function of the shear rate of the reagents reported in the previous section. All the components show Newtonian behaviour, i.e. constant viscosity and linear dependency between shear stress and shear rate. Among the reagents, the TMPTA shows the higher viscosity (η= 136 mPa·s), due to its branched structure, and the HDDA which has a linear structure shows the lowest value (η= 7 mPa·s). The commercial mixture, Spot-LV, used as reference, presents an intermediate value of (η= 44 mPa·s). The exact structure of this product is not disclosed by the manufacturing company. For robocasting applications, a viscosity of some Pa·s is optimum for keeping the slurry flowing through the needle [232], [373]. *Wozniak et al.* [326] reported that the viscosity of the organic mixture (before solid loading) should be maintained low (between 10 mPa·s and 25 mPa·s) since the viscosity increases with the addition of the ceramic load.
HDDA has been used to lower the viscosity of the TMPTA-based vehicles [338]. Organic TMPTA vehicles with different amounts of HDDA (from 1 to 10 wt%) have been formulated and rheologically characterized. Figure 3.12 presents the dependency of viscosity (Figure 3.12a) and shear stress (Figure 3.12b) as a function of shear rate. The value of shear stress of pure HDDA (0.173 Pa at 25 s^{-1}) is compared with literature (0.177 Pa reported by *Badev et al.* [338]), showing good agreement. Regarding the new formulations, the whole set of mixtures show Newtonian behaviour, constant viscosity over shear rate and linear increase of shear stress as function of the shear rate. Moreover, the viscosity decreases when increasing the amount of HDDA,

which makes it tunable in the range of interest.

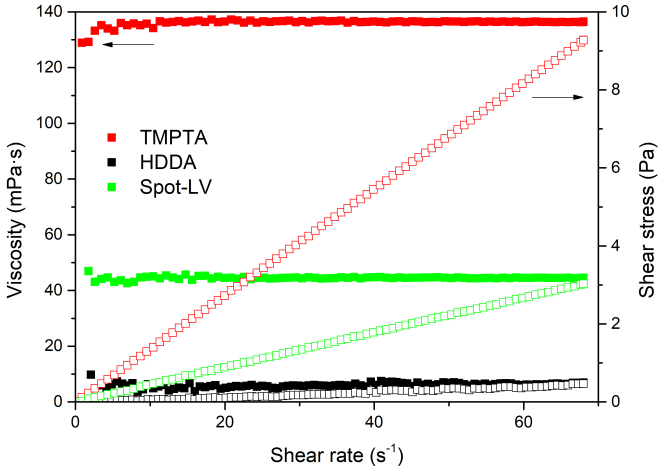

Figure 3.11: *Viscosity (closed symbols) and shear stress (open symbols) as a function of the shear rate for the different organics employed in the robocasting slurries.*

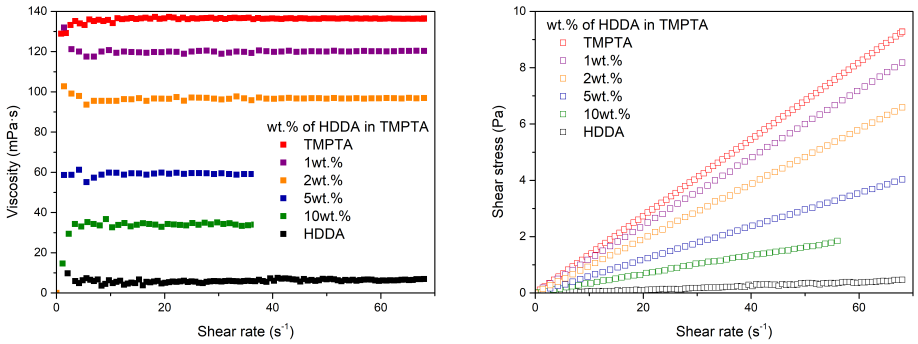

(a) Viscosity of the different mixtures (b) Shear stress of the different mixtures

Figure 3.12: *Flow curve of TMPTA and HDDA mixtures.*

3.1.3 Printable feedstock

In the previous sections, the ceramic and organic compounds have been analyzed and validated separately, but the feeding material to the printer is a

proper combination of both. When adding the ceramic loading, Monofax is added as dispersant (see Section 2.2.2.2), to avoid the agglomeration of the particles withouth affecting the cure depth.
In additive manufacturing process driven by light polymerization, the cure depth is a critical parameter, giving information about the effectiveness of the reaction. On this parameter is established the thickness of the layer of each printing step in order to guarantee a good adhesion between the layers and consequently good properties of the final piece.
The interaction of light with turbid suspensions have been studied widely, since the development of photo-curable slurries suitable for 3D printing [184], [213], [214], [324], [374]. An empirical correlation between cure depth and the energy of the light source, the dimensions of the ceramic particles and, of course, a component related to the light interaction with the medium and the particles has been expressed as:

$$C_d = D_p ln\left(\frac{E}{E_c}\right) \tag{3.1}$$

where C_d indicate the cure depth, D_p the resin sensitivity, depending on particle size, ceramic load, scattering efficiency and refractive index (Equation 2.3), E the energy dose (in J/cm^2) and E_c the critical energy dose to cause the polymerization or gellation of the resin. Since this model is valid for slurry in which the scattering is predominant on the absorbance [226], [324], trial and error tests were required to evaluate the real cure depth of the inks developed in this work. The standard curing test consisted on systematically exposing squared samples (with excess of slurry) to a line hatch pattern, with a spacing of 100 µm, at the laser exposure of 600 J/cm^2 with a wavelength of 355 nm.

3.1.3.1 Formulation of fuel electrode ink

A proper ratio between monomer and photo-initiator is necessary to ensure the success of the curing process. From the data reported in Figure 3.9, we already know the minimum value for DMPA, needed to show absorbance of the light, i.e. starts the photo-polymerization process, which convert to the total amount corresponds to 0.15wt.% in our formulation. A set of different contents of photo-initiator (0.15-3 wt.%) were formulated aiming to define the most suitable composition to reach a high polymerization (Table 3.1). As can be observed in Figure 3.13, a slightly higher polymerization depth is observed for higher amounts of photo-initiator. The values of photopolymerization obtained are below the required for 3D printing since overcuring of the layers is required to ensure a good attachment to the layers underneath. In general, the criterion is to have a curing depth at least four times the thickness of the printed layer. Other parameters were tuned for increasing it

(see Section 3.2.3). For its highest cure depth, the formulation characterized by the 3wt.% of photo-initiator and called *NiO-YSZ+DMPA300* has been chosen for the printing process. The viscosity of the inks is not affected by the amount of DMPA, and shows values of 9 Pa·s.

Test ID	**Powder**	**TMPTA**	**DMPA**	**Monofax**
	wt.%	wt.%	wt.%	wt.%
NiO-YSZ+DMPA015	70	28.85	0.15	1.0
NiO-YSZ+DMPA150	70	27.5	1.5	1.0
NiO-YSZ+DMPA300	70	26.0	3.0	1.0

Table 3.1: *Composition of the samples for the optimization of the ratio photo-initiator/monomer for the ink of the fuel electrode.*

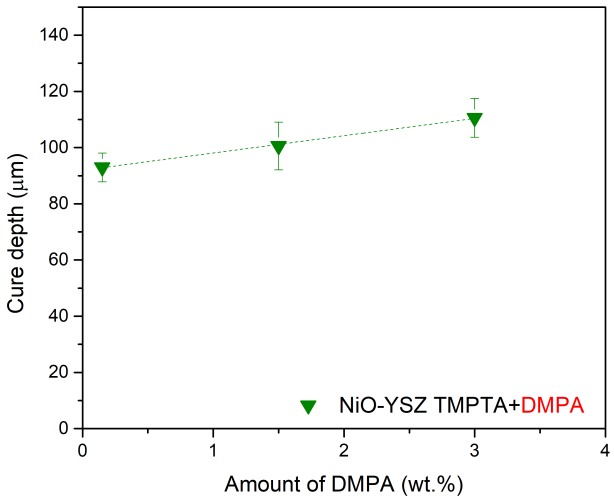

Figure 3.13: *Cure depth as a function of the amount of DMPA introduced in the formulation of NiO-YSZ inks for robocasting. Dashed line as a guide for the reader.*

3.1.3.2 Formulation of the air electrode ink

Since the LSM powder absorbs more light than the nickel oxide, the photo-initiator amount is initially increased in case of the LSM-YSZ slurry. The behaviour is analyzed over the composition range reported in Table 3.2.

Test ID	Powder	TMPTA	DMPA	Monofax
	wt.%	wt.%	wt.%	wt.%
LSM-YSZ+DMPA050	70	28.5	0.5	1.0
LSM-YSZ+DMPA100	70	28.0	1.0	1.0
LSM-YSZ+DMPA300	70	27.0	2.0	1.0
LSM-YSZ+DMPA500	70	24.0	5.0	1.0

Table 3.2: *Composition of the samples for the optimization of the ratio photo-initiator/monomer for the ink of the air electrode.*

For the LSM-YSZ inks, the addition of the photo-initiator is also shown to be a good way to increase the cure depth, as it can be observed in Figure 3.14. In this case, a maximum conversion is obtained in the sample *LSM-YSZ+DMPA300*, used in further experiments. The presence of a maximum in conversion in function of the amount of photo-initiator is in accordance with the analysis reported in Section 3.1.2.1. This maximum is shifted towards higher concentration of photo-initiator due to the competitive absorbance of photons between powders and photo-initiator. As previously reported for NiO-YSZ, the obtained curing depth is not enough for fulfilling the standards. An improvement of this was carried out in Section 3.2.3 by tuning laser parameters.

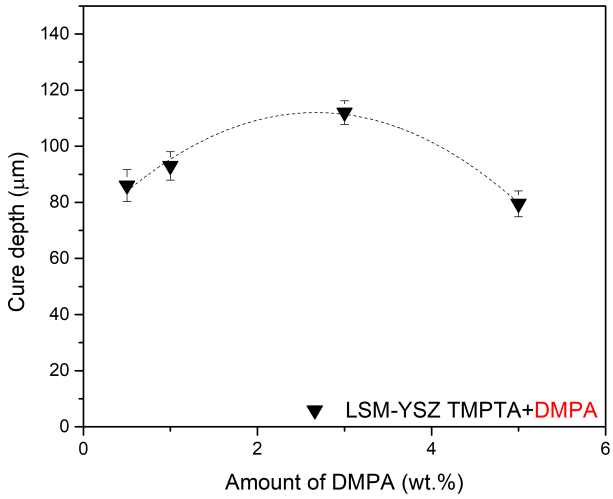

Figure 3.14: *Cure depth as a function of the amount of DMPA introduced in the formulation of LSM-YSZ ink for robocasting. Dashed line as a guide for the reader.*

Since first deposition trials revealed some flowing problems through the nozzle, a diluent (HDDA) was added to the mixture to reduce the viscosity (Table 3.3). The viscosity decrease with the increment of HDDA content is presented in Figure 3.15. The resulting behavior, which is in good agreement with the one reported by *Hinczewski et al.* for SLA slurries [214]. The TMPTA, having a branched structure, shows higher thickness after polymerization, but higher viscosity. On the other hand, HDDA offers less reaction sites, but less steric hindrance due to its linear structure. Combining these two compounds, which are characterized by the same active sites, enable the tuning of the slurry behaviour pursuing a balance between viscosity and cure depth. *Faes et al.* reported values of 10 Pa·s for a similar robocasting ink based on zirconia powders [242]. According to the trend reported in Figure 3.15, this value can be achieved for HDDA value higher than 5wt.%.

Test ID	**Powder**	**TMPTA**	**HDDA**	**DMPA**	**Monofax**
	wt.%	wt.%	wt.%	wt.%	wt.%
LSM-YSZ +HDDA000	70	26.0	0.0	3.0	1.0
LSM-YSZ +HDDA100	70	25.0	1.0	3.0	1.0
LSM-YSZ +HDDA200	70	23.0	3.0	3.0	1.0
LSM-YSZ +HDDA500	70	21.0	5.0	3.0	1.0
LSM-YSZ +HDDA1000	70	16.0	10.0	3.0	1.0

Table 3.3: *Composition of the samples for the optimization of the ratio monomer/diluent for the ink of the air electrode.*

Beyond the viscosity, the amount of HDDA to be added in the LSM-YSZ ink has been finally chosen according to the polymerization depth. As seen in Figure 3.16, no big differences were detected in the cure depth until 5wt.% of HDDA is added, while a reduction in the thickness is observed for samples with a load of 10wt.%. This is due to the structure of the acrylates, the HDDA can be used as monomer itself, but showing lower conversion rates due to a linear structure instead of a branched one [338]. Based on the observed behaviours, we chose to use the formulation called "LSM-YSZ +HDDA200", for its proper flowing through the needle and highest value of cure depth among the tested samples.

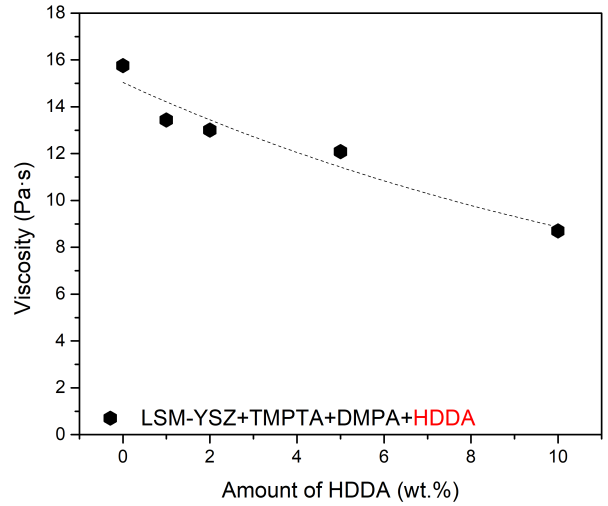

Figure 3.15: *Viscosity in function of the amount of HDDA, for the LSM-YSZ ink. Dashed line as a guide for the reader.*

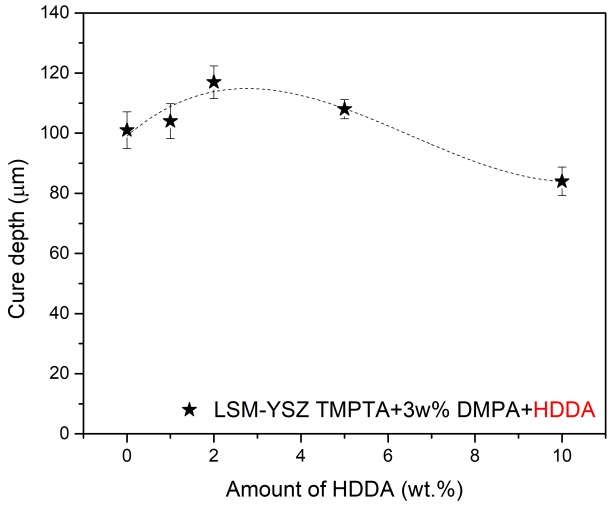

Figure 3.16: *Cure depth as a function of the amount of HDDA introduced in the formulation of LSM-YSZ ink for robocasting. Dashed line as a guide for the reader.*

3.1.3.3 Formulation of the interconnect ink

Taking advantage of the acquired knowledge during the development of the electrode inks, we were able to straightforwardly produce inks for LCTM, the interconnect material, which were suitable for the printing process. The formulated compositions are reported in Table 3.4. For this material, we tried to increase the ceramic loading (from 70 to 75wt.%) and evaluate its effect on the polymerization since the final requirement of the application in SOCs is to generate a dense layer of LCTM. In this regard, results of curing depth presented in Figure 3.17 show a very low change with the amount of ceramic powders in the used range.

Test ID	Powder	TMPTA	DMPA	Monofax
	wt.%	wt.%	wt.%	wt.%
LCTM70	70	26.0	3.0	1.0
LCTM75	75	21.66	2.5	0.84

Table 3.4: *Composition of the samples for the study of the ceramic load for the ink of the interconnect.*

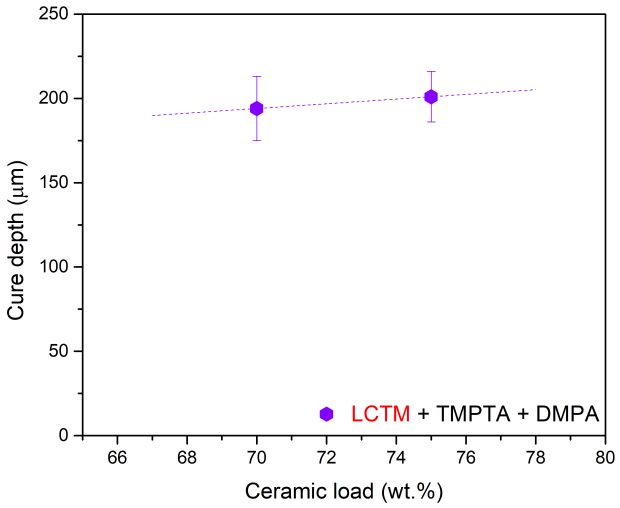

Figure 3.17: *Cure depth behaviour as a function of the ceramic load in the LCTM ink. Dashed line as a guide for the reader.*

On the basis of the viscosity reduction effect observed for LSM-YSZ inks after adding HDDA (Figure 3.15), steply increasing content of HDDA was

added to the mixture for reaching the desired fluidity.
The effect of HDDA addition on the polymerization (cure depth) was stud-

Test ID	Powder	TMPTA	HDDA	DMPA	Monofax
	wt.%	wt.%	wt.%	wt.%	wt.%
LCTM75-HDDA000	75	21.66	0.0	2.5	0.84
LCTM75-HDDA200	75	20.0	1.66	2.5	0.84
LCTM75-HDDA500	75	18.34	4.16	2.5	0.84

Table 3.5: *Composition of the samples for the optimization of the ratio monomer/diluent for the ink of the interconnect.*

ied and reported in Figure 3.18. After 4 wt.% addition of HDDA, the polymerization decreases, due to a minor number of active sites in the linear structure of HDDA compared with the branch one of the TMPTA [338]. The final chosen composition corresponds to the one named "*LCTM75-HDDA200*", which components are reported in Table 3.5, and represents a trade off between the maximum cure depth and a proper fluidity.

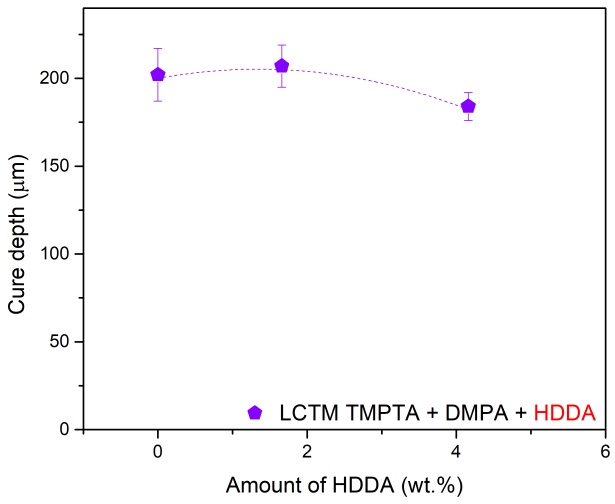

Figure 3.18: *Cure depth as a function of the amount of HDDA introduced in the formulation of LCTM ink for robocasting. Dashed line as a guide for the reader.*

3.2 Optimization of the printing parameters for multi-material parts

As previously mentioned, a unique hybrid printer combining SLA and robocasting, has been developed by 3DCERAM in the frame of the European project *Cell3Ditor*. After the development of the necessary robocasting inks presented in the previous section, we focus on presenting the results of the optimization of the printing parameters, which general introduction is given in Section 2.1.2. More specifically, the attention is on the optimization of: i) SLA material removal required for the deposition of a second material (Section 3.2.1); ii) robocasting printing of different materials (Section 3.2.2); iii) curing of robocasting depositions (Section 3.2.3).

3.2.1 Removal of SLA material prior to robocasting deposition

As explained in Section 2.2.2, the hybridization of two technologies such as robocasting and SLA requires the removal of material of the first technique to give space to the one deposited by the second method. According to our approach, the second material deposited by robocasting is embedded in the first one deposited by SLA. Then, we need removal of the SLA material to form a "pool" that will be filled by the robocasted ink. At the end of the multi-material deposition, all the materials remain at the same level, allowing the blades to scrap a new SLA layer and continue the printing, without damaging the previously deposited layers. This section is devoted to the optimization of the SLA material removal. In this thesis, the removal of material has been mainly performed by: i) laser milling of the polymerized layers or ii) air blowing of uncured layers.

3.2.1.1 Removal of SLA material by laser milling of cured layers

Reducing the frequency of the laser pulses, from the typical values employed for polymerization of 120.5 kHz to 30 kHz, the power of the laser increases an order of magnitude from 140 mW to 1440 mW. This power causes vaporization and/or chemical degradation of the polymeric matrix milling it. The remaining ceramic powders are blown by a directed flow of compressed air [375].
The shape and the depth of the milled region are defined by a series of laser parameters (see Section 2.1 for a detailed description) such as:

- Laser power
- Laser speed

- Laser hatch style (the pattern the laser follows)
- Laser hatch spacing (distance between two laser pitch)

In order to evaluate the depth and shape of the milled regions by different laser exposures, we used optical profilometry (an example for a simple laser shot is shown in Figure 3.19).

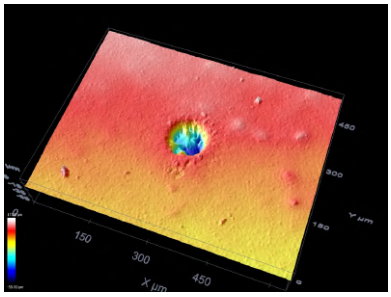

Figure 3.19: *Optical topography of a laser shot in the cured paste*

Laser power and speed

Figure 3.20 shows the change in depth and diameter of milled holes for a fixed laser frequency of 30kHz and a change in the laser power (from 600 to 1400 mW). The dimensions of the hole remain roughly constant (within the error of the measurements) in the whole range of study. Since the dimensions are in the desired values for the optimization of the printing process, we decided to fix 940 mW as laser power in the next studies.

The effect of the laser rastering speed on the etching dimensions was also evaluated. To assess the impact of this parameter, several lines, of a laser spot wide, were engraved at different speeds on a squared SLA printed piece of YSZ (in green). A picture of the resulting marks is reported in Figure 3.21. At first sight, it is possible to notice that at lower speed the mark is better defined and deeper. This effect is confirmed by optical profilometry for a series of etchings within the range of 10 mm/s to 300mm/s (Figure 3.22). The depth decreases almost exponentially up to 100 mm/s, to stabilize around 150 mm/s. The width follows a similar trend, becoming bigger at low speed and almost stabilizing as the depth. The chosen laser speeds used in the printing process are in the range 40 mm/s - 60 mm/s.

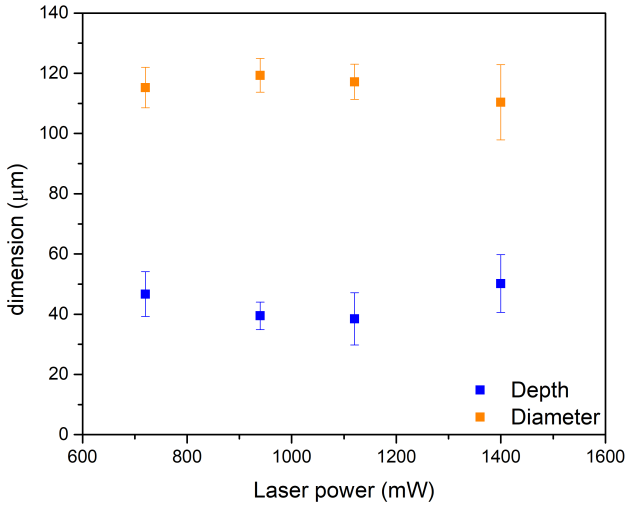

Figure 3.20: *Dependence of the size of the engrave in function of the laser current diode.*

Figure 3.21: *Image of an 8YSZ SLA printed part engraved with lines at different laser rastering speeds (the laser speed is specified besides each line).*

Laser hatch style and spacing

Laser power and speed determine the dimensions of line engraving. However, the necessity of removing material from a region requires to raster the laser over the corresponding area. This laser rastering is automatically controlled by the printing software, which allows different hatch style. The efficiency in the removal of material all over the surface is ruled by the combination of the rastering or hatch style and the hatch distance between the laser paths.

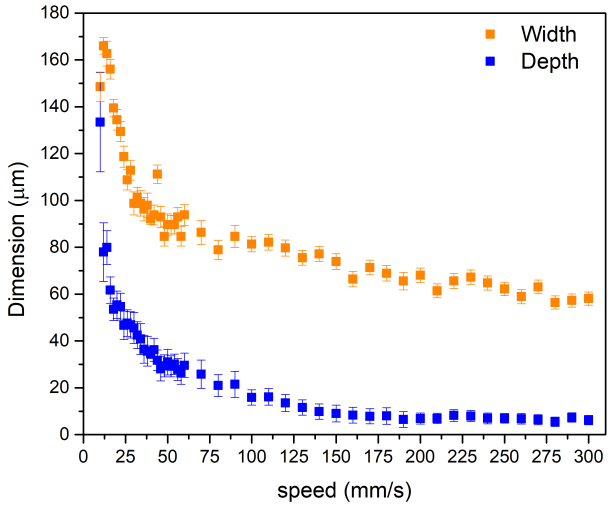

Figure 3.22: *Dependence of the size of the engraving as a function of the rastering speed of 940 mW.*

More specifically, the laser patterns available in the software of the printing machine can be defined as follows:

- "Line": the laser defines the pattern in parallel lines
- "Cross": the laser define two perpendicular "line" pattern
- "Stripe": the laser define "line" perpendicular to the contour of the shape
- "Contour": the laser follows a concentric profile to the shape, i.e. defining circles in the case of a circular shape, squares for a squared shape, etc.

Figure 3.23 presents the morphological differences between all these milling patterns for a rectangular shape. Each type of patterning presents its particular features in the form or remaining material between the hatching lines, namely, pillars in "cross" and parallel or perpendicular bumps in "line", "stripe" or "countour", respectively. To minimize the remaining material in between lines, the pitch distance of the rastering should be adjusted.

The effect of the hatching pitch distance is evaluated for the more promising patterns, namely, "line", "contour" and "cross" (the "stripe" pattern has been discarded due to low removal of material compared with the others). Figures 3.24, 3.25 and 3.26 show optical profilometry of these patterns with

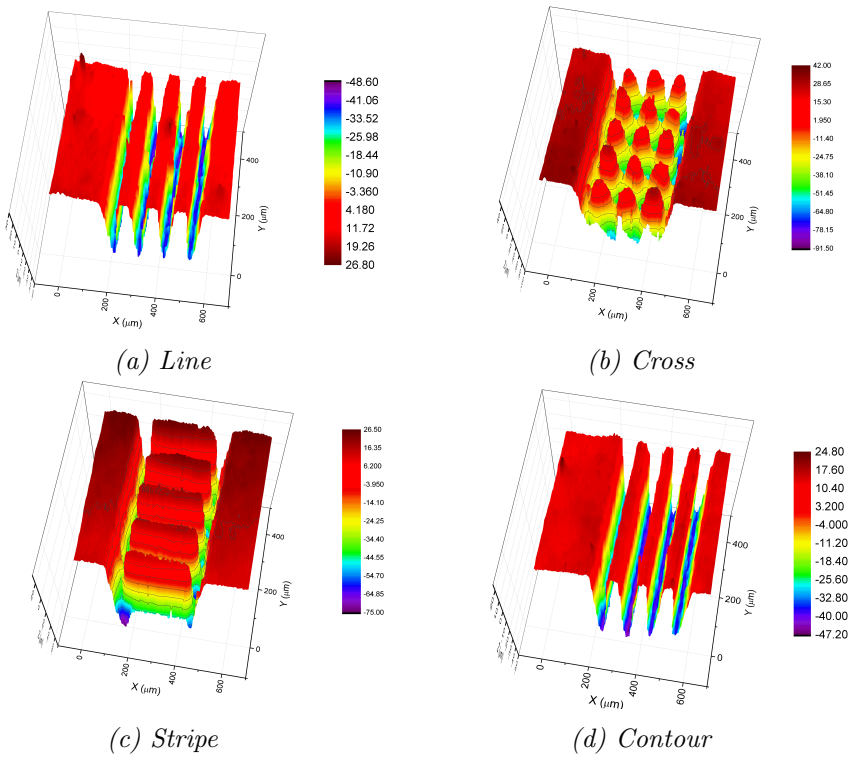

(a) Line *(b) Cross*

(c) Stripe *(d) Contour*

Figure 3.23: *Depth profiles obtained by confocal microscopy for the different milling patterns on 8YSZ SLA printed parts*

hatch distances ranging from 0.025 to 0.1 mm. In general, reducing the distance improves the shape of the etching. However, the depth is substantially increased. When overlapped passes of the laser occur, for example for the "cross" pattern, a deeper engrave is formed. Moreover, some shapes are better defined using specific patterns. As an example, the contour is the best option to define circular shapes like the button cells.

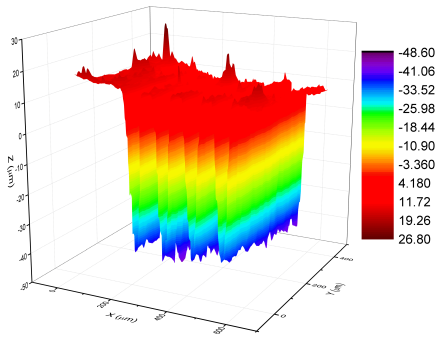

(a) Lines, hatching: 0.1 mm, depth: 80 µm

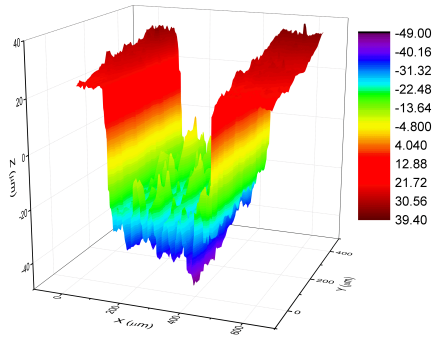

(b) Lines, hatching: 0.05 mm, depth: 100 µm

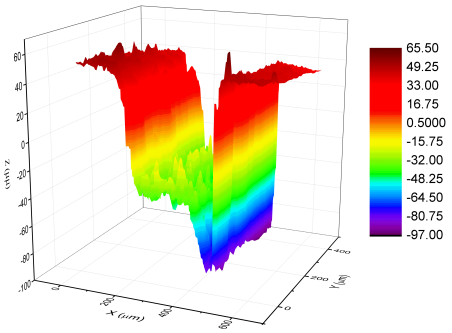

(c) Lines, hatching: 0.025 mm, depth: 170 µm

Figure 3.24: *Laser hatch spacing effects on line hatch style.*

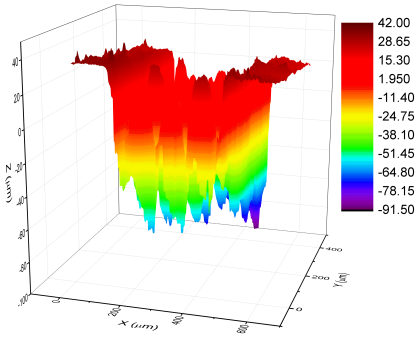

(a) Cross, hatching: 0.1 mm, depth: 130 µm

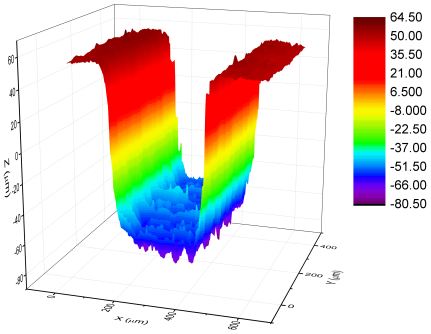

(b) Cross, hatching: 0.05 mm, depth: 150 µm

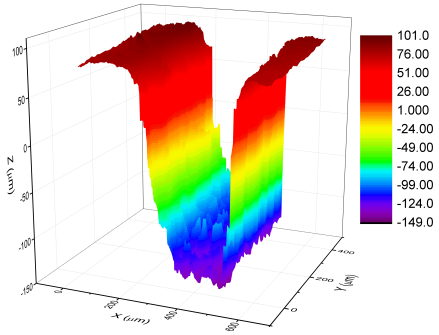

(c) Cross, hatching: 0.025 mm, depth: 250 µm

Figure 3.25: *Laser hatch spacing effects on line hatch style.*

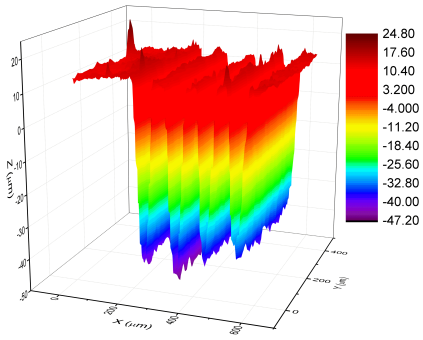

(a) Contour, hatching: 0.1 mm, depth: 70 µm

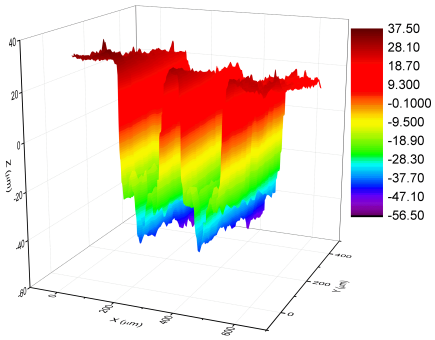

(b) Contour, hatching: 0.05 mm, depth: 90 µm

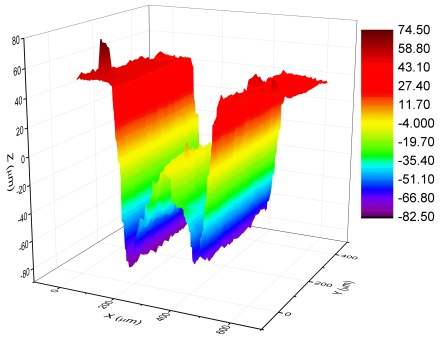

(c) Contour, hatching: 0.025 mm, depth: 130 µm

Figure 3.26: *Laser hatch spacing effects on contour hatch style.*

The whole analysis carried out in this section allowed to solve all the particular situations found in this thesis. In particular, it is worth mentioning a very common scenario where a 200 µm-thick layer of SLA YSZ has to be removed. For this specific case, a cross shape hatching with a small distance at a speed of 60 mm/s has been typically applied.

3.2.1.2 Removal of SLA material by air blowing of uncured layers

A second strategy for the material removal is the use of a compressed air jet instead of a laser milling (this concept was proposed by 3DCERAM within the Cell3Ditor project and independently implemented at IREC). One of the nozzles of the robocasting multimaterial arm is substituted by a home-made blower head able to selectively jet air at high speed (from a reservoir at 2 bar). The ejected air is employed to remove uncured paste remaining after doctor blade deposition and curing. Its operation can be controlled by the software, enabling the integration of this step in the printing routine. Figure 3.27 presents the original robotic arm (3.27a) and the arm assembled with the blower (3.27b).

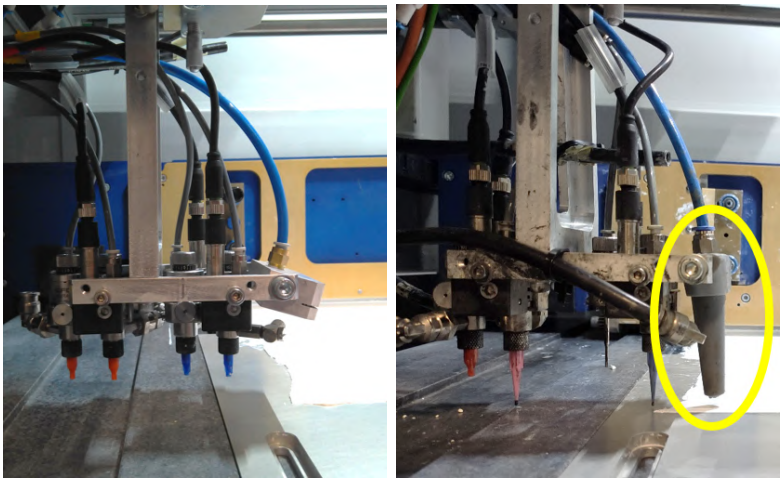

(a) Original multi-nozzle robocasting arm

(b) Final configuation with the home-made blower

Figure 3.27: *Implementation of the material removal, the blower is highlighted in yellow in its final configuration.*

For the removal of paste by compressed air, it is necessary to use a "cross" hatching profile, with hatching of 250 µm at 60 mm/s. We noticed an adequate removal of the paste inside a cured "pool" defined by SLA, accumulating blown uncured paste outside the cell. This spare paste will be spread in the subsequent scraping carried out by the blades. It is important to remark here that, opposite to laser milling, the use of the blowing approach does not require from an accurate control of the depth since all the uncured paste will be removed (until finding the already cured layer underneath).

3.2.2 Deposition of ceramic printable feedstock by robocasting

The capability of printing with different materials is given by the robocasting system, this technology allows the controlled extrusion of the material through a needle. The printable feedstock is stored in refillable cartridges. The original cartridges were of 960 ml of capacity (Figure 2.26a) but were substituted by small volume tanks of 30 ml (Figure 3.28). The extrusion of material takes place by applying pressure through a piston to the each of the cartridges. The original big cartridges presented inhomogeneity in the extrusion and a certain delay due to long tubes until the deposition needle. These issues were solved with the implementation of small cartridges directly connected to the nozzles.

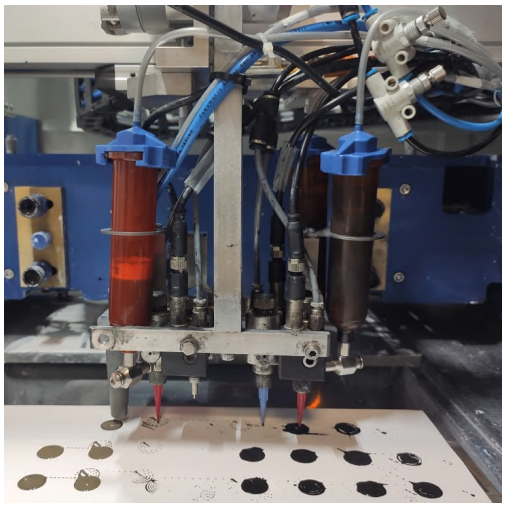

Figure 3.28: *Modified cartridges system for robocasting to solve inhomogeinity and delays occuring in the originally installed unit.*

The software controls the deposition of material in a similar way that for the laser milling, namely, it is possible to change the speed of the head, the hatch style and the hatch spacing. Moreover, the size of the needle, the extrusion pressure and the gap between the needle and the platform are tunable parameters to fix at the beginning of the printing process. In these regards, the internal diameters of the needles were 250 µm and 410 µm for the for the NiO-YSZ and LSM-YSZ inks, respectively. Bigger diameters were used for the LSM-YSZ inks to compensate the already discussed flowing issues. The pressure was calibrated before each printing in order to ensure one drop per second of ink (usually the values oscillate between 0.8 and 1.2 bar). Finally, the optimum needle-substrate gap was determined based on tests in which

the inks were deposited at different distances and the size and shape of the obtained trenches were measured. Figure 3.29 is an example of the obtained deposition with different gaps. Inappropriate distances between the needle and the substrate generates discontinuous lines, separated in dots. The same procedure of printing lines has been used to evaluate the effect of the deposition speed on the shape and dimensions of the printed layers.

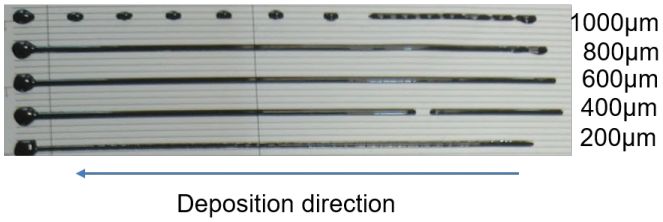

Figure 3.29: *Robocasting deposition of LSM-YSZ ink at different needle-substrate gaps, the lattice underneath has 1 mm spacing.*

Figure 3.30 reports the effects of the gap and speed on the final dimensions of robocasted NiO-YSZ lines. As it can be observed, the thickness reaches a minimum value of 1.2 mm in the range of 400/600 µm, suddenly increasing afterwards. On the other hand, the dimension of the deposition decreases when increasing the speed, obtaining 600 µm-thick layers for speeds of 60 mm/s. Although the deposition could in principle go faster, strong vibrations have been detected in the machine at higher rates, which prevents the use of deposition speeds above 80 mm/s. In the frame of this work, speeds of 60 mm/s were typically employed for NiO-YSZ.

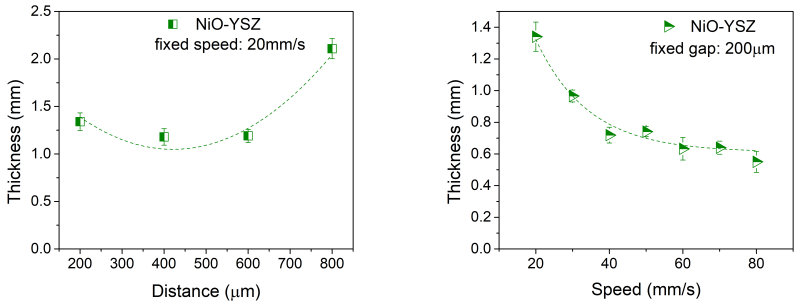

(a) Effect of gap distance *(b) Effect of speed*

Figure 3.30: *Thickness of robocasted lines of NiO-YSZ inks as a function of the needle-substrate distance and printhead speed. Dashed lines as guides for the reader.*

A similar behaviour is observed in the case of LSM-YSZ ink and reported in Figure 3.31. Slight decrease of the thickness when increasing the gap is observed, presenting the lowest values between 400/600 µm. Complementary, it is shown that the thickness decreases with the increase of the speed. In the frame of this work, speeds of 60 mm/s were typically employed for LSM-YSZ.

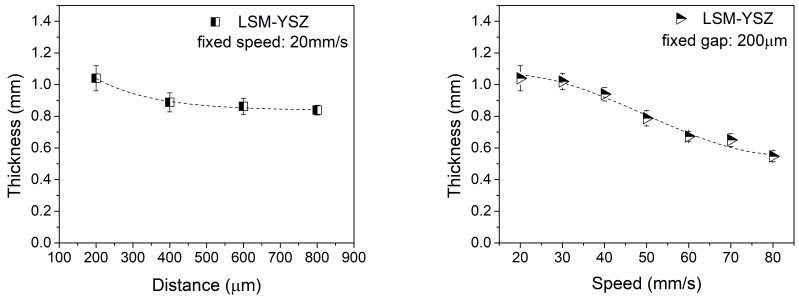

(a) Effect of gap distance *(b) Effect of speed*

Figure 3.31: *Thickness of robocasted lines of LSM-YSZ inks as a function of the needle-substrate distance and printhead speed. Dashed lines as guides for the reader.*

After the determination of pressure, gap and speed, it was necessary to optimize the best hatching parameters for covering extended areas (ensuring there is not overdeposition). As discussed in the previous section for the laser milling, the hatching pattern and the pitch distance are key parameters to optimize. However, since the inks present a certain fluidity after deposition, they spread filling the milled/blown "pool", which makes the mentioned parameters less critical that in the case of the etching. Indeed, the most important parameter here is the total volume of paste deposited, which control was largely improved with the small cartridge configuration. A set of optimized parameters for each robocasting ink is listed in Table 3.6.

Material	**ID tip [μm]**	**Pressure [bar]**	**Gap [μm]**	**Hatch type**	**Hatch spacing [mm]**	**Printhead speed [mm/s]**
NiO-YSZ	250	0.8	400	Contour	1.5	60
LSM-YSZ	410	1.1	400	Contour	1.2	60
LCTM	250	1.0	400	Contour	1.0	60

Table 3.6: *Optimized deposition parameters for the different inks employed in this thesis.*

Nevertheless, these conditions were always tested and fine-tuned for each printing in case of necessity, e.g. when a change of viscosity of the paste takes place due to the ambient temperature.

3.2.3 Curing of robocasting inks

Due to the high absorbance of LSM and NiO powders, the curing process has been one of the most important issues for the developing of the hybrid printing. This is because an incomplete curing of the robocasting ink represents its spread on the SLA paste in the subsequent scraping. In order to reach a proper curing, the thickness of the deposited layers should be lower than the estimated cure depth.
The control in the thickness of the robocasted layers has been presented in the previous section. Now, the cure depth as a function of the laser parameters is discussed (complementing the Section 3.1.3, where the cure depth was already discussed for the optimization of the formulation of the paste). The main parameters of the laser for controlling the polymerization step are the rastering speed and the power. During the curing of YSZ deposited by SLA, the speed is set at 5000 mm/s. However, this speed does not allow any type of polymerization for high absorbance materials like LSM, NiO or LCTM. In order to solve this problem, a wide range of speeds were tried from 10 mm/s to 5000 mm/s. Only for values lower than 250 mm/s, a certain polymerization effect is observed. Figure 3.32 reports the numerical values of the polymerization as a function of the speed (in the low range below 250 mm/s) for the materials used in this work. On the light of these results, the lowest speed (10 mm/s) was chosen to ensure the curing of the typical thickness of robocasted electrodes, which are in the order of hundreds of microns. The other parameter that plays an important role in the polymerization process is the power of the laser. Figure 3.33 shows the cure depth as a function of the laser power (at a fixed speed of 10 mm/s) for the inks under study. It is clear how the thickness of the polymerized layer increases with the increasing of the power of the laser. In order to ensure a penetration comparable with the deposited layers, the power typically employed was around 600 mW. Power above this value eventually presented burning of the organics.

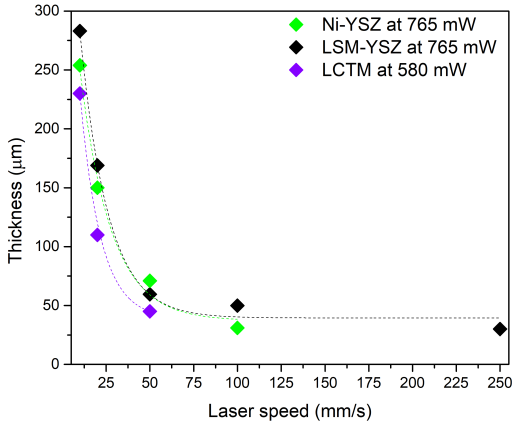

Figure 3.32: *Cure depth in function of the laser speed. Dashed lines as guides for the reader.*

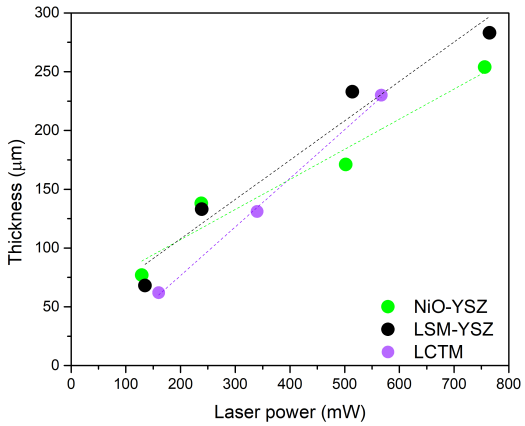

Figure 3.33: *Cure depth in function of the laser power. Dashed lines as guides for the reader.*

This indicates that the local temperature increases during curing in our approach. Figure 3.34 shows a thermal image obtained by recording the curing process in our machine with a thermal camera (spot size $\sim$ 3 mm), which confirms this point. This local temperature increase could contribute to improve the polymerization of our highly absorbent pastes as proposed by *Bartolo et al.* for thermo-stereo-lithography [185], [376]. Indeed, *Bae et al.* reported that DMPA can thermally decompose and start a polymerization reaction around 200 °C [184]. Further work is in progress to confirm this

possibility and improve the curing of the robocasted layers by combining UV- and thermal-polymerization.

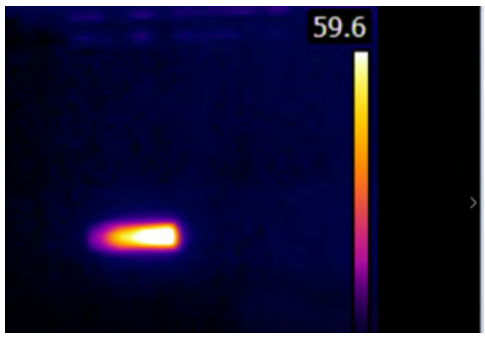

Figure 3.34: *Thermal image after the laser passing during the polymerization test.*

After these optimization process, a reasonable curing of the robocasted electrode layers was achieved. Figure 3.35 shows typical images of as-deposited and cured layers of NiO-YSZ.

(a) As deposited *(b) Cured*

Figure 3.35: *Typical image of a robocasted NiO-YSZ layer before and after curing.*

3.2.4 Summary of the whole printing process of multi-materials parts

Finally, as a summary report of the whole fabrication process of multimaterial parts inside the hybrid printer, pictures of the different steps were collected in Figure 3.36. Moving from left to right, it is possible to observe the deposition of the SLA scaffold, the removal of material by laser milling, the deposition and curing of the bottom electrode (NiO-YSZ), another double scraping for SLA YSZ, the deposition by robocasting of the other electrode (LSM-YSZ) and its curing. From the pictures it is noticeable the spreading

of some uncured robocasting ink in the second SLA step. Although the small amounts spread does not seem to affect the obtained solid oxide cells, further work is needed (already in progress) to avoid this issue.

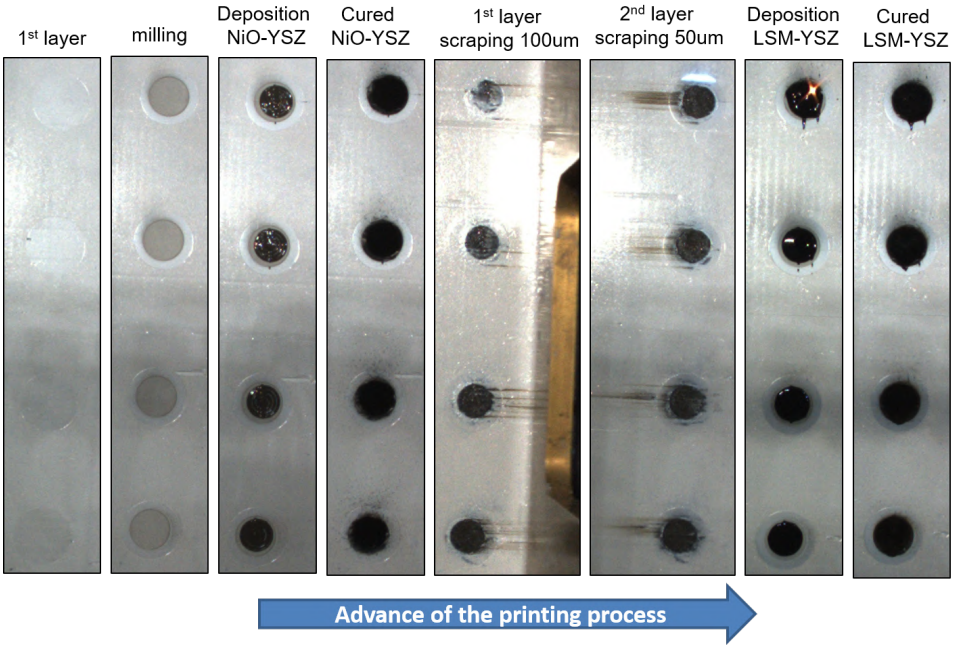

Figure 3.36: *Advance during time of the printing of an entire SOC.*

3.3 Optimization of the thermal treatment of the green printed parts

At the end of the printing the polymerized pieces are embedded in uncured slurry (Figure 2.30). The pieces have to be detached from the printing platform and cleaned with the help of solvents. At this point the parts are consistent, with mechanical properties closer to the polymeric material than to the ceramics. Once the pieces are extracted and cleaned from uncured paste, the organics from the polymerized part have to be removed. This is done by a thermal treatment called debinding in which the organics are vaporized and removed from the piece by a continuous flow of gas [377]. The debinding is characterized by a low heating rate ($<$0.5 K/min), to avoid uncontrolled uptake of the polymers, which could generate cracks. The final step is the sintering, which leads to ceramic parts with properties comparable with parts manufactured by conventional techniques.
The SLA slurries produced by 3DCERAM are provided with optimized thermal treatments. This treatment consist of a debinding cycle including a pre-sintering step above 1000°C, which keeps the piece in shape and easy to handle, and a sintering step to the final temperature. The debinding can be carried out under a flow of air or inert atmosphere. Inert atmosphere is preferred for thicker parts to avoid cracks. The sintering step in air is conventional with a final temperature depending on the material, e.g. 1300°C for 8YSZ (as optimized within the Cell3Ditor project) or 1700°C for alumina. In this section, we provide a characterization of the SLA fabricated parts (alumina and 8YSZ) all along the different steps of the thermal treatment (section 3.3.1).
On the basis of the thermal treatment employed for SLA, we developed the thermal treatment for multi-material parts. Section 3.3.2 is devoted to describe this process and the resulting materials and pieces.

3.3.1 Monomaterial

Alumina

The phase of the printed pieces has been analyzed at each step of the fabrication process by X-Rays Diffraction. As it can be seen in Figure 3.37, the alumina keeps the α-phase (reference pattern num.: ICDD-01-081-2266) during all the sintering steps. Additional peaks not corresponding to the alpha-alumina are observed in the green body. This indicates that these secondary phases are already present in the original slurry (likely due to the use of low grade alumina powder) or the formation of a crystalline polymer. Since alumina is mainly employed in this thesis for the fabrication of catalytic reactors, the major presence of the α-phase is highly convenient due to its

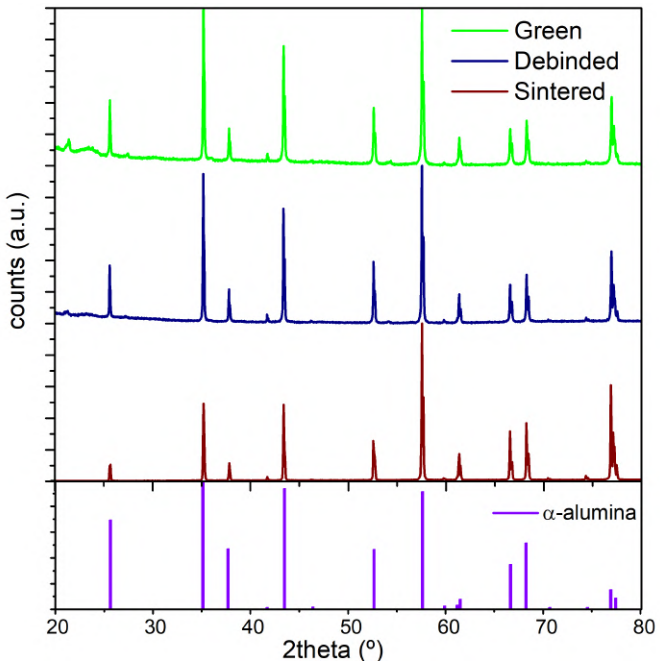

Figure 3.37: *XRD pattern of the alumina parts in each stage of fabrication. Reference pattern num. α-alumina: ICDD-01-081-2266.*

excellent thermal properties, mechanical stability and chemical compatibility with most of the catalysts systems [378], [379]. The thermal treatment for the alumina pieces is not correlated to any phase variation. As consequence, debinding in nitrogen is usually preferred to improve the vaporization instead of a burning phenomenon, especially for catalysis applications that require complex geometries and often massive pieces (the evacuation of the organics becomes more difficult in such pieces).

Yttria Stabilized Zirconia

In the case of printed 8YSZ, the XRD patterns vary in different moments of the production. The major contribution is from the tetragonal or cubic phases. As it can be noticed in Figure 3.38, the characteristic peaks of these two phases are overlapping, which is a well-known fact reported in literature [352]. On the sides of the major peak, corresponding to the plane (111), two peaks appear. These are identified as the two major peaks from the monoclinic phase, corresponding to the peaks (-111) and (111). The intensity of these peaks is ten orders of magnitude lower than the main peak, reason why the other peaks of monoclinic phase, with a lower intensity, do not appear. The monoclinic phase is clearly present in the green piece. Its presence decreases in the debinded one and has not been detected in the sintered final piece.

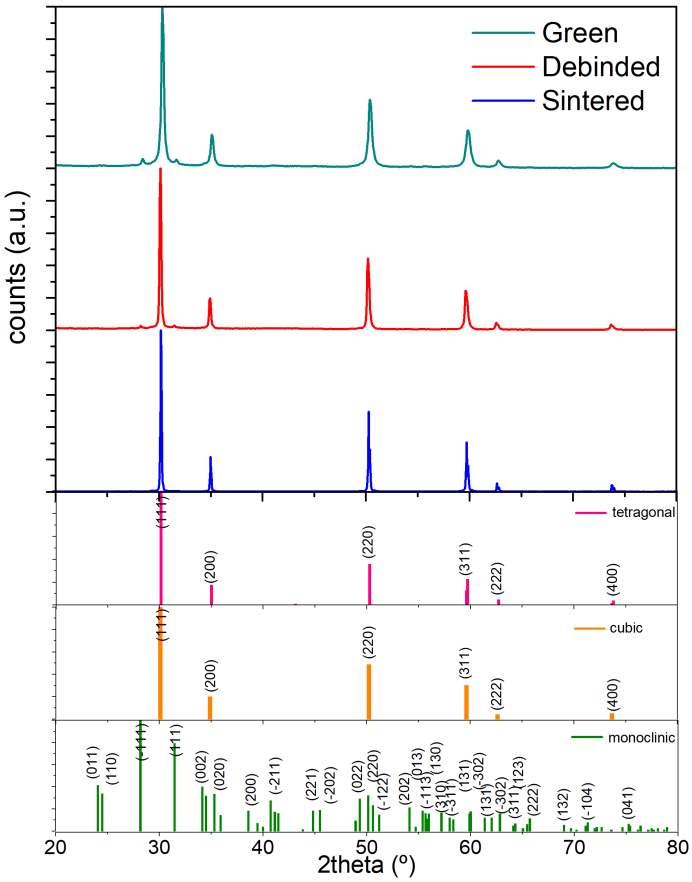

Figure 3.38: *XRD pattern of 8YSZ in each stage of fabrication. Reference pattern num. tetragonal zirconia: ICDD-01-070-4431, cubic: ICDD-01-070-4436, monoclinic: ICDD-01-078-0047.*

According to *Hemberger* [353] and *Yashima* [354], Raman Spectroscopy is one of the most suitable techniques to identify the stabilized zirconia phases. A Raman study is reported in Figure 3.39 for the green and debinded pieces, while the sintered ones are presented in Figure 3.40 (for the sake of clarify). The green piece shows a mixture of monoclinic and tetragonal phases, with traces of the cubic one, in particular the signal results noisy due to the organic components presented in the part (which give Raman signal at higher Raman shift). After the removal of the organics, i.e. the debinding, the noise disappears, but in case of the debinding in air, the monoclinic phase persists with clear characteristic peaks in the sample. In the case of the thermal treatment in nitrogen up to 800°C, followed by a progressive change to oxidising atmosphere, the tetragonal phase is the main constituent of the

sample, although traces of the two characteristic peaks of the monoclinic before the 200 cm^{-1} can be identified.

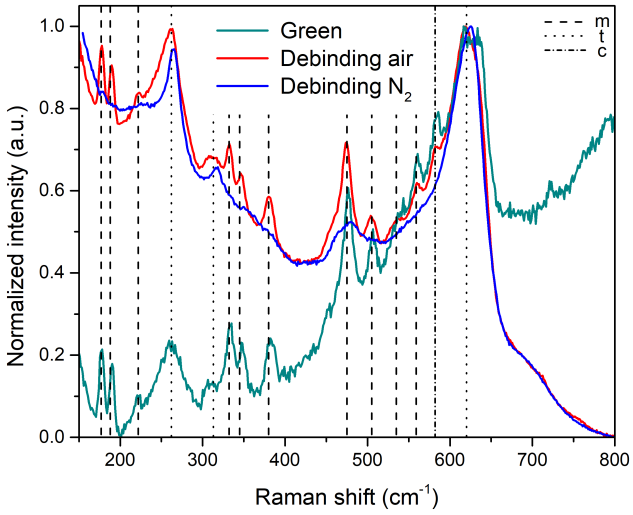

Figure 3.39: *Raman spectra of the 8YSZ pieces in green state and after debinding in two different atmospheres.*

With the purpose of avoiding monoclinic phase, the debinding in mixed atmosphere has been preferred during this work.
Figure 3.40 shows the Raman spectra of final pieces obtained with a single cycle of debinding and sintering (called D+s-single) and with a cooling step in between (called D-s-2steps). The lines indicate the significant peaks of monoclinic and tetragonal phase that must be taken into account to detect detrimental peaks. Both of the samples show tetragonal phase. In the case of the piece cooled down between the two cycles signal at 180 cm^{-1} and 480 cm^{-1} indicate traces of monoclinic phase. Considering this point and the saved time, the thermal treatment has been carried out in a single step.
The previous discussion on the YSZ phase evolution during the fabrication process is relevant since the monoclinc-to-tetragonal transition generates a volume change around 4% in the unit cell, resulting in cracks that can invalidate the gas-tightness of the YSZ acting as electrolyte [380]. Moreover the monoclinic phase presents the lowest ionic conductivity of the material, affecting negatively the performance of the obtained device. The maximum conductivity is observed for 8mol% doping, stabilizing the cubic phase [381].

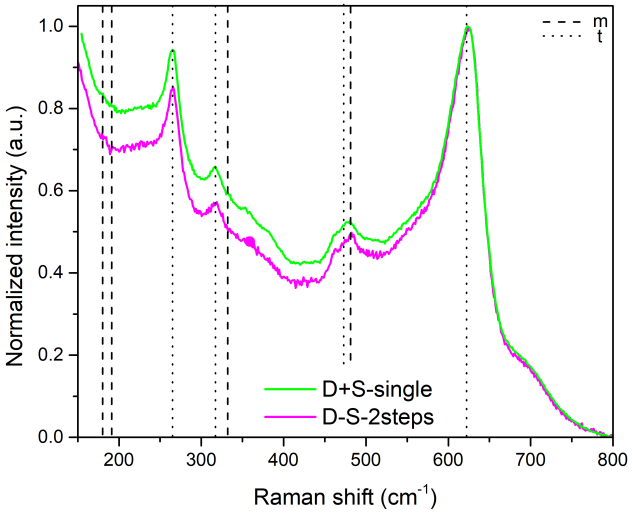

Figure 3.40: *Raman spectra of the 8YSZ pieces sintered with different thermal cycles.*

3.3.2 Multimaterial co-sintering optimization

The co-sintering of all the layers of a fuel cell has to be conducted in such a way that produces the proper densification of the interconnect and electrolyte, to guarantee the gas tightness between the oxidant and reducing atmospheres, while at the same time maintaining a certain degree of porosity in the electrodes to allow the diffusion of the gases to the Triple Phase Boundary. The evaporation of organic compounds has to take place with a proper kinetics to avoid explosive reaction. All the materials have their own Thermal Expansion Coefficient (TEC). Although some mixtures (LSM-YSZ and NiO-YSZ) have been realized to match as much as possible these parameters, the differences are still substantial enough to make the co-sintering the critical step and a major cause of failures.
In the previous section, we already discussed the advantage of using an inert atmosphere during the debinding to avoid the presence of monoclinic phase in the zirconia pieces. *Goswami et al.* reported a study on the thermal degradation in air and nitrogen of mixtures of TMPTA and HDDA. They observed a multi stage exothermic degradation when the treatment is carried out in air, indicating the burning of the compounds, while it is governed by diffusion in the case of nitrogen flowing [336]. Based on these facts, the debinding is carried out in nitrogen to avoid the burning of organics which can generate delaminations and failures. To reduce the risk of failures during the handling of the pieces, the thermal treatments have been realized in a

single furnace without cooling down between debinding and sintering. Thermogravimetric analyses have been performed to evaluate the critical steps of the debinding and to find eventual incompatibility between the developed slurries for robocasting and the SLA ones, reported in Figure 3.41. The robocasting slurries present an important mass loss at 400°C. After 600°C no organic residue is detected, as expected from literature, confirmed by the stabilization of the plateaus at the corresponding ceramic loads [336]. NiO-YSZ based ink shows other minor variations with the red-ox cycle of the oxide. The commercial 8YSZ paste presents an additional small mass loss around 120°and a major event at 400°C as well. The higher residual weight at the end of the process is due to the higher ceramic load in the slurry for SLA compared with the ones for robocasting. These results show an apparent compatibility between the different pastes and have been used to develop the final debinding cycle.

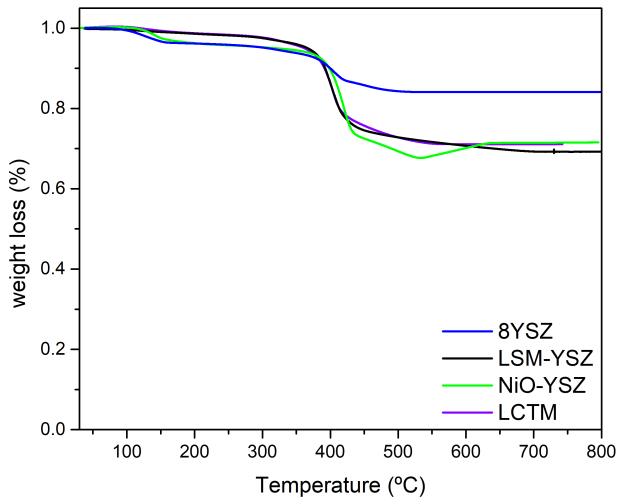

Figure 3.41: *Weight loss of the robocasting and SLA slurries as a function of the temperature (obtained by TGA analysis).*

Following the work of *Weingarten et al.*, the debinding cycle was modified with an initial step up to 270°C in a powder bed, to support the sample, homogenize the temperature and help the removal of organics by capillary forces [382]. Removed the powder bed, we applied a thermal cycle up to 800°C (ramp of 0.4 K/min) in nitrogen. At 800°C, where no organic compound is inside the piece, we change step by step from an inert to an oxidant atmosphere. A dwell of one hour at 900°C is added to allow the stabilization before the sintering itself. Most of the failures were characterized by a

complete deintegration, being the electrodes completely detached from the electrolyte. In order to improve the success rate, the variation from inert to oxidizing atmosphere has been conducted in a more progressive way. The total time devoted to this process is six hours (compared with the previous two hours), starting at 800°C, with steps 5 ml/min step until a flow of 50 ml/min, afterwards 10 ml/min up to 100 ml/min and 50 ml/min up to 500 ml/min. In order to control the oxidation of the nickel, happening a such temperature in a oxygen rich atmosphere.
At this point, the proper sintering of the ceramic has to take place. As anticipated before, this part of the cycle is critical for the densification, microstructure and attachment between the layers. To optimize the thermal cycle, optical dilatometry has been performed at Francisco Albero S.A.U. withiin the frame of the Cell3Ditor project. The profiles of cylindrical samples were recorded and analysed as a function of temperature. Figure 3.42 presents the obtained curves. The curves present the relative height of the sample as a function of the temperature, a shrinkage indicates the sintering of the specimens. The shrinkage of NiO-YSZ and YSZ starts around 1050°C, while for LCTM the curve starts to decrease at 1100°C. The LSM-YSZ faces previous contraction below 700°C. In the range between 1200°and 1300°C, the sintering itself takes place. At this point the curves for LSM-YSZ and YSZ start to stabilize, approaching a complete sintering, while LCTM and NiO-YSZ ones maintain the same slope, indicating the possibility to continue the sintering process up to higher densification.
Due to the requirements to guarantee a working SOCs, the electrolyte and the interconnect need to be gas-tight, i.e. achieve high densifications, while the electrodes necessitate residual porosity, ideally 40% at the operation condition [383]. In the case of the fuel electrode, this level of porosity can be straightforwardly achieved by the reduction of the NiO into metallic Ni occurring in reducing atmospheres employed in SOCs operation [49]. Because of this, the porosity of the fuel electrode is not a concern at this point of the study. More attention should be paid for the air-electrode.
According to the previous paragraph, the choice of the sintering treatment is dictated by the necessity of high temperature for the densification of the electrolyte and interconnect and low temperature to ensure the diffusion of gas in the air electrode. Trying to balance all the components different sintering cycle have been proposed:

- 1300°C, 4 hours (cycle used for 8YSZ printed electrolytes);
- 1100°C, 4 hours and 1300°C, 2 hours;
- 1100°C, 4 hours and 1250°C, 2 hours;
- 1200°C, 10 hours.

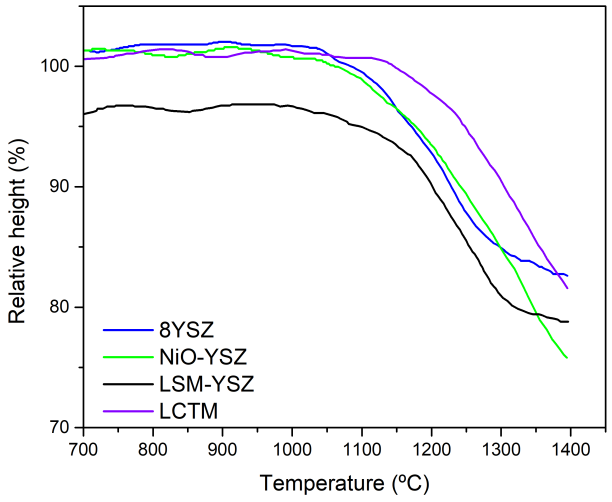

Figure 3.42: *Optical dilatometry on cured samples of the player materials in this study.*

At first the thermal treatment proposed for the 8YSZ has been applied, to evaluate its effect of the layers. The cycle based on the one recommended for 8YSZ, it was proven effective for the NiO-YSZ|YSZ|NiO-YSZ pieces and used for the production of symmetrical cells of this materials (described in Section 4.2.1.1). On the other hand, this cycle presents some issues when it is applied to LSM-YSZ layers, generating a dense structure that does not allow the diffusion of the gases, resulting in bad performance of the realized symmetrical cells (more details can be find in Section 4.2.1.2).
With the purpose of reducing the sintering temperature, we tried a cycle with dwell at 1200°C and longer time, ten hours. Since the sintering process starts around 1100°C, a step of four hours at this temperature is added, to short the dwell at high temperature, chosen as 1300°C or 1250°C.
The effect of the different temperatures on the layers of a complete SOC cell (excluding the LCTM interconnect) have been analysed by Scanning Electron Microscopy, in particular to estimate the porosity of the different components of the cell. In the following figures, each cell will be analysed according to the four different thermal cycles, these images are from an entire SOC co-sintered at the reported temperature.

As previously discussed, the densification of the fuel electrode is not limiting in principle (as far as is well attached to the electrolyte). Figures 3.43c, 3.43f, 3.44c and 3.44f shows the microstructure of the NiO-YSZ printed layers after sintering. A sufficient level of porosity is achieved in all the cases

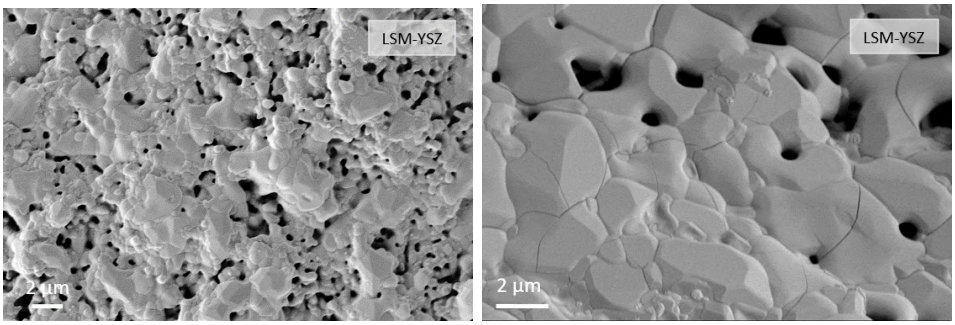

(a) LSM-YSZ sintered at 1300° C for four hours

(d) LSM-YSZ sintered at 1100° C for 4 hours and at 1300° C for 2 hours

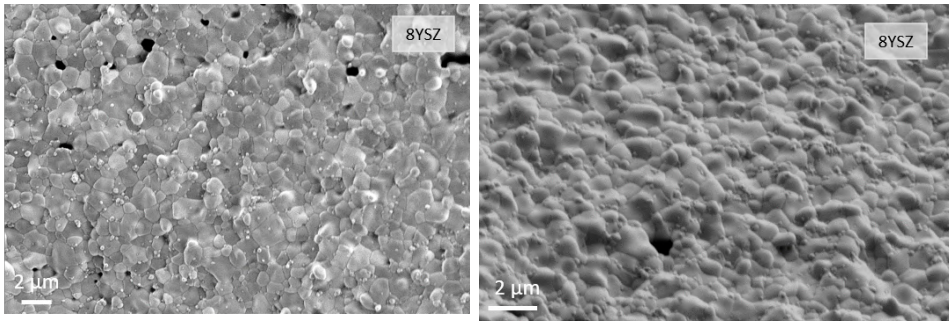

(b) YSZ sintered at 1300° C for four hours

(e) YSZ sintered at 1100° C for 4 hours and at 1300° C for 2 hours

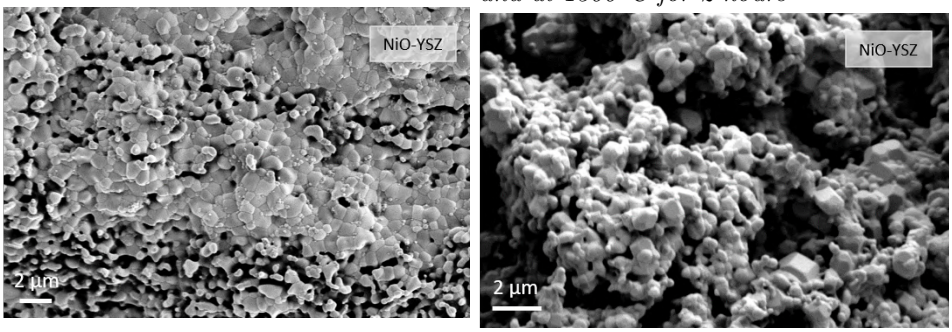

(c) NiO-YSZ sintered at 1300° C for four hours

(f) NiO-YSZ sintered at 1100° C for 4 hours and at 1300° C for 2 hours

Figure 3.43: *SEM micrographies of the cell layers sintered at 1300° C with different dwell times.*

(even before the NiO reducing step). On the other hand, the air electrode is the most sensitive to the sintering temperature. As already commented, temperatures of 1300°C already generate a dense layer, which is detrimental for the oxygen conduction (as later proven by the electrochemical characterization in Section 4.2.1.2). Adding a step at 1100°C has even showed a worse effect reducing the porosity of the layer (see comparison in Figure 3.43a and

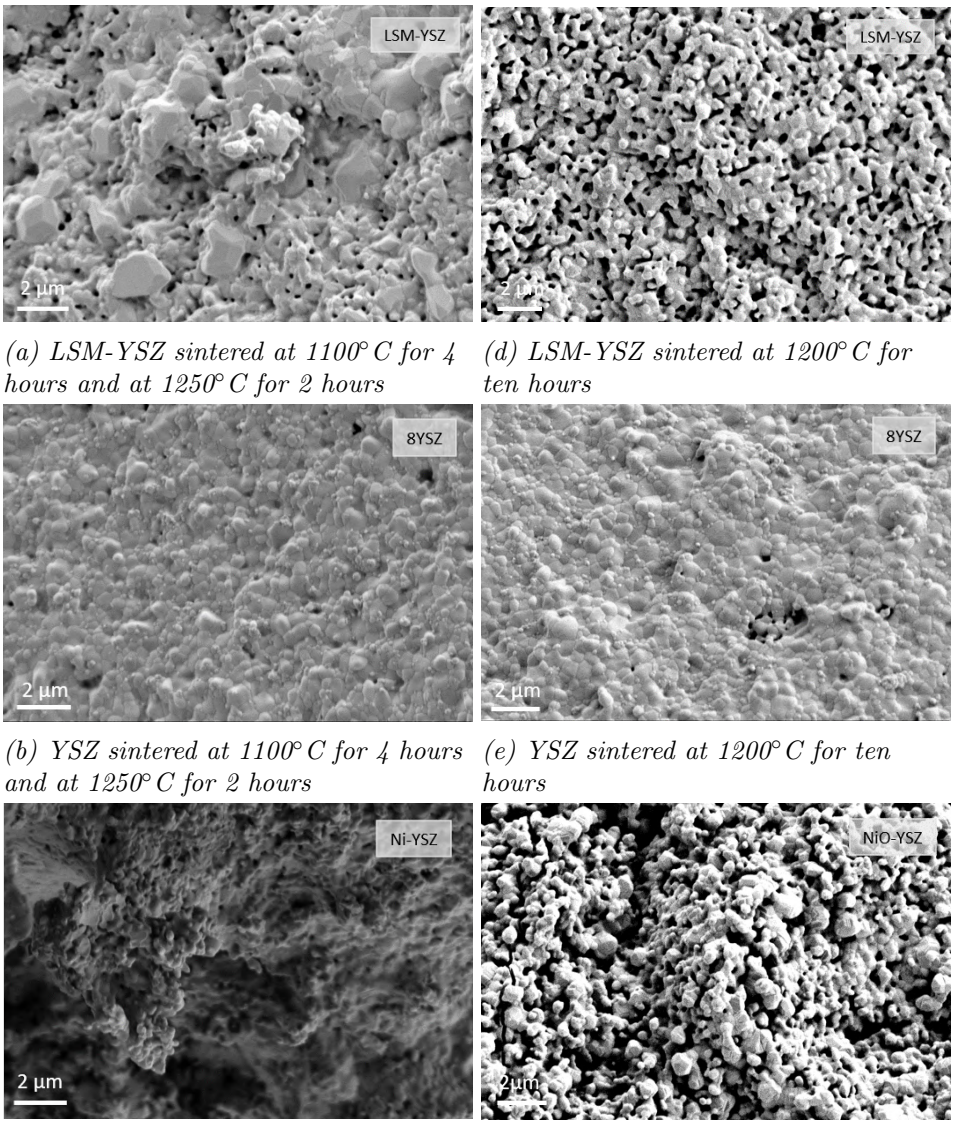

(a) LSM-YSZ sintered at 1100° C for 4 hours and at 1250° C for 2 hours

(d) LSM-YSZ sintered at 1200° C for ten hours

(b) YSZ sintered at 1100° C for 4 hours and at 1250° C for 2 hours

(e) YSZ sintered at 1200° C for ten hours

(c) NiO-YSZ 1sintered at 1100° C for 4 hours and at 1250° C for 2 hours

(f) NiO-YSZ sintered at 1200° C for ten hours

Figure 3.44: *SEM micrographies of the cell layers sintered at different temperatures (1250° C and 1200° C).*

3.43d). Regarding the sintering at lower temperatures, the porosity is higher in the sample treated at 1200°C than at 1250°C, although even in this case there is room for further improvement on the composition of the slurry. Work in progress is devoted to include pore formers in the robocasting inks.
Finally, the density of the electrolyte, which is a critical aspect for the proper working of a SOC, is guaranteed in the case of the highest sintering temperat-

ure (Figures 3.43b and 3.43e). Although lowering the maximum temperature to 1200°and 1250°C seems to induce some porosity (Figures 3.44e and 3.44b), the observed density still is very high with some closed porosity not crossing the electrolytes. From the previous analysis and the electrochemical measurements presented in other sections (Section 4.2.1.2), the sintering cycle of choice is the one characterized by a dwell of four hours at 1100°C and two hours at 1250°C. The entire cycle is presented in Figure 3.45.

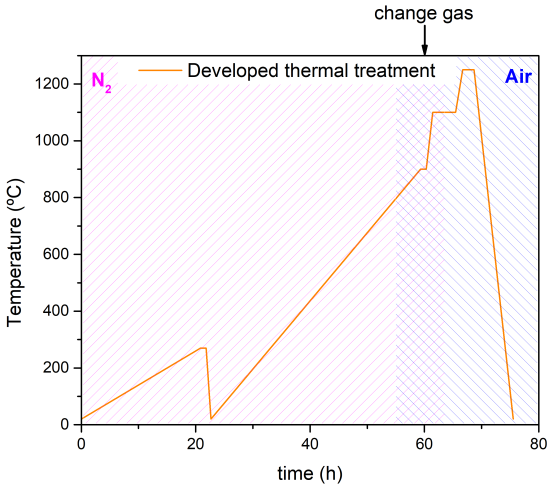

Figure 3.45: *Developed debinding and sintering cycle for the multi-material printed parts (SOC cells).*

Beyond the co-sintering of the whole cell, it is necessary to include the LCTM interconnect to generate single repeating units. As a first trial, LCTM was sintered by using the thermal treatment of choice for the cell, i.e. dwell of four hours at 1100°C and two hours at 1250°C. Figure 3.46 shows the SEM image of the LCTM layer on a complete cell after the thermal ramp. A high level of porosity is clearly observed indicating that further work is necessary to reduce the sintering temperature of the material. This problem was already anticipated after the dilatometry analysis (Figure 3.42). Now, the goal is to adjust the shrinkage curve of the LCTM to the one of our YSZ electrolyte. For reaching this reduction in the sintering temperature, two strategies are currently in progress (beyond the scope of this thesis), namely, i) the use of high energy milling for decreasing the crystallite size and modifying the particle size distribution of the initial powder; ii) the use of sintering aids.

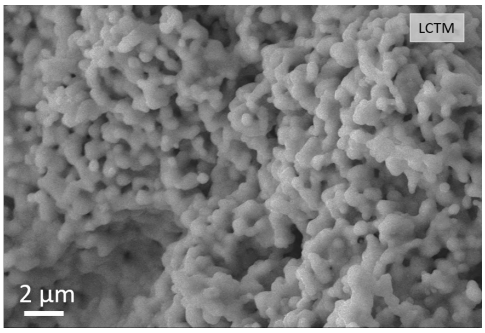

Figure 3.46: *SEM image of the interconnect sintered at 1250°C for two hours*

3.4 Microstructural and electrochemical characterization of optimized printed parts

Although different characterization of the parts was already presented in the previous sections to discuss the optimization of the printing and thermal steps, here we intend to briefly include the characterization of the optimized pieces. In particular, we will present the characterization of SLA printed parts made of alumina (Section 3.4.1) and 8YSZ (Section 3.4.2) and robocasted printed parts made of the materials of the electrodes and interconnect (Section 3.4.3). Further information, regarding the characterization of related devices (reactors or full cells) are discussed in the next chapters (Chapter 4 and 5).

3.4.1 SLA printed alumina parts

Structural analysis of the optimized SLA printed and sintered alumina parts has been carried out by X-Ray Diffraction. Figure 3.47 presents the diffractogram of alumina pieces. The patterns shows a single α-alumina phase without noticeable secondary phases. Since the alumina is going to be employed for the fabrication of catalytic reactors (in substitution of stainless steel), the presence of the alpha phase of the alumina is very convenient due to its excellent thermal properties and resonable performance as a catalytic support of the active phase. Although other oxides show better performance as supports (e.g. CeO_2 or γ-alumina) and a whole cover of the reactor is expected, some studies confirm the interest in the use of α-alumina as a bed [344], [367], [384].

Complementary to the structural analysis, Scanning Electron Microscopy has been used to study the microstructure and morphology of the sintered pieces. Top-view and cross-section images presented in Figure 3.48 show that full density was not achieved for the typical sintering temperatures (T=1550°C). This point is confirmed by density calculations carried out on well-shaped pieces (3.1 g/cm^3). This is mainly due to the maximum temperature reachable in our current facilities, namely, T=1550°C, which is below the required for full densification of alumina T=1700°C. Despite full density is not achieved, the sintered alumina keeps the full functionality for the purpose of this thesis. Moreover, a certain level of surface roughness is maintained at these temperatures, which is highly beneficial for the adhesion of the catalyst system.

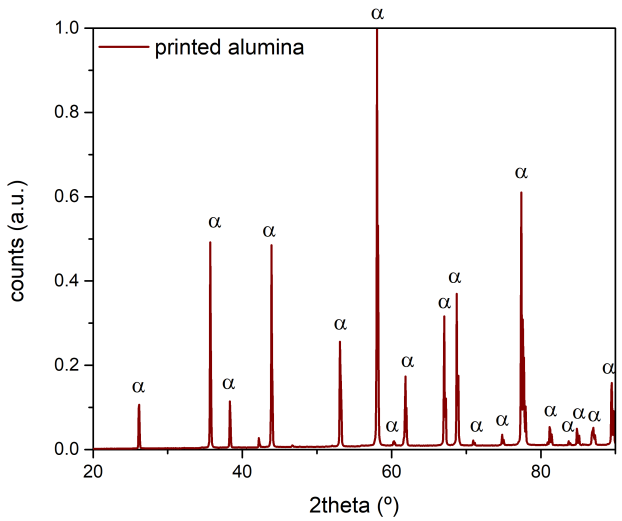

Figure 3.47: *XRD pattern of SLA printed and sintered piece of alumina. Reference pattern num. α-alumina: ICDD-01-081-2266.*

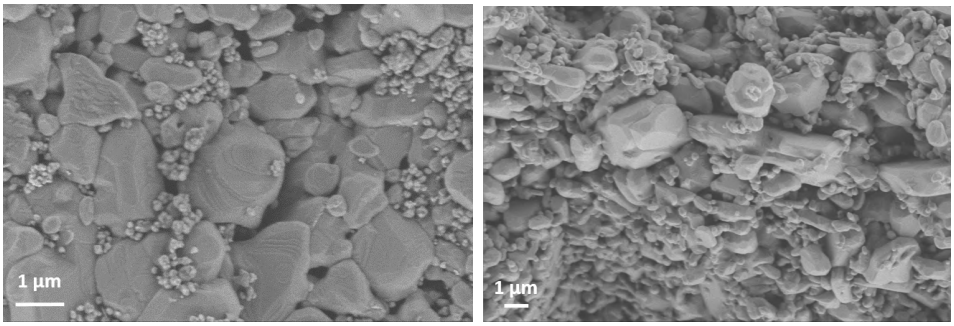

(a) Top view *(b) Cross section*

Figure 3.48: *SEM micrographies of printed pieces in alumina sintered at 1550°C for 90 minutes.*

3.4.2 SLA printed 8mol% yttria stabilized zirconia parts

Structural characterization of 8YSZ printed parts was carried out by XRD. From the diffractogram presented in Figure 3.49, it is possible to conclude that the phase of the sintered pieces can be ascribed to a cubic (reference pattern num.: ICDD-01-070-4436) or tetragonal zirconia (reference pattern num.: ICDD-01-070-4431). It is well known the difficulty to differentiate between tetragonal and cubic zirconia by means of X-Ray Diffraction. For

this reason, further studies by Raman spectroscopy were carried out. Nevertheless, importantly, the presence of deleterious monoclinic phase (see discussion in Section 3.3.1) can be discarded from the X-Rays difrattograms.

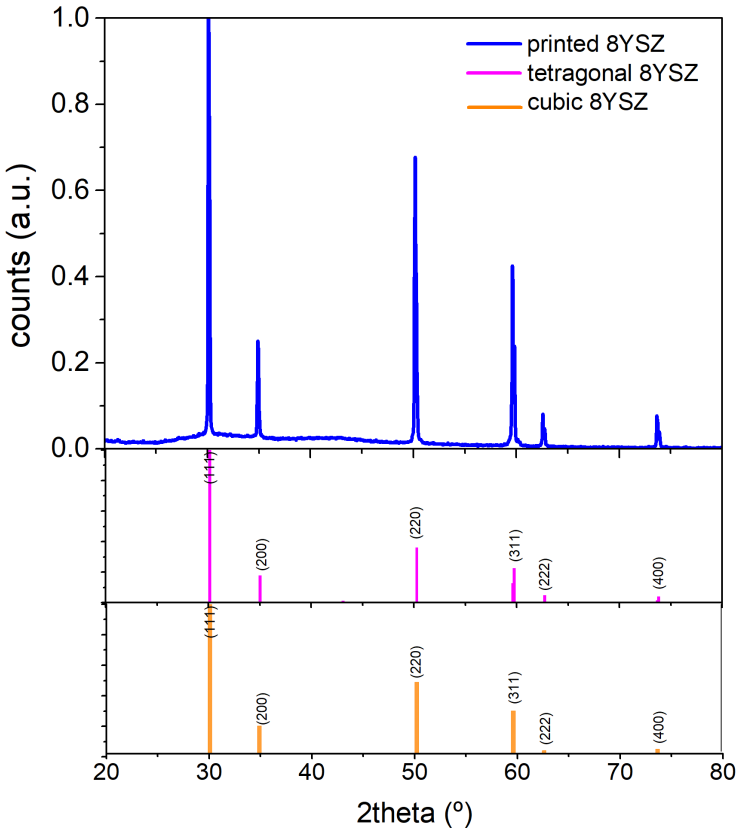

Figure 3.49: *XRD pattern of the printed and sintered 8YSZ pieces with reference patterns of tetragonal and cubic phases. Tetragonal reference pattern num.: ICDD-01-070-4431 and num.: ICDD-01-070-4436 for the cubic one.*

Figure 3.50 presents the Raman spectrum of the optimized YSZ pieces. The analysis reveals the co-existence of tetragonal, cubic and t" phases. The t"-phase presents almost the same lattice parameter compared with the cubic one, but oxygen displacement. All these phases present high ionic conductivity and, in any case, no detrimental monoclinic phase have been detected [353], [354].

Figure 3.51 show top-view and cross-section SEM images of the microstructure of the optimized 8YSZ pieces. From the pictures one can easily conclude that a full densification of the parts takes place for the thermal treatment of

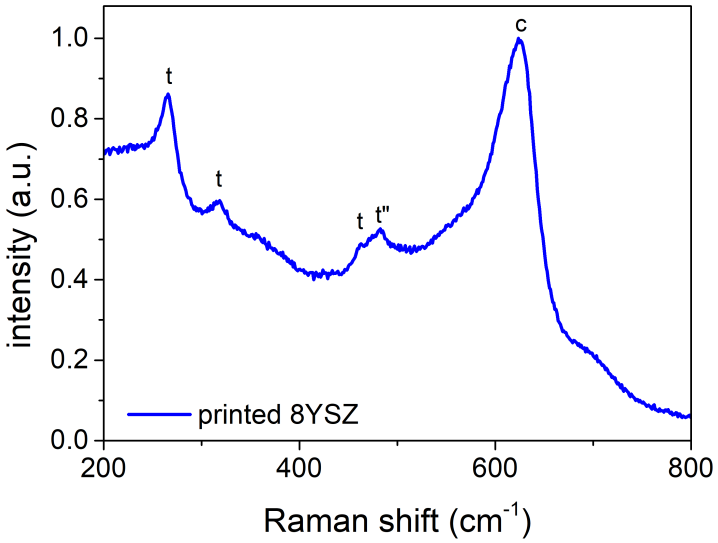

Figure 3.50: *Raman spectrum of the printed 8YSZ pieces with phase identification.*

choice. Well-defined grains of few micrometers in diameter are observed in the top view image. Moreover, the surface appears homogeneous and smooth with residual closed porosity (only visible in the cross-section pictures). Such a high density is remarkable since the sintering temperature employed in this work (T=1300°C) is far below typical values of 1450°-1500°C required for a full densification. This reduction in temperature was achieved by using highly reactive powder specifically designed for the Cell3Ditor project to enable the co-sintering of multi-layers at temperatures below 1300°C. Reaching a high density is required to avoid the diffusion of gases across the electrolyte in SOCs.

The ionic conductivity of the 8YSZ was also measured to evaluate the functionality of the printed pieces as electrolytes for SOCs. The conductivity is an intrinsic property of the material but, on practice, it depends on several factors such as the presence of secondary phases and impurities, the production route, the sintering temperature or the residual porosity [385]. Therefore, measuring the values for the optimized pieces and the comparison with reported values in the literature is important to confirm their suitability to be used as electrolytes. To perform such evaluation, we fabricated symmetrical cells based on printed and sintered round tapes of YSZ coverd by gold layers employed here as inert electrodes (see details in Figure 2.33b and Section 2.2). These cells were characterized by Electrochemical Impedance Spectroscopy in the range of temperature between 500°and 900°C, which is typically used for operation of 8YSZ ESCs. Figure 3.52 represents

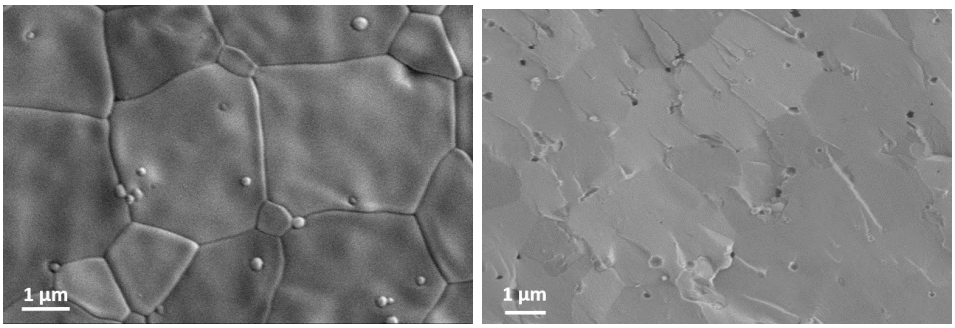

(a) Top view *(b) Cross section*

Figure 3.51: *SEM micrographies of printed pieces in 8YSZ.*

Nyquist plots of the impedance spectra obtained at different temperatures. The equivalent circuit models used to fit these spectra and determine relevant parameters such as the electrolyte conductivity are presented as insets of Figures 3.52a and 3.52b (points represent the experimental values, the continuous lines are the fitted ones). The arc at higher frequency is typically ascribed to the bulk YSZ (capacity around $10^{-12}\,\mathrm{F\,cm^{-1}}$), while the grain boundary contribution is associated to intermediate frequencies (capacity in the range $10^{-8}/10^{-11}\,\mathrm{F\,cm^{-1}}$). These two arcs are mainly visible at low temperatures (T<650°C in our case). Above this temperature, grain and grain boundary contributions become indistinguishable and were fitted as a single resistance. Even at lower frequency, the electrode contributions are observed (expected to be ion blocking in this case). From the fitting of the equivalent circuits we can calculate the ionic conductivity of the electrolyte, which is mainly related to the serial resistance of the cell by the following equation:

$$R = \frac{1}{\sigma}\frac{l}{S} \tag{3.2}$$

Where l is the thickness of the electrolyte and S the area of the electrodes. Figure 3.53 represents the calculated conductivity as a function of the inverse of temperature. The observed linear dependence confirms that the ionic conductivity of the sintered 8YSZ follows an Arrhenius behaviour, i.e. that the conductivity is a temperature activated phenomenon that obey the following equation [386]:

$$\sigma = \frac{\sigma_0}{T} e^{-\frac{E_a}{kT}} \tag{3.3}$$

where σ_0 is the pre-exponential factor, T is the temperature in Kelvin and k is the Boltzmann constant.

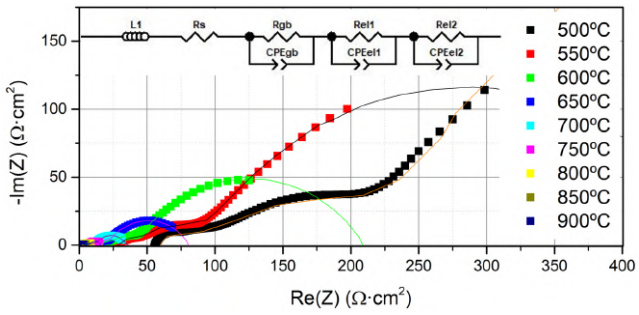

(a) Nyquist plot of the impedance in the range 500° - 900° C.

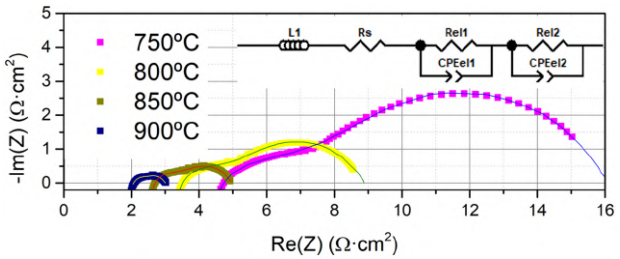

(b) Nyquist plot of the impedance in the range 700° - 900° C.

Figure 3.52: *Representation of the impedance of Au/8YSZ/Au cells over the range of temperatures between T=500° and 900° C. Inset: equivalent circuit used for the fitting of the Nyquist plots: Rs represents the ohmic resistance of the cell, ascribed to the electrolyte and current collection, while R_{gb} is the grain boundary contribution, R_{el1} and R_{el2} are the polarization resistances related with the electrodes.*

From the slope of this plot, it is possible to obtain the activation energy of the ion transport. The activation energy is estimated in Ea=1.01 eV, a value which is in good agreement with the ones typically reported in the literature, e.g. Ea=1.08 eV by *Ahamer et al.* [385].
In the same figure, the conductivities of an electrolyte produced at 1300°C and the one fabricated with the optimized thermal cycle employed for hybrid cells are reported (4 hours dwell at 1100°C, 2 hours at 1250°C). Both measurements are roughly equivalent confirming the suitability of the 8YSZ SLA printed and sintered parts for being used SOCs.

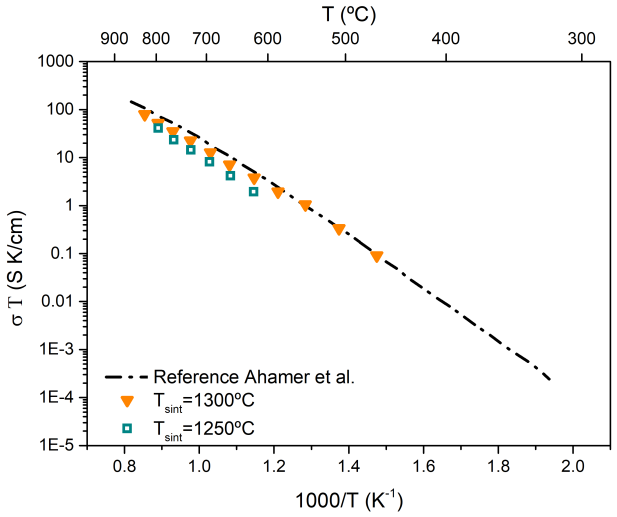

Figure 3.53: *Arrhenius behaviour of the ionic conductivity in function of the test temperature, compared with values reported in literature in ref. [385]*

3.4.3 Robocasted electrodes and interconnect material parts

Structural analysis of the sintered robocasted layers (printed in multi-material parts using the hybrid machine) were carried out by employing XRD. Figures 3.54, 3.55 and 3.56 include XRD patterns of the NiO-YSZ, LSM-YSZ and LCTM layers, respectively. These figures include original powder diffractograms for comparison.
In the case of the fuel electrode, NiO and YSZ single phases were indexed and no presence of secondary phases were detected (Figure 3.54).
Similarly, in the case of the air electrode, single phases of LSM and YSZ are indexed (Figure 3.55). Although the formation of lanthanum or strontium zirconates would be possible, the presence of these compounds was not noticeable.
Finally, for the XRD diffractogram acquired on LCTM layers, it is possible to index the reflections of the original powder but with additional contribution from the LSM-YSZ layer, reported in Figure 3.56. This diffactrogram appears more noisy compared to the other due to the roughness of the surface, in which YSZ powder from the powder bed during the thermal treatment remained trapped, generating additional peaks.

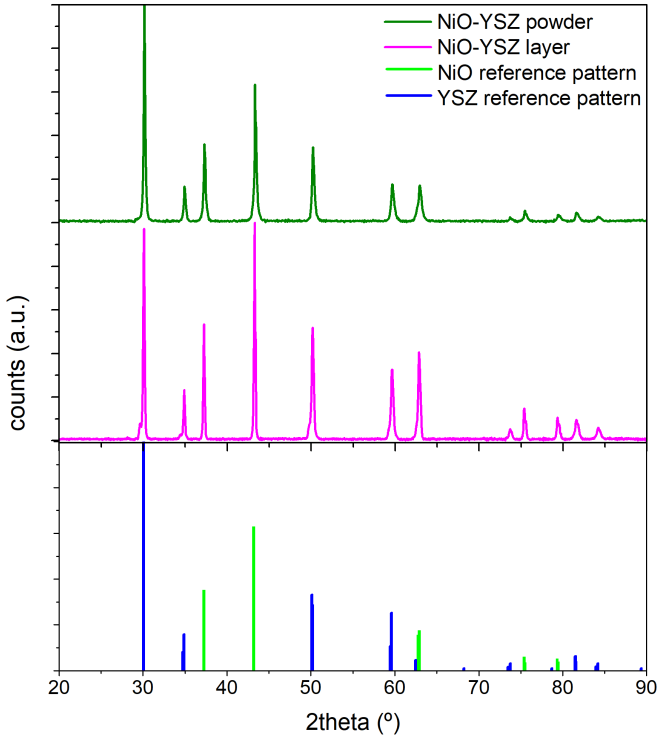

Figure 3.54: *XRD pattern of fuel electrode compared with starting powder, the peaks of the constituent materials are reported. NiO reference pattern num.: ICDD-03-065-6920, YSZ reference pattern num.: ICDD-01-070-4431*

The microstructure of the resulting electrodes were extensively discussed in Section (Section 3.3.2), in the frame of the optimization of the thermal process of the multi-material parts. Despite this and for the shake of completeness, we include here an extract of the Figure 3.44 including the SEM images of the layers subjected to the optimized thermal treatment (see Figure 3.57).
Due to the novelty of the technology and the trade-off required to obtain valid SOCs, these results are considered acceptable for the first obtained samples, but at the same time indicate the research lines to follow in the next studies.

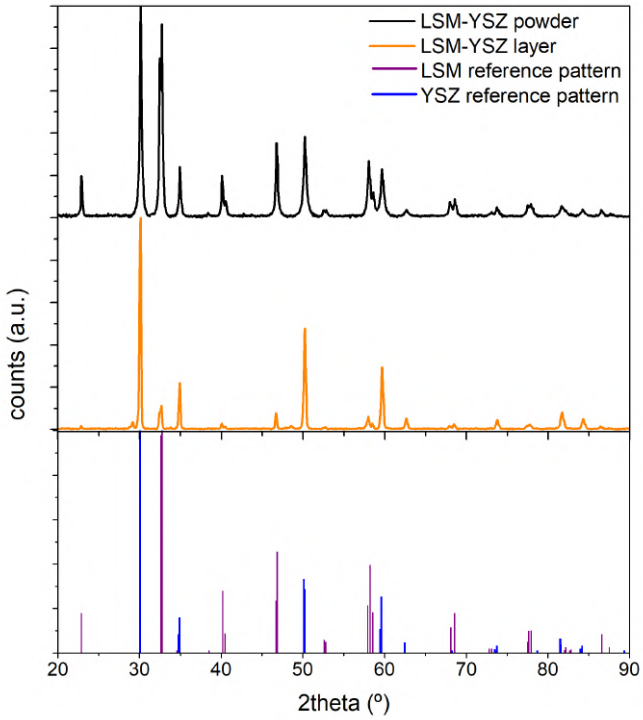

Figure 3.55: *XRD pattern of air electrode compared with starting powder, the peaks of the constituent materials are reported. LSM reference pattern num.: ICDD-01-089-0649, YSZ reference pattern num.: ICDD-01-070-4431.*

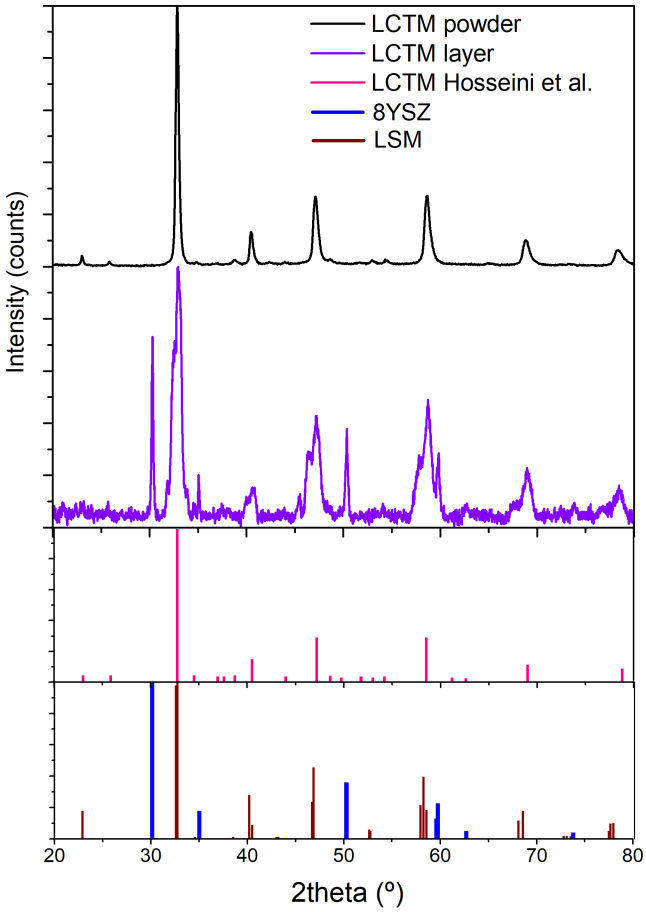

Figure 3.56: *XRD pattern of interconnect compared with starting powder and literature reference [320]. LSM reference pattern num.: ICDD-01-089-0649, YSZ reference pattern num.: ICDD-01-070-4431.*

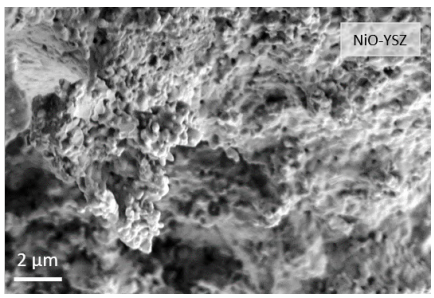

(a) Fuel electrode

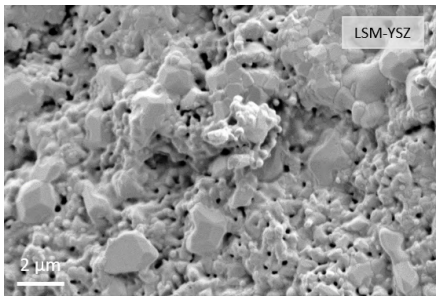

(b) Air electrode

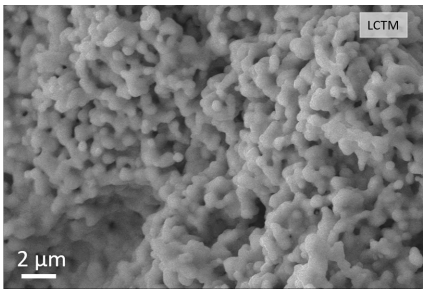

(c) Interconnect

Figure 3.57: *Microstructre of the robocasted layer subject to the optimized thermal treatment.*

3.5 Conclusion

The final goal of this chapter was the production of high quality mono-material and multi-material printed parts with a reliable materialization of the defined designs and properties close to the ones of the pieces produced by conventional technologies. For reaching this objective, we characterized printable feedstock for all the materials relevant for this thesis, namely, alumina, 8YSZ, and the developed one based on LSM-YSZ, NiO-YSZ and LCTM . Afterwards, relevant printing parameters were optimized to achieve a proper deposition of the materials and the required compatibility of SLA and robocasting methods in the hybrid printing of multi-material parts. In particular, laser milling and paste blowing methods were developed and optimized to allow embedding a material deposited by robocasting into a matrix of printed SLA. Finally, thermal treatments were designed and optimized with especial attention to co-sintering of multi-material parts.

In the particular case of 8YSZ, the SLA formulations and thermal treatments were developed by 3DCERAM under the frame of the Cell3Ditor EU project coordinated by IREC. In this thesis, we carried out the characterization of the final pieces proving that YSZ SLA-printed parts: i) reach high densities above 97% at temperatures below T=1300°C; ii) are in the form of highly conducting cubic and tetragonal zirconia phases and iii) present ionic conductivities as high as 3.0×10^{-2} S/cm^2 at 800°C. All these features prove the suitability of the obtained 8YSZ parts for being used as an electrolyte in SOC applications.

The development of the robocasting inks for completing the set of materials, the hybrid printing methods and the co-sintering treatments were entirely carried out at IREC. First, to reach printable inks different factors were investigated including the UV-Vis absorption of the materials, the rheological behaviour of the pastes and the thermal degradation of the materials. The high absorbance of some of the ceramic materials was identified as a critical issue since this absorption directly competes with the initiation of the polymerization phenomenon characteristic of the UV-curable inks. Photo-initiator contents of 3 wt.% were proved to be effective for curing in combination with a high energy dose provided by the laser. Regarding the rheology properties, a Newtonian behaviour of the organic compounds was ensured to allow a proper flow of the inks throught the printing needle.
The sintering has been optimized based on TGA and optical profilometry analyses, resulting in a thermal treatment suitable for co-sintering NiO-YSZ|YSZ|LSM-YSZ parts. The optimized treatement includes an intermediate step at 1100°C for 4 hours to reduce the densification of the electrodes and a final stage at the temperature of 1250°for 2 hours. The implementation of an inert atmosphere has shown to be a key factor for the proper debinding of the robocasting ink.

Overall, the foundings for a single-step printing and co-sintering of complete solid oxide cells were settled in this chapter. Moreover, the development of a methodology for hybrid printing of multi-material ceramic parts opens the way for further advances in this and related fields involving functional oxides.

Chapter 4

3D printing of Solid Oxide Cells

In this chapter, we present and discuss the performance of the Solid Oxide Cells 3D printed either by simple SLA (Electrolyte-Supported Cells, ESC) or hybrid SLA-Robocasting tecnology (Self-Supported Cells, SSC). In Section 4.1, electrolyte supported cells are analysed starting from the evaluation of the manufacturing process and the optimization of the functionalization with electrodes. Proved the suitability of the printed electrolyte and optimized the functionalization process, we proved the unfair advantages of 3D printing technologies in the manufacturing of electrolytes for SOCs. These electrolytes are characterized by innovative geometries, not achievable by traditional manufacturing techniques. We perform the electrochemical characterization as fuel and electrolysis cells, in this last case, the suitability for converting carbon dioxide (co-electrolysis) is also evaluated.
Section 4.2 presents the preliminary results for fully printed SOCs manufactured by hybrid printing technology. Structural, microstructural and electrochemical characterization of symmetrical cells (of both electrodes) and an entire fuel cell are presented.

4.1 Electrolyte Supported Cells by stereolithography

After proving the suitability of the printed YSZ parts for being used as electrolytes in SOCs (Section 3.4.2), this section is devoted to optimize the deposition of the electrodes and carry out the electrochemical characterization (including long term test). The final goal of this section is to straightforwardly evidence the advantage of 3D structured electrolytes fabricated by 3D printing instead of traditional manufacturing techniques.
The designs of choice, proposed in Section 2.2.1.1, were selected with the main aim to show a better electrochemical performance.

(a) Flat cell used

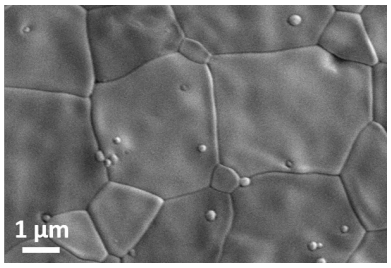

(b) Surface of the used cell

Figure 4.1: *Flat cell used for the optimization study, Figure 4.1a reports the picture of the cell, while Figure 4.1b reports the SEM image of the surface of the cell.*

4.1.1 Optimization of 3D printed Electrolyte Supported Cells with flat geometry

Once we have demonstrated the suitability of the printed pieces as supporting electrolyte (Section 3.4.2), we need to introduce both fuel and oxygen electrodes in order to have functional cells. As described in Section 2.2.1.2, the used electrodes are based on Ni-YSZ and LSM-YSZ deposited on the sintered electrolyte produced by 3D printing. In order to have an optimum performance, it is of major importance to generate good electrodes and electrode/electrolyte interfaces. This section is devoted to the optimization of the electrode deposition and their attachment to the electrolyte support. In order to carry out this characterization flat 3D printed electrolytes, as the one shown in Figure 4.1 were employed. Finally, fuel cell measurements of the optimized cells will be presented.

4.1.1.1 Optimization of the attachment temperature of the electrodes

As the attachment of the electrode to the electrolyte is produced by high temperature, it is necessary to optimize the attachment temperature (for each individual electrode). As a parameter of optimization, we employed the serial and polarization resistances obtained for symmetrical cells. Therefore, symmetrical cells of Ni-YSZ|8YSZ|Ni-YSZ and LSM-YSZ|8YSZ|LSM-YSZ have been produced and characterized by Electrochemical Impedance Spectroscopy (EIS) between 750°C and 900°C. The attachment temperatures were chosen according to typical values reported in literature and previous experience from our research group, namely, for the fuel electrode T_{att}= 1400°C, 1450°C and 1500°C and for the air electrode T_{att}= 1200°C, 1250°C and 1300°C.

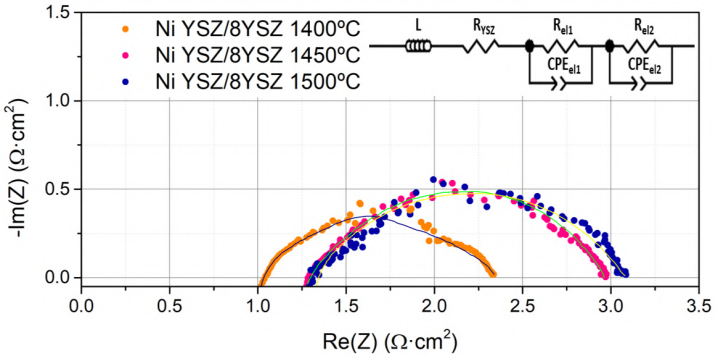

Figure 4.2: *Nyquist plots of the measurements at 850° C under pure H_2 for the attachment optimization of the fuel electrode. In the inset, the equivalent circuit used for the fitting (continuous lines of the graphs) of the elements.*

Figure 4.2 represents Nyquist plots of the obtained impedance at 850°C under hydrogen atmosphere for the Ni-YSZ|YSZ symmetrical cells fabricated employing the three temperatures under investigation. It can be observed directly from the graph that the resistance of the samples increases with the attachment temperature. By simple analysis, it can be easily concluded that the minimization of the resistance (both the serial and polarization) is obtained for the sample calcined at 1400°C.
This conclusion is confirmed by a deeper analysis presented in Figure 4.3, where the fitted value of polarization resistance (obtained by employing the equivalent circuit inserted in Figure 4.2) is reported as a function of the test temperature for the different samples. As a general trend, the resistance increases at the decreasing of the test temperature, due to lower conductivity of the materials.

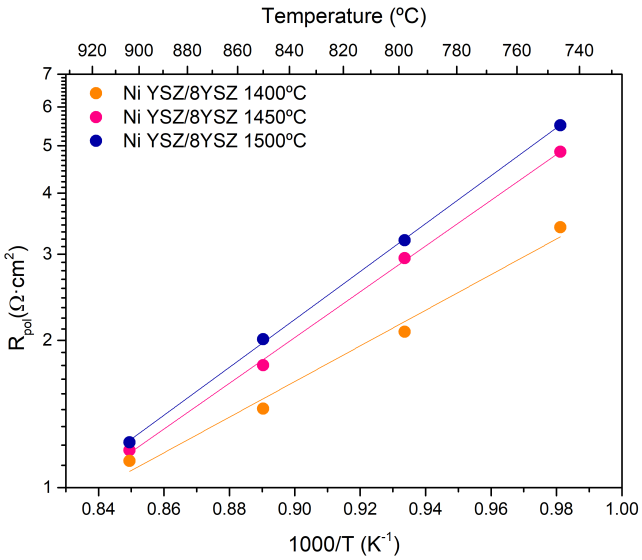

Figure 4.3: *Polarization resistance as a function of the temperature (for the attachment optimization of the fuel electrode).*

The same optimization was realized with symmetrical cells based on air electrodes. In this case, the chosen attachment temperatures were T_{att}= 1200°C, 1250°C and 1300°C.

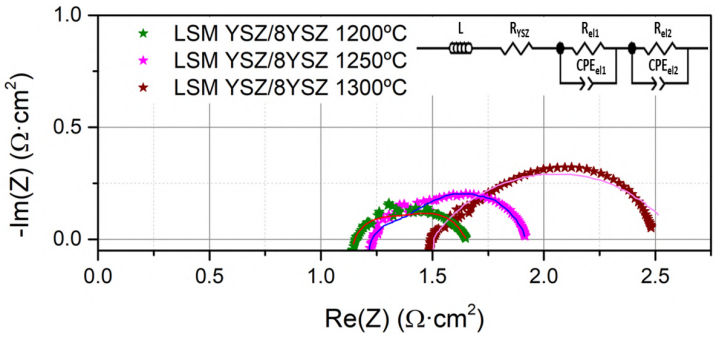

Figure 4.4: *Nyquist plots of the measurements at 850°C under synthetic air for the attachment optimization of the air electrode, in the inset, the equivalent circuit used for the fitting (continuous lines of the graphs) of the elements.*

Representative Nyquist plots recorded at 850°C are reported in Figure 4.4. It is also clear, from this representation, how both the serial and po-

larization resistances decrease with the decreasing of the attachment temperature. The behaviour of the resistance with the attachment temperature is confirmed plotting the numerical values obtained by the fitting, as it is reported in Figure 4.5. The polarization resistance shows lower values for the sample fired at 1200°C, being this the chosen temperature for the attachment in the future tests.

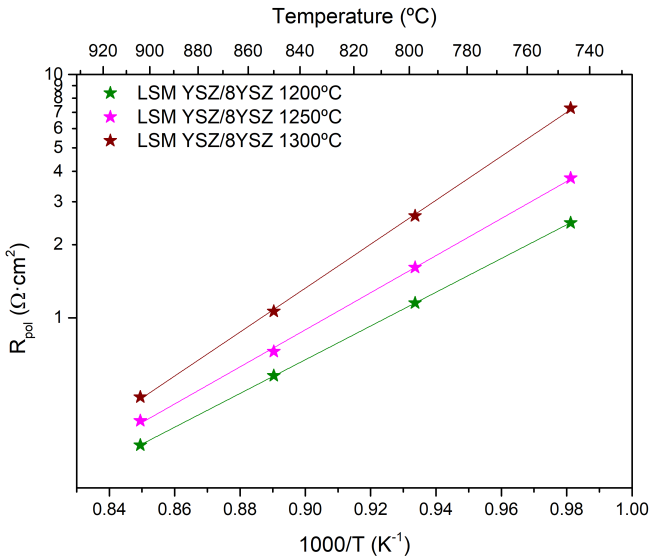

Figure 4.5: *Polarization resistance as a function of the temperature for the attachment optimization of the air electrode.*

4.1.1.2 Improvement of the attachment of the electrodes

While the optimum temperature attachment has been determined, the total resistances of the cells are still higher than the typical targets (i.e. between $0.25\,\Omega \cdot \mathrm{cm}^2$ and $1.0\,\Omega \cdot \mathrm{cm}^2$ at the working temperature [20]). A potential reason for this can be related to attachment issues associate with a flat surface, as the one expected for sintered YSZ produced by SLA (as typically observed for tape casted electrolytes). Microstructural analysis by SEM showed substantial delamination of the layers then supporting this hypothesis (see Figure 4.6). In the case of the fuel electrode (Figure 4.6a), a certain lack of adhesion is observed. However, the effect is more severe in the air electrode (Figure 4.6b), where areas with complete detached layers are present.

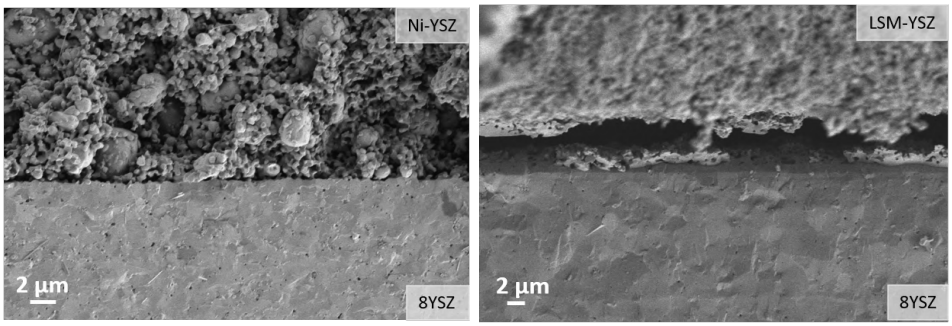

(a) Cross section of the fuel electrode/electrolyte interface

(b) Cross section of the oxygen electrode/electrolyte interface

Figure 4.6: *SEM images of the electrodes/electrolyte interface in the cell used or the preliminary study.*

In order to overcome this issue, further improvements are pursued in the electrode/electrolyte interfaces by the introduction of an intermediate layer that, eventually, could improve the attachment. The goal of including this layer is similar to the effect reached by *Murray et al.* by grinding the electrolyte surface with abrasive paper to improve the adhesion [387]. We deposited 8mol% yttria stabilized zirconia layers by powder wet deposition, as described in Section 2.2.1.2, with the aim of creating a certain level of roughness at the surface. After deposition by spray and thermal treatment at T=1150°C, the effect on the electrochemical performance in full cells has been evaluated. Figure 4.7 shows top-view SEM images of the printed electrolytes without (Figure 4.7a) and with (Figure 4.7b) adhesion layer. SEM micrographs clearly show how the roughness increases.

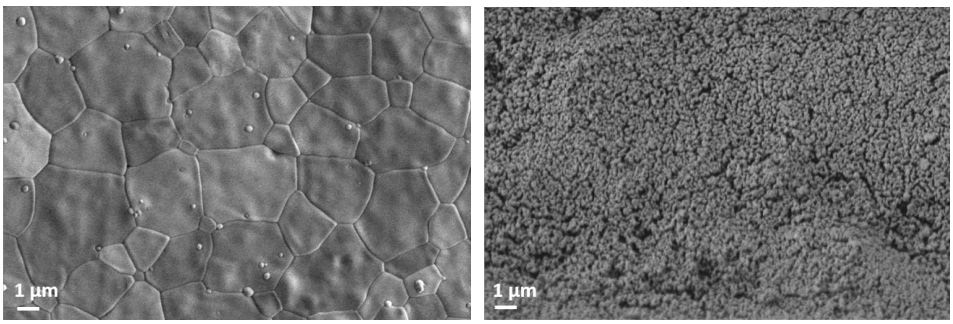

(a) Surface of sintered electrolyte

(b) Surface of sintered electrolyte with adhesion layer sintered at 1150° C

Figure 4.7: *SEM migrograpies of 8YSZ electrolyte surfaces with and without adhesion layer*

The positive effect on the attachment of the electrodes is reported in Figure 4.8, where is clearly visible the improvement in the attachment of the electrodes. Comparing the interfaces with Figure 4.6, the fuel electrode shows more point of contacts with the electrolyte, the air electrode benefits more from this layer, achieving a proper attachment of the electrode where before complete delamination was present.

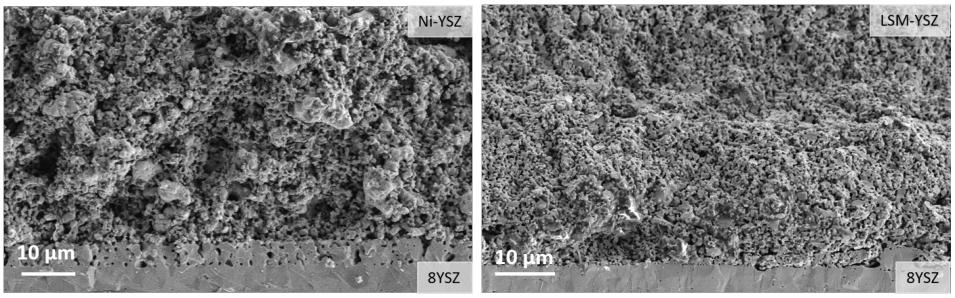

(a) Cross section at the fuel electrode/electrolyte interface

(b) Cross section at the air electrode/electrolyte interface

Figure 4.8: *SEM migrograpies of the interfaces electrode/electrolyte applying the adhesion layer.*

The clear improvement in the adhesion of the electrodes after including this intermediate layer (as shown in the SEM pictures) resulted in a great improvement of the electrochemical properties. As a preliminary test, we fabricated equivalent 3D printed flat cells with and without the adhesion layer. Both cells where fabricated following the procedure detailed in section 2.2.1.2. Electrolyte Supported Cells of Ni-YSZ|YSZ|LSM-YSZ with 250 µm in thickness were measured at 850°C under hydrogen and air atmospheres. Figure 4.9 shows V-j curves of both cells. The results show a remarkable increase in the maximum power density from $50\,\mathrm{mW/cm^2}$ to $195\,\mathrm{mW/cm^2}$, when employing the adhesion layer.

EIS was also carried out resulting in ASR values of ASR= $5.0\,\Omega \cdot \mathrm{cm^2}$ and $1.5\,\Omega \cdot \mathrm{cm^2}$ at 850°C for the cells without and with roughness layer, respectively (see Figure 4.10). From the Nyquist plots is evident the source of the improvement detected in the V-j curves. The serial resistance is halved with the use of the attachment layer, indicating how the complete delamination is no longer present in the cell. The value of the polarization resistance decreases as well, pointing out the efficiency of the adhesion layer on the attachment.

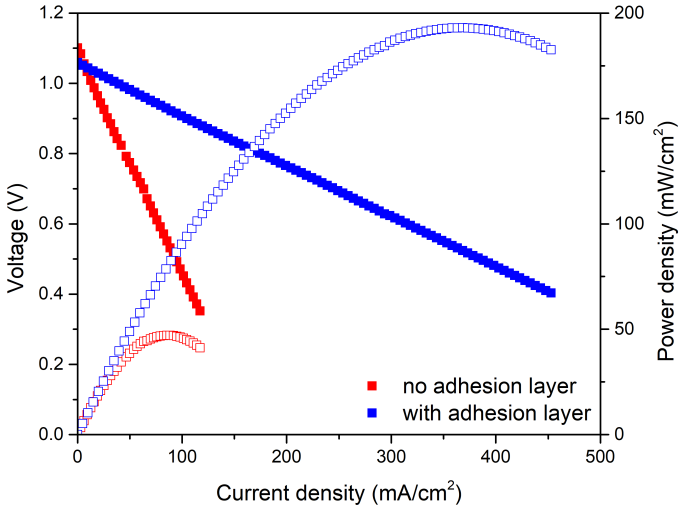

Figure 4.9: *Comparison between the two V-j curves of fuel cells based on printed electrolytes in planar design, with, in blue, and without, in red, adhesion layer (T=850° C, pure H_2 and synthetic air atmospheres).*

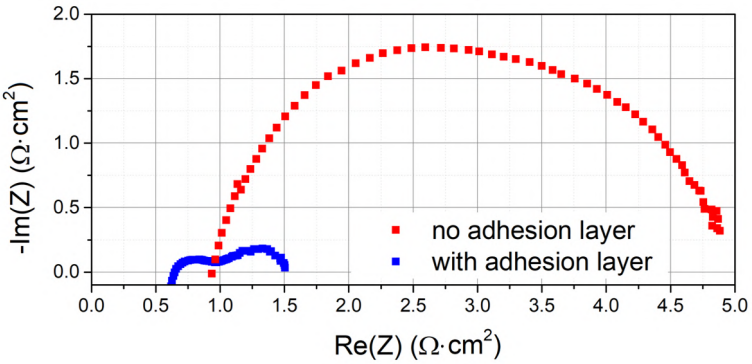

Figure 4.10: *Comparison between the impedance spectra of fuel cells based on printed electrolytes in planar design, with, in blue, and without, in red, adhesion layer (T=850° C, pure H_2 and synthetic air atmospheres, operating condition V=0.7 V).*

The value of the cell with intermediate layer is comparable with the ones reported in the literature for similar kind of cells from reference technology at DTU ($1.1\,\Omega \cdot \mathrm{cm}^2$ at 850°C), Jülich ($1.2\,\Omega \cdot \mathrm{cm}^2$ at 800°C) or Westinghouse ($1.0\,\Omega \cdot \mathrm{cm}^2$ at 900°C) [388]. Therefore it is possible to conclude that the 3D printed cells are within the standards of the technology in flat form.

4.1.2 Enhanced cells by 3D structuration of the electrolyte

The previous section was devoted to improve the fabrication of 3D printed electrolyte supported cells with simple (flat) geometries showing a cell performance comparable with similar cells reported in the literature. These developments gave a robust base for further implementation of improvement strategies only accessible by 3D printing methods.
Beyond reproducing cells fabricated with conventional techniques, the main advantage of 3D printing is to manufacture 3D-structured cells which are costly, or simply impossible to reach, using traditional manufacturing.

Focusing on the development of 3D-structured electrolytes of yttria stabilized zirconia (presened in Section 2.2.1.1), our group employed 3mol% and 8mol% YSZ slurries and SLA printing to fabricate advanced ESCs. Following a preliminary study carried out in the group [267], a first generation of cells based on 3YSZ electrolytes was fabricated and fully characterized. In this thesis, equivalent flat designs were fabricated with 8YSZ (with higher ionic conductivity than 3YSZ). Figure 4.11 reports the comparison of the V-j curve of planar full cells printed with 3- and 8-YSZ (with the very same thickness of 250 µm and analogous deposited electrodes).

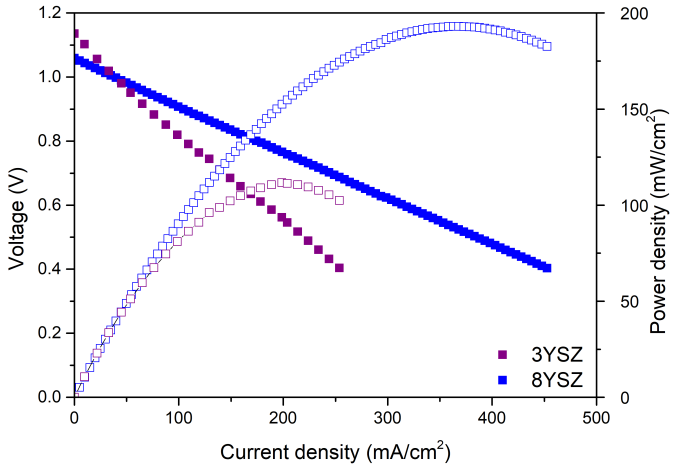

Figure 4.11: *V-j curves of ECSs based on planar SLA printed electrolytes (*250 µm *in thickness) for 3mol% and 8mol% yttria stabilized zirconia (T=850° C and pure H_2 and synthetic air atmospheres).*

As a matter of fact, the use of 8YSZ substantially improved the whole performance of the cells showing and increase of 55% in the maximum power

at 850°C, which roughly corresponds to the expected reduction in the resistance associated to the electrolyte (ASR=2.8 $\Omega \cdot cm^2$ and ASR=1.5 $\Omega \cdot cm^2$ for 3YSZ and 8YSZ, respectively). Therefore, 8YSZ was the choice for developing the rest of the structured electrolytes of the thesis. Beyond this first result, full structural and electrochemical characterization of the flat 8YSZ ESC is presented in the next section.

4.1.2.1 3D-structured electrolytes for ESCs: design and fabrication

Different 3D-structured electrolytes were proposed in Section 2.2.1.1. The printed electrolytes with a sufficient robustness were the planar, the hexagonal, the corrugated and the square. Figure 4.12 shows the chosen designs for 2 cm-diameter cells with a real area of 2.00, 2.40, 3.15 and 3.12 cm^2, respectively.

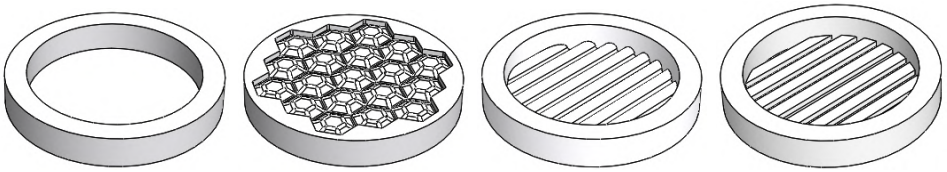

(a) Planar cell (Pl), 2.00 cm^2 | *(b) Hexagonal cell (Hex),* 2.40 cm^2 | *(c) Corrugated cell (Corr),* 3.15 cm^2 | *(d) Square aligned cell (SA),* 3.12 cm^2

Figure 4.12: *Best candidate for the electrochemical characterization.*

It is important to realize that, in case of the planar and corrugated designs, the thickness of 250 µm is homogeneous over the entire electrolyte and all the area of the cell contribute in the same way to the performance. However, other designs that present thicker and thinner parts will present different serial resistance associated to different parts of the electrolyte, which could make the performance enhancement not directly proportional to the increase in area. This aspect will be very important for the interpretation of the performance enhancement (see Section 4.1.2.2).
Regarding the morphological characterization of the proposed 3D-structured electrolytes, Figures 4.13, 4.14, 4.15 and 4.17 show cross section images of the fabricated designs. Figure 4.13a shows a detail of the cross section of the CAD design of a planar electrolyte and the related optical and SEM images of the fabricated cell (Figures 4.13b and 4.13c). In this design, the active area is straightforwardly the area covered by the electrodes, i.e. 2.00 cm^2.

The corrugated cell (Figure 4.14) presents a 57% increase of area up to 3.15 cm^2. As shown in Figure 4.14 and previously mentioned, the thickness

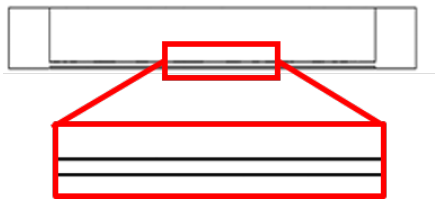

(a) Cross section of the planar design

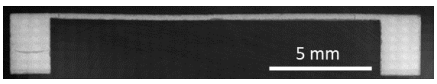

(b) Optical image of the cross section

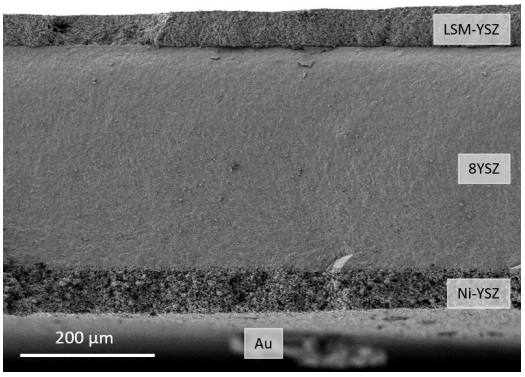

(c) SEM cross section of the planar design

Figure 4.13: *Cross section of planar cell.*

in the corrugated cell is constant over the entire electrolyte. The composed optical cross-section of the whole cells show a great homogeneity and lack of substantial bending for planar and corrugated cells (Figures 4.13 and 4.14).

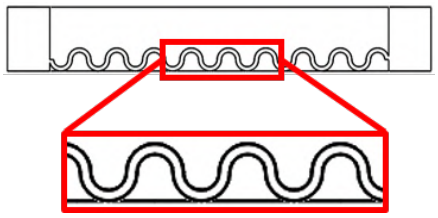

(a) Cross section of the corrugated design

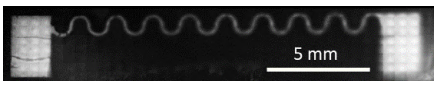

(b) Optical image of the cross section

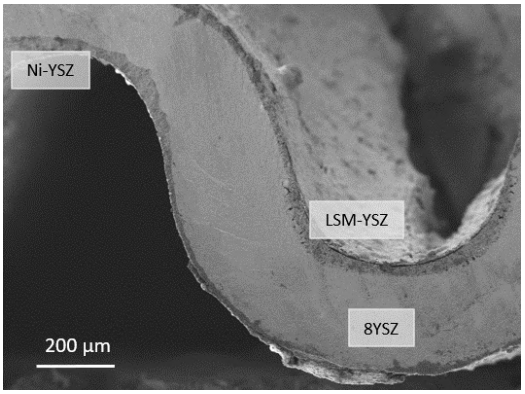

(c) SEM cross section of the corrugated design

Figure 4.14: *Cross section of corrugated cell.*

Different cases are the hexagonal and square aligned designs, since, by definition, these electrolytes present non-homogeneous thickness over the membrane, which will partially hinder the utilization of the whole area due to favourable oxygen conduction pathways in the thinner parts. In case of the hexagonal cell, the nerves which connect the faces of the structure, are thicker than the membrane, as it can be seen in Figure 4.15. Despite a certain loss of performance, this solution enable better mechanical behaviour of the membrane due to the nerve patterns, which can be used to produce

thinner membranes (out of the nerves) or give more sustain to larger structures (big area cells).

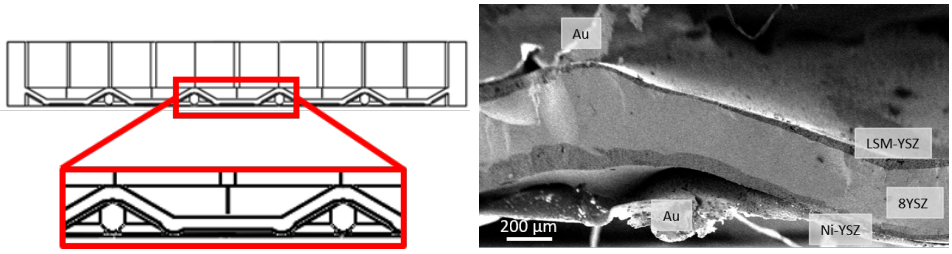

(a) Cross section of the hexagonal design

(b) SEM cross section of the hexagonal design

Figure 4.15: *Cross section of hexagonal cell.*

A deeper study of the profile used to design the electrolyte is necessary to a proper evaluation of the final performance of the cell. As it is pointed out by the sketch of Figure 4.16, the faces present a thickness of 250 µm, while the nerves, a maximum of 300 µm. The area corresponding to a homogeneous thickness is 2.20 cm^2, while the remaining (0.20 cm^2) presents a variable thickness due to the radius of the nerves.

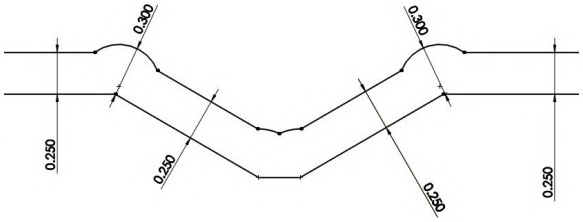

Figure 4.16: *Sketch used for the design of the hexagonal electrolytes.*

The square aligned corrugation presents as well a non-uniform thickness of the electrolyte. While for the wave one the change between a valley and a hill is smooth, in case of the square one it follows sharp edges, as can be seen in Figure 4.17. The drawing of the piece is built on extrusion in one direction of the profile presented in Figure 4.18. The conduction is supposed to happen easily in the walls of 250 µm, which represent an active area of 2.10 cm^2. While around 1.02 cm^2 of the electrolyte present a thickness between 250 µm and 355 µm.

The expected performances of these cells with non-homogeneous thickness have been evaluated based on geometrical calculation. The power density at a given potential (E_0) is correlated to the one of a planar cell already

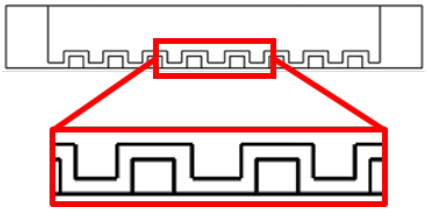

(a) Cross section of the square aligned design

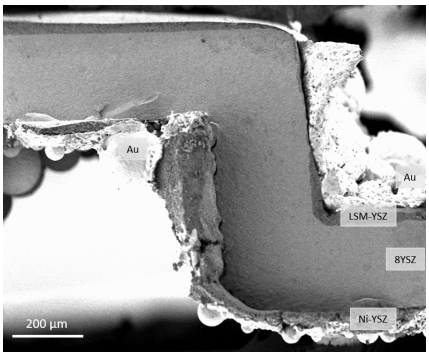

(b) SEM cross section of the square aligned design

Figure 4.17: *Cross section of square aligned cell.*

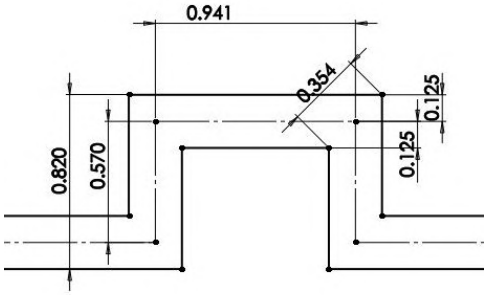

Figure 4.18: *Sketch used for the design of the square aligned corrugated electrolytes*

characterized (P_1), considering each part of the electrolyte with its proper area (A_i) and thickness (t_i):

$$P_t(E_0) = P_1 \left(1 + \sum_{i=1}^{n} \frac{t_1}{A_1} \frac{A_i}{t_i}\right) \tag{4.1}$$

4.1.2.2 3D-structured electrolyte ESCs: performance

The electrolytes were functionalized with the deposition of an adhesion layer and NiO-YSZ and LSM-YSZ electrodes as described in Section 2.2.1.2 and 4.1.1. The obtained Solid Oxide Cells were test in the high temperature set-up described in Section 2.4.1 and characterized following the protocol described in Section 2.4.2 and 2.4.3. The OCV was measured over the reduction time, to detect leakages in the cell or in the sealing. Values above 1.1 V (at 900°C) were considered proof of a good sealing, cells with values below

1.0 V were discarded considering the leakage too important to get a good measurement. We realized polarization curves to evaluate the performance of the cell, high current indicates an higher maximum power and a better performance of the cell.

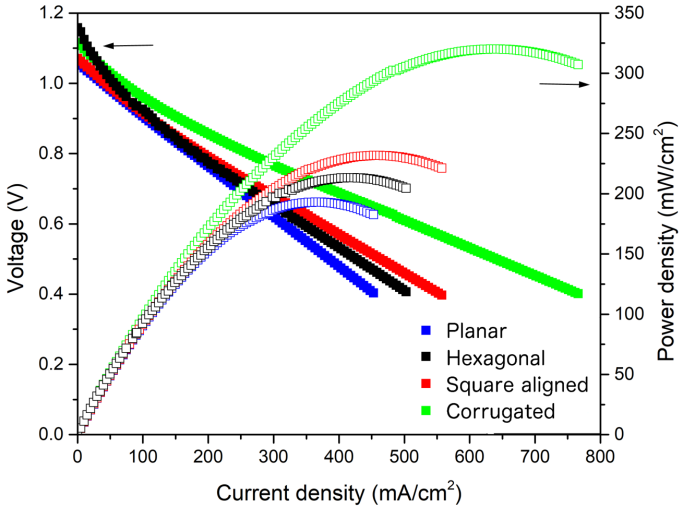

Figure 4.19: *V-j curves of cells based on the most promising designs, tested at 850°C, pure H_2 and synthetic air atmospheres. Solid points represent the voltage (left axis) and the open ones the power density (right axis).*

Figure 4.19 reports the obtained results for the different types of cell at 850°C under pure hydrogen and synthetic air atmospheres. The planar cell is used as reference since it was proven to be comparable to ones produced by traditional manufacturing techniques. All the structured cells present an improved compared with the planar one (numerical values are reported in Table 4.1 and compared with the calculated value from the model reported in Equation 4.1). The hexagonal cell presents an improvement in performance of 11% (maximum output power increasing from 195 mW/cm^2 to 216 mW/cm^2). Although the total area is 2.40 cm^2, we have already discussed in the previous section, that the homogeneous path of 250 µm is obtained over an area of 2.20 cm^2. The thicker area contributes to the conduction as well, although offering more resistance.
In case of the square aligned electrolyte, the resulting cell shows an enhance around 21% (maximum power of 235 mW/cm^2) compared with the planar one. In this case the calculated area with a thickness of the electrolyte of 250 µm is 2.10 cm^2, while the calculated improvement is around 40%, taking into account areas with more resistive behaviour. The experimental data

confirm that the enlargement of the interface area has more advantages than the disadvantage on the ohmic losses and overpotential [389], [390].
For these two designs, the difference between calculated and experimental power density may be due to the presence of corners and consequently increase in the area in different position for the two electrodes.
Finally, the corrugated cell achieved a maximum power of 315 mW/cm^2 (which is as well the maximum power achieved), which corresponds to 60% increase compared to the planar one. This increase agrees with the increase of the area, which was 57%. As expected, and opposite to the previous hexagonal and squared designs, the corrugated cell keeps the positive advantage of enlargement of the area all along the cell (due to a constant thickness over the electrolyte). Since high outputs were obtained, a detailed analysis of the performance of the corrugated cell has been carried out to extend the obtained results in different temperatures, operation modes and in the long term. These results will be presented in the following sections.

Type of cell	**Max power**	**Max power cell/planar**	**Expected improvement cell/planar (model)**
Planar	195	1	1
Hexagonal	216	1.11	1.18
Square aligned	235	1.21	1.41
Corrugated	315	1.6	1.57

Table 4.1: *Maximum power of the different types of cell, compared with the expected values calculated with Equation 4.1.*

4.1.3 Enhanced cells based on corrugated electrolytes

The cell based on an electrolyte with a corrugation based on the wave profile has been chosen for deeper electrochemical analysis due to the homogeneous resistive behaviour over the entire designed area. Since the thickness is constant, all the area is active for the ion conduction, being the highest value (3.15 cm^2) of the proposed designs.

4.1.3.1 Performance in SOFC, SOEC and co-SOEC mode

The performance of the planar and corrugated LSM-YSZ|YSZ|Ni-YSZ solid oxide fuel cells was evaluated by measuring polarization curves under pure hydrogen (fuel electrode) and synthetic air (oxygen electrode) atmospheres in the temperature range between 800°C and 900°C. Figure 4.20 shows the

V-j polarization curves of both cells measured at 900°C (results obtained at 800°C and 850°C present similar behaviour and are not reported here). Open Circuit Voltages (OCVs) close to 1.10 V were measured for both cells, which is in good agreement with the expected values estimated by the Nernst law, confirming the gas tightness of the printed electrolytes (planar and corrugated) and the high quality of the measurement. The maximum power density (P_{max}=V·j) obtained at 900°C for the planar cell reaches P_{pl}=260 mW/cm^2, which is slightly above similar cells produced with conventional techniques compiled in reference [391]. More interestingly, the corrugated cell design presents P_{corr}=410 mW/cm^2, which corresponds to an increase of 57% in power compared to the planar. This improvement, which is roughly maintained all along the whole range of tested temperatures, is likely associated to the increase of the active area of the corrugated cell fixed by design, i.e. A_{corr}/A_{pl}=1.57.

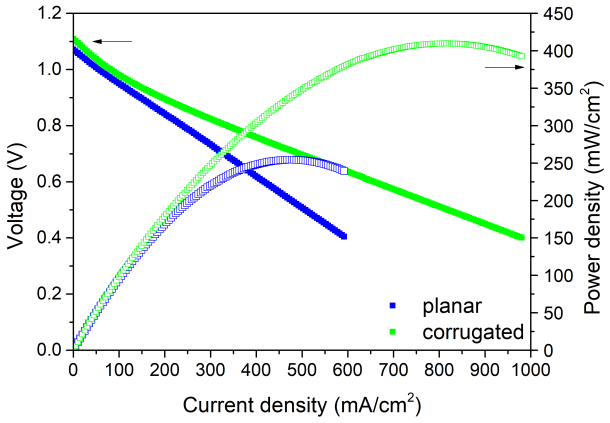

Figure 4.20: *V-j curves in SOFC mode at 900°C, solid points represent the voltage (left axis) and the open ones the power density (right axis).*

In order to clearly split the different contributions to the total polarization resistance of the cells and, therefore, identify the origin of this enhancement, Electrochemical Impedance Spectroscopy (EIS) measurements were carried out for both cells (Figure 4.21). These different contributions can be obtained by deconvoluting the obtained spectra using a simple equivalent circuit consisting of an inductance (L) in series with a resistance (R_{YSZ}) and two ZARC elements (see insert Figure 4.21). The serial resistance (R_{YSZ}) can be mainly associated to the 8YSZ electrolyte while the addition of the resistance of the two ZARC elements (R_{el}=R_{el1}+R_{el2}) corresponds to the electrodes. Table 4.2 compiles all the resistances obtained by fitting the spectra in the form of Area Specific Resistances, where the considered area

is the projected area of the cell).

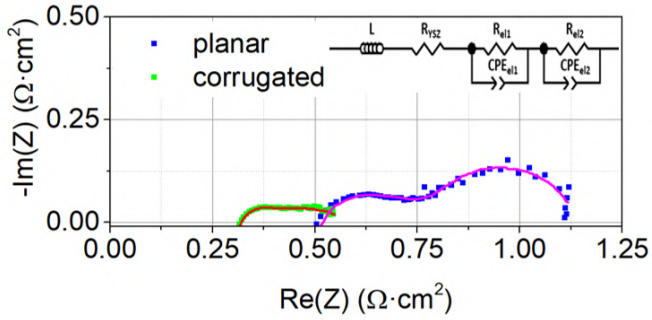

Figure 4.21: *Nyquist plots of the electrochemical impedance at 900°C in SOFC mode at operative condition (V=0.7 V), solid points represent the measured values and lines the fitted curves with the equivalent circuit presented in the inset.*

Therefore, one can clearly conclude that the increase of area by corrugation has an equivalent positive impact in both the electrolyte and the electrodes, which indicates that all the dominating phenomena are directly proportional to the area as theorized by other studies [330], [331], [392] (the same behaviour, with small variations in absolute values is maintained in all the temperature range).

In order to study the reversibility of the printed cells, the planar and corrugated LSM-YSZ|YSZ|Ni-YSZ printed cells were evaluated in electrolysis and co-electrolysis mode. In the first case the cell is converting steam into oxygen and hydrogen, while a polarization in forced, in the last one it is converting a combination of steam and CO_2 into syngas (CO and hydrogen) by current injection. Characteristic potentiostatic V-j curves are reported in Figure 4.22. Similar OCV values (OCV$\sim$ 0.8V) were observed for both cells corresponding to the expected voltages for the specific combination of input gases. Although in these cases it is not possible to determine a maximum performance (like the maximum power density calculated in SOFC), it is clear from the different slopes in the V-j curves that the corrugated cell significantly improves the behaviour of the planar one, although it shows a noisy measurements due to water supply issues. In case of co-SOEC the presence of CO_2 facilitate the transport of steam to the reaction sites, reducing the noise.
In these cases the performance are evaluated comparing the injected current (or the amount of compound produced) at a fixed value, chosen to be 1.3 V, usually in the linear trend of the curve, to avoid activation and diffusion

effects. The corrugation of the electrolyte improves the performance in electrolysis modes as well as in fuel mode. The wave corrugated cell shows an injected current of $500\,\mathrm{mA/cm^2}$ ($3.14\,\mathrm{ml/cm^2 \cdot min}$ of produced hydrogen), improving the achieved value for the planar one, $405\,\mathrm{mA/cm^2}$ (corresponding to $2.85\,\mathrm{ml/cm^2 \cdot min}$ of H_2). For co-electrolysis a typical operation voltage of V=1.3 V is considered as well, showing an improvement in the injection of a current density of $600\,\mathrm{mA/cm^2}$ in the corrugated cell compared to $460\,\mathrm{mA/cm^2}$ available in the planar cell, i.e. corresponding to a 30% of enhancement.

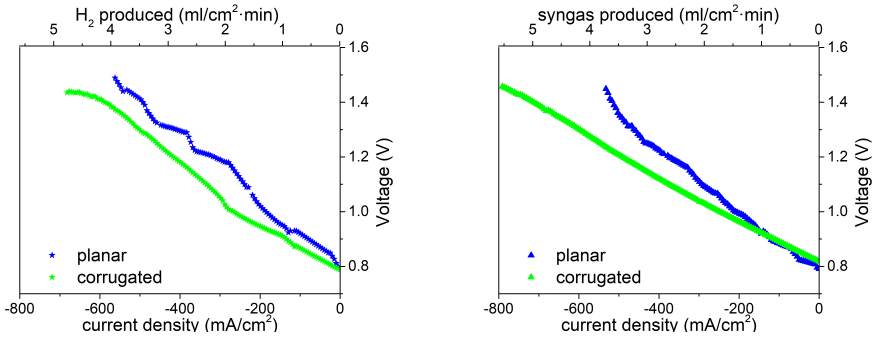

(a) V-j curves at 900° C in SOEC mode *(b) V-j curves at 900° C in co-SOEC mode*

Figure 4.22: *V-j curves at 900° C in electrolysis and co-electrolysis mode.*

To clarify if the observed improvement correlates well with the increase in area of the corrugated cell, impedance spectroscopy analyses were carried out in a similar way as for the fuel cell mode (Figure 4.23). ASR values for the serial and polarization resistances associated to the electrolyte and the electrodes, respectively, were listed in Table 4.2 after fitting the impedance spectra obtained at V=1.3 V with an equivalent circuit (insets Figure 4.23). As observed in the fuel cell mode, the reduction in the ASR is equally distributed between the electrolyte and the electrode and can be proportionally ascribed to the increase of area.
In case of SOEC mode, a possible diffusion problem seems to appear in the low frequency arc, causing an underestimation of the polarization and consequently overall resistance. The obtained values of ASR are respectively $0.70\,\Omega \cdot \mathrm{cm^2}$, and $1.10\,\Omega \cdot \mathrm{cm^2}$ for the corrugated and planar design. The polarization resistance decreases from $0.60\,\Omega \cdot \mathrm{cm^2}$ to $0.40\,\Omega \cdot \mathrm{cm^2}$. More significant is the diminution of the serial component, which decreases from $0.50\,\Omega \cdot \mathrm{cm^2}$ to $0.30\,\Omega \cdot \mathrm{cm^2}$. Further optimization of the test set-up and protocols, could lead to reduced noise and higher performance.
In co-SOEC mode a better resolution of the arcs is achieved, measuring ASR values of $1.20\,\Omega \cdot \mathrm{cm^2}$ and $0.70\,\Omega \cdot \mathrm{cm^2}$ for the planar and wave respectively,

corresponding to a decrease around 60%. The reduction of the overall resistance is due to the decreasing of both its component. The serial resistance drops from $0.55\,\Omega \cdot \mathrm{cm}^2$ to $0.30\,\Omega \cdot \mathrm{cm}^2$ applying the corrugation of the electrolyte and polarization resistance from $0.65\,\Omega \cdot \mathrm{cm}^2$ to $0.40\,\Omega \cdot \mathrm{cm}^2$. The trend of the resistance, linear with the one of the active area, confirmed the source of the improvement as the different active area of the cell.

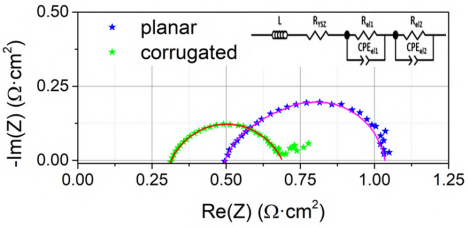

(a) Nyquist plot of EIS at 900° C in SOEC mode

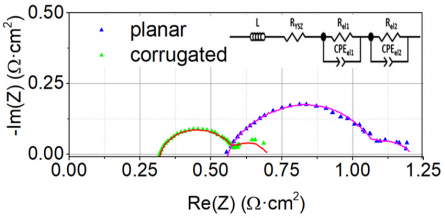

(b) Nyquist plot of EIS at 900° C in co-SOEC mode

Figure 4.23: *Nyquist plots of the electrochemical impedance at operating condition (V=1.3 V) in electrolysis and co-electrolysis mode, solid points represent the measured values and lines the fitted curves with the equivalent circuit presented in the insets.*

SOFC mode			
	$\mathbf{ASR_{pl}}$ $(\Omega \cdot cm^2)$	$\mathbf{ASR_{corr}}$ $(\Omega \cdot cm^2)$	$\mathbf{ASR_{corr}/ASR_{pl}}$
Total	1.10	0.65	0.6
Electrolyte	0.50	0.30	0.6
Electrodes	0.60	0.35	0.6
SOEC mode			
	$\mathbf{ASR_{pl}}$ $(\Omega \cdot cm^2)$	$\mathbf{ASR_{corr}}$ $(\Omega \cdot cm^2)$	$\mathbf{ASR_{corr}/ASR_{pl}}$
Total	1.10	0.70	0.6
Electrolyte	0.50	0.30	0.6
Electrodes	0.60	0.40	0.6
co-SOEC mode			
	$\mathbf{ASR_{pl}}$ $(\Omega \cdot cm^2)$	$\mathbf{ASR_{corr}}$ $(\Omega \cdot cm^2)$	$\mathbf{ASR_{corr}/ASR_{pl}}$
Total	1.20	0.70	0.6
Electrolyte	0.55	0.30	0.6
Electrodes	0.65	0.40	0.6

Table 4.2: *Values of area specific resistance (total, electrolyte and electrode contributions) obtained from equivalent circuit fitting of the EIS spectra for both planar and corrugated cells measured in fuel cell, electrolysis and co-electrolysis mode at 900° C*

All the reported analysis have been carried out at 900°C, 850°C and 800°C, confirming the validity of the approach to increase the performance of SOCs through additive manufacturing. Since the discussed trend is present over all the temperature range, the numerical analysis is not presented here.

4.1.3.2 Long-term test of corrugated cells in SOFC mode

In order to corroborate the quality of the printed cells and the capability of reaching quality standards similar to the current state of the art cells fabricated by conventional techniques, a long-term degradation test was carried out on the corrugated cell operating in fuel cell mode. Figure 4.24 shows the voltage evolution as a function of time for a galvanostatic experiment fixing a current density of j=360 mA/cm^2 at 850°C.

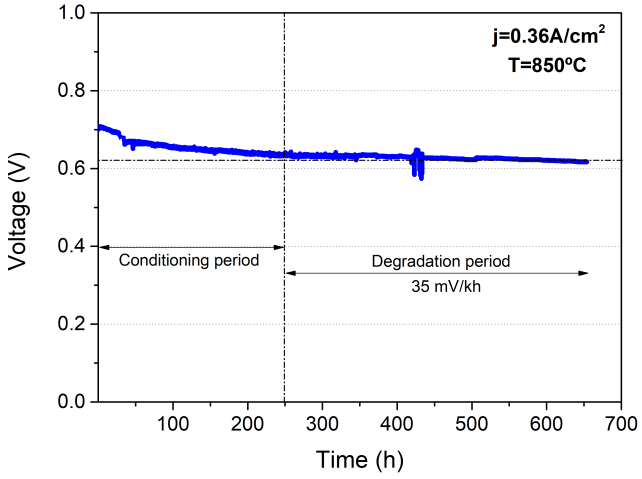

Figure 4.24: *Degradation of voltage during over 650 h in the corrugated cell at* 360 mA/cm^2*, T=850° C, pure H_2 and synthetic air atmospheres.*

After an initial conditioning period of 250 h (typically required to stabilize the behaviour of a SOFC [366]), the degradation of the cell was measured over 400h showing a remarkably stable behaviour. A low degradation rate of 35±5 mV/kh was measured indicating a good behaviour according to the combination of materials used in the fabrication of the cell. Overall, it is confirmed that the 3D printing structuration of the electrolyte carried out in this work represents a straightforward method to enhance the performance of solid oxide cells for both fuel cell and electrolysis applications, obtaining an enhancement directly proportional to the increase in area as a first

approximation. Moreover, the performance stability proved in SOFC mode anticipates the future impact of this technology approach for real applications.
Electrochemical characterization of the cell was carried out at the beginning, and at the end of the test and the results are reported in Figure 4.25.

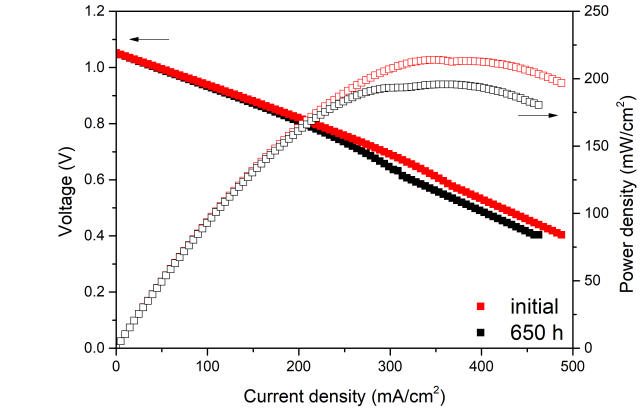

(a) V-j curve over time

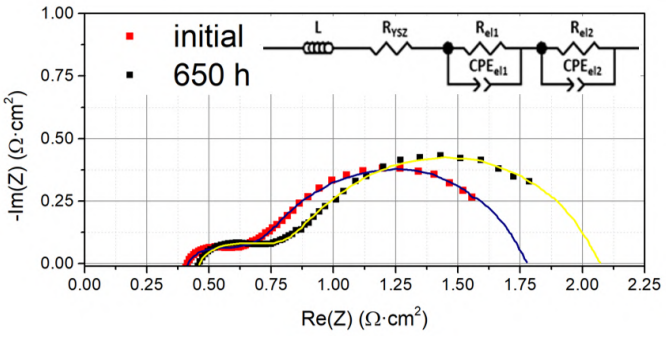

(b) Nyquist plot of EIS over time

Figure 4.25: *Electrochemical characterization during the degradation study by means of polarization curves (Fig. 4.25a) and electrochemical impedance spectroscopy (Fig. 4.25b).*

The V-j curves reported in Figure 4.25a shows how the output power decreases as a consequence of the long term operation. At initial, the maximum output power is of 214 mW/cm^2, after 650 hours this decrease of 11% to 195 mW/cm^2. In particular the reduction of performance is clearly noticeable at higher current density. The reason of the degradation can be identified by the impedance analysis, reported in Figure 4.25b, the equivalent circuit is presented in the inset. The total ASR increases around 14%, from 1.78 $\Omega \cdot$ cm^2 to 2.08 $\Omega \cdot$ cm^2. While small increase is observed in the

serial resistance (from $0.29\,\Omega \cdot cm^2$ to $0.32\,\Omega \cdot cm^2$), probably due to an evolution of the current collection or a reduction of the active area of the cell. The major difference is found in the contribution from electrodes. The low frequency arc of the Nyquist plot increases over time from $1.01\,\Omega \cdot cm^2$, at the initial state, to $1.19\,\Omega \cdot cm^2$ at the end of the test. To identify which of the two electrode is connected with this arc different composition of fuels have been supplied and impedances have been recorded, the results are reported in Figure 4.26, showing how the second arc change as a function of the hydrogen concentration, which allows ascribing it as the fuel electrode. Consequently the fuel electrode is the one suffering more severe degradation in the studied time. Usually the main mechanisms of nickel degradation are the red-ox cycling of the material, that can be excluded in this specific case, since no leakage are detected between the two chambers, and the Ni coarsening under operation, which is probably happening in the fuel electrode.

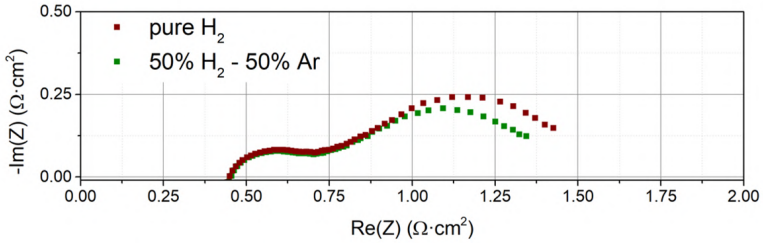

Figure 4.26: *EIS recorded at different fuel composition.*

The obtaining degradation value (5.4%/kh) is comparable with accepted value in the literature on the laboratory level [393], [394]. The degradation rate can be improved optimizing all the process steps as happen for the stack level at Jülich, achieving a degradation rate of 0.4%/kh for a stack running over 19000 hours [395].

4.1.3.3 Post-mortem analysis of corrugated cells

Analyses by Scanning Electron Microscopy have been carried out to confirm the microstructure of the cells, as from the point of view of the printed electrolytes, as to confirm the proper attachment, thickness and microstructure of the electrodes. The thickness of the YSZ layer, in both types of cells, is of 270 µm with a standard deviation of ± 18 µm, which proves an excellent thickness uniformity even for highly complex shapes (Figure 4.27). This electrolyte thickness homogeneity avoids the formation of detrimental hot spots in operation caused by Joule effect when high current densities are passing through thinner regions. In this regard, the insert in Figure 4.27b

shows the typical height of the layer-by-layer 3D printing step (estimated in 25 µm), which determines the accuracy in the z-axis of the here-presented methodology.

Figure 4.28 shows cross-section SEM images of the different layers and in-

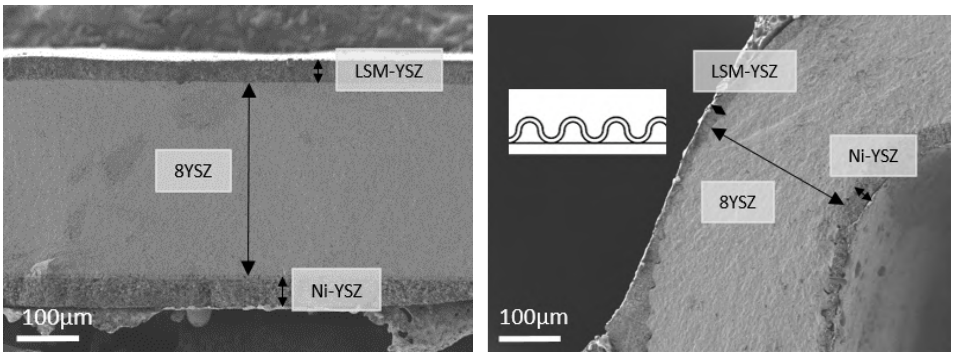

(a) SEM image of cross section of flat cell

(b) SEM image of cross section of corrugated cell, detail highlighted from an hill, as reported in the inset with the CAD design

Figure 4.27: *SEM micrographies of the cells cross section.*

terfaces for the planar (Figures 4.28a, 4.28c and 4.28e) and corrugated cells (Figures 4.28b, 4.28d and 4.28f). Regarding the electrolyte membrane (Figure 4.28c and 4.28d), defect-free and homogeneous layers were observed in both cells with density above 97% of the theoretical value (6.10 g/cm^3). Limited closed porosity was observed in the electrolyte indicating the suitability of the 3D printing technology to reach gas-tight self-standing membranes. The gas-tightness of the printed electrolytes was later confirmed by the open circuit voltage (OCV) obtained in fuel cell mode (see previous section). Despite the full densification of the YSZ electrolyte, good adhesion of the air and fuel electrodes, after the introduction of the adhesion layer reported in Section 4.1.1, was confirmed by detailed observation of the interfaces in the planar (Figures 4.28a and 4.28e) and corrugated cells (Figures 4.28b and 4.28f), overcoming the problems reported by Cebollero et al. [332], [333] Moreover, the same set of figures shows a suitable homogeneous and highly porous microstructure for the different electrodes confirming the high quality of the fabricated cells.

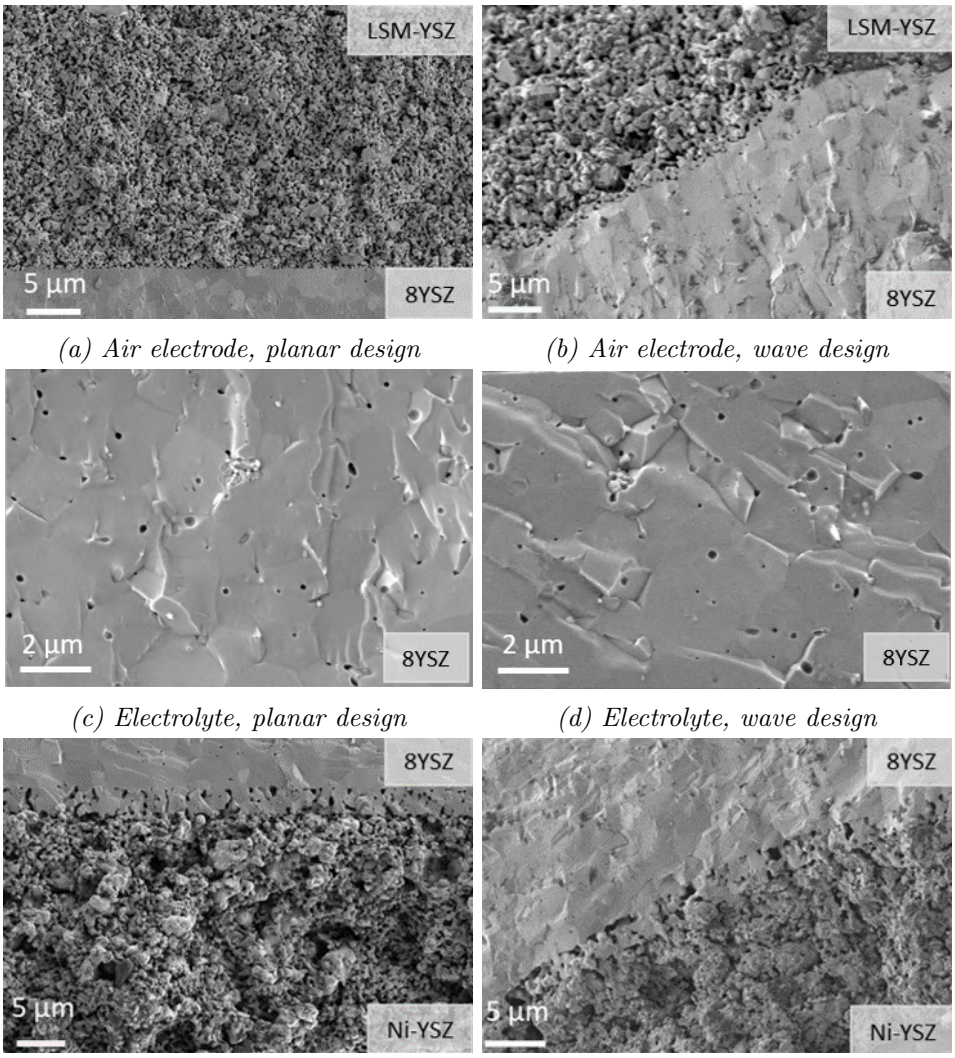

(a) Air electrode, planar design *(b) Air electrode, wave design*

(c) Electrolyte, planar design *(d) Electrolyte, wave design*

(e) Fuel electrode, planar design *(f) Fuel electrode, wave design*

Figure 4.28: *Detailed micrograpies of the different functional layers of the planar (on the left) and the corrugated (on the right) cells.*

In Figure 4.29, the microstructure of the cell after the degradation study is compared with the one of a cell in pristine state. The air electrode does not presents evident signs of degradation, a good attachment is maintained after operation. The printed electrolyte shows the same porosity before and after running for 650 hours. No pinholes have been detected over an analysed area of 1 cm length, proving the stability of the printed pieces after operation, confirming also on the long time the suitability of this technology. In case of the fuel electrode a Ni coarsening can be observed, and the formation of big pores, that can locally reduce the attachment with the electrolyte.

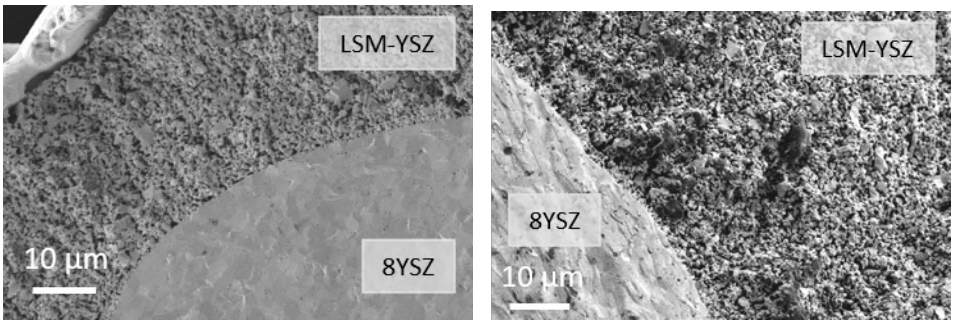

(a) Air electrode, pristine state

(b) Air electrode, 650h degradation

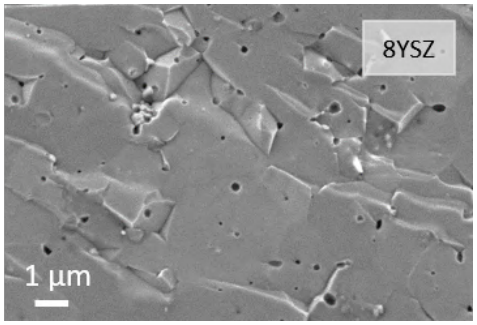

(c) Electrolyte, pristine state

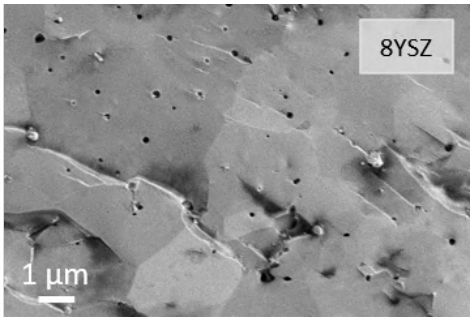

(d) Electrolyte, 650h degradation

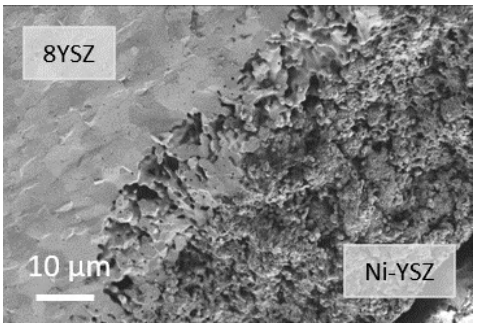

(e) Fuel electrode, pristine state

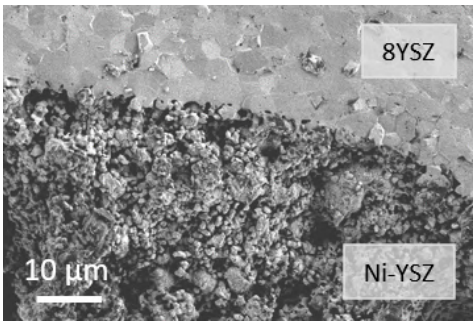

(f) Fuel electrode, 650h degradation

Figure 4.29: *Detailed micrograpies of the different functional layers of pristine state (on the left) and after 650 h (on the right).*

4.2 Solid Oxide Cells fabricated in a single printing step

This section reports the electrochemical characterization of the cells produced using the hybridization of two printing processes in the same 3D printing machine: sterolithography and robocasting. In Section 4.2.1, we present the fabrication and characterization of symmetrical cells based on NiO-YSZ (fuel electrode) and LSM-YSZ (air electrode). After achieving an optimized combination of design and thermal treatment (work reported in Section 3.3.2), we provide measurements on a self-supported 3D printed cell entirely produced in a single fabrication step (Section 4.2.2).

4.2.1 Symmetrical cells based on SLA electrolytes and robocasted electrodes

Fully printed and co-sintered symmetrical cells have been realized to study the suitability of robocasted printed layer based on in-house developed slurries to be used as electrodes in SOCs.

4.2.1.1 Fully printed symmetrical cells of fuel electrodes

To prove the suitability of the robocasting technology for the deposition of the fuel electrodes in SOCs, we produced symmetrical cells based on the developed slurry of NiO-YSZ to be used as fuel electrode (Section 3.1.3.1) and the already known YSZ paste in SOCs (Section 2.1.2.1). Recalling the design described in Section 2.2, symmetrical cells of SLA printed electrolyte (560 µm in thickness in green state) and NiO-YSZ robocasted electrodes (380 µm in thickness in green) were fabricated. The fully printed cell was subjected to a thermal treatment of debinding and sintering (as for 8YSZ alone) of 4 hours at 1300°C. After sintering, the symmetrical cell presents 420 µm thickness for the electrolyte and 230 µm for each electrode (Figure 4.30a).

The cell presents good attachment between the electrode and the electrolyte (Figure 4.30b), presenting a dense electrolyte (detailed view in Figure 4.30c) and a proper porosity of the electrode (Figure 4.30d). The sintering temperature (1300°C for 4 hours) has been proved to generate suitable attachment and microstructure to produce fully printed fuel electrode symmetrical cells. However, some electrolyte material has not been removed properly, as can be noticed in Figure 4.30b, resulting embedded in the electrode, further improvements in the removal of SLA material resolved the issue.

Apart from the microstructural characterization, the symmetrical cell has been characterized by Electrochemical Impedance Spectroscopy (EIS) between

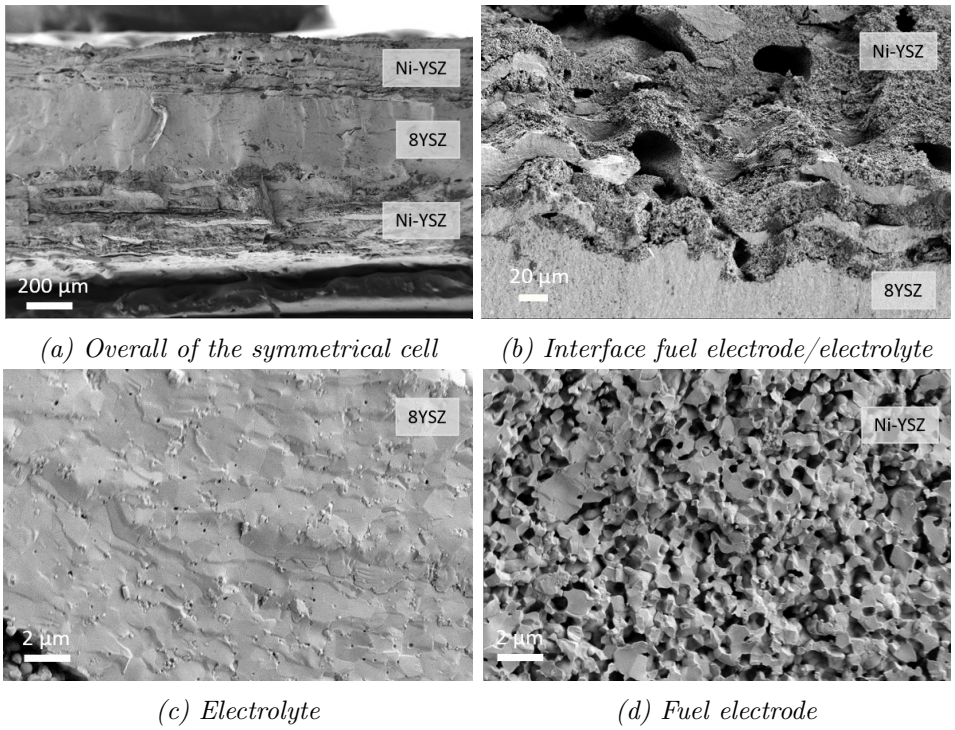

(a) Overall of the symmetrical cell

(b) Interface fuel electrode/electrolyte

(c) Electrolyte

(d) Fuel electrode

Figure 4.30: *Microstructure analysis of the fuel electrode fully printed symmetrical cell.*

500°C and 900°C, taking a measurement each 50°C, under pure hydrogen. The Nyquist plots are reported in Figure 4.31. The data have been fitted with a LR(RQ)(RQ) circuit to follow the two arc contribution of the impedance (see equivalent circuit in the insets of Figure 4.31).
Figure 4.32 reports the Arrhenius plot of the polarization resistance of the Ni-YSZ electrodes as obtained after fitting. The activation energy of the printed anode is 0.94 eV, in good agreement with the one reported in literature, which is of 1.07 eV [396]. The discrepancy can be considered acceptable since there is a certain dispersion in the literature. Despite this small discrepancy, the values of polarization resistance are matching the one reported as a reference. Overall, the obtained values indicate a successful hybrid printing and co-sintering of the half-cell of Ni-YSZ (robocasting)|YSZ (SLA).

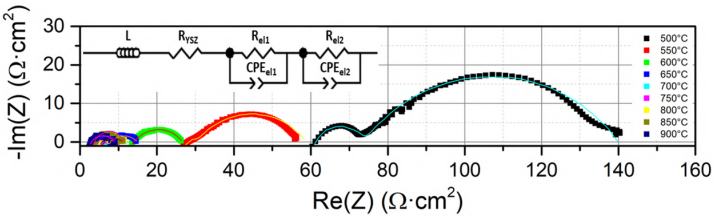

(a) Nyquist plot in temperature range 500° -900° C

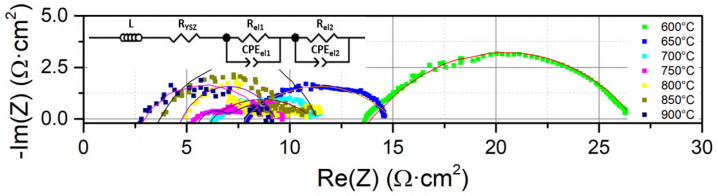

(b) Nyquist plot in temperature range 600° -900° C

Figure 4.31: *Nyquist plot of symmetrical cell based on Ni-YSZ over the range of temperature, in the inset the equivalent circuit used in the fitting.*

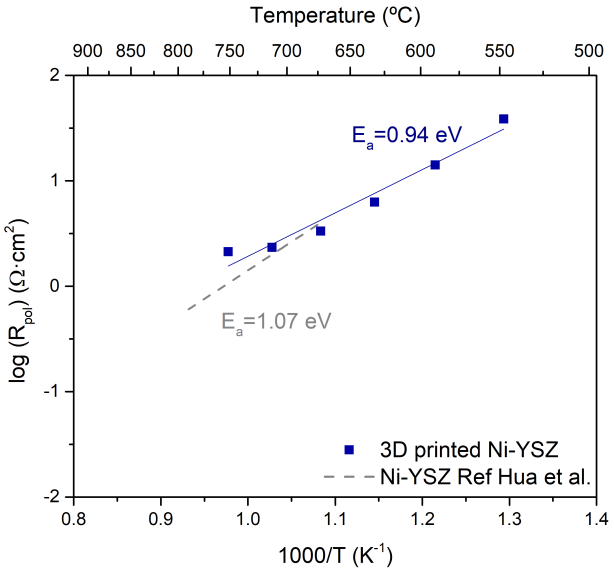

Figure 4.32: *Arrhenius plot of Ni-YSZ polarization resistance as a function of the test temperature. A reference from the literature is reported [396].*

4.2.1.2 Fully printed symmetrical cells of air electrodes

As described in the previous chapter, air electrode materials (either LSM or LSM-YSZ) presents some major challenges compared to nickel (the absorption of the curing UV-light, cause of difficulties to reach a proper polymerization and the need of sintering at lower temperature than the electrolyte complicates the co-sintering step). Keeping in mind the aim of fabricating single-step printed and sintered cells, symmetrical cells based on LSM-YSZ were printed in the hybrid SLA + robocasting machine and co-sintered following the thermal treatment of the electrolyte (1300°C for 4 hours), at 1250°C for 4 hours and at 1250°C for two hours after a dwell at 1100°C for 4 hours. This range of temperature represents a trade-off between the needed for the electrolyte to densify (and to ensure gas tightness) and to keep a certain porosity for the electrode.
Recalling the results presented in the previous chapter, the highest sintering temperature produces dense electrodes, as it has been observed in the symmetrical cells manufactured at such temperature. The interface electrode/electrolyte is reported in Figure 4.33 showing similar microstructure between electrode and electrolyte, translating in a poor gas diffusion through the electrode and consequently not suitability of the manufactured layer, as proven by further electrochemical characterization here presented.

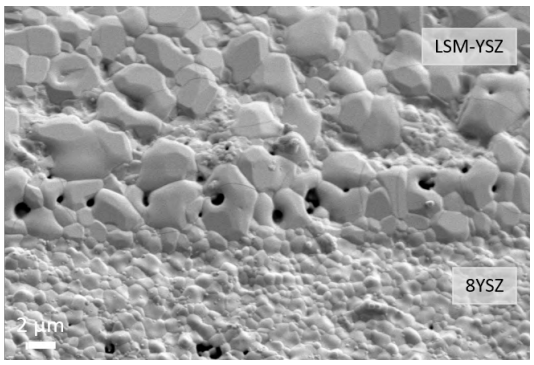

Figure 4.33: *Interface LSM-YSZ/YSZ/LSM-YSZ symmetrical cell sintered 1300° C*

The lowering of the sintering temperature has been proved to positively effect the porosity of the electrode and allow the diffusion of the gas. The thermal treatment at 1250°C for four hours produced symmetrical cell with completely delaminated electrode and has been discarded.
The introduction of an intermediate dwell step at 1100°C, enable to reduce the dwell at 1250°C, resulting in a consistent symmetrical cell (Figure 4.34a). The electrolyte thickness is 320 µm, while the electrodes present thickness

estimated around 70 µm over the area of observation, confirming the validity of the robocasting production. The electrodes appear well attached to the electrolyte, as shown in Figure 4.34b, thanks to the improvement carried out with the removal of material. Applying this thermal treatment, the electrolyte presents major porosity compared with the one sintered at 1300°C (Figure 4.30c), but it is characterized by close porosity, which does not undermine the gas tightness of the electrolyte. The electrode presents a porosity estimated (by image analysis) around 10%, still far from the optimal value of 40% [383], [397], but enabling the gas diffusion and open to further improvements.

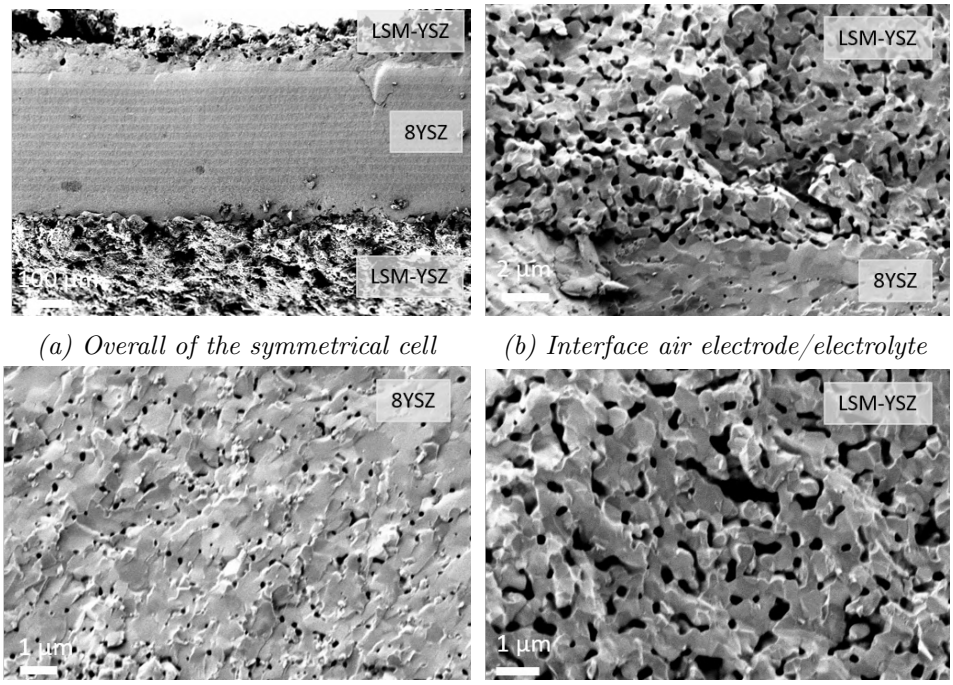

(a) Overall of the symmetrical cell *(b) Interface air electrode/electrolyte*

(c) Electrolyte *(d) Air electrode*

Figure 4.34: *Microstructure analysis of the air electrode fully printed symmetrical cell, sintered at 1300°C for 2 hours after a dwell of 4 hours at 1100°C.*

Electrolchemical chracterization of cells sintered with the three thermal treatments was carried out and discussed in the following paragraphs and graphs. Figure 4.35 reports the Nyuist plots for the sample sintered at 1300°for 4 hours, Figure 4.36 for the cycle at 1250°C for 4 hours and Figure 4.37 for the cycle with the dwell at 1100°C. This characterization has been the base for developing the different thermal cycles applied.

For the highest sintering temperature (Figure 4.35), the Nyquist clearly shows a diffusion-limited regime, also called Warburg contribution (straight line with slope of 45°at low frequencies). This diffusion-limited regime indicates a poor access of the gas to the TPB, i.e. the region where electrode-electrolyte-air are in contact. In other words (as observed in Figure 4.33), the electrode densified in excess at 1300°C.

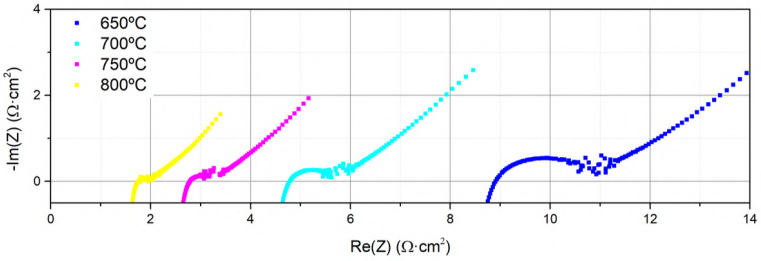

Figure 4.35: *Nyquist plot of the EIS for LSM-YSZ symmetrical cell sintered at 1300° C for 4 hours.*

For the symmetrical cells fabricated at lower temperature for 4 hours (Figure 4.36), the impedance spectra do not present the Warburg element. Despite this, which indicates an improvement in the gas diffusion limitation, the obtained values of resistance are in the order of thousands of $\Omega \cdot cm^2$ in the whole range of measured temperatures (T=600°-800°C). This huge numbers represent values well above the ones reported in the literature. At the disassembly of the cell from the test rig, the problem has been detected, as a complete delamination of the electrode took place. Consequently, the origin of this huge resistance is likely due to the strong loss of electrolyte-electrode contact due to a poor physical contact.

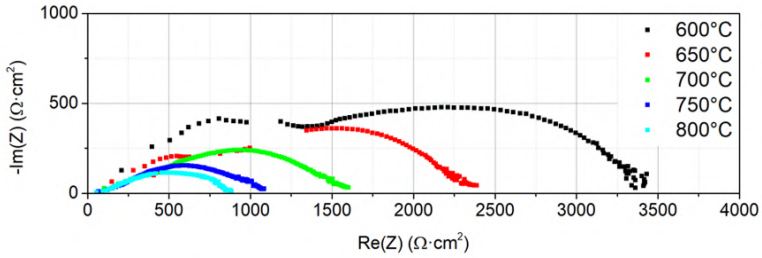

Figure 4.36: *Nyquist plot of the EIS for LSM-YSZ symmetrical cell sintered at 1250° C for 4 hours.*

Taking advantage of the possibility of laser engraving using the 3D printing hybrid machine, we introduced a laser milling step before the robocasting

deposition of the electrode in order to increase the roughness of the electrolyte, which could improve the attachment and partially solve the delamination problem. The symmetrical cells so fabricated were sintered at lower temperatures and during less time (4 hours at 1100°C and 2 hours at 1250°C) to complementary reduce the high density. The improvement in the performance is clearly visible in the impedance spectra collected in Figure 4.37. Polarization resistances in the order of $\Omega \cdot cm^2$ were obtained in the high temperature range, 800°-900°C. Looking at the shape of the impedance spectra, typically observed double depressed arcs were obtained with a contribution at low frequency becoming more important for temperatures below 800°C [387].

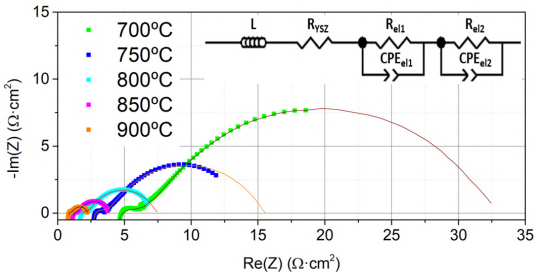

(a) Nyquist plot in temperature range 700°-900° C

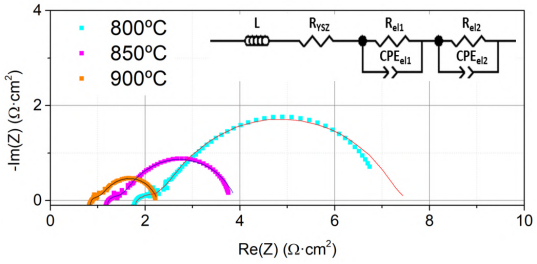

(b) Nyquist plot in temperature range 800°-900° C

Figure 4.37: *Nyquist plot of the EIS for LSM-YSZ symmetrical cell sintered at 1250° C for 2 hours. The insets contain the equivalent circuit employed in the fitting.*

Figure 4.38 shows the Arrhenius plot of the values of polarization resistance fitted using the equivalent circuit in Figure 4.37. The values of resistance are higher compared with the ones reported in literature [398], likely due to a still too high density of the electrodes. However, the activation energy E_a= 1.57 eV is in good agreement with the values reported in the literature that range from 1.49 eV by *Murray et al.* to 1.84 eV by *Jørgens et al.* [398]. Further work is required to end up with an optimized air electrode. Due to the restrictions imposed by the required densification of the electrolyte, i.e.

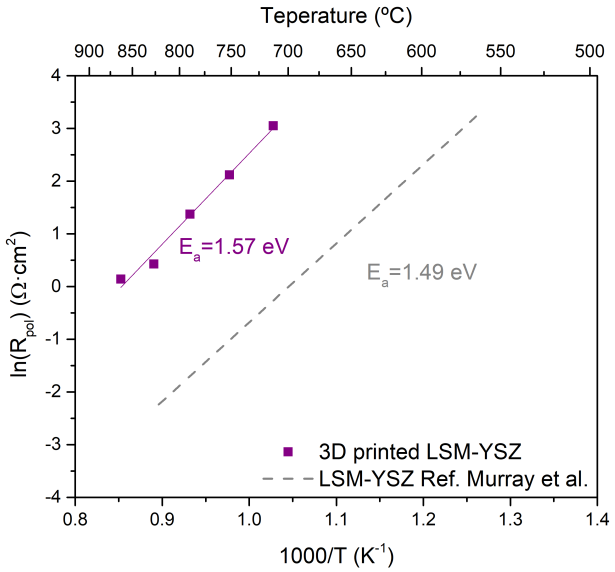

Figure 4.38: *Arrhenius plot of LSM-YSZ sintered 1250º C for 2 hours. The calculated activation energy is reported and compared with values from the literature [387].*

high co-sintering temperatures, other strategies requiring the introduction of pore-formers in the printed pastes seem to be necessary. We are positive that these modifications will lead to electrodes with a competitive performance comparable with the state of the art.

4.2.2 Preliminary results on fully 3D printed solid oxide fuel cells

Despite the electrode deposition and sintering were not fully optimized, the fabrication of a whole cell produced by hybrid stereolithography plus robocasting has been undertaken to foresee further challenges involving the co-sintering of the three different layers at a single temperature. Based on the previously described limitations imposed by the air electrode, the co-sintering temperature was set at 1250°C.

Figure 4.39 shows an overview and details of the cross-section of the co-sintered cell. In the overall image, the interfaces between the different layers are not easy to identify due to the co-sintering process, which generates interdiffusion of the different elements. In particular, it is possible to notice that the thickness of the electrolyte is not perfectly homogeneous as presented in the other cells. The reason can be found in the manufacturing step of laser milling, which does not generate perfect finished surfaces like the ones

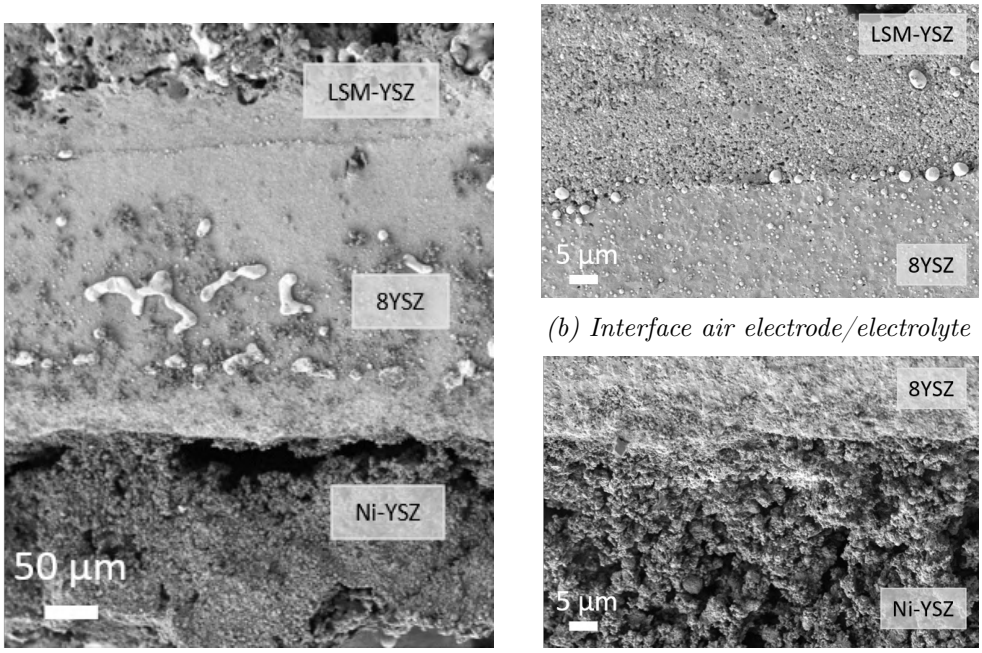

(a) Cross section of the cell

(b) Interface air electrode/electrolyte

(c) Interface fuel electrode/electrolyte

Figure 4.39: *SEM images of overall view of the hybrid cell in cross section. Details of the cross-section of the electrode-electrolytes interfaces.*

produced by stereolithography. These defects were intentionally created for improving the attachment of the top layer. When looking more in detail, it is possible to see that the good adhesion of the air electrode was certainly reached (Figure 4.39b). However, due to the high co-sintering temperature, the layer also presents a very low porosity. Regarding the Ni-YSZ layer, it shows attachment issues in some areas of the cell (for comparison refer to Figure 4.39a and 4.39c). The lack of attachment is likely due to a poor curing of the Ni-YSZ paste combined with the relatively low sintering temperature, which do not favour the good Ni-YSZ|YSZ attachment, although delamination during preparation of the sample cannot be discarded (see comment below). A finer analysis of the porosity of the different layers (Figure 4.40) yielded some important conclusions. First, the high density of the LSM-YSZ layer is confirmed showing porosity values around 10% (by image analysis). These numbers are far from the recommended value of 40%. Second, regarding the electrolyte, which has to be dense to ensure gas-tightness, it seems to be fully dense and comparable with commercial ones showing only small closed porosity. This is a very important result since the chosen temperature of 1250°C is lower than the one recommended for a full densification ($T > 1350$°C). Finally, the Ni-YSZ layer shows an adequate porosity after reduction of the NiO into metallic Ni.

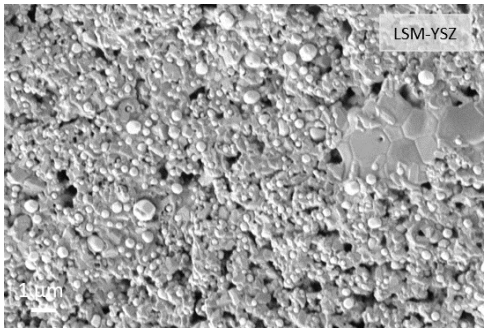

(a) Air electrode

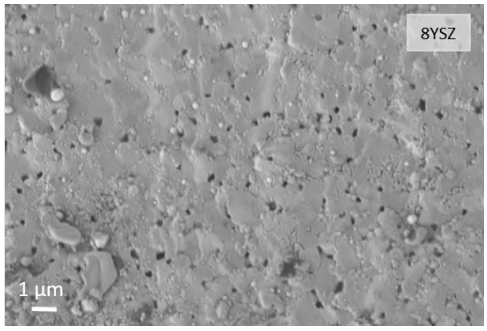

(b) Electrolyte

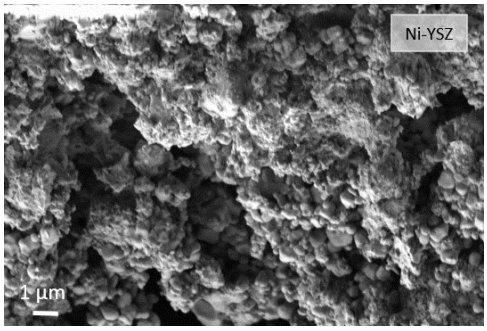

(c) Fuel electrode

Figure 4.40: *SEM micrographies analysing the microstructure of the different layers of the hybrid cell.*

The electrochemical characterization of this preliminary printed cell was carried out at T=850°and 900°C under pure hydrogen and synthetic air atmospheres. Figure 4.41 shows the V-I curves of the cell in the mentioned conditions. In this figure, the maximum voltage obtained at open circuit (OCV) is very low OCV= 0.8 V, while the expected value is above 1.1 V for these operating conditions. Since the electrolyte presented a full densification, the drop in the expected OCV is likely due to sealing problems derived

from a non-flat cell. Taking into consideration this non-ideal measurement conditions, it was not surprising to obtain maximum power densities of only ~60 and 80 mW/cm^2 at 850°and 900°C, respectively. This performance is considerably low compared to the obtained for the electrolyte supported cells in this thesis (~260 mW/cm^2 at the same temperature). Beyond the incomplete sealing, it is expected an important voltage drop due to the excess density of the air electrode and a poor attachment of the fuel electrode.

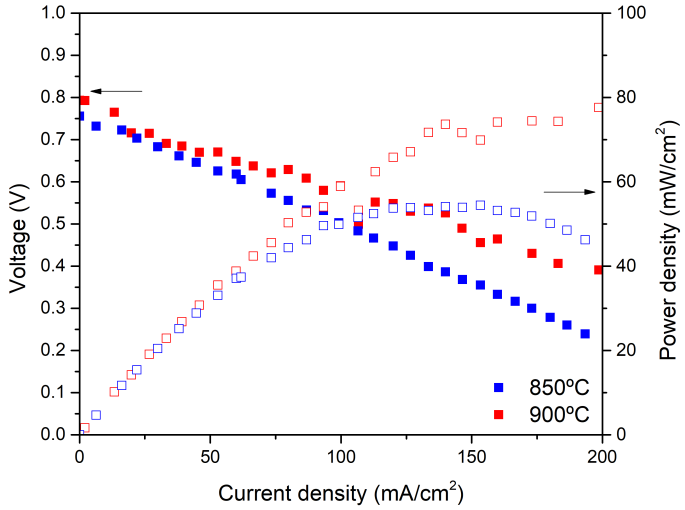

Figure 4.41: *V-j curve of the hybrid cell co-sintered over the range of test temperatures under pure H_2 and synthetic air atmospheres. Solid points represent the voltage (left axis) and the open ones the power density (right axis).*

In order to better understand these possible effects, an EIS analysis was carried out. Figure 4.42 reports the Nyquist plots of the fully printed cell compared to a cell based on SLA printed electrolyte (similar to the one analysed is Section 4.1.3, but 300 µm thick, more comparable with the thickness of the hybrid cell) at operation conditions (linear part of the curve, 0.7 V for the ESC and 0.4 V for the hybrid one). The hybrid cell shows slightly higher serial resistance (R_s=0.95 $\Omega \cdot cm^2$) while the polarization resistance (R_p=1.13 $\Omega \cdot cm^2$) is comparable with the cells described in the previous section [388]. These results suggest that, despite an elevated density of the air electrode and an apparent delamination of the fuel electrode (now probably assigned to a bad preparation of the cross-section), the fully printed cell preserves the necessary features for a good performance and the hybrid printing process represents a promising tool to produce high quality SOFC

and SOEC complete cells.

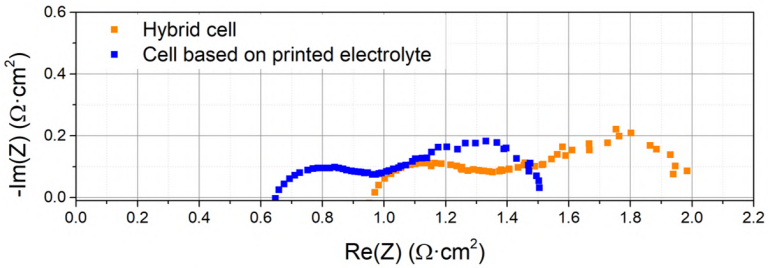

Figure 4.42: *Comparison between the impedance spectroscopy of an entire printed cell and a cell based on a printed electrolyte at T= 850° C and operative condition (0.4 V and 0.7 V respectively).*

4.3 Conclusion

The results reported and discussed in this chapter deal with the use of additive manufacturing as a novel route for fabricating electrochemical devices. First, the suitability of stereolithography to produce electrolytes for solid oxide cells has been proved, obtaining dense and homogeneous pieces with the desired design, showing proper ionic conductivity, compared with the literature. Planar reference cells have been printed showing ASR of $1.10\,\Omega \cdot cm^2$ at 900°C, which is comparable with the ones reported in the literature, for similar kind of cells fabricated with conventional techniques at DTU ($1.1\,\Omega \cdot cm^2$ at 850°C), Jülich ($1.2\,\Omega \cdot cm^2$ at 800°C) or Westinghouse ($1.0\,\Omega \cdot cm^2$ at 900°C) [388]. Once confirmed the possibility of achieving good electrochemical performance in 3D printed electrolyte supported cells. The main distinctive characteristic of the 3D printing techniques, which is the ability of providing shape freedom, has been applied to boost the performance of such cells by design. This enhancement was obtained by developing 3D-structured electrolytes beyond the planar geometries. Electrolytes based on hexagons, waves and squares have been realized, proving in all cases an increment on the performance related to an increase of the active area (keeping the projected area). The one based on a wave corrugated profile has shown the highest improvement. These cells have been subjected to a complete electrochemical characterization and to tests in different operation modes. The corrugation of the electrolyte resulted in an enhancement of the performance per projected area. In SOFC mode, corrugated cells generated a maximum power output of $410\,mW/cm^2$, proving an increase of 57% compared to the $260\,mW/cm^2$ obtained in the planar cell of the same projected area. Similar results have been obtained in this cell operating in electrolysis and co-electrolysis modes: the corrugation decreases the ASR of the cell according to the increase of the area. High current densities were injected in a corrugated solid oxide electrolysis cell operating in electrolysis mode ($500\,mW/cm^2$ at 1.3 V at 900°C) and co-electrolysis mode ($600\,mW/cm^2$ at 1.3 V at 900°C). The obtained results prove how additive manufacturing techniques may open new frontiers for enhancing the performance of the SOCs by the implementation of new designs.

Further investigation on the 3D printing capabilities were dedicated to explore the first-time realization of fully printed self-supported cells. For this, it was necessary to hybridize two complementary printing techniques such as robocasting and stereolithography. Moreover, a single-step printing was combined with a single-step sintering, which also represents a big challenge. Our first preliminary results provided a promising performances of $80\,mW/cm^2$ at 900°C. Despite this power density is considered low (far from the $260\,mW/cm^2$ obtained for comparable electrolyte printed cells in

this chapter), the EIS analysis showed that such a bad performance is mainly due to a poor sealing of the cell to the test station (due to non-flat samples) and not to the cell itself. This encourages further work in 3D printing of SOCs to fabricated a new generation of highly performing solid oxide cells able to reduce production time and costs.

Chapter 5

3D printed catalysis reactors for methanation

The capability of additive manufacturing technologies to produce free-form ceramic materials has arisen the interest of researchers working in the catalysis field. For such applications, the capability of producing materials able to withstand high temperature with free-form design is particularly interesting with the aim of increasing the surface area and consequentially the conversion of the system. Moreover, a high level of shape freedom opens the way for a better management of mass and heat transport, which is critical for the final performance of the reactors.
Among the different catalytic applications, we focus here on the CO_2 methanation reaction, by studying the effect of materials and designs. The final aim of this study is to develop a monolithic reactor in the next future (see Annex 2).
In Section 5.1 we present and characterize the developed samples, focusing on the surface finishing, a critical aspect for the catalyst adhesion.
Section 5.2 is devoted to the deposition of the active phase, the catalyst, which is analysed, during all the production steps.
The central part of this chapter is Section 5.3, where we discuss the results on conversion of carbon dioxide and hydrogen into methane. In order to propose an improvement mechanism of the obtained results, we also present simulations on the gas flow distribution inside the microchannels manufactured by additive manufacturing.
Part of the work presented here was carried out during a research stay at the Fraunhofer Institute for Microengineering and Microsystems (IMM, Mainz, Germany), under the supervision of Prof. Kolb, head of the group "Energy and Chemical Technology".

5.1 Fabrication and characterization of support plates for CO_2 methanation reaction

The main player in catalysis is obviously the catalytic system, which is usually formed by an active metallic phase and a support phase that enhances the surface area, the stability, the dispersion and the diffusion of species. Nevertheless, the catalytic system performance strongly depends on the reactor, which has the role to keep the catalyst in place and gives routes for the supply of gases and release of products including the evacuation/intake of heat. All these aspects affect the conversion, the stability and the selectivity and should be taken into consideration when designing a catalytic reactor.
In these regards, the freedom of design represents an unfair advantage in the fabrication of a reactor since it can improve the flow distribution and the heat management and, consequently, the performance of the device. Additive manufacturing even offers the opportunity to materialize joint-less reactors with complex geometries and integrated manifolds. A further step in the exploitation of additive manufacturing technologies is the possibility of multi-materials manufacturing to produce the bed and the catalyst at the same time, in a ready-to-use reactor.
Moving forward to the realization of a monolithic reactor, a simpler system based on test-plates has been develop to be further implemented in the printed reactor.
In order to reach the final goal of the fabrication of complex monolithic reactors, a simpler system based on test plates has been develop first in order to prove the suitability of 3D printed structures for this purpose. To reach this goal, we employed an already optimized catalyst system such as nickel dispersed on ceria powder [343] deposited on different reactor materials and designs. Test plates with engraved micro-channels were used in a standard face-to-face configuration to obtain a microchannel-like reactor (Figure 5.1).
Starting with this common configuration of catalyst system and test plate, the study is divided into two parts: i) the study of the influence of the test plate material and ii) the evaluation of the effect of the test plate design on the performance. For the first part of the study, three batches of samples composed by four plates, each with 16 channels of 1 mm in width by 0.5 mm in depth (32 channels of 1 mm by 1 mm) were fabricated (Figure 5.2a). These plates were fabricated in stainless steel 316L by mechanical machining and Selective Laser Sintering (SLS), and in alumina by stereolithography. With the aim of exploiting the design flexibility of SLA, a deeper study on the possibilities of a complex design has also been carried out in the second part of the work. The selected geometry consists on herringbone grooves, which use has been reported in literature with the purpose of increasing the mixing of the reactive gases and their residence time [399], [400]. A herringbone engraving of 200 µm in depth has been produced on the channels

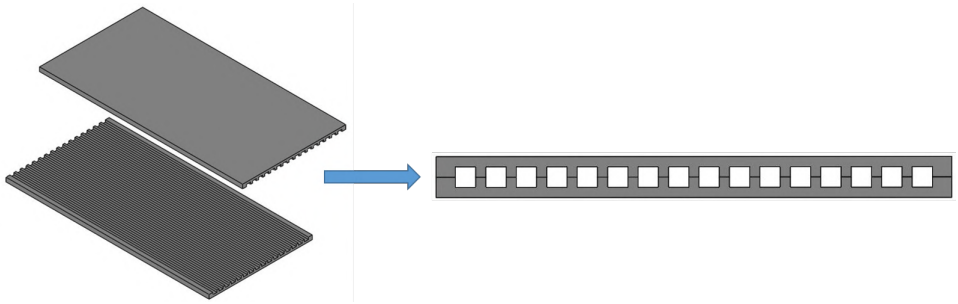

Figure 5.1: *Scheme of the assembly of support plate. The plates are placed face to face, resulting in the formation of micro-channels. The alignment of these two parts becomes very important for ensuring a proper operation of the reactor.*

(Figure 5.2b). To compare the results a batch of straight channels was produced with lower depth but the same volume. Details on the dimensions are reported in Section 2.2.3.1.

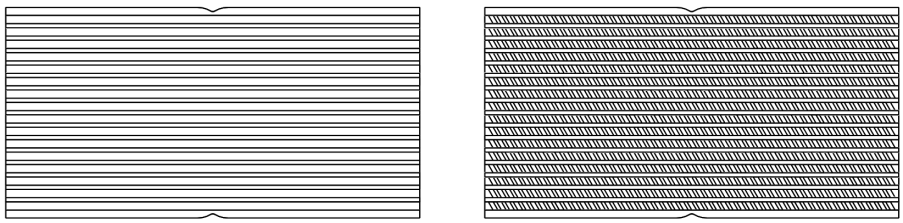

(a) Flat design *(b) Herringbone design*

Figure 5.2: *CAD designs of the test-plates.*

All these measurements were carried out in a re-usable housing inspired by the work of *Knitter et Liauw* [319]. The housing has been fabricated in stainless steel and present two triangular alignment notches (circled in yellow in Figure 5.3).

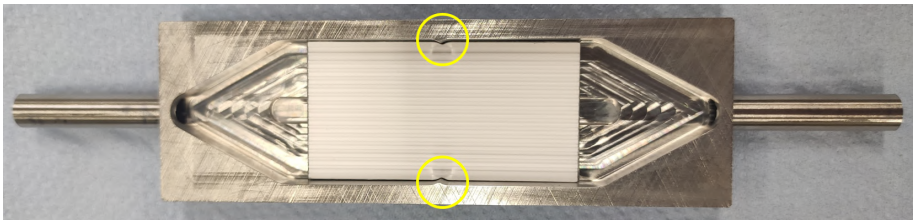

Figure 5.3: *Stainless steel housing with a test-plate in position, highlighted in yellow the clamp to enable the placing and holding of the test-plates.*

These notches ensure the correct alignment of plates for granting them to be precisely placed in front of each other. Flexible shaped graphite gaskets were used to absorb the unequal pressure applied during the assembling. This can be especially important in the case of brittle alumina plates. Two standard 1/4" tubes have been welded to the housing and ended with Swagelok connections to facilitate further tubing. For measuring, a lid is placed and welded on top of the housing, which ensures gas tightness and sufficient resistance to operation pressure. After the test, the welded cover can be mechanically removed for re-use.

5.1.1 Surface finishing of the test plates

The surface finishing is an important parameter, mainly affecting the attachment of the catalyst to the reactor plates. The ultimate performance and the stability of the reactor will dramatically depend on this attachment (see Section 5.2.1). SEM planar views of the channels produced by different methods and with different materials are presented in Figure 5.4. The plates produced by mechanical milling of stainless steel sheets present sharp edges and flat surfaces (Figure 5.4a). On the other hand, the produced by SLS, show a rough surface due to the manufacturing technique, which is powder based (Figure 5.4c). The side of the channels of the alumina plates are better defined than the ones produced by SLS, although a little rounding of the edges can be observed (Figure 5.4e). Looking into detail to the microstructure of each part, different materials and manufacturing techniques present their specific features. The milled surface appears uniform and smooth showing circular lines, which correspond to marks left by the tools used during the milling process (Figure 5.4b). SLS parts present a very different microstructure with a surface full of residual powder partially sintered (Figure 5.4d). The alumina plates are characterized by flat surfaces, but at higher magnification the microstructure reveals the sintering domains, smaller than the residual particles of the SLS, but more pronounced than the milled ones (Figure 5.4f).
The difference in the surface finishing of the different samples has been evaluated by carrying out roughness measurements (performed with specific roughness measuring instruments such as MarSurf PS10 by Mahr and a Bruker Dektak XT). The results are reported in Table 5.1. As observed by SEM, the milled surface is the smoothest with the lower value of roughness (Ra=0.14 µm). The plates produced by additive manufacturing present higher roughness. In the case of the alumina SLA parts, the value is still very low, although higher than the one measured for the stainless steel (Ra=1.38 µm), with a difference between the maximum and the minimum of 8.69 µm (due to residual paste deposition). The steel plates produced by SLS

present the highest roughness (Ra=7.98 µm) and irregularity (Rz=44.22 µm). These values are relevant since they typically correlate with the quality of the attachment of the catalyst, foreseeing an higher adhesion on surfaces characterized by higher roughness [298], [299], [401].

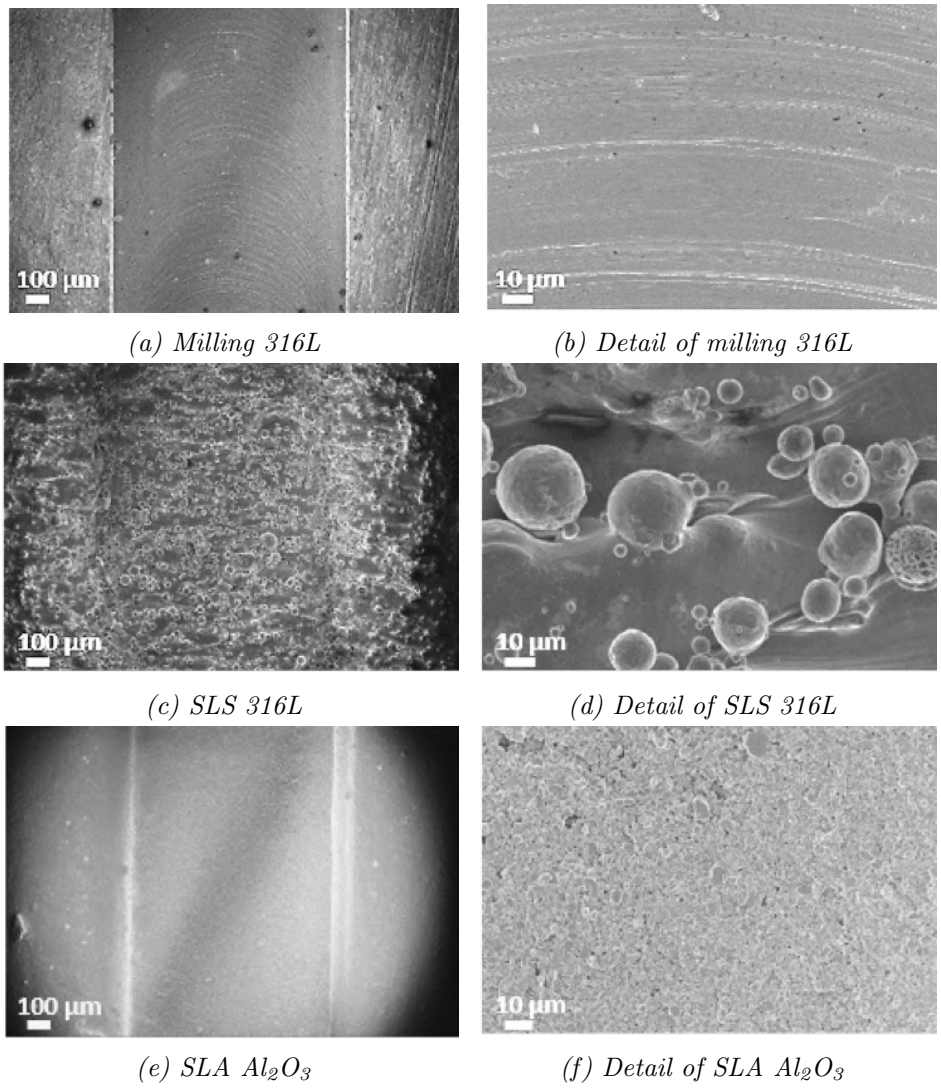

(a) Milling 316L *(b) Detail of milling 316L*

(c) SLS 316L *(d) Detail of SLS 316L*

(e) SLA Al_2O_3 *(f) Detail of SLA Al_2O_3*

Figure 5.4: *Top-view SEM pictures of a single channel produced by different techniques and material, relative details on the right.*

Beyond simple planar microchannels, alumina plates were also printed with a herringbone structuration (of the bottom part of the channel). Figure 5.5 shows the optical topographies for the two different designs. In the case of the flat channels, they are 380 µm in depth to ensure the same

Manufacturing process/material	Ra [μm]	Rq [μm]	Rz [μm]
Milling / 316L	0.143	0.170	0.699
SLS / 316L	7.981	9.911	44.218
SLA / Al_2O_3	1.376	1.935	8.699

Table 5.1: *Roughness measurements of the different test-plates.*

volume of the herringbone channel, which is 500 µm at the lowest point (inside the engrave) and 300 µm in the straight part. The microstructure and the roughness do not change depending on the design, since the material and the manufacturing technique are the same.

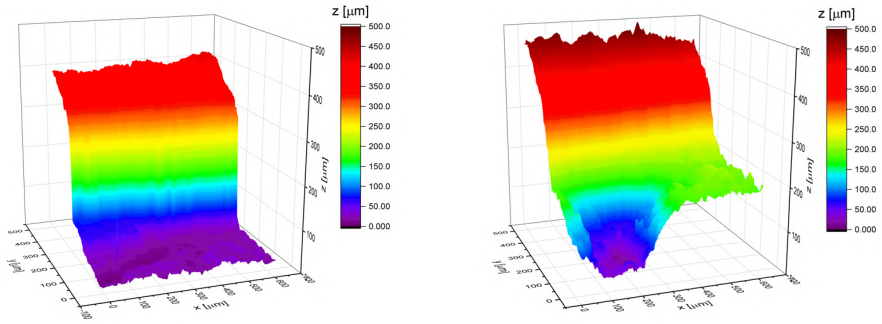

(a) Flat design *(b) Herringbone design*

Figure 5.5: *Topography of alumina plates.*

5.2 Preparation and deposition of the catalyst system

The employed catalyst is nickel dispersed on ceria particles in a ratio of 20:80 (the preparation of the catalyst is described in Section 2.2.3.2). The microchannels of the test-plates are filled with a suspension of this catalyst, which excess is removed by means of a sharp blade. After drying, the catalyst is calcined at 450°C for six hours in air. The process is repeated to obtain a total amount of around 40 mg of catalyst for each plate, to be able to apply a fix space velocity (within the range of the mass flow controllers). After calcination, the catalyst forms a layer of around 15 µm in thickness on the walls of the test-plates (Figure 5.6).

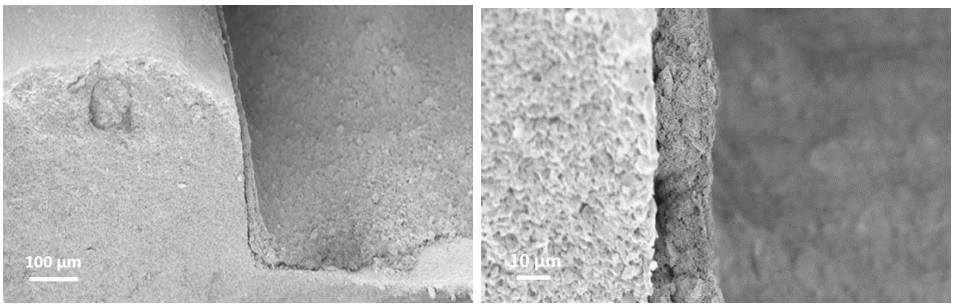

(a) Overview of the channel *(b) Detail of the channel vertical wall*

Figure 5.6: *SEM images of the catalyst layer inside the channel after calcination.*

The attachment of the catalyst on the plates is deeply affected by the substrate material and processing, as can be seen in the series of pictures included in Figure 5.7. We can observe how the same catalyst deposition procedure gives rise to very different results. On the milled ss surface, which is the smoothest, cracks are formed in the catalyst layer, especially close to the step of the channel, indicating a difficult attachment of the layer (Figure 5.7a). The same material produced by a different technology, and a higher roughness, still shows small cracks in the same position, but eventually hidden by the globally rough top layer structure (Figure 5.7c). On the other hand, the alumina plates do not show this defect in the catalyst deposited on top, appearing as an homogeneous layer well attached on the printed surface (Figure 5.7e).

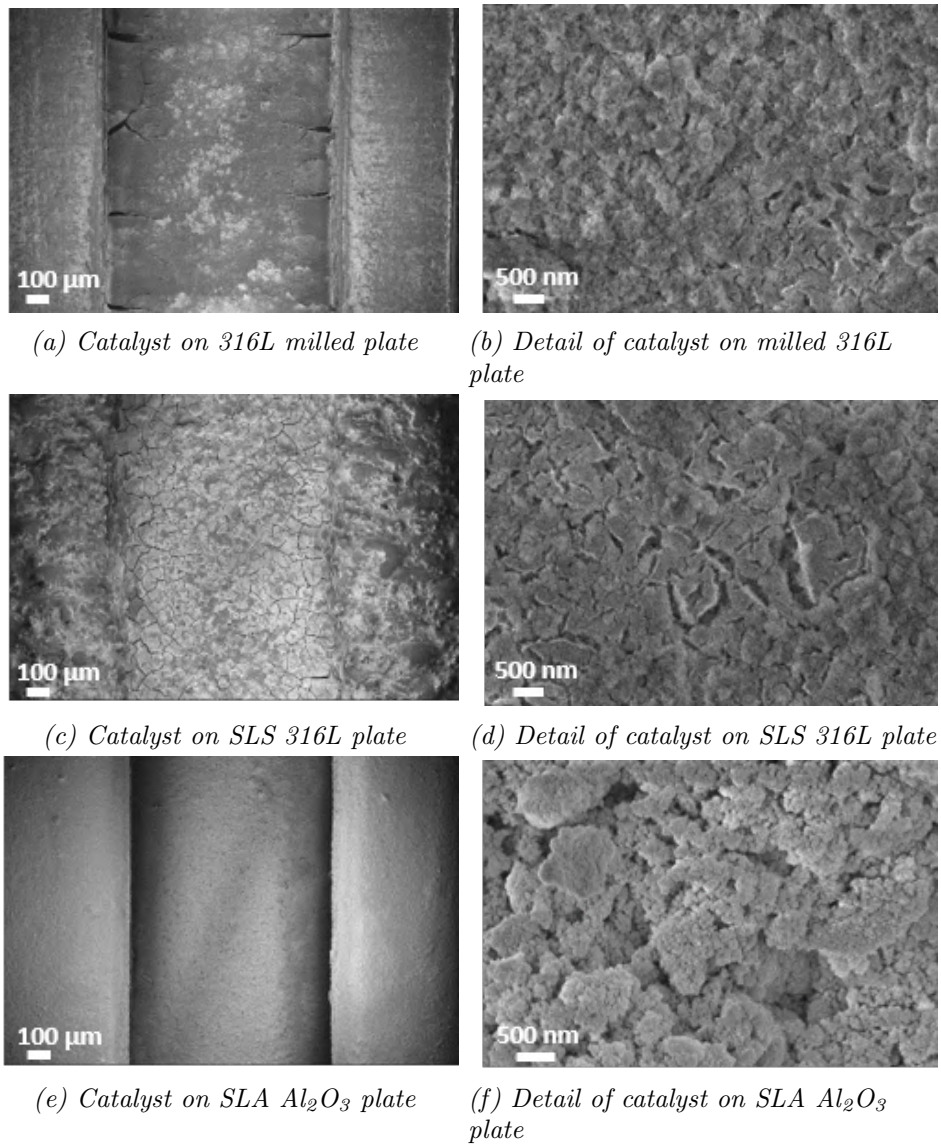

(a) Catalyst on 316L milled plate

(b) Detail of catalyst on milled 316L plate

(c) Catalyst on SLS 316L plate

(d) Detail of catalyst on SLS 316L plate

(e) Catalyst on SLA Al_2O_3 plate

(f) Detail of catalyst on SLA Al_2O_3 plate

Figure 5.7: *SEM pictures of the catalyst deposited in the channels produced by different techniques and material, relative details reported on the right.*

In the case of the milled stainless steel plate, even in areas where the catalyst appears to be intact, a closer inspection shows the presence of small cracks below 1 µm in length (Figure 5.7b). These sub-micron cracks indicate an adhesion problem and are likely formed during the expansion and shrinkage of the different component along the thermal treatment, due to a different TEC of the materials involved. Indeed, the TEC of ceria is reported to be $10.6 \times 10^{-6}\,\mathrm{K}^{-1}$ [402], while for stainless steel 316L is $19.8 \times 10^{-6}\,\mathrm{K}^{-1}$ [403]. This indicates a major expansion of the steel, while the deposited layer

faces a lower expansion, which generates cracks during the thermal cycling. SLS ss plates show the same problem but, due to a higher roughness, major cracks are not clearly observed. However, small cracks are present as observed in the magnified image (Figure 5.7d). In the case of the alumina plates, the crack formation is not noticeable neither looking at the overall deposition over the channel (Figure 5.7e) nor at the detail of the catalyst layer (Figure 5.7f). The appearance of the deposited layer indicates a better compatibility between the alumina and the catalyst, mainly due to a closer TEC ($6.7 \times 10^{-6}\,K^{-1}$ [404]) to the ceria one ($10.6 \times 10^{-6}\,K^{-1}$) than stainless steel one ($19.8 \times 10^{-6}\,K^{-1}$), and a better chemical affinity.

5.2.1 Evaluation of adhesion of the catalyst

Some works reported the evaluation of the catalyst adhesion through the weight of catalyst before and after a high-intensity ultrasonic bath [299], [401]. However, the ultrasonic bath is not representative of the stresses suffered during the assembly and handling of the plates, therefore we developed a dedicated system for vibration testing (Figure 5.8a). The plate is subjected to an acceleration imposed by an electrically controlled piston (Figure 5.8b). The acceleration was fixed for all the sample to 2.5 G for five minutes. The samples were weight before and after this event, to evaluate the amount of catalyst lost. The vibration has been chosen to be comparable with the movement of the operator and the assembling of the plates (measured in the range of 1.0 G and 2.0 G), but not strong enough to break the alumina plate (noticed to happen when the acceleration exceeds 3.5 G).

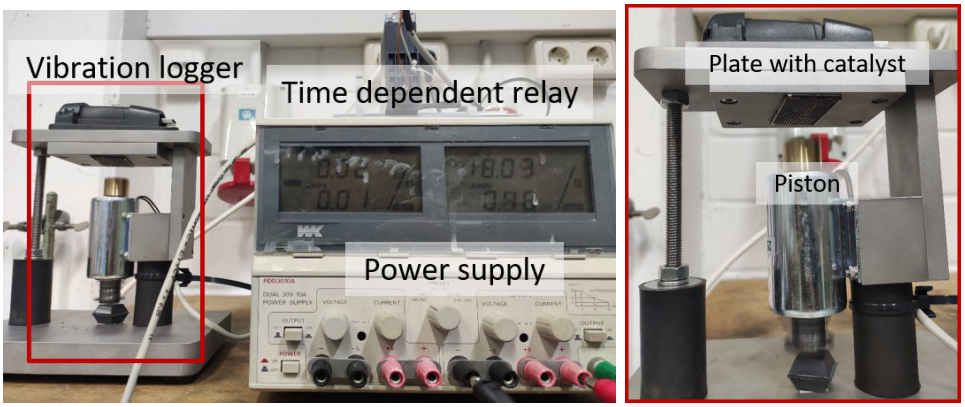

(a) Overview of the set-up

(b) Detail of the assembly of the plates

Figure 5.8: *Set-up for the evaluation of the catalyst loss.*

The percentage of catalyst lost is reported in Table 5.2. As it has been observed by the SEM images, the adhesion between the catalyst and the milled stainless steel is the weakest among the samples analysed. This can be ascribed to the low roughness of the substrate. The loss of catalyst decreases when the roughness increases, in case of the plates produced by SLS, although the material is the same, indicating how the surface roughness plays an important role on the attachment. The alumina plates, although present a lower roughness compared with the SLS ones (1.38 µm vs 7.98 µm), show better attachment of the catalyst. This is connected with different aspects: i) a better matching of TECs of the two materials, which reduces the cracks formation and the delamination after the thermal treatment and ii) the compatibility between two oxides. In this last regard, some cases in literature reported the use of a layer of α-alumina to improve the adhesion between catalyst and metal substrates [405], [406].

Manufacturing process/material	**wt.% catalyst lost**
Milling / 316L	2.43
SLS / 316L	1.39
SLA / Al_2O_3	1.06

Table 5.2: *Catalyst loss for the different test plates after the vibration test.*

In all cases, the loss of catalyst can be been considered acceptable since it is kept below 2.5wt.% [401]. Dramatic losses are referred in the literature for values above 10-12wt.% [298], [299].

5.2.2 Evolution of the catalyst during the fabrication of the reactor

The crystal structure of the catalyst has been investigated over all the production and operation stages for each of the three supports considered in this study, namely, milled stainless steel, SLS printed stainless steel and SLA printed alumina. In this section, we show the comparison between the catalyst: i) as produced in powder form; ii) as deposited and calcined over the plates and iii) after running the methanation test. The results obtained after mehanation will be discussed in the following section.
XRD spectra of the catalyst deposited on milled ss are presented in Figure 5.9. The as-produced catalyst powder presents the characteristic peaks of ceria and nickel oxide, which after reduction becomes nickel metal. After the deposition and calcination at 450°C, the ceria and NiO peaks are still clearly observable and some secondary phases appear. On one hand, traces of iron and cromium oxides from the substrate are detected at low angles (25.5°, 26.7°, 31°, 32°), while the formation of $CeFeO_3$ (peak at ∼57.5°) can

be identified. The dimension of the peak indicates a minor presence of this phase, which is indeed not even detected in the catalyst after reduction. Regarding the catalyst deposited and characterized on SLS produced plates (Figure 5.10), a FeNi alloy seems to be formed in the calcined sample (peak at 50.8°, enlargement of peak at 43.5°). The formation of the cerium ferrite is not clearly observed although, presumably, it will also be present in small amounts. In the case of the alumina plate, the XRD spectra shows no interaction between the catalyst and the substrate (Figure 5.11).

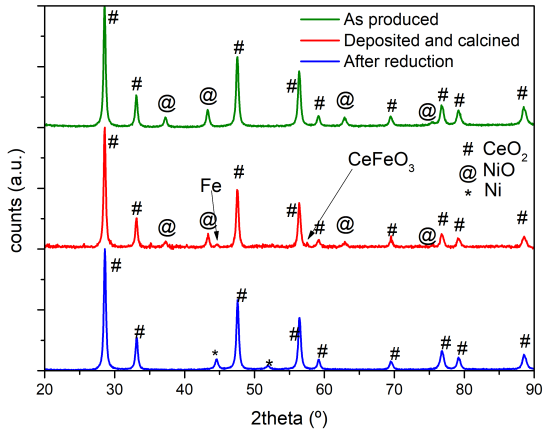

Figure 5.9: *XRD spectra of the catalyst deposited on the stainless steel plates produced by mechanical milling. Reference pattern numbers for the analysis: CeO_2: ICDD-01-081-0792, NiO: ICDD-01-078-0429 and Ni: ICDD-00-001-1258.*

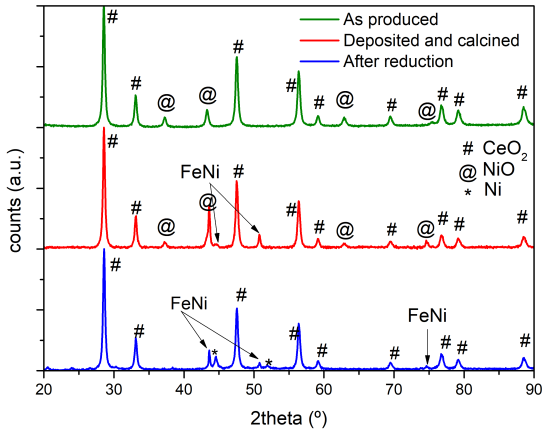

Figure 5.10: *XRD spectra of the catalyst deposited on the stainless steel plates produced by SLS. Reference pattern numbers for the analysis: CeO_2: ICDD-01-081-0792, NiO: ICDD-01-078-0429 and Ni: ICDD-00-001-1258.*

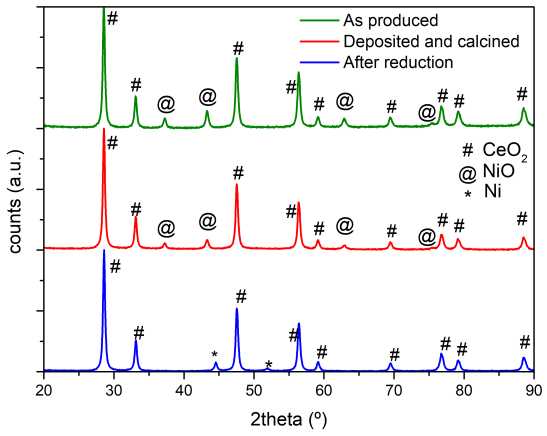

Figure 5.11: *XRD spectra of the catalyst deposited on the alumina plates produced by SLA. Reference pattern numbers for the analysis: CeO_2: ICDD-01-081-0792, NiO: ICDD-01-078-0429 and Ni: ICDD-00-001-1258.*

5.3 CO_2 conversion

After carrying out a detailed analysis of the catalyst attachment to the supports and their structural characterization, the test plates coated with catalyst were assembled into the test housing to form a reactor ready for operation. To evaluate its performance as a methanation reactor, it was placed in a heating platform able to reach the test temperature. This platform is built with heated pipelines to avoid the condensation of water produced during the reaction. A mixture of carbon dioxide and hydrogen is supplied to the set-up in a ratio 1:4, while a minor fixed flow of nitrogen is employed for the calibration of the gas-chromatographer. The conversion is calculated based on the following expression:

$$X_{\mathrm{CO_2}} = \frac{nCO_{2,in} - nCO_{2,out}}{nCO_{2,in}} \times 100 \tag{5.1}$$

Figure 5.12 shows the results of the CO_2 conversion at different temperatures for the plates produced with different materials and manufacturing techniques. The conversion of CO_2 presents a characteristic sigmoid shape. Initially, at low temperature the conversion is low (10-20%), and it increases up to complete conversion at around 340°C, as expected according to the literature [367]. It can be noticed that the performance for the stainless

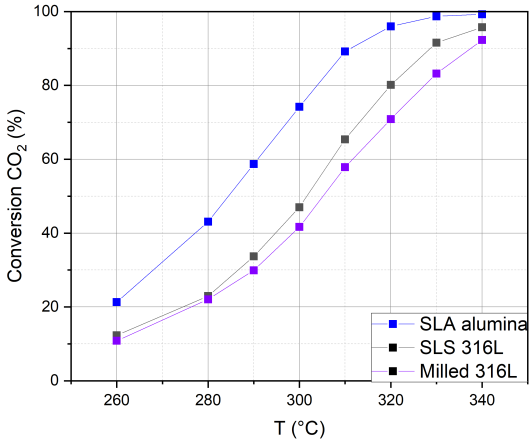

Figure 5.12: *CO_2 conversion as function of temperature for different test-plates material and manufacturing techniques. The reactors were operated at P=6 bar and a gas flow of WHSV=45 L/h·g_{cat}.*

steel plates, either milled or SLS printed, are comparable between them. A slight improvement, around 7% at 300°C, is observed for the SLS plate, which can be ascribed to the increased roughness of the plate and the res-

ulting increase of the active area of the catalyst. Moreover, as it has been proved in Section 5.2.1, the manufacturing by SLS partially reduces the losing of catalyst during operation, which could also justify part of the observed small enhancement [407]. On the other hand, the improvement using alumina plates is evident, reaching 20% increase of CO_2 conversion at 300°C. Beyond the 3D printed nature of the plates, the origin of this enhancement can be straightforwardly found in the high compatibility between the active phase of the catalyst and the alumina of the plates, used often as a support for the Ni particles [119], [298]. Furthermore, the alumina (α-alumina as established by XRD analysis reported in Section 3.4.1) shows a lower thermal conductivity compared with stainless steel in the temperatures of interest (see Figure 5.13). The difference between thermal conductivity causes a different release of the heat in the reactors based on different materials. In case of alumina the heat produced by the reaction is released slower, generating a local increase in the temperature, improving the conversion rate. At the same time this contained heat can cause the degradation of the catalyst due to the presence of hot spots.

Figure 5.14 reports 50 hours of continuous operation of the SLS stainless

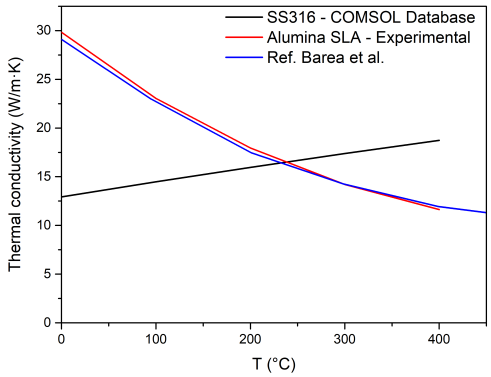

Figure 5.13: *Thermal conductivity of printed alumina in comparison with stainless steel. Reference of α-alumina produced by hot pressing at 1500°C [408].*

steel and SLA alumina test plates. The initial performance of the plates is different, as already presented in Figure 5.12. Both curves are characterized by an initial conditioning period (∼10-15h), which generates the strongest degradation, for a further stabilization during the rest of the operation, where the ss and alumina reactors present a degradation rate of 0.27%/h and 0.13%/h, respectively.

In addition, XRD experiments were carried out after testing (see Figures 5.9, 5.10 and 5.11). In all the cases, it was possible to observe the formation of

nickel metal (after reduction of nickel oxide) and not remarkable degradation of the catalyst or support were observed in the duration of the experiment. Overall, alumina plates are considered a better option after the series of experiments carried out in this study.

After the positive validation of using alumina as material for the support

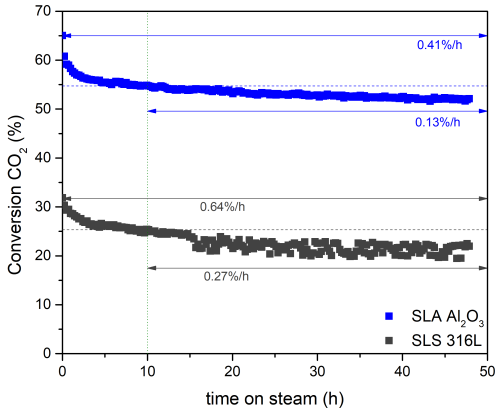

Figure 5.14: *Degradation over time of the CO_2 conversion, operating condition: T=290° C, WHSV=45 L/h·g_{cat}, P=6 bar.*

plates in the methanation reaction, the effect of 3D designs has been evaluated, following the same protocol. In particular, a herringbone pattern engraved in the microchannels was compared to a flat design. The conversion of CO_2 into methane for both approaches is presented in Figure 5.15 showing a better performance in the 3D structured channels. This improvement of ca. 15% in CO_2 conversion at 300°C can be simply explained by the increase of the area due to the engraving (+25%). Although the designs were defined to have the very same volume, bigger areas involve more exposure of the catalyst, which consequently increases the conversion of gas molecules.

Beyond the exposed area, another aspect to consider is the distribution of flow speed inside the channel and the residence time of the gas particles. To evaluate this parameter, COMSOL simulations were carried out for both designs (Figure 5.16). From the simulations, it is evidenced that the flat channel presents a distributed flow over its section, with a maximum speed of 0.18 m/s. On the other side, the herringbone design presents a higher speed in the central part of the channel (up to 0.25 m/s), while close to the walls and inside the engrave the speed is at a minimum, offering more time for the reaction to take place [302].

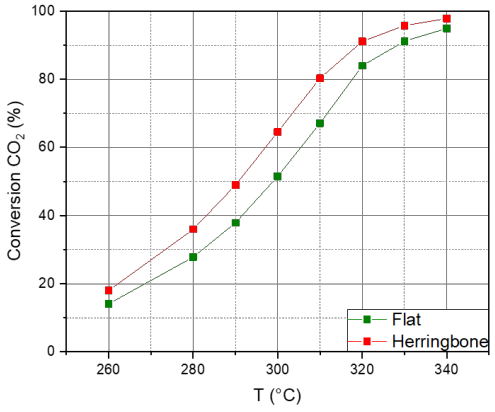

Figure 5.15: *CO_2 conversion for different test-plates designs produced in alumina by SLA as a function of temperature. Operating condition: WHSV=45 L/h g_{cat}, P=6 bar.*

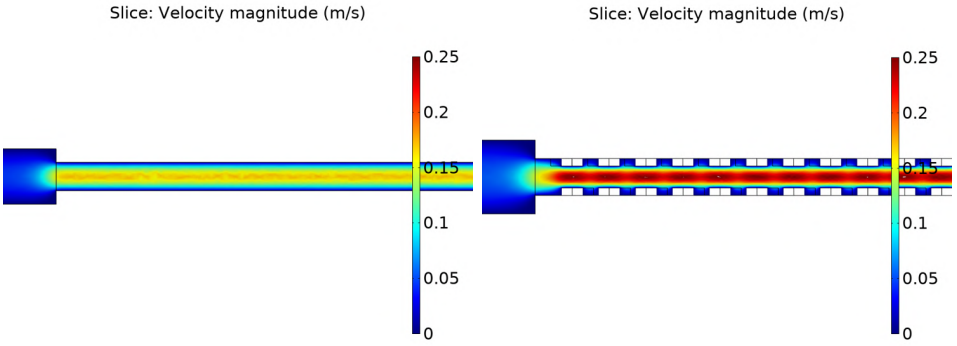

(a) Flat channel *(b) Herringbone channel*

Figure 5.16: *Simulation of the speed profiles inside flat and herringbone channels.*

The residence time has been evaluated studying the number of particles per unit time going out of the channel after simulated injection of N_{in}=3000 particles at t=0 (using the previously determined speed distribution). Figure 5.17 shows that the number of particles leaving the channel after the integration time is the same for both designs (N_{out}=2600). However, the shape of the curves reported is different depending on the pattern. In the case of the flat channel the curve keeps rising, while in the herringbone reaches a plateau. This trend has been interpreted as the particles in the centre of the channel are leaving quicker due to the higher speed profile, while the particles close to the walls, on the contrary, proceed slowly and get trapped

in the engraves. These slower particles have a higher residence time in the channel and have higher probability to react and be converted into methane, explaining the higher performance of this design.

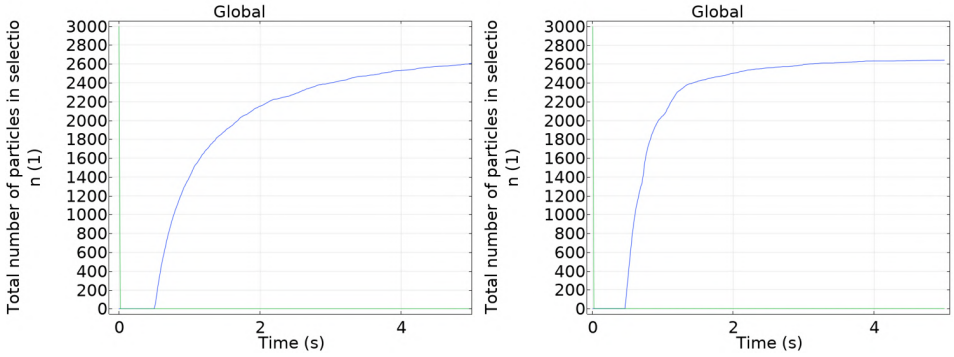

(a) Flat channel *(b) Herringbone channel*

Figure 5.17: *Simulation of the residence time inside the channels.*

All in all, the 3D printed alumina design shows a better performance and opens the way for further improvement of patterning strategies applied to methanation or other type of reactors.

5.4 Conclusion

Methanation beds fabricated with different materials (stainless steel and alumina) and conventional and additive manufacturing techniques have been tested in this chapter for the conversion of carbon dioxide and hydrogen into methane. The adhesion of a state-of-the-art catalyst on the different test plates has been investigated and correlated with the roughness and nature of the substrate surfaces. A better adhesion is achieved by a rough surface, as the one produced by powder sintering in SLS printed plates. A high compatibility has been detected between the catalyst and the alumina plates, due to a better matching thermal expansion coefficients and an excellent chemical affinity, which resulted in crack-free stable layers. XRD analysis was employed to structurally characterize the catalyst showing a proper reduction of the nickel oxide during operation and only few secondary phases (in ss reactors) introduced during the fabrication of the reactor. The amount of these phases is not considered high enough to reduce the activity of the catalyst. The analysis of the CO_2 conversion rate of these plates to methane shows better performance in the case of the alumina plates. This behaviour is ascribed to the lower thermal conductivity of the alumina compared with the one of the stainless steel, leading to a local increasing of the temperature in the reactor and consequently a higher performance. The advantage of using 3D printed plates in alumina has been proved by implementation of a patterned plate (herringbone-like microchannels) able to show better performance by design. The functionality of 3D printed plates and the relevance of 3D structuration proved here open a new pathway for design and fabrication of highly performing catalytic reactors based on 3D printing of ceramics.

Chapter 6

Conclusions and future developments

Conclusions

This work has been devoted to develop, implement and prove the suitability of additive manufacturing for the production of functional ceramics for energy application, in detail for SOCs and Sabatier reactor.
Two 3D printing techniques have been study in this framework, stereolithography and robocasting, and in particular their hybridization.
Developments and optimizations have been carried out in all the production steps, starting from the ceramic materials, the development of printable slurries, their process parameters, the dispensing system itself up to the thermal treatment to conclude with the performance characterization of the produced devices.
The achieved results can be divided in the achievements obtained thanks to the freedom of design, investigation carried out with a more consolidated technology such as the monomaterial printing of commercial pastes. The other part of the thesis has been devoted to the hybridization of stereolithography and robocasting technology with the aim to produce a single printed stack.

The use of stereolithography to produce **3D printed SOC electrolytes** based on 8mol% yttria stabilized zirconia has been validated, achieving comparable properties than the ones produced by traditional manufacturing such as tape casting. The advantage of using additive manufacturing is to **enhance the electrochemical performance through the design**. Both results have been achieved during this work, in detail:

- The printing process was optimized to achieve high quality and dense electrolyte of a thickness of 250 µm.
- Thermal cycles have been optimized to obtained electrolytes without traces of detrimental monoclinic phase.
- The electrolytes have been structural characterized (by XRD, SEM and Raman Spectroscopy) showing proper properties, comparable with 8YSZ produced by other technologies.
- Scanning electron microscopy to confirm the reproduction of the design with a resolution of 25 µm in the three direction.
- The generated pieces present properties comparable with the ones produced by traditional technologies, such as ionic conductivity of $3.0 \times 10^{-2}\,\mathrm{S/cm^2}$ at 800°C and an activation energy of 1.02 eV.
- Crack-free electrolytes with different designs unreachable by other manufacturing techniques have been printed. These designs are based on

square and wave corrugation and hexagons connected in the three dimensions.

- The attachment temperatures of the electrodes have been optimized on printed planar eñectrolytes, obtaining for NiO-YSZ a cycle at 1400°C and for LSM-YSZ at 1100°C. These temperatures have been used for the manufacturing of all the cells.

- The implementation of an adhesion layer has been developed and its beneficial effects have been proved achieving higher maximum output current compared with samples without such layer. No delamination at the electrolyte/electrodes interface were observed when the attachment layer is applied.

- The designs have been optimized on the base of two approaches: the printability, including the rate of success and the maximum of the performance, obtained by an increase of the area and the minimization of the ohmic losses due to the electrolyte shape. On these bases, the most promising design is a corrugated electrolyte based on a wave profile. This design presents homogeneous thickness over the electrolyte, offering an enhance of the active area of 57%, keeping the same outer dimension of a planar cell printed as comparison of the traditional manufacturing techniques.

- The wave corrugated cell has been electrochemically characterized in fuel cell, electrolysis and co-electrolysis mode between 800°C and 900°C, achieving excellent maximum power density of 410 mW/cm^2 in SOFC and a current density at 1.3 V of 600 mA/cm^2 in co-SOEC.

- High values of OCV (higher than 1.0 V) proved the gas-tightness of the electrolytes.

- Post-mortem analysis shows proper density of the electrolyte and porosity in the electrodes.

- This characteristic cell has operated in SOFC mode for over 650 hours, showing a degradation rate of 35 mV/kh after a conditioning period, proven the stability of the cells based on this technology.

Stereolithography have been used to produce **alumina support plates for Sabatier reaction**, the relative properties and effect on the CO_2 conversion have been evaluated:

- Printed alumina samples were structurally characterized, observing α phase in all the production steps.

- Better adhesion of Ni-CeO_2 catalyst has been proved on ceramic plates compared with milled and SLS printed stainless steel.
- Higher CO_2 conversion has been achieved in case of alumina test-plates, improving of 20% the results obtained on stainless steel.
- A herringbone base structuration has been developed on the alumina plates, generating a further improve of 15% compared to a planar design of the channel.

A hybrid prototype system, realized in the frame of the project Cell3Ditor, is devoted to the **production of SOC stacks in a single manufacturing step and co-sintering process**.

- Printable slurries for robocasting of material used in the SOCs technology (NiO-YSZ, LSM-YSZ, LCTM) have been developed from the ground up.
- Ceramic powders of the mentioned materials have been characterized by XRD to prove the composition.
- The absorbance of the powders have been evaluated, showing values above 90% at the laser wavelength (YSZ is around 30%).
- Proper monomers, diluent and photo-initiator have been investigated based on their reactivity with the laser wavelength.
- Organic mixtures showing Newtonian behavior proper for the formulation of ceramic slurries have been realized.
- Ink based on NiO-YSZ, LSM-YSZ and LCTM have been developed, reaching cure depths higher than 200 µm
- Removal of SLA material have been optimized to ensure the leveling of robocasting and SLA layers.
- Deposition of the robocasting inks have been optimized according to the machine possibilities.
- Thermal treatments have been optimized to avoid strong exothermic reactions, which damage the pieces. Co-sintering of the layers has been achieved with intermediate step at 1100°C for four hours and a final step at 1250°C for two hours. This leads to a sufficient density of the electrolyte, although the porosity of the air electrode needs to be further improved.
- The electrochemical characterization of single printed cell shows a maximum output power of $78\,mW/cm^2$ and a promising ASR of $2.0\,\Omega \cdot cm^2$.

Future perspective

This thesis has proved the unfair advantage of the 3D printing in the energy storage sector, as for the freedom of design and consequently the increase of outputs, as for the automatization and reduction of manufacturing steps. The improvement of the performance through the design has been proved as for SOCs as for methanation support, on the laboratory scale. The use of a commercial device will enable the scale-up of the proved advantages of additive manufacturing, to be competitive on the industrial point of view. Thanks to the intrinsic properties of additive manufacturing, the scale-up of the obtained systems is not restrain to a simple enlargement of the dimensions. Hierarchical, monolithic structures with integrated manifolds are the next step of the application of 3D printing to the energy sector.
Despite the promising outputs, several topics have been identified for further developments. Robocasting inks require deeper rheological analysis, with the purpose of tuning the viscoelasticity properties to be able of shaping more complex geometries, such as interdigitated channels. The air electrode requires a higher porosity, achievable with the use of pore former. Complex geometries and combination of ablation systems can further improve the performance of the hybrid cells.
It is worth to mention that this is the first PhD thesis on this topic in the group of research, which have led to start other two PhD projects.

Bibliography

[1] Matthew D. Leonard, Efstathios E. Michaelides and Dimitrios N. Michaelides. "Energy storage needs for the substitution of fossil fuel power plants with renewables". In: *Renewable Energy* 145 (2020), pp. 951–962. ISSN: 18790682. DOI: 10.1016/j.renene.2019.06.066. URL: https://doi.org/10.1016/j.renene.2019.06.066.

[2] World Health Organization. *Health, environment and climate change. Road map for an enhanced global response to the adverse health effects of air pollution.* Tech. rep. April. 2018, pp. 1–8.

[3] Georges Alexandre Lenferna. "Can we equitably manage the end of the fossil fuel era?" In: *Energy Research and Social Science* 35.March 2017 (2018), pp. 217–223. ISSN: 22146296. DOI: 10.1016/j.erss.2017.11.007. URL: https://doi.org/10.1016/j.erss.2017.11.007.

[4] Christopher Graves, Sune D. Ebbesen, Mogens Mogensen et al. "Sustainable hydrocarbon fuels by recycling CO2 and H 2O with renewable or nuclear energy". In: *Renewable and Sustainable Energy Reviews* 15.1 (2011), pp. 1–23. ISSN: 13640321. DOI: 10.1016/j.rser.2010.07.014.

[5] Ilgi Karapinar Kapdan and Fikret Kargi. "Bio-hydrogen production from waste materials". In: *Enzyme and Microbial Technology* 38.5 (2006), pp. 569–582. ISSN: 01410229. DOI: 10.1016/j.enzmictec.2005.09.015.

[6] C. V. Miguel, M. A. Soria, A. Mendes et al. "A sorptive reactor for CO2 capture and conversion to renewable methane". In: *Chemical Engineering Journal* 322 (2017), pp. 590–602. ISSN: 13858947. DOI: 10.1016/j.cej.2017.04.024. URL: http://dx.doi.org/10.1016/j.cej.2017.04.024.

[7] Leonhard Brandeis, David Sprake, Yuriy Vagapov et al. "Analysis of electrical energy storage technologies for future electric grids". In: *Proceedings of the 2016 IEEE North West Russia Section Young Researchers in Electrical and Electronic Engineering Conference, EIConRusNW 2016* (2016), pp. 513–518. DOI: 10.1109/EIConRusNW.2016.7448235.

[8] Muhammad H. Rashid, ed. *Power Electronics Handbook*. 2018, p. 1522. DOI: 10.1016/b978-0-12-811407-0.09995-5.

[9] Odne Stokke Burheim. *Engineering Energy Storage*. 2017, p. 252. DOI: 10.1016/b978-0-12-814100-7.00011-0.

[10] Imene Yahyaoui, ed. *Advances in Renewable Energies and Power Technologies*. Vol. 2. 2018, p. 536. DOI: 10.1016/b978-0-12-813185-5.09990-3.

[11] Soteris A. Kalogirou. *Solar Energy Engineering*. 2014, p. 840. DOI: 10.1016/b978-0-12-397270-5.01001-3.

[12] Paul Breeze. *Fuel Cells*. 2017, p. 100. ISBN: 9780081010396. DOI: 10.1016/b978-0-08-101039-6.00012-1.

[13] Ziyad Salameh. *Renewable Energy System Design*. 2014, p. 404. DOI: 10.1016/b978-0-12-374991-8.09996-7.

[14] Takao Watanabe. "Molten Carbonate Fuel Cells". In: *Handbook of Climate Change Mitigation*. Ed. by Wei-Yin Chen, John Seiner, Toshio Suzuki et al. Vol. 4. l. New York, NY: Springer US, 2012, pp. 1729–1754. ISBN: 978-1-4419-7991-9. DOI: 10.1007/978-1-4419-7991-9{_}45. URL: https://doi.org/10.1007/978-1-4419-7991-9_45.

[15] Ibrahim Dincer and Marc A. Rosen. *Exergy*. 2013, p. 576. DOI: 10.1016/b978-0-08-097089-9.01001-9.

[16] Frano Barbir, Angelo Basile and T. Nejat Veziroğlu, eds. *Compendium of Hydrogen Energy*. 2016, p. 328. ISBN: 9781845693305. DOI: 10.1016/b978-1-78242-363-8.09987-4.

[17] Patrick T Moseley and Jürgen Garche, eds. *Electrochemical Energy Storage for Renewable Sources and Grid Balancing*. 2015, p. 492. DOI: 10.1016/b978-0-444-62616-5.01001-9.

[18] "Science and Engineering of Hydrogen Based Energy Technologies". In: ed. by Paulo Emilio V. de Miranda. 2018, p. 438. DOI: 10.1016/b978-0-12-814251-6.01001-7.

[19] Paul Breeze. "CHAPTER 7 The Solid Oxide Fuel Cell". In: *Fuel Cells*. 2017, pp. 63–73. ISBN: 9780081010396. DOI: 10.1016/B978-0-08-101039-6.00007-8.

[20] N.P. Brandon and M.A. Parkes. "Fuel Cells: Materials". In: *Reference Module in Materials Science and Materials Engineering*. 2016, pp. 1–6. ISBN: 9780128035818. DOI: 10.1016/b978-0-12-803581-8.01726-4.

[21] K. Kendall. "Introduction to SOFCs". In: *High-Temperature Solid Oxide Fuel Cells for the 21st Century: Fundamentals, Design and Applications: Second Edition*. 2nd ed. 1. Elsevier Ltd., 2016, pp. 1–24. ISBN: 9780124104532. DOI: 10.1016/B978-0-12-410453-2.00001-4. URL: http://dx.doi.org/10.1016/B978-0-12-410453-2.00001-4.

[22] Samuel J. Cooper and Nigel P. Brandon. *An Introduction to Solid Oxide Fuel Cell Materials, Technology and Applications*. Elsevier Ltd, 2017, pp. 1–18. ISBN: 9780128097243. DOI: 10.1016/B978-0-08-101102-7.00001-5. URL: http://dx.doi.org/10.1016/B978-0-08-101102-7.00001-5.

[23] Roland Peters, Robert Deja, Maximilian Engelbracht et al. "Efficiency analysis of a hydrogen-fueled solid oxide fuel cell system with anode off-gas recirculation". In: *Journal of Power Sources* 328.1 (2016), pp. 105–113. ISSN: 03787753. DOI: 10.1016/j.jpowsour.2016.08.002. URL: http://dx.doi.org/10.1016/j.jpowsour.2016.08.002.

[24] Richard Payne, Michael Kah and Jonathan Love. "Generating Electricity at 60% Electrical Efficiency from 1-2 kWe SOFC Products". In: *ECS Transactions* 25.2 (2009), pp. 231–239. ISSN: 1098-6596. DOI: 10.1017/CBO9781107415324.004.

[25] Isabel Frenzel, Alexandra Loukou, Dimosthenis Trimis et al. "Development of an SOFC based micro-CHP system in the framework of the European project FC-DISTRICT". In: *Energy Procedia* 28.December (2012), pp. 170–181. ISSN: 18766102. DOI: 10.1016/j.egypro.2012.08.051.

[26] Ligang Wang, Ming Chen, Rainer Küngas et al. "Power-to-fuels via solid-oxide electrolyzer: Operating window and techno-economics". In: *Renewable and Sustainable Energy Reviews* 110.May (2019), pp. 174–187. ISSN: 18790690. DOI: 10.1016/j.rser.2019.04.071. URL: https://doi.org/10.1016/j.rser.2019.04.071.

[27] M. Cassidy, P. A. Connor, J. T.S. Irvine et al. "Anodes". In: *High-Temperature Solid Oxide Fuel Cells for the 21st Century: Fundamentals, Design and Applications: Second Edition* (2016), pp. 133–160. DOI: 10.1016/B978-0-12-410453-2.00005-1.

[28] J. A. Kilner, J. Druce and T. Ishihara. *Electrolytes*. 2016, pp. 85–132. ISBN: 9780124104532. DOI: 10.1016/B978-0-12-410453-2.00004-X.

[29] T. Kawada and T. Horita. *Cathodes*. 2016, pp. 161–193. ISBN: 9780124104532. DOI: 10.1016/B978-0-12-410453-2.00006-3.

[30] San Ping Jiang. *Development of lanthanum strontium manganite perovskite cathode materials of solid oxide fuel cells: A review*. Vol. 43. 21. 2008, pp. 6799–6833. ISBN: 1085300829666. DOI: 10.1007/s10853-008-2966-6.

[31] M. A. Laguna-Bercero. "Recent advances in high temperature electrolysis using solid oxide fuel cells: A review". In: *Journal of Power Sources* 203 (2012), pp. 4–16. ISSN: 03787753. DOI: 10.1016/j.jpowsour.2011.12.019. URL: http://dx.doi.org/10.1016/j.jpowsour.2011.12.019.

[32] Giovanni Cinti, Arianna Baldinelli, Alessandro Di Michele et al. "Integration of Solid Oxide Electrolyzer and Fischer-Tropsch: A sustainable pathway for synthetic fuel". In: *Applied Energy* 162 (2016), pp. 308–320. ISSN: 03062619. DOI: 10.1016/j.apenergy.2015.10.053. URL: http://dx.doi.org/10.1016/j.apenergy.2015.10.053.

[33] Daniel J.L. Brett, Alan Atkinson, Nigel P. Brandon et al. "Intermediate temperature solid oxide fuel cells". In: *Chemical Society Reviews* 37.8 (2008), pp. 1568–1578. ISSN: 03060012. DOI: 10.1039/b612060c.

[34] F. Tietz. "Materials selection for solid oxide fuel cells". In: *Materials Science Forum* 426-432.5 (2003), pp. 4465–4470. ISSN: 02555476. DOI: 10.4028/www.scientific.net/MSF.426-432.4465.

[35] Ellen Ivers-Tiffée, André Weber and Dirk Herbstritt. "Materials and technologies for SOFC-components". In: *Journal of the European Ceramic Society* 21.10-11 (2001), pp. 1805–1811. ISSN: 09552219. DOI: 10.1016/S0955-2219(01)00120-0.

[36] Keegan C. Wincewicz and Joyce S. Cooper. "Taxonomies of SOFC material and manufacturing alternatives". In: *Journal of Power Sources* 140.2 (2005), pp. 280–296. ISSN: 03787753. DOI: 10.1016/j.jpowsour.2004.08.032.

[37] S. P.S. Badwal, F. T. Ciacchi and D. Milosevic. "Scandia-zirconia electrolytes for intermediate temperature solid oxide fuel cell operation". In: *Solid State Ionics* 136-137 (2000), pp. 91–99. ISSN: 01672738. DOI: 10.1016/S0167-2738(00)00356-8.

[38] Masanori Hirano, Takayuki Oda, Kenji Ukai et al. "Effect of Bi2O3 additives in Sc stabilized zirconia electrolyte on a stability of crystal phase and electrolyte properties". In: *Solid State Ionics* 158.3-4 (2003), pp. 215–223. ISSN: 01672738. DOI: 10.1016/S0167-2738(02)00912-8.

[39] Hideaki Inaba and Hiroaki Tagawa. "Ceria-based solid electrolytes". In: *Solid State Ionics* 83.1–2 (1996), pp. 1–16. ISSN: 0167-2738. DOI: http://dx.doi.org/10.1016/0167-2738(95)00229-4. URL: http://www.sciencedirect.com/science/article/pii/0167273895002294.

[40] M. Morales, A. Pesce, A. Slodczyk et al. "Enhanced Performance of Gadolinia-Doped Ceria Diffusion Barrier Layers Fabricated by Pulsed Laser Deposition for Large-Area Solid Oxide Fuel Cells". In: *ACS Applied Energy Materials* 1.5 (2018). ISSN: 25740962. DOI: 10.1021/acsaem.8b00039.

[41] K. Eguchi, T. Setoguchi, T. Inoue et al. "Electrical properties of ceria-based oxides and their application to solid oxide fuel cells". In: *Solid State Ionics* 52.1-3 (1992), pp. 165–172. ISSN: 01672738. DOI: 10.1016/0167-2738(92)90102-U.

[42] Tatsumi Ishihara. "Development of new fast oxide ion conductor and application for intermediate temperature Solid Oxide Fuel Cells". In: *Bulletin of the Chemical Society of Japan* 79.8 (2006), pp. 1155–1166. ISSN: 00092673. DOI: 10.1246/bcsj.79.1155.

[43] B. Singh, S. Ghosh, S. Aich et al. "Low temperature solid oxide electrolytes (LT-SOE): A review". In: *Journal of Power Sources* 339.November 2016 (2017), pp. 103–135. ISSN: 03787753. DOI: 10.1016/j.jpowsour.2016.11.019. URL: http://dx.doi.org/10.1016/j.jpowsour.2016.11.019.

[44] Swee Leong Sing, Wai Yee Yeong, Florencia Edith Wiria et al. "Direct selective laser sintering and melting of ceramics: a review". In: *Rapid Prototyping Journal* 23.3 (2017). ISSN: 1355-2546. DOI: 10.1108/RPJ-11-2015-0178.

[45] Eric D. Wachsman and Kang Taek Lee. "Lowering the temperature of solid oxide fuel cells". In: *Science* 334 (2011), pp. 935–939.

[46] Zhan Gao, Liliana Veronica Mogni, Elizabeth C. Miller et al. "A perspective on low-temperature solid oxide fuel cells". In: *Energy Environ. Sci.* 9.5 (2016), pp. 1602–1644. ISSN: 1754-5692. DOI: 10.1039/C5EE03858H. URL: http://pubs.rsc.org/en/content/articlehtml/2016/ee/c5ee03858h%5Cnhttp://xlink.rsc.org/?DOI=C5EE03858H.

[47] Neelima Mahato, Amitava Banerjee, Alka Gupta et al. "Progress in material selection for solid oxide fuel cell technology: A review". In: *Progress in Materials Science* 72 (2015), pp. 141–337. ISSN: 00796425. DOI: 10.1016/j.pmatsci.2015.01.001. URL: http://dx.doi.org/10.1016/j.pmatsci.2015.01.001.

[48] A. Atkinson, S. Barnett, R. J. Gorte et al. "Advanced anodes for high-Temperature fuel cells". In: *Nature Materials* 3 (2004), pp. 17–27. ISSN: 03603199. DOI: 10.1016/j.ijhydene.2011.03.057.

[49] Antonin Faes, Aïcha Hessler-Wyser, Amédée Zryd et al. "A review of RedOx cycling of solid oxide fuel cells anode". In: *Membranes* 2.3 (2012), pp. 585–664. ISSN: 20770375. DOI: 10.3390/membranes2030585.

[50] T. Klemenso, C. Chung, P. H. Larsen et al. "The Mechanism Behind Redox Instability of Anodes in High-Temperature SOFCs". In: *Journal of The Electrochemical Society* 152.11 (2005), A2186. ISSN: 00134651. DOI: 10.1149/1.2048228.

[51] Mark Cassidy, Dragos Neagu, Cristian Savaniu et al. *New Materials for Improved Durability and Robustness in Solid Oxide Fuel Cell*. Elsevier Ltd, 2017, pp. 193–216. ISBN: 9780128097243. DOI: 10.1016/B978-0-08-101102-7.00010-6. URL: http://dx.doi.org/10.1016/B978-0-08-101102-7.00010-6.

[52] Kenji Ukai and Osamu Yamamoto. "Current Status of SOFC Development Using Scandia Doped Zirconia". In: *ECS Proceedings Volumes* 2001-16.1 (2001), pp. 375–383. ISSN: 0161-6374. DOI: 10.1149/200116.0375pv.

[53] Olga A. Marina, Carsten Bagger, Søren Primdahl et al. "A solid oxide fuel cell with a gadolinia-doped ceria anode: Preparation and performance". In: *Solid State Ionics* 123.1-4 (1999), pp. 199–208. ISSN: 01672738. DOI: 10.1016/s0167-2738(99)00111-3.

[54] O. A. Marina, S. Primdahl, C. Bagger et al. "Ceria-Based Anodes on a YSZ Electrolyte: Preparation and Electrochemical Performance". In: *ECS Proceedings Volumes* 1997-40.1 (1997), pp. 540–548. ISSN: 0161-6374. DOI: 10.1149/199740.0540pv.

[55] Ranran Peng, Changrong Xia, Xingqin Liu et al. "Prepared By Screen-Printing". In: *Solid State Ionics* 153 (2002), pp. 561–565.

[56] N. Kiratzis, P. Holtappels, C.E. Hatchwell et al. "Preparation and Characterization of Copper/Yttria Titania Zirconia Cermets for Use as Possible Solid Oxide Fuel Cell Anodes". In: *Fuel Cells* 1.3-4 (2001), pp. 211–218. ISSN: 1615-6846. DOI: 10.1002/1615-6854(200112)1:3/4<211::aid-fuce211>3.0.co;2-h.

[57] Sung Pil Yoon, Jonghee Han, Suk Woo Nam et al. "Performance of anode-supported solid oxide fuel cell with with La0,85Sr0,15MnO3 cathode modified by sol-gel coating technique". In: *Journal of Power Sources* 106 (2002), pp. 160–166. URL: https://ac-els-cdn-com.prx.library.gatech.edu/S0378775301010370/1-s2.0-S0378775301010370-main.pdf?_tid=e575d80c-0f5d-11e8-9cf2-00000aab0f6b&acdnat=1518375847_c6f4ab1f28e29cf7017cf175ad8f26ff.

[58] S. P.S. Badwal. "Stability of solid oxide fuel cell components". In: *Solid State Ionics* 143.1 (2001), pp. 39–46. ISSN: 01672738. DOI: 10.1016/S0167-2738(01)00831-1.

[59] N. T. Hart, N. P. Brandon, M. J. Day et al. "Functionally graded composite cathodes for solid oxide fuel cells". In: *Journal of Power Sources* 106.1-2 (2002), pp. 42–50. ISSN: 03787753. DOI: 10.1016/S0378-7753(01)01035-7.

[60] Steven P. Simner, J. F. Bonnett, N. L. Canfield et al. "Development of lanthanum ferrite SOFC cathodes". In: *Journal of Power Sources* 113.1 (2003), pp. 1–10. ISSN: 03787753. DOI: 10.1016/S0378-7753(02)00455-X.

[61] Rajiv Doshi. "Development of Solid-Oxide Fuel Cells That Operate at 500°C". In: *Journal of The Electrochemical Society* 146.4 (1999), p. 1273. ISSN: 00134651. DOI: 10.1149/1.1391758.

[62] Lei Wang, Rotraut Merkle and Joachim Maier. "Surface Kinetics and Mechanism of Oxygen Incorporation Into Ba[sub 1x]Sr[sub x]Co[sub y]Fe[sub 1y]O[sub 3δ] SOFC Microelectrodes". In: *Journal of The Electrochemical Society* 157.12 (2010), B1802. ISSN: 00134651. DOI: 10.1149/1.3494224.

[63] Dengjie Chen, Ran Ran, Kun Zhang et al. "Intermediate-temperature electrochemical performance of a polycrystalline PrBaCo2O5+δ cathode on samarium-doped ceria electrolyte". In: *Journal of Power Sources* 188.1 (2009), pp. 96–105. ISSN: 03787753. DOI: 10.1016/j.jpowsour.2008.11.045.

[64] S. J. Skinner and J. A. Kilner. "Oxygen diffusion and surface exchange in La2-xSrxNiO4+δ". In: *Solid State Ionics* 135.1-4 (2000), pp. 709–712. ISSN: 01672738. DOI: 10.1016/S0167-2738(00)00388-X.

[65] Maya Sase, Keiji Yashiro, Kazuhisa Sato et al. "Enhancement of oxygen exchange at the hetero interface of (La,Sr)CoO3/(La,Sr)2CoO4 in composite ceramics". In: *Solid State Ionics* 178.35-36 (2008), pp. 1843–1852. ISSN: 01672738. DOI: 10.1016/j.ssi.2007.11.039.

[66] F. Mauvy, J. M. Bassat, E. Boehm et al. "Oxygen electrode reaction on Nd2NiO4+δ cathode materials: Impedance spectroscopy study". In: *Solid State Ionics* 158.1-2 (2003), pp. 17–28. ISSN: 01672738. DOI: 10.1016/S0167-2738(02)00689-6.

[67] W. Z. Zhu and S. C. Deevi. "Development of interconnect materials for solid oxide fuel cells". In: *Materials Science and Engineering A* 348.1-2 (2003), pp. 227–243. ISSN: 09215093. DOI: 10.1016/S0921-5093(02)00736-0.

[68] L. Niewolak, F. Tietz and W. J. Quadakkers. *Interconnects*. 2016, pp. 195–254. ISBN: 9780124104532. DOI: 10.1016/B978-0-12-410453-2.00007-5.

[69] Sean Giles, Guangyong Lin, Aravind Mohanram et al. "Saint-Gobain's All Ceramic SOFC Stack: Architecture and Performance". In: *ECS Transactions* 57.1 (2013), pp. 105–114. ISSN: 1098-6596. DOI: 10.1017/CBO9781107415324.004.

[70] R. W. Jackson, F. S. Pettit and G. H. Meier. "The behavior of nickel and silver in a simulated solid oxide fuel cell environment". In: *Journal of Power Sources* 185.2 (2008), pp. 1030–1039. ISSN: 03787753. DOI: 10.1016/j.jpowsour.2008.08.056.

[71] Yoshio Matsuzaki and Isamu Yasuda. "Dependence of SOFC Cathode Degradation by Chromium-Containing Alloy on Compositions of Electrodes and Electrolytes". In: *Journal of The Electrochemical Society* 148.2 (2001), A126. ISSN: 00134651. DOI: 10.1149/1.1339869.

[72] S. P.S. Badwal, R. Deller, K. Foger et al. "Interaction between chromia forming alloy interconnects and air electrode of solid oxide fuel cells". In: *Solid State Ionics* 99.3-4 (1997), pp. 297–310. ISSN: 01672738. DOI: 10.1016/s0167-2738(97)00247-6.

[73] E. Konysheva, J. Mertens, H. Penkalla et al. "Chromium Poisoning of the Porous Composite Cathode". In: *Journal of The Electrochemical Society* 154.12 (2007), B1252. ISSN: 00134651. DOI: 10.1149/1.2784197.

[74] Anita Neumann, Norbert H. Menzler, Ico Vinke et al. "Systematic Study of Chromium Poisoning of LSM Cathodes - Single Cell Tests". In: *ECS Transactions* 25.2 (2009), pp. 2889–2898. ISSN: 19385862. DOI: 10.1149/1.3205854.

[75] N.H. Menzler, Peter Batfalsky, Sonja Groß et al. "Post-Test Characterization of an SOFC Short-Stack after 17,000 Hours of Steady Operation". In: 35.1 (2011), pp. 195–206. ISSN: 19385862. DOI: 10.1149/1.3569994.

[76] K. Fujita, K. Ogasawara, Y. Matsuzaki et al. "Prevention of SOFC cathode degradation in contact with Cr-containing alloy". In: *Journal of Power Sources* 131.1-2 (2004), pp. 261–269. ISSN: 03787753. DOI: 10.1016/j.jpowsour.2003.12.051.

[77] X. Montero, N. Jordán, J. Pirón-Abellán et al. "Spinel and Perovskite Protection Layers Between Crofer22APU and La[sub 0.8]Sr[sub 0.2]FeO[sub 3] Cathode Materials for SOFC Interconnects". In: *Journal of The Electrochemical Society* 156.1 (2009), B188. ISSN: 00134651. DOI: 10.1149/1.3025914.

[78] X. Montero, F. Tietz, D. Stöver et al. "Comparative study of perovskites as cathode contact materials between an La0.8Sr0.2FeO3 cathode and a Crofer22APU interconnect in solid oxide fuel cells". In: *Journal of Power Sources* 188.1 (2009), pp. 148–155. ISSN: 03787753. DOI: 10.1016/j.jpowsour.2008.11.083.

[79] Jong Jin Choi, Joo Hee Lee, Dong Soo Park et al. "Oxidation resistance coating of LSM and LSCF on SOFC metallic interconnects by the aerosol deposition process". In: *Journal of the American Ceramic Society* 90.6 (2007), pp. 1926–1929. ISSN: 00027820. DOI: 10.1111/j.1551-2916.2007.01641.x.

[80] Zhenguo Yang, Guan-Guang Xia, Gary D. Maupin et al. "Evaluation of Perovskite Overlay Coatings on Ferritic Stainless Steels for SOFC Interconnect Applications". In: *Journal of The Electrochemical Society* 153.10 (2006), A1852. ISSN: 00134651. DOI: 10.1149/1.2239371.

[81] M. Stanislowski, J. Froitzheim, L. Niewolak et al. "Reduction of chromium vaporization from SOFC interconnectors by highly effective coatings". In: *Journal of Power Sources* 164.2 (2007), pp. 578–589. ISSN: 03787753. DOI: 10.1016/j.jpowsour.2006.08.013.

[82] L. Blum, P. Batfalsky, L. G. J. de Haart et al. "Overview on the Jülich SOFC Development Status L. Blum". In: *ECS Transactions* 57.1 (2013), pp. 23–33.

[83] F. Tietz, A. Schmidt and M. Zahid. "Investigation of the quasi-ternary system LaMnO3-LaCoO 3-"LaCuO3" - I: The series La(Mn 0.5Co0.5)1-xCuxO3-δ". In: *Journal of Solid State Chemistry* 177.3 (2004), pp. 745–751. ISSN: 00224596. DOI: 10.1016/j.jssc.2003.08.029.

[84] F. Tietz, I. Arul Raj, Q. X. Fu et al. "Investigation of the quasi-ternary system LaMnO3-LaCoO 3-"LaCuO3". II: The series LaMn0.25-x Co0.75-x Cu2x O3-δ and LaMn 0.75-x Co0.25-x Cu2x O3-δ". In: *Journal of Materials Science* 44.18 (2009), pp. 4883–4891. ISSN: 00222461. DOI: 10.1007/s10853-009-3746-7.

[85] W. J. Quadakkers, J. Piron-Abellan, V. Shemet et al. "Metallic interconnectors for solid oxide fuel cells- A review". In: *Materials at High Temperatures* 20.2 (2003), pp. 115–127. ISSN: 09603409. DOI: 10.3184/096034003782749071.

[86] Worawarit Kobsiriphat and Scott Barnett. "Ag-Cu-Ti braze materials for sealing SOFCs". In: *Journal of Fuel Cell Science and Technology* 5.1 (2008), pp. 1–7. ISSN: 1550624X. DOI: 10.1115/1.2784279.

[87] Martin Bram, Leszek Niewolak, Nikhil Shah et al. "Interaction of sealing material mica with interconnect steel for solid oxide fuel cells application at 600 °c". In: *Journal of Power Sources* 196.14 (2011), pp. 5889–5896. ISSN: 03787753. DOI: 10.1016/j.jpowsour.2011.02.086. URL: http://dx.doi.org/10.1016/j.jpowsour.2011.02.086.

[88] Norbert H. Menzler, Frank Tietz, Sven Uhlenbruck et al. "Materials and manufacturing technologies for solid oxide fuel cells". In: *Journal of Materials Science* 45.12 (2010), pp. 3109–3135. ISSN: 00222461. DOI: 10.1007/s10853-010-4279-9.

[89] V. A.C. Haanappel, V. Shemet, S. M. Gross et al. "Behaviour of various glass-ceramic sealants with ferritic steels under simulated SOFC stack conditions". In: *Journal of Power Sources* 150.1-2 (2005), pp. 86–100. ISSN: 03787753. DOI: 10.1016/j.jpowsour.2005.02.015.

[90] Yeong Shyung Chou, Jeffry W. Stevenson and Prabhakar Singh. "Effect of aluminizing of Cr-containing ferritic alloys on the seal strength of a novel high-temperature solid oxide fuel cell sealing glass". In: *Journal of Power Sources* 185.2 (2008), pp. 1001–1008. ISSN: 03787753. DOI: 10.1016/j.jpowsour.2008.09.004.

[91] Nima Shaigan, Wei Qu, Douglas G. Ivey et al. "A review of recent progress in coatings, surface modifications and alloy developments for solid oxide fuel cell ferritic stainless steel interconnects". In: *Journal of Power Sources* 195.6 (2010), pp. 1529–1542. ISSN: 03787753. DOI: 10.1016/j.jpowsour.2009.09.069.

[92] Cuijuan Zhang, Chengxiang Ji, Wensheng Wang et al. "A dynamic solid oxide fuel cell empowered by the built-in iron-bed solid fuel". In: *Energy and Environmental Science* 9.12 (2016), pp. 3746–3753. ISSN: 17545706. DOI: 10.1039/c6ee02419j.

[93] Toshio Suzuki, Toshiaki Yamaguchi, Koichi Hamamoto et al. "A functional layer for direct use of hydrocarbon fuel in low temperature solid-oxide fuel cells". In: *Energy and Environmental Science* 4.3 (2011), pp. 940–943. ISSN: 17545692. DOI: 10.1039/c0ee00231c.

[94] Beom Kyeong Park, Jong Won Lee, Seung Bok Lee et al. "A flat-tubular solid oxide fuel cell with a dense interconnect film coated on the porous anode support". In: *Journal of Power Sources* 213 (2012), pp. 218–222. ISSN: 03787753. DOI: 10.1016/j.jpowsour.2012.04.025. URL: http://dx.doi.org/10.1016/j.jpowsour.2012.04.025.

[95] N. Q. Minh. *Cell and Stack Design, Fabrication and Performance*. 2nd ed. Elsevier Ltd., 2016, pp. 255–282. ISBN: 9780124104532. DOI: 10.1016/B978-0-12-410453-2.00008-7. URL: http://dx.doi.org/10.1016/B978-0-12-410453-2.00008-7.

[96] M. Kawalec, R. Kluczowski and M. Krauz. "Manufacturing technology of AS-SOFC prepared with different commercially available precursors". In: *E3S Web of Conferences* 10 (2016), pp. 0–3. ISSN: 22671242. DOI: 10.1051/e3sconf/20161000033.

[97] Michael Day, Scott L. Swartz and Gene Arkenberg. "NexTech's FlexCell Technology for Planar SOFC Stacks". In: (2011), pp. 385–391. ISSN: 19385862. DOI: 10.1149/1.3570013.

[98] Anna Evans, Anja Bieberle-Hütter, Jennifer L.M. Rupp et al. "Review on microfabricated micro-solid oxide fuel cell membranes". In: *Journal of Power Sources* 194.1 (2009), pp. 119–129. ISSN: 03787753. DOI: 10.1016/j.jpowsour.2009.03.048.

[99] Subhash C. Singhal. "Solid oxide fuel cells for power generation". In: *Wiley Interdisciplinary Reviews: Energy and Environment* 3.2 (2014), pp. 179–194. ISSN: 20418396. DOI: 10.1002/wene.96.

[100] Osamu Yamamoto. "Solid oxide fuel cells: Fundamental aspects and prospects". In: *Electrochimica Acta* 45.15-16 (2000), pp. 2423–2435. ISSN: 00134686. DOI: 10.1016/S0013-4686(00)00330-3.

[101] Muneeb Irshad, Khurram Siraj, Rizwan Raza et al. "A brief description of high temperature solid oxide fuel cell's operation, materials, design, fabrication technologies and performance". In: *Applied Sciences (Switzerland)* 6.3 (2016). ISSN: 20763417. DOI: 10.3390/app6030075.

[102] "HIGH-TEMPERATURE SOLID-OXIDE FUEL CELLS (SOFCs)". In: *Assessment of Research Needs for Advanced Fuel Cells* (1986), pp. 209–229. DOI: 10.1016/b978-0-08-033990-0.50011-3.

[103] Inc. EG&G Technical Services. *Fuel Cell Handbook*. 2004. DOI: 10.1016/s0031-9422(00)82398-5.

[104] Bernd Bitterlich, Christiane Lutz and Andreas Roosen. "Rheological characterization of water-based slurries for the tape casting process". In: *Ceramics International* 28 (2002), pp. 675–683. ISSN: 09240136. DOI: 10.1016/j.jmatprotec.2005.03.007.

[105] Niels Christiansen, J B. Hansen, H H. Larsen et al. "Solid Oxide Fuel Cell Development at Topsoe Fuel Cell A/S and Riso National Laboratory". In: *ECS Transactions* 7.1 (2007), pp. 31–38. DOI: 10.1149/1.2729070.

[106] Nader Hedayat, Yanhai Du and Hoda Ilkhani. "Review on fabrication techniques for porous electrodes of solid oxide fuel cells by sacrificial template methods". In: *Renewable and Sustainable Energy Reviews* 77.March (2017), pp. 1221–1239. ISSN: 18790690. DOI: 10.1016/j.rser.2017.03.095. URL: http://dx.doi.org/10.1016/j.rser.2017.03.095.

[107] W. A. Meulenberg, N. H. Menzler, H. P. Buchkremer et al. "Manufacturing routes and state-of-the-art of the planar Julich anode-supported concept for solid oxide fuel cells". In: *Materials for Electrochemical Energy Conversion and Storage*. Ed. by Arumugam Manthiram, Prashant N. Kumta, S. K. Sundaram et al. Vol. 127. 2002. Chap. 11, pp. 99–108. DOI: 10.1002/adma.201703044.

[108] F. J. Gardner, M. J. Day, N. P. Brandon et al. "SOFC technology development at Rolls-Royce". In: *Journal of Power Sources* 86.1 (2000), pp. 122–129. ISSN: 03787753. DOI: 10.1016/S0378-7753(99)00428-0.

[109] Peter Ried, Christiane Lorenz, Anke Brönstrup et al. "Processing of YSZ screen printing pastes and the characterization of the electrolyte layers for anode supported SOFC". In: *Journal of the European Ceramic Society* 28.9 (2008), pp. 1801–1808. ISSN: 09552219. DOI: 10.1016/j.jeurceramsoc.2007.11.018.

[110] K. U. Birnbaum, R. Steinberger-Wilkens and P. Zapp. *Solid Oxide Fuel Cells, Sustainability Aspects*. Ed. by R.A. Meyers. Spriger, 2012. ISBN: 9781441908513. DOI: 10.1007/978-1-4419-0851-3.

[111] Wen Shuo Hsieh, Pang Lin and Sea Fue Wang. "Fabrication of electrolyte supported micro-tubular SOFCs using extrusion and dip-coating". In: *International Journal of Hydrogen Energy* 38.6 (2013), pp. 2859–2867. ISSN: 03603199. DOI: 10.1016/j.ijhydene.2012.12.056. URL: http://dx.doi.org/10.1016/j.ijhydene.2012.12.056.

[112] Xingyan Xu, Changrong Xia, Shouguo Huang et al. "YSZ thin films deposited by spin-coating for IT-SOFCs". In: *Ceramics International* 31.8 (2005), pp. 1061–1064. ISSN: 02728842. DOI: 10.1016/j.ceramint.2004.11.005.

[113] O. Buchler, M. Bram, R. Mucke et al. "Preparation of Thin Functional Layers for Anode-Supported SOFC By The Roll Coating Process O." In: *ECS Transactions* 25.2 (2009), pp. 655–663. ISSN: 1098-6596. DOI: 10.1017/CBO9781107415324.004.

[114] D. Hathiramani, R. Vaßen, D. Stöver et al. "Comparison of atmospheric plasma sprayed anode layers for SOFCs using different feedstock". In: *Proceedings of the International Thermal Spray Conference* 15.December (2006), pp. 593–597. ISSN: 10599630. DOI: 10.1361/105996306X146811.

[115] A. A. Syed, Z. Ilhan, J. Arnold et al. "Improving plasma-sprayed yttria-stabilized zirconia coatings for solid oxide fuel cell electrolytes". In: *Proceedings of the International Thermal Spray Conference* 15.December (2006), pp. 617–622. ISSN: 10599630. DOI: 10.1361/105996306X147207.

[116] Hwa Young Jung, Kug-Sun Hong, Hyoungchul Kim et al. "Characterization of Thin-Film YSZ Deposited via EB-PVD Technique in Anode-supported SOFCs". In: *Journal of The Electrochemical Society* 153.6 (2006), A961. ISSN: 00134651. DOI: 10.1149/1.2186209.

[117] Tsepin Tsai. "Bias Sputter Deposition of Dense Yttria-Stabilized Zirconia Films on Porous Substrates". In: *Journal of The Electrochemical Society* 142.9 (1995), p. 3084. ISSN: 00134651. DOI: 10.1149/1.2048692.

[118] U. B. Pal. "Electrochemical Vapor Deposition of Yttria-Stabilized Zirconia Films". In: *ECS Proceedings Volumes* 1989-11.1 (1989), pp. 41–56. ISSN: 0161-6374. DOI: 10.1149/198911.0041pv.

[119] Stefan Rönsch, Jens Schneider, Steffi Matthischke et al. "Review on methanation - From fundamentals to current projects". In: *Fuel* 166 (2016), pp. 276–296. ISSN: 00162361. DOI: 10.1016/j.fuel.2015.10.111.

[120] Wei Wang and Jinlong Gong. "Methanation of carbon dioxide: An overview". In: *Frontiers of Chemical Engineering in China* 5.1 (2011), pp. 2–10. ISSN: 16737369. DOI: 10.1007/s11705-010-0528-3.

[121] F. Fisher, H. Tropsch and P. Dilthey. "Reduction of carbon monoxide to methane in the presence of various metals". In: *Brennst. Chem.* 6 (1925), pp. 265–271.

[122] G Alex Mills and Fred W Steffgen. "Catalysis Reviews : Science and Engineering Catalytic Methanation". In: *Catalysis Reviews* 8.1 (1974), pp. 159–210. DOI: http://dx.doi.org/10.1080/01614947408071860.

[123] Jiajian Gao, Qing Liu, Fangna Gu et al. "Recent advances in methanation catalysts for the production of synthetic natural gas". In: *RSC Advances* 5.29 (2015), pp. 22759–22776. ISSN: 20462069. DOI: 10.1039/c4ra16114a.

[124] Sudhanshu Sharma, Zhenpeng Hu, Peng Zhang et al. "CO2 methanation on Ru-doped ceria". In: *Journal of Catalysis* 278.2 (2011), pp. 297–309. ISSN: 00219517. DOI: 10.1016/j.jcat.2010.12.015. URL: http://dx.doi.org/10.1016/j.jcat.2010.12.015.

[125] Takayuki Abe, Masaaki Tanizawa, Kuniaki Watanabe et al. "CO2 methanation property of Ru nanoparticle-loaded TiO 2 prepared by a polygonal barrel-sputtering method". In: *Energy and Environmental Science* 2.3 (2009), pp. 315–321. ISSN: 17545692. DOI: 10.1039/b817740f.

[126] Ja Hun Kwak, Libor Kovarik and János Szanyi. "CO2 reduction on supported Ru/Al2O3 catalysts: Cluster size dependence of product selectivity". In: *ACS Catalysis* 3.11 (2013), pp. 2449–2455. ISSN: 21555435. DOI: 10.1021/cs400381f.

[127] Wenlong Zhen, Bo Li, Gongxuan Lu et al. "Enhancing catalytic activity and stability for CO2 methanation on Ni-Ru/γ-Al2O3via modulating impregnation sequence and controlling surface active species". In: *RSC Advances* 4.32 (2014), pp. 16472–16479. ISSN: 20462069. DOI: 10.1039/c3ra47982j.

[128] Changkun Yuan, Nan Yao, Xinde Wang et al. "The SiO2 supported bimetallic Ni-Ru particles: A good sulfur-tolerant catalyst for methanation reaction". In: *Chemical Engineering Journal* 260 (2015), pp. 1–10. ISSN: 13858947. DOI: 10.1016/j.cej.2014.08.079. URL: http://dx.doi.org/10.1016/j.cej.2014.08.079.

[129] Wen Jie Shen, Mitsutaka Okumura, Yasuyuki Matsumura et al. "The influence of the support on the activity and selectivity of Pd in CO hydrogenation". In: *Applied Catalysis A: General* 213.2 (2001), pp. 225–232. ISSN: 0926860X. DOI: 10.1016/S0926-860X(01)00465-3.

[130] J. Martins, N. Batail, S. Silva et al. "CO2hydrogenation with shape-controlled Pd nanoparticles embedded in mesoporous silica: Elucidating stability and selectivity issues". In: *Catalysis Communications* 58 (2015), pp. 11–15. ISSN: 15667367. DOI: 10.1016/j.catcom.2014.08.027.

[131] Alessandro Trovarelli, Carla de Leitenburg, Giuliano Dolcetti et al. *CO2 methanation under transient and steady-state conditions over Rh/CeO2 and CeO2-Promoted Rh/SiO2: The role of surface and bulk ceria*. 1995. DOI: 10.1006/jcat.1995.1014.

[132] Myoung Yeob Kim, Seung Bong Ha, Dong Jun Koh et al. "CO methanation over supported Mo catalysts in the presence of H 2S". In: *Catalysis Communications* 35 (2013), pp. 68–71. ISSN: 15667367. DOI: 10.1016/j.catcom.2013.02.004. URL: http://dx.doi.org/10.1016/j.catcom.2013.02.004.

[133] Baowei Wang, Yuqin Yao, Minhong Jiang et al. "Effect of cobalt and its adding sequence on the catalytic performance of MoO3/Al2O3 toward sulfur-resistant methanation". In: *Journal of Energy Chemistry* 23.1 (2014), pp. 35–42. ISSN: 20954956. DOI: 10.1016/S2095-4956(14)60115-7. URL: http://dx.doi.org/10.1016/S2095-4956(14)60115-7.

[134] Rauf Razzaq, Hongwei Zhu, Li Jiang et al. "Catalytic methanation of CO and CO2 in coke oven gas over Ni-Co/ZrO2-CeO2". In: *Industrial and Engineering Chemistry Research* 52.6 (2013), pp. 2247–2256. ISSN: 08885885. DOI: 10.1021/ie301399z.

[135] Selim Alayoglu, Simon K. Beaumont, Fan Zheng et al. "CO2 hydrogenation studies on Co and CoPt bimetallic nanoparticles under reaction conditions using TEM, XPS and NEXAFS". In: *Topics in Catalysis* 54.13-15 (2011), pp. 778–785. ISSN: 10225528. DOI: 10.1007/s11244-011-9695-9.

[136] Samuel H. Huang, Peng Liu, Abhiram Mokasdar et al. "Additive manufacturing and its societal impact: A literature review". In: *International Journal of Advanced Manufacturing Technology* 67.5-8 (2013). ISSN: 02683768. DOI: 10.1007/s00170-012-4558-5.

[137] Peter Munnik, Marjolein E.Z. Velthoen, Petra E. De Jongh et al. "Nanoparticle growth in supported nickel catalysts during methanation reaction - Larger is better". In: *Angewandte Chemie - International Edition* 53.36 (2014), pp. 9493–9497. ISSN: 15213773. DOI: 10.1002/anie.201404103.

[138] Guoquan Zhang, Tianjun Sun, Jiaxi Peng et al. "A comparison of Ni/SiC and Ni/Al2O3 catalyzed total methanation for production of synthetic natural gas". In: *Applied Catalysis A: General* 462-463 (2013), pp. 75–81. ISSN: 0926860X. DOI: 10.1016/j.apcata.2013.04.037. URL: http://dx.doi.org/10.1016/j.apcata.2013.04.037.

[139] Xiuli Wang and Michael Economides. "Gas-To-Liquids (GTL)". In: *Advanced Natural Gas Engineering* (2009), pp. 243–287. DOI: 10.1016/b978-1-933762-38-8.50014-9.

[140] Sanaa Hafeez, Elena Pallari, George Manos et al. *Catalytic conversion and chemical recovery*. Elsevier Inc., 2018, pp. 147–172. ISBN: 9780128131404. DOI: 10.1016/B978-0-12-813140-4.00006-6. URL: http://dx.doi.org/10.1016/B978-0-12-813140-4.00006-6.

[141] P. R. Gunjal and V. V. Ranade. *Catalytic Reaction Engineering*. Elsevier Inc., 2016, pp. 263–314. ISBN: 9780128014578. DOI: 10.1016/B978-0-12-801457-8.00007-0. URL: http://dx.doi.org/10.1016/B978-0-12-801457-8.00007-0.

[142] Vaibhav Dhyani and Thallada Bhaskar. "Pyrolysis of biomass". In: *Biomass, Biofuels, Biochemicals: Biofuels: Alternative Feedstocks and Conversion Processes for the Production of Liquid and Gaseous Biofuels* (2019), pp. 217–244. DOI: 10.1016/B978-0-12-816856-1.00009-9.

[143] Flavio Fanelli, Giovanna Parisi, Leonardo Degennaro et al. "Contribution of microreactor technology and flow chemistry to the development of green and sustainable synthesis". In: *Beilstein Journal of Organic Chemistry* 13.Figure 1 (2017), pp. 520–542. ISSN: 18605397. DOI: 10.3762/bjoc.13.51.

[144] Jun Ichi Yoshida, Heejin Kim and Aiichiro Nagaki. "Green and sustainable chemical synthesis using flow microreactors". In: *ChemSusChem* 4.3 (2011), pp. 331–340. ISSN: 1864564X. DOI: 10.1002/cssc.201000271.

[145] Gunther Kolb. "Review: Microstructured reactors for distributed and renewable production of fuels and electrical energy". In: *Chemical Engineering and Processing: Process Intensification* 65 (2013), pp. 1–44. ISSN: 02552701. DOI: 10.1016/j.cep.2012.10.015. URL: http://dx.doi.org/10.1016/j.cep.2012.10.015.

[146] Ulrich Krtschil, Christian Hofmann, Patrick Löb et al. "Novel manufacturing techniques for microstructured reactors in industrial dimensions". In: *Green Processing and Synthesis* 2.5 (2013), pp. 451–463. ISSN: 21919550. DOI: 10.1515/gps-2013-0066.

[147] J P Strakey, A J Forney and W P Haynes. *Methanation in coal gasification processes*. Tech. rep. 1975.

[148] U.S. Department of Energy (USDE). *Practical experience gained during the first twenty years of operation of the Great Plains Gasification Plant and implications of future projects*. Tech. rep. Office of Fossil Energy, 2006.

[149] Hans Harms, Bernd Höhlein and Allan Skov. "Methanisierung kohlenmonoxidreicher Gase beim Energie-Transport". In: *Chemie Ingenieur Technik* 52.6 (1980), pp. 504–515. ISSN: 15222640. DOI: 10.1002/cite.330520605.

[150] Jan Kopyscinski, Tilman J. Schildhauer and Serge M.A. Biollaz. "Methanation in a fluidized bed reactor with high initial CO partial pressure: Part II- Modeling and sensitivity study". In: *Chemical Engineering Science* 66.8 (2011), pp. 1612–1621. ISSN: 00092509. DOI: 10.1016/j.ces.2010.12.029. URL: http://dx.doi.org/10.1016/j.ces.2010.12.029.

[151] Manuel Götz, Siegfried Bajohr, Frank Graf et al. "Einsatz eines Blasensäulenreaktors zur Methansynthese". In: *Chemie-Ingenieur-Technik* 85.7 (2013), pp. 1146–1151. ISSN: 0009286X. DOI: 10.1002/cite.201200212.

[152] Fanhui Meng, Zhong Li, Jun Liu et al. "Effect of promoter Ce on the structure and catalytic performance of Ni/Al2O3 catalyst for CO methanation in slurry-bed reactor". In: *Journal of Natural Gas Science and Engineering* 23 (2015), pp. 250–258. ISSN: 18755100. DOI: 10.1016/j.jngse.2015.01.041. URL: http://dx.doi.org/10.1016/j.jngse.2015.01.041.

[153] Toshimasa Utaka, Tatsuya Takeguchi, Ryuji Kikuchi et al. "CO removal from reformed fuels over Cu and precious metal catalysts". In: *Applied Catalysis A: General* 246.1 (2003), pp. 117–124. ISSN: 0926860X. DOI: 10.1016/S0926-860X(03)00048-6.

[154] O. Görke, P. Pfeifer and K. Schubert. "Highly selective methanation by the use of a microchannel reactor". In: *Catalysis Today* 110.1-2 (2005), pp. 132–139. ISSN: 09205861. DOI: 10.1016/j.cattod.2005.09.009.

[155] Kriston P. Brooks, Jianli Hu, Huayang Zhu et al. "Methanation of carbon dioxide by hydrogen reduction using the Sabatier process in microchannel reactors". In: *Chemical Engineering Science* 62.4 (2007), pp. 1161–1170. ISSN: 00092509. DOI: 10.1016/j.ces.2006.11.020.

[156] Hamidreza Bakhtiary-Davijany, Fatemeh Hayer, Xuyen Kim Phan et al. "Characteristics of an Integrated Micro Packed Bed Reactor-Heat Exchanger for methanol synthesis from syngas". In: *Chemical Engineering Journal* 167.2-3 (2011), pp. 496–503. ISSN: 13858947. DOI: 10.1016/j.cej.2010.08.074. URL: http://dx.doi.org/10.1016/j.cej.2010.08.074.

[157] Gunther Kolb, Yong Men, Georgios Nikolaidis et al. "Carbon monoxide fine clean-up of fuel cell reformate in microchannel reactors by selective oxidation and methanation". In: *CHISA 2008 - 18th International Congress of Chemical and Process Engineering* (2008), pp. 1–10.

[158] Pan Minqiang, Zeng Dehuai, Tang Yong et al. "CFD-based study of velocity distribution among multiple parallel microchannels". In: *Journal of Computers* 4.11 (2009), pp. 1133–1138. ISSN: 1796203X.

[159] L. C. Almeida, F. J. Echave, O. Sanz et al. "Fischer-Tropsch synthesis in microchannels". In: *Chemical Engineering Journal* 167.2-3 (2011), pp. 536–544. ISSN: 13858947. DOI: 10.1016/j.cej.2010.09.091.

[160] Luciano C. Almeida, Oihane Sanz, Jorge D'Olhaberriague et al. "Microchannel reactor for Fischer-Tropsch synthesis: Adaptation of a commercial unit for testing microchannel blocks". In: *Fuel* 110 (2013), pp. 171–177. ISSN: 00162361. DOI: 10.1016/j.fuel.2012.09.063.

[161] Deqing Mei, Yanbing Feng, Miao Qian et al. "An innovative micro-channel catalyst support with a micro-porous surface for hydrogen production via methanol steam reforming". In: *International Journal of Hydrogen Energy* 41.4 (2016), pp. 2268–2277. ISSN: 03603199. DOI: 10.1016/j.ijhydene.2015.12.044. URL: http://dx.doi.org/10.1016/j.ijhydene.2015.12.044.

[162] Enrico Tronconi, Gianpiero Groppi and Carlo Giorgio Visconti. "Structured catalysts for non-adiabatic applications". In: *Current Opinion in Chemical Engineering* 5 (2014), pp. 55–67. ISSN: 22113398. DOI: 10.1016/j.coche.2014.04.003. URL: http://dx.doi.org/10.1016/j.coche.2014.04.003.

[163] Thorsten Boger and Achim K. Heibel. "Heat transfer in conductive monolith structures". In: *Chemical Engineering Science* 60.7 (2005), pp. 1823–1835. ISSN: 00092509. DOI: 10.1016/j.ces.2004.11.031.

[164] Nan Yao, Huafeng Ma, Yan Shao et al. "Effect of cation-oligomer interactions on the size and reducibility of NiO particles on NiRu/SiO2 catalysts". In: *Journal of Materials Chemistry* 21.43 (2011), pp. 17403–17412. ISSN: 09599428. DOI: 10.1039/c1jm13029c.

[165] James A. Schwarz, Cristian Contescu and Adriana Contescu. "Methods for Preparation of Catalytic Materials". In: *Chemical Reviews* 95.3 (1995), pp. 477–510. ISSN: 15206890. DOI: 10.1021/cr00035a002.

[166] Guoquan Zhang, Jiaxi Peng, Tianjun Sun et al. "Effects of the oxidation extent of the SiC surface on the performance of Ni/SiC methanation catalysts". In: *Cuihua Xuebao/Chinese Journal of Catalysis* 34.9 (2013), pp. 1745–1755. ISSN: 02539837. DOI: 10.1016/s1872-2067(12)60639-1.

[167] Jiajian Gao, Chunmiao Jia, Meiju Zhang et al. "Template preparation of high-surface-area barium hexaaluminate as nickel catalyst support for improved CO methanation". In: *RSC Advances* 3.39 (2013), pp. 18156–18163. ISSN: 20462069. DOI: 10.1039/c3ra41660g.

[168] Jiajian Gao, Chunmiao Jia, Jing Li et al. "Nickel catalysts supported on barium hexaaluminate for enhanced CO methanation". In: *Industrial and Engineering Chemistry Research* 51.31 (2012), pp. 10345–10353. ISSN: 08885885. DOI: 10.1021/ie300566n.

[169] Hongwei Zhu, Rauf Razzaq, Li Jiang et al. "Low-temperature methanation of CO in coke oven gas using single nanosized Co 3O 4 catalysts". In: *Catalysis Communications* 23 (2012), pp. 43–47. ISSN: 15667367. DOI: 10.1016/j.catcom.2012.02.029. URL: http://dx.doi.org/10.1016/j.catcom.2012.02.029.

[170] Anmin Zhao, Weiyong Ying, Haitao Zhang et al. "Ni/Al 2O 3 catalysts for syngas methanation: Effect of Mn promoter". In: *Journal of Natural Gas Chemistry* 21.2 (2012), pp. 170–177. ISSN: 10039953. DOI: 10.1016/S1003-9953(11)60350-2. URL: http://dx.doi.org/10.1016/S1003-9953(11)60350-2.

[171] Bo Liu and Shengfu Ji. "Comparative study of fluidized-bed and fixed-bed reactor for syngas methanation over Ni-W/TiO2-SiO2 catalyst". In: *Journal of Energy Chemistry* 22.5 (2013), pp. 740–746. ISSN: 20954956. DOI: 10.1016/S2095-4956(13)60098-4. URL: http://dx.doi.org/10.1016/S2095-4956(13)60098-4.

[172] Sunhwan Hwang, Joongwon Lee, Ung Gi Hong et al. "Methane production from carbon monoxide and hydrogen over nickel-alumina xerogel catalyst: Effect of nickel content". In: *Journal of Industrial and Engineering Chemistry* 17.1 (2011), pp. 154–157. ISSN: 1226086X. DOI: 10.1016/j.jiec.2010.12.015. URL: http://dx.doi.org/10.1016/j.jiec.2010.12.015.

[173] Sunhwan Hwang, Joongwon Lee, Ung Gi Hong et al. "Methanation of carbon dioxide over mesoporous Ni-Fe-Ru-Al2O3 xerogel catalysts: Effect of ruthenium content". In: *Journal of Industrial and Engineering Chemistry* 19.2 (2013), pp. 698–703. ISSN: 1226086X. DOI: 10.1016/j.jiec.2012.10.007. URL: http://dx.doi.org/10.1016/j.jiec.2012.10.007.

[174] Jie Liu, Changming Li, Fei Wang et al. "Enhanced low-temperature activity of CO2 methanation over highly-dispersed Ni/TiO2 catalyst". In: *Catalysis Science and Technology* 3.10 (2013), pp. 2627–2633. ISSN: 20444753. DOI: 10.1039/c3cy00355h.

[175] Jiaying Zhang, Zhong Xin, Xin Meng et al. "Synthesis, characterization and properties of anti-sintering nickel incorporated MCM-41 methanation catalysts". In: *Fuel* 109 (2013), pp. 693–701. ISSN: 00162361. DOI: 10.1016/j.fuel.2013.03.037. URL: http://dx.doi.org/10.1016/j.fuel.2013.03.037.

[176] Andreas Borgschulte, Noris Gallandat, Benjamin Probst et al. "Sorption enhanced CO2 methanation". In: *Physical Chemistry Chemical Physics* 15.24 (2013), pp. 9620–9625. ISSN: 14639076. DOI: 10.1039/c3cp51408k.

[177] Alejandro Karelovic and Patricio Ruiz. "Improving the hydrogenation function of Pd/γ-Al2O 3 catalyst by Rh/γ-Al2O3 Addition in CO2 methanation at low temperature". In: *ACS Catalysis* 3.12 (2013), pp. 2799–2812. ISSN: 21555435. DOI: 10.1021/cs400576w.

[178] Anmin Zhao, Weiyong Ying, Haitao Zhang et al. "Ni-Al 2O 3 catalysts prepared by solution combustion method for syngas methanation". In: *Catalysis Communications* 17 (2012), pp. 34–38. ISSN: 15667367. DOI: 10.1016/j.catcom.2011.10.010. URL: http://dx.doi.org/10.1016/j.catcom.2011.10.010.

[179] Zhifeng Qin, Jun Ren, Maoqian Miao et al. "The catalytic methanation of coke oven gas over Ni-Ce/Al2O3 catalysts prepared by microwave heating: Effect of amorphous NiO formation". In: *Applied Catalysis B: Environmental* 164 (2015), pp. 18–30. ISSN: 09263373. DOI: 10.1016/j.apcatb.2014.08.047. URL: http://dx.doi.org/10.1016/j.apcatb.2014.08.047.

[180] Shohei Tada, Ochieng James Ochieng, Ryuji Kikuchi et al. "Promotion of CO2 methanation activity and CH4 selectivity at low temperatures over Ru/CeO2/Al2O 3 catalysts". In: *International Journal of Hydrogen Energy* 39.19 (2014), pp. 10090–10100. ISSN: 03603199. DOI: 10.1016/j.ijhydene.2014.04.133. URL: http://dx.doi.org/10.1016/j.ijhydene.2014.04.133.

[181] Meng Guo and Gongxuan Lu. "The effect of impregnation strategy on structural characters and CO 2 methanation properties over MgO modified Ni/SiO2 catalysts". In: *Catalysis Communications* 54 (2014), pp. 55–60. ISSN: 15667367. DOI: 10.1016/j.catcom.2014.05.022. URL: http://dx.doi.org/10.1016/j.catcom.2014.05.022.

[182] Adriano Ambrosi and Martin Pumera. "3D-printing technologies for electrochemical applications". In: *Chemical Society Reviews* 45.10 (2016), pp. 2740–2755. ISSN: 14604744. DOI: 10.1039/c5cs00714c.

[183] Tuan D. Ngo, Alireza Kashani, Gabriele Imbalzano et al. "Additive manufacturing (3D printing): A review of materials, methods, applications and challenges". In: *Composites Part B: Engineering* 143 (2018). ISSN: 13598368. DOI: 10.1016/j.compositesb.2018.02.012.

[184] Chang-jun Bae, Arathi Ramachandran, Kyeongwoon Chung et al. "Ceramic Stereolithography: Additive Manufacturing for 3D Complex Ceramic Structures". In: 54.6 (2017), pp. 470–477.

[185] P. J. Bartolo and J. Gaspar. "Metal filled resin for stereolithography metal part". In: *CIRP Annals - Manufacturing Technology* 57.1 (2008), pp. 235–238. ISSN: 00078506. DOI: 10.1016/j.cirp.2008.03.124.

[186] Zhangwei Chen, Ziyong Li, Junjie Li et al. "3D printing of ceramics: A review". In: *Journal of the European Ceramic Society* 39.4 (2019), pp. 661–687. ISSN: 1873619X. DOI: 10.1016/j.jeurceramsoc.2018.11.013.

[187] Zhangwei Chen, Dichen Li and Weizhao Zhou. "Process parameters appraisal of fabricating ceramic parts based on stereolithography using the Taguchi method". In: *Proceedings of the Institution of Mechanical Engineers, Part B: Journal of Engineering Manufacture* 226.7 (2012), pp. 1249–1258. ISSN: 09544054. DOI: 10.1177/0954405412442607.

[188] W. Z. Zhou, D. Li, Z. W. Chen et al. "Direct fabrication of an integral ceramic mould by stereolithography". In: *Proceedings of the Institution of Mechanical Engineers, Part B: Journal of Engineering Manufacture* 224.2 (2010), pp. 237–243. ISSN: 09544054. DOI: 10.1243/09544054JEM1628.

[189] S. J. Leigh, C. P. Purssell, J. Bowen et al. "A miniature flow sensor fabricated by micro-stereolithography employing a magnetite/acrylic nanocomposite resin". In: *Sensors and Actuators, A: Physical* 168.1 (2011), pp. 66–71. ISSN: 09244247. DOI: 10.1016/j.sna.2011.03.058. URL: http://dx.doi.org/10.1016/j.sna.2011.03.058.

[190] Ngoc Tinh Nguyen, Nicolas Delhote, Mauro Ettorre et al. "Design and characterization of 60-GHz integrated lens antennas fabricated through ceramic stereolithography". In: *IEEE Transactions on Antennas and Propagation* 58.8 (2010), pp. 2757–2762. ISSN: 0018926X. DOI: 10.1109/TAP.2010.2050447.

[191] Francesca Scalera, Carola Esposito Corcione, Francesco Montagna et al. "Development and characterization of UV curable epoxy/hydroxyapatite suspensions for stereolithography applied to bone tissue engineering". In: *Ceramics International* 40.10 (2014). ISSN: 02728842. DOI: 10.1016/j.ceramint.2014.06.117.

[192] Dajiang Du, Teruo Asaoka, Takashi Ushida et al. "Fabrication and perfusion culture of anatomically shaped artificial bone using stereolithography". In: *Biofabrication* 6.4 (2014). ISSN: 17585090. DOI: 10.1088/1758-5082/6/4/045002.

[193] Ferry P.W. Melchels, Jan Feijen and Dirk W. Grijpma. "A review on stereolithography and its applications in biomedical engineering". In: *Biomaterials* 31.24 (2010), pp. 6121–6130. ISSN: 01429612. DOI: 10.1016/j.biomaterials.2010.04.050. URL: http://dx.doi.org/10.1016/j.biomaterials.2010.04.050.

[194] Jeffrey W. Stansbury and Mike J. Idacavage. "3D printing with polymers: Challenges among expanding options and opportunities". In: *Dental Materials* 32.1 (2016), pp. 54–64. ISSN: 01095641. DOI: 10.1016/j.dental.2015.09.018. URL: http://dx.doi.org/10.1016/j.dental.2015.09.018.

[195] Quanyi Mu, Lei Wang, Conner K. Dunn et al. "Digital light processing 3D printing of conductive complex structures". In: *Additive Manufacturing* 18 (2017). ISSN: 22148604. DOI: 10.1016/j.addma.2017.08.011.

[196] Luyang Wei, Jinjin Zhang, Fangyong Yu et al. "A novel fabrication of yttria-stabilized-zirconia dense electrolyte for solid oxide fuel cells by 3D printing technique". In: *International Journal of Hydrogen Energy* 44.12 (2019), pp. 6182–6191. ISSN: 03603199. DOI: 10.1016/j.ijhydene.2019.01.071. URL: https://doi.org/10.1016/j.ijhydene.2019.01.071.

[197] Brian Derby. "Inkjet Printing of Functional and Structural Materials: Fluid Property Requirements, Feature Stability, and Resolution". In: *Annual Review of Materials Research* 40.1 (2010), pp. 395–414. ISSN: 1531-7331. DOI: 10.1146/annurev-matsci-070909-104502. URL: http://www.annualreviews.org/doi/abs/10.1146/annurev-matsci-070909-104502.

[198] M Mott and J.R.G Evans. "Zirconia/alumina functionally graded material made by ceramic ink jet printing". In: *Materials Science and Engineering: A* 271.1-2 (1999), pp. 344–352. ISSN: 09215093. DOI: 10.1016/S0921-5093(99)00266-X. URL: http://www.sciencedirect.com/science/article/pii/S092150939900266X.

[199] Ignasi Burgués-Ceballos, Marco Stella, Paul Lacharmoise et al. "Towards industrialization of polymer solar cells: Material processing for upscaling". In: *Journal of Materials Chemistry A* 2.42 (2014), pp. 17711–17722. ISSN: 20507496. DOI: 10.1039/c4ta03780d.

[200] K. H. Tan, C. K. Chua, K. F. Leong et al. "Scaffold development using selective laser sintering of polyetheretherketone-hydroxyapatite biocomposite blends". In: *Biomaterials* 24.18 (2003), pp. 3115–3123. ISSN: 01429612. DOI: 10.1016/S0142-9612(03)00131-5.

[201] Insup Lee. "Densification of porous Al2O3-Al4B2O9 ceramic composites fabricated by SLS process". In: *Journal of Material Science Letters* 18 (1999), pp. 1557–1561. ISSN: 10040609.

[202] I. Shishkovsky, I. Yadroitsev, Ph Bertrand et al. "Alumina-zirconium ceramics synthesis by selective laser sintering/melting". In: *Applied Surface Science* 254.4 (2007), pp. 966–970. ISSN: 01694332. DOI: 10.1016/j.apsusc.2007.09.001.

[203] Ph Bertrand, F. Bayle, C. Combe et al. "Ceramic components manufacturing by selective laser sintering". In: *Applied Surface Science* 254.4 (2007), pp. 989–992. ISSN: 01694332. DOI: 10.1016/j.apsusc.2007.08.085.

[204] J. A. Gonzalez, J. Mireles, Y. Lin et al. "Characterization of ceramic components fabricated using binder jetting additive manufacturing technology". In: *Ceramics International* 42.9 (2016). ISSN: 02728842. DOI: 10.1016/j.ceramint.2016.03.079.

[205] Dustin Gilmer, Lu Han, Eunice Hong et al. "An in-situ crosslinking binder for binder jet additive manufacturing". In: *Additive Manufacturing* 35.May (2020), p. 101341. ISSN: 22148604. DOI: 10.1016/j.addma.2020.101341. URL: https://doi.org/10.1016/j.addma.2020.101341.

[206] Omar A. Mohamed, Syed H. Masood and Jahar L. Bhowmik. "Optimization of fused deposition modeling process parameters: a review of current research and future prospects". In: *Advances in Manufacturing* 3.1 (2015). ISSN: 21953597. DOI: 10.1007/s40436-014-0097-7.

[207] Pedram Parandoush, Levi Tucker, Chi Zhou et al. "Laser assisted additive manufacturing of continuous fiber reinforced thermoplastic composites". In: *Materials and Design* 131 (2017). ISSN: 18734197. DOI: 10.1016/j.matdes.2017.06.013.

[208] Ian Gibson, David Rosen and Brent Stucker. *Additive manufacturing technologies: 3D printing, rapid prototyping, and direct digital manufacturing, second edition*. 2015. ISBN: 9781493921133. DOI: 10.1007/978-1-4939-2113-3.

[209] Bewketu Gizachew Mekonnen, Glen Bright and Anthony Walker. "A Study on State of the Art Technology of Laminated Object Manufacturing (LOM) Bewketu". In: *CAD/CAM, Robotics and Factories of the Future. Lecture Notes in Mechanical Engineering*. Ed. by Mandal D.K. and Syan C.S. Springer India, 2016, pp. 207–216. ISBN: 9783642523250. DOI: 10.1007/978-81-322-2740-3.

[210] Peng Wu, Jun Wang and Xiangyu Wang. *A critical review of the use of 3-D printing in the construction industry*. 2016. DOI: 10.1016/j.autcon.2016.04.005.

[211] Xin Wang, Man Jiang, Zuowan Zhou et al. *3D printing of polymer matrix composites: A review and prospective*. 2017. DOI: 10.1016/j.compositesb.2016.11.034.

[212] Mattia Mele, Giampaolo Campana and Giulia D'Avino. "Life cycle impact assessment of desktop stereolithography". In: *Journal of Cleaner Production* 244 (2020), p. 118743. ISSN: 09596526. DOI: 10.1016/j.jclepro.2019.118743. URL: https://doi.org/10.1016/j.jclepro.2019.118743.

[213] Michelle L. Griffith and John W. Halloran. "Freeform fabrication of ceramics via stereolithography". In: *Journal American Ceramic Society* 79.10 (1996), pp. 2601–2608.

[214] C. Hinczewski, S. Corbel and T. Chartier. "Ceramic suspensions suitable for stereolithography". In: *Journal of the European Ceramic Society* 18.6 (1998), pp. 583–590. ISSN: 09552219. DOI: 10.1016/S0955-2219(97)00186-6.

[215] C. Hinczewski, S. Corbel and T. Chartier. "Stereolithography for the fabrication of ceramic three- dimensional parts". In: *Rapid Prototyping Journal* 4.3 (1998), pp. 104–111. ISSN: 1355-2546. DOI: 10.1108/13552549810222867.

[216] Christophe Chaput, Thierry Chartier and Franck Doreau. *Method and composition for making ceramic parts by stereolithography and use in dentistry*. 2003.

[217] Christophe Chaput and Richard Gaignon. *Procede et machine de fabricacion de pieces crues en materiau ceramique et/ou metallique per la technique des procedes additifs*. 2017.

[218] Thierry Chartier, Christophe Chaput and Franck Doreau. *Ceramic paste composition and prototyping method*. 2000.

[219] Franck Doreau, Christophe Chaput and Thierry Chartier. "Stereolithography for manufacturing ceramic parts". In: *Advanced Engineering Materials* 2.8 (2000), pp. 493–496. ISSN: 14381656. DOI: 10.1002/1527-2648(200008)2:8<493::AID-ADEM493>3.0.CO;2-C.

[220] Arianna Pesce, Aitor Hornés, Marc Núñez et al. "3D printing the next generation of enhanced solid oxide fuel and electrolysis cells". In: *Journal of Materials Chemistry A* (2020). ISSN: 2050-7488. DOI: 10.1039/d0ta02803g.

[221] Christophe Chaput and Thierry Chartier. "Fabrication of ceramics by stereolithography". In: *RTejournal - Forum fur Rapid Technologie* 4 (2007), pp. 1–15.

[222] Joël Brie, Thierry Chartier, Christophe Chaput et al. "A new custom made bioceramic implant for the repair of large and complex craniofacial bone defects". In: *Journal of Cranio-Maxillofacial Surgery* 41.5 (2013), pp. 403–407. ISSN: 10105182. DOI: 10.1016/j.jcms.2012.11.005. URL: http://dx.doi.org/10.1016/j.jcms.2012.11.005.

[223] Richard Voo, M. Mariatti and L. C. Sim. "Flexibility improvement of epoxy nanocomposites thin films using various flexibilizing additives". In: *Composites Part B: Engineering* 43.8 (2012), pp. 3037–3043. ISSN: 13598368. DOI: 10.1016/j.compositesb.2012.05.032. URL: http://dx.doi.org/10.1016/j.compositesb.2012.05.032.

[224] B. Stucker I. Gibson D. W. Rosen. *Additive Manufacturing Technologies*. 2010, p. 459. ISBN: 9781441911193. DOI: 10.1007/978-1-4419-1120-9.

[225] Michelle L. Griffith and John W. Halloran. "Scattering of ultraviolet radiation in turbid suspensions". In: *Journal of Applied Physics* 81.6 (1997), pp. 2538–2546. ISSN: 00218979. DOI: 10.1063/1.364311.

[226] Guojiao Ding, Rujie He, Keqiang Zhang et al. "Stereolithography-based additive manufacturing of gray-colored SiC ceramic green body". In: *Journal of the American Ceramic Society* 102.12 (2019), pp. 7198–7209. ISSN: 15512916. DOI: 10.1111/jace.16648.

[227] Xingbang Li, Jingxian Zhang, Yusen Duan et al. "Rheology and curability characterization of photosensitive slurries for 3D printing of Si3N4 ceramics". In: *Applied Sciences (Switzerland)* 10.18 (2020). ISSN: 20763417. DOI: 10.3390/APP10186438.

[228] Cheng Sun and Xiang Zhang. "The influences of the material properties on ceramic micro-stereolithography". In: *Sensors and Actuators, A: Physical* 101.3 (2002), pp. 364–370. ISSN: 09244247. DOI: 10.1016/S0924-4247(02)00264-9.

[229] Rong Ji Huang, Qiang Guo Jiang, Hai Dong Wu et al. "Fabrication of complex shaped ceramic parts with surface-oxidized Si3N4 powder via digital light processing based stereolithography method". In: *Ceramics International* 45.4 (2019), pp. 5158–5162. ISSN: 02728842. DOI: 10.1016/j.ceramint.2018.11.116. URL: https://doi.org/10.1016/j.ceramint.2018.11.116.

[230] Pan Jiang, Zhongying Ji, Xiaoqin Zhang et al. "Recent advances in direct ink writing of electronic components and functional devices". In: *Progress in Additive Manufacturing* 3.1-2 (2018), pp. 65–86. ISSN: 23639520. DOI: 10.1007/s40964-017-0035-x. URL: http://dx.doi.org/10.1007/s40964-017-0035-x.

[231] Erwin Peng, Danwei Zhang and Jun Ding. *Ceramic Robocasting: Recent Achievements, Potential, and Future Developments*. 2018. DOI: 10.1002/adma.201802404.

[232] Jennifer A. Lewis, James E. Smay, John Stuecker et al. "Direct ink writing of three-dimensional ceramic structures". In: *Journal of the American Ceramic Society* 89.12 (2006), pp. 3599–3609. ISSN: 00027820. DOI: 10.1111/j.1551-2916.2006.01382.x.

[233] Yan Zhang, Changqing Liu and David Whalley. "Direct-write techniques for maskless production of microelectronics: A review of current state-of-the-art technologies". In: *2009 International Conference on Electronic Packaging Technology and High Density Packaging, ICEPT-HDP 2009* (2009), pp. 497–503. DOI: 10.1109/ICEPT.2009.5270702.

[234] Sarosh S. Nadkarni and James E. Smay. "Concentrated barium titanate colloidal gels prepared by bridging flocculation for use in solid freeform fabrication". In: *Journal of the American Ceramic Society* 89.1 (2006), pp. 96–103. ISSN: 00027820. DOI: 10.1111/j.1551-2916.2005.00646.x.

[235] Imen Grida and Julian R.G. Evans. "Extrusion freeforming of ceramics through fine nozzles". In: *Journal of the European Ceramic Society* 23.5 (2003), pp. 629–635. ISSN: 09552219. DOI: 10.1016/S0955-2219(02)00163-2.

[236] I. Gibson, D. W. Rosen and B. Stucker. "Direct write technologies". In: *Additive Manufacturing Technologies*. Ed. by Springer. 2010. Chap. 10, pp. 259–282.

[237] Dimitri Kokkinis, Manuel Schaffner and André R. Studart. "Multimaterial magnetically assisted 3D printing of composite materials". In: *Nature Communications* 6 (2015). ISSN: 2041-1723. DOI: 10.1038/ncomms9643.

[238] Joseph Cesarano. "A review of robocasting technology". In: *Materials Research Society Symposium - Proceedings* 542 (1999), pp. 133–139. ISSN: 02729172. DOI: 10.1557/proc-542-133.

[239] Kiran Yadav, Manjeet Jassal and Ashwini K. Agrawal. "Shear reversible alumina gels for direct writing". In: *Journal of the American Ceramic Society* 97.12 (2014), pp. 4031–4036. ISSN: 15512916. DOI: 10.1111/jace.13195.

[240] Adam E. Jakus, Shannon L. Taylor, Nicholas R. Geisendorfer et al. "Metallic Architectures from 3D-Printed Powder-Based Liquid Inks". In: *Advanced Functional Materials* 25.45 (2015), pp. 6985–6995. ISSN: 16163028. DOI: 10.1002/adfm.201503921.

[241] Ezra Feilden, Esther GarcÃa TuÃ±Ã³n Blanca, Finn Giuliani et al. "Robocasting of structural ceramic parts with hydrogel inks". In: *Journal of the European Ceramic Society* 36.10 (2016). ISSN: 1873619X. DOI: 10.1016/j.jeurceramsoc.2016.03.001.

[242] M. Faes, J. Vleugels, F. Vogeler et al. "Extrusion-based additive manufacturing of ZrO2 using photoinitiated polymerization". In: *CIRP Journal of Manufacturing Science and Technology* 14 (2016), pp. 28–34. ISSN: 17555817. DOI: 10.1016/j.cirpj.2016.05.002. URL: http://dx.doi.org/10.1016/j.cirpj.2016.05.002.

[243] Yoram de Hazan, Madlen Thänert, Martin Trunec et al. "Robotic deposition of 3d nanocomposite and ceramic fiber architectures via UV curable colloidal inks". In: *Journal of the European Ceramic Society* 32.6 (2012), pp. 1187–1198. ISSN: 09552219. DOI: 10.1016/j.jeurceramsoc.2011.12.007. URL: http://dx.doi.org/10.1016/j.jeurceramsoc.2011.12.007.

[244] Barry Berman. "3-D printing: The new industrial revolution". In: *Business Horizons* 55.2 (2012), pp. 155–162. ISSN: 00076813. DOI: 10.1016/j.bushor.2011.11.003. URL: http://dx.doi.org/10.1016/j.bushor.2011.11.003.

[245] Christian Weller, Robin Kleer and Frank T. Piller. "Economic implications of 3D printing: Market structure models in light of additive manufacturing revisited". In: *International Journal of Production Economics* 164 (2015). ISSN: 09255273. DOI: 10.1016/j.ijpe.2015.02.020.

[246] M. A. Modestino, D. Fernandez Rivas, S. M.H. Hashemi et al. "The potential for microfluidics in electrochemical energy systems". In: *Energy and Environmental Science* 9.11 (2016), pp. 3381–3391. ISSN: 17545706. DOI: 10.1039/c6ee01884j.

[247] Malte Gebler, Anton J.M. Schoot Uiterkamp and Cindy Visser. "A global sustainability perspective on 3D printing technologies". In: *Energy Policy* 74.C (2014). ISSN: 03014215. DOI: 10.1016/j.enpol.2014.08.033.

[248] Doojin Vak, Kyeongil Hwang, Andrew Faulks et al. "3D printer based slot-die coater as a lab-to-fab translation tool for solution-processed solar cells". In: *Advanced Energy Materials* 5.4 (2015), pp. 1–8. ISSN: 16146840. DOI: 10.1002/aenm.201401539.

[249] Bok Y. Ahn, Eric B. Duoss, Michael J. Motala et al. "Omnidirectional printing of flexible, stretchable, and spanning silver microelectrodes". In: *Science* 323.5921 (2009), pp. 1590–1593. ISSN: 00368075. DOI: 10.1126/science.1168375.

[250] Ryan R. Kohlmeyer, Aaron J. Blake, James O. Hardin et al. "Composite batteries: A simple yet universal approach to 3D printable lithium-ion battery electrodes". In: *Journal of Materials Chemistry A* 4.43 (2016), pp. 16856–16864. ISSN: 20507496. DOI: 10.1039/c6ta07610f.

[251] Hailong Ning, James H. Pikul, Runyu Zhang et al. "Holographic patterning of high-performance on-chip 3D lithium-ion microbatteries". In: *Proceedings of the National Academy of Sciences of the United States of America* 112.21 (2015), pp. 6573–6578. ISSN: 10916490. DOI: 10.1073/pnas.1423889112.

[252] Gengzhi Sun, Jia An, Chee Kai Chua et al. "Layer-by-layer printing of laminated graphene-based interdigitated microelectrodes for flexible planar micro-supercapacitors". In: *Electrochemistry Communications* 51 (2015), pp. 33–36. ISSN: 13882481. DOI: 10.1016/j.elecom.2014.11.023. URL: http://dx.doi.org/10.1016/j.elecom.2014.11.023.

[253] Mary A. Sukeshini, Ryan Cummins, Thomas L. Reitz et al. "Ink-jet printing: A versatile method for multilayer solid oxide fuel cells fabrication". In: *Journal of the American Ceramic Society* 92.12 (2009), pp. 2913–2919. ISSN: 00027820. DOI: 10.1111/j.1551-2916.2009.03349.x.

[254] A. M. Sukeshini, R. Cummins, T. L. Reitz et al. "Inkjet Printing of Anode Supported SOFC: Comparison of Slurry Pasted Cathode and Printed Cathode". In: *Electrochemical and Solid-State Letters* 12.12 (Dec. 2009), B176. ISSN: 10990062. DOI: 10.1149/1.3243468. URL: http://esl.ecsdl.org/cgi/doi/10.1149/1.3243468.

[255] Vincenzo Esposito, Christophe Gadea, Johan Hjelm et al. "Fabrication of thin yttria-stabilized-zirconia dense electrolyte layers by inkjet printing for high performing solid oxide fuel cells". In: *Journal of Power Sources* 273 (2015), pp. 89–95. ISSN: 03787753. DOI: 10.1016/j.jpowsour.2014.09.085. URL: http://dx.doi.org/10.1016/j.jpowsour.2014.09.085.

[256] M. Rosa, P. N. Gooden, S. Butterworth et al. "Zirconia nano-colloids transfer from continuous hydrothermal synthesis to inkjet printing". In: *Journal of the European Ceramic Society* 39.1 (2019), pp. 2–8. ISSN: 1873619X. DOI: 10.1016/j.jeurceramsoc.2017.11.035.

[257] Chao Li, Huangang Shi, Ran Ran et al. "Thermal inkjet printing of thin-film electrolytes and buffering layers for solid oxide fuel cells with improved performance". In: *International Journal of Hydrogen Energy* 38.22 (2013), pp. 9310–9319. ISSN: 03603199. DOI: 10.1016/j.ijhydene.2013.05.025. URL: http://dx.doi.org/10.1016/j.ijhydene.2013.05.025.

[258] Chingfu Wang, Simon C. Hopkins, Rumen I. Tomov et al. "Optimisation of CGO suspensions for inkjet-printed SOFC electrolytes". In: *Journal of the European Ceramic Society* 32.10 (2012), pp. 2317–2324. ISSN: 09552219. DOI: 10.1016/j.jeurceramsoc.2012.03.001. URL: http://dx.doi.org/10.1016/j.jeurceramsoc.2012.03.001.

[259] M. Mosiadz, R. I. Tomov, S. C. Hopkins et al. "Inkjet printing of Ce0.8Gd0.2O2 thin films on Ni-5%W flexible substrates". In: *Journal of Sol-Gel Science and Technology* 54.2 (2010), pp. 154–164. ISSN: 09280707. DOI: 10.1007/s10971-010-2170-4.

[260] Ahmed Mohamed El-Toni, Toshiaki Yamaguchi, Sota Shimizu et al. "Development of a dense electrolyte thin film by the ink-jet printing technique for a porous LSM substrate". In: *Journal of the American Ceramic Society* 91.1 (2008), pp. 346–349. ISSN: 00027820. DOI: 10.1111/j.1551-2916.2007.02151.x.

[261] D. Young, A. M. Sukeshini, R. Cummins et al. "Ink-jet printing of electrolyte and anode functional layer for solid oxide fuel cells". In: *Journal of Power Sources* 184.1 (2008), pp. 191–196. ISSN: 03787753. DOI: 10.1016/j.jpowsour.2008.06.018.

[262] A. Bertei, F. Tariq, V. Yufit et al. "Guidelines for the rational design and engineering of 3D manufactured solid oxide fuel cell composite electrodes". In: *Journal of the Electrochemical Society* 164.2 (2017), F89–F98. ISSN: 19457111. DOI: 10.1149/2.0501702jes.

[263] Chih-Che Chueh, Antonio Bertei and Cristiano Nicolella. "Design guidelines for the manufacturing of the electrode-electrolyte interface of solid oxide fuel cells". In: *Journal of Power Sources* 437.July (Oct. 2019), p. 226888. ISSN: 03787753. DOI: 10.1016/j.jpowsour.2019.226888. URL: https://doi.org/10.1016/j.jpowsour.2019.226888.

[264] Nick Farandos, Lisa Kleiminger, Anna Hankin et al. "3D Printing of Functional Layers for Solid Oxide Fuel Cells and Electrolysers". In: *Meeting Abstracts* MA2015-03.1 (July 2015), p. 343. ISSN: 2151-2041. URL: http://ma.ecsdl.org/content/MA2015-03/1/343.abstract.

[265] N. M. Farandos, L. Kleiminger, T. Li et al. "Three-dimensional Inkjet Printed Solid Oxide Electrochemical Reactors. I. Yttria-stabilized Zirconia Electrolyte". In: *Electrochimica Acta* 213 (2016), pp. 324–331. ISSN: 00134686. DOI: 10.1016/j.electacta.2016.07.103.

[266] Chingfu Wang, Rumen I. Tomov, R. Vasant Kumar et al. "Inkjet printing of gadolinium-doped ceria electrolyte on NiO-YSZ substrates for solid oxide fuel cell applications". In: *Journal of Materials Science* 46.21 (2011), pp. 6889–6896. ISSN: 00222461. DOI: 10.1007/s10853-011-5653-y.

[267] S. Masciandaro, M. Torrell, P. Leone et al. "Three-dimensional printed yttria-stabilized zirconia self-supported electrolytes for solid oxide fuel cell applications". In: *Journal of the European Ceramic Society* 39.1 (2019), pp. 9–16. ISSN: 1873619X. DOI: 10.1016/j.jeurceramsoc.2017.11.033. URL: https://doi.org/10.1016/j.jeurceramsoc.2017.11.033%20http://dx.doi.org/10.1016/j.jeurceramsoc.2017.11.033.

[268] Soshu Kirihara. "Creation of Functional Ceramics Structures by Using Stereolithographic 3D printing". In: *Transactions of JWRI* 43.1 (2014), pp. 5–10.

[269] Zuying Feng, Liang Liu, Lingyao Li et al. "3D printed Sm-doped ceria composite electrolyte membrane for low temperature solid oxide fuel cells". In: *International Journal of Hydrogen Energy* 44.26 (2019), pp. 13843–13851. ISSN: 03603199. DOI: 10.1016/j.ijhydene.2019.03.254. URL: https://doi.org/10.1016/j.ijhydene.2019.03.254.

[270] Rongxuan He, Wei Liu, Ziwei Wu et al. "Fabrication of complex-shaped zirconia ceramic parts via a DLP- stereolithography-based 3D printing method". In: *Ceramics International* 44.3 (2018), pp. 3412–3416. ISSN: 02728842. DOI: 10.1016/j.ceramint.2017.11.135.

[271] Amir Ghazanfari, Wenbin Li, Ming Leu et al. "Mechanical characterization of parts produced by ceramic on-demand extrusion process". In: *International Journal of Applied Ceramic Technology* 14.3 (2017). ISSN: 17447402. DOI: 10.1111/ijac.12665.

[272] Wenbin Li, Amir Ghazanfari, Devin McMillen et al. "Characterization of zirconia specimens fabricated by ceramic on-demand extrusion". In: *Ceramics International* 44.11 (2018), pp. 12245–12252. ISSN: 02728842. DOI: 10.1016/j.ceramint.2018.04.008. URL: https://doi.org/10.1016/j.ceramint.2018.04.008.

[273] Emre Özkol. "Rheological characterization of aqueous 3Y-TZP inks optimized for direct thermal ink-jet printing of ceramic components". In: *Journal of the American Ceramic Society* 96.4 (2013), pp. 1124–1130. ISSN: 00027820. DOI: 10.1111/jace.12285.

[274] KENNETH TAN HONG Yi, SU PEI-CHEN, SUN CHEN-NAN et al. "EFFECTS OF LASER PROCESSING ON NICKEL OXIDE – YTTRIA STABILIZED ZIRCONIA". In: *Proc. of the 2nd Intl. Conf. on Progress in Additive Manufacturing* (2016). DOI: doi:10.3850/2424-8967V02-206.

[275] Mary Sukeshini A., Frederick Meisenkothen, Paul Gardner et al. "Aerosol Jet® Printing of functionally graded SOFC anode interlayer and microstructural investigation by low voltage scanning electron microscopy". In: *Journal of Power Sources* 224 (2013), pp. 295–303. ISSN: 03787753. DOI: 10.1016/j.jpowsour.2012.09.094. URL: http://dx.doi.org/10.1016/j.jpowsour.2012.09.094.

[276] Shengyao Wang, Xiao Hai, Xing Ding et al. "Light-Switchable Oxygen Vacancies in Ultrafine Bi5O7Br Nanotubes for Boosting Solar-Driven Nitrogen Fixation in Pure Water". In: *Advanced Materials* 1701774 (2017), pp. 1–7. ISSN: 15214095. DOI: 10.1002/adma.201701774.

[277] T. B. Mitchell-Williams, R. I. Tomov, S. A. Saadabadi et al. "Infiltration of commercially available, anode supported SOFC's via inkjet printing". In: *Materials for Renewable and Sustainable Energy* 6.2 (2017), pp. 1–9. ISSN: 21941467. DOI: 10.1007/s40243-017-0096-2.

[278] M. Dudek, R. I. Tomov, C. Wang et al. "Feasibility of direct carbon solid oxide fuels cell (DC-SOFC) fabrication by inkjet printing technology". In: *Electrochimica Acta* 105 (2013), pp. 412–418. ISSN: 00134686. DOI: 10.1016/j.electacta.2013.04.139. URL: http://dx.doi.org/10.1016/j.electacta.2013.04.139.

[279] R. I. Tomov, M. Dudek, S. C. Hopkins et al. "Inkjet printing of direct carbon solid oxide fuel cell components". In: *ECS Transactions* 57.1 (2013), pp. 1359–1369. ISSN: 19386737. DOI: 10.1149/05701.1359ecst.

[280] H. Shimada, F. Ohba, X. Li et al. "Electrochemical Behaviors of Nickel/Yttria-Stabilized Zirconia Anodes with Distribution Controlled Yttrium-Doped Barium Zirconate by Ink-jet Technique". In: *Journal of the Electrochemical Society* 159.7 (2012), F360–F367. ISSN: 0013-4651. DOI: 10.1149/2.068207jes. URL: http://jes.ecsdl.org/cgi/doi/10.1149/2.068207jes.

[281] Zhangwei Chen, Jing Ouyang, Wenlang Liang et al. "Development and characterizations of novel aqueous-based LSCF suspensions for inkjet printing". In: *Ceramics International* 44.11 (2018), pp. 13381–13388. ISSN: 02728842. DOI: 10.1016/j.ceramint.2018.04.174. URL: http://dx.doi.org/10.1016/j.ceramint.2018.04.174.

[282] Theresa Y. Hill, Thomas L. Reitz, Michael A. Rottmayer et al. "Controlling inkjet fluid kinematics to achieve SOFC cathode micropatterns". In: *ECS Journal of Solid State Science and Technology* 4.4 (2015), P3015–P3019. ISSN: 21628777. DOI: 10.1149/2.0031504jss.

[283] Gwon Deok Han, Ke Chean Neoh, Kiho Bae et al. "Fabrication of lanthanum strontium cobalt ferrite (LSCF) cathodes for high performance solid oxide fuel cells using a low price commercial inkjet printer". In: *Journal of Power Sources* 306 (2016), pp. 503–509. ISSN: 03787753. DOI: 10.1016/j.jpowsour.2015.12.067. URL: http://dx.doi.org/10.1016/j.jpowsour.2015.12.067.

[284] Naoki Yashiro, Tomohiro Usui and Koichi Kikuta. "Application of a thin intermediate cathode layer prepared by inkjet printing for SOFCs". In: *Journal of the European Ceramic Society* 30.10 (2010), pp. 2093–2098. ISSN: 09552219. DOI: 10.1016/j.jeurceramsoc.2010.04.012. URL: http://dx.doi.org/10.1016/j.jeurceramsoc.2010.04.012.

[285] Eleonora Venezia, Massimo Viviani, Sabrina Presto et al. "Inkjet printing functionalization of SOFC LSCF cathodes". In: *Nanomaterials* 9.4 (2019), pp. 1–16. ISSN: 20794991. DOI: 10.3390/nano9040654.

[286] R. I. Tomov, Tom Mitchell-Williams, Chenlong Gao et al. "Performance optimization of LSCF/Gd:CeO2 composite cathodes via single-step inkjet printing infiltration". In: *Journal of Applied Electrochemistry* 47.5 (2017), pp. 641–651. ISSN: 15728838. DOI: 10.1007/s10800-017-1066-1.

[287] R. I. Tomov, T. B. Mitchel-Williams, R. Maher et al. "The synergistic effect of cobalt oxide and Gd-CeO2 dual infiltration in LSCF/CGO cathodes". In: *Journal of Materials Chemistry A* 6.12 (2018), pp. 5071–5081. ISSN: 20507496. DOI: 10.1039/c7ta10990c.

[288] Eman Husni Da'As, John T.S. Irvine, Enrico Traversa et al. "Controllable impregnation via inkjet printing for the fabrication of solid oxide cell air electrodes". In: *ECS Transactions* 57.1 (2013), pp. 1851–1857. ISSN: 19386737. DOI: 10.1149/05701.1851ecst.

[289] Chen Chiang Yu, Jong Dae Baek, Chun Hao Su et al. "Inkjet-Printed Porous Silver Thin Film as a Cathode for a Low-Temperature Solid Oxide Fuel Cell". In: *ACS Applied Materials and Interfaces* 8.16 (2016), pp. 10343–10349. ISSN: 19448252. DOI: 10.1021/acsami.6b01943.

[290] Chao Li, Huili Chen, Huangang Shi et al. "Green fabrication of composite cathode with attractive performance for solid oxide fuel cells through facile inkjet printing". In: *Journal of Power Sources* 273 (2015), pp. 465–471. ISSN: 03787753. DOI: 10.1016/j.jpowsour.2014.09.143. URL: http://dx.doi.org/10.1016/j.jpowsour.2014.09.143.

[291] N. M. Farandos, T. Li and G. H. Kelsall. "3-D inkjet-printed solid oxide electrochemical reactors. II. LSM - YSZ electrodes". In: *Electrochimica Acta* 270 (2018), pp. 264–273. ISSN: 00134686. DOI: 10.1016/j.electacta.2018.03.095.

[292] A. M. Sukeshini, Paul Gardner, Frederick Meisenkothen et al. "Aerosol Jet Printing and Microstructure of SOFC Electrolyte and Cathode Layers". In: 35.1 (2011), pp. 2151–2160. ISSN: 19385862 19386737. DOI: 10.1149/1.3570207. URL: http://ecst.ecsdl.org/cgi/doi/10.1149/1.3570207.

[293] Mary A. Sukeshini, Frederick Meisenkothen, Paul Gardner et al. "Aerosol Jet Printing of functionally graded SOFC anode interlayer and microstructural investigation by low voltage scanning electron microscopy". In: *Journal of Power Sources* 224 (2013), pp. 295–303. ISSN: 0378-7753. DOI: 10.1016/j.jpowsour.2012.09.094.

[294] R. I. Tomov, M. Dudek, S. C. Hopkins et al. "Inkjet printing of direct carbon solid oxide fuel cell components". In: *ECS Transactions* 57.1 (2013), pp. 1359–1369. ISSN: 19386737. DOI: 10.1149/05701.1359ecst.

[295] Anne Hauch, Sune Dalgaard Ebbesen, Søren Højgaard Jensen et al. "Highly efficient high temperature electrolysis". In: *Journal of Materials Chemistry* 18.20 (2008), pp. 2331–2340. ISSN: 09599428. DOI: 10.1039/b718822f.

[296] Diane L. Linne, Maria A. Kuczmarski, James Christopher Johnston et al. "Advanced manifolds for improved solid oxide electrolyzer performance". In: *2018 AIAA SPACE and Astronautics Forum and Exposition* September (2018), pp. 1–6. DOI: 10.2514/6.2018-5174.

[297] Jasper Lefevere, Marijn Gysen, Steven Mullens et al. "The benefit of design of support architectures for zeolite coated structured catalysts for methanol-to-olefin conversion". In: *Catalysis Today* 216 (2013), pp. 18–23. ISSN: 09205861. DOI: 10.1016/j.cattod.2013.05.020. URL: http://dx.doi.org/10.1016/j.cattod.2013.05.020.

[298] Simge Danaci, Lidia Protasova, Jasper Lefevere et al. "Efficient CO2 methanation over Ni/Al2O3 coated structured catalysts". In: *Catalysis Today* 273 (2016), pp. 234–243. ISSN: 09205861. DOI: 10.1016/j.cattod.2016.04.019. URL: http://dx.doi.org/10.1016/j.cattod.2016.04.019.

[299] Simge Danaci, Lidia Protasova, Frans Snijkers et al. "Innovative 3D-manufacture of structured copper supports post-coated with catalytic material for CO2 methanation". In: *Chemical Engineering and Processing - Process Intensification* 127.March (2018), pp. 168–177. ISSN: 02552701. DOI: 10.1016/j.cep.2018.03.023. URL: https://doi.org/10.1016/j.cep.2018.03.023.

[300] Simge Danaci, Lidia Protasova, Vesna Middelkoop et al. "Scaling up of 3D printed and Ni/Al2O3 coated reactors for CO2 methanation". In: *Reaction Chemistry and Engineering* 4.7 (2019), pp. 1318–1330. ISSN: 20589883. DOI: 10.1039/c9re00092e.

[301] Susana Pérez, Jorge J. Aragón, Iñigo Peciña et al. "Enhanced CO2 Methanation by New Microstructured Reactor Concept and Design". In: *Topics in Catalysis* 62.5-6 (2019), pp. 518–523. ISSN: 15729028. DOI: 10.1007/s11244-019-01139-4. URL: http://dx.doi.org/10.1007/s11244-019-01139-4.

[302] Jie Liu, Yu Gao, Yanbin Fan et al. "Fabrication of porous metal by selective laser melting as catalyst support for hydrogen production microreactor". In: *International Journal of Hydrogen Energy* 45.1 (2020), pp. 10–22. ISSN: 03603199. DOI: 10.1016/j.ijhydene.2019.10.173. URL: https://doi.org/10.1016/j.ijhydene.2019.10.173.

[303] Thomas Stiegler, Katharina Meltzer, Alexander Tremel et al. "Development of a Structured Reactor System for CO2 Methanation under Dynamic Operating Conditions". In: *Energy Technology* 7.6 (2019), pp. 1–12. ISSN: 21944296. DOI: 10.1002/ente.201900047.

[304] Laura Fratalocchi, Gianpiero Groppi, Carlo Giorgio Visconti et al. "Adoption of 3D printed highly conductive periodic open cellular structures as an effective solution to enhance the heat transfer performances of compact Fischer-Tropsch fixed-bed reactors". In: *Chemical Engineering Journal* 386.August 2019 (2020), p. 123988. ISSN: 13858947. DOI: 10.1016/j.cej.2019.123988. URL: https://doi.org/10.1016/j.cej.2019.123988.

[305] Nafeezuddin Mohammad, Richard Y. Abrokwah, Robert G. Stevens-Boyd et al. "Fischer-Tropsch studies in a 3D-printed stainless steel microchannel microreactor coated with cobalt-based bimetallic-MCM-41 catalysts". In: *Catalysis Today* January (2020), pp. 1–13. ISSN: 09205861. DOI: 10.1016/j.cattod.2020.02.020. URL: https://doi.org/10.1016/j.cattod.2020.02.020.

[306] Sarah Couck, Jasper Lefevere, Steven Mullens et al. "CO2, CH4 and N2 separation with a 3DFD-printed ZSM-5 monolith". In: *Chemical Engineering Journal* 308 (2017), pp. 719–726. ISSN: 13858947. DOI: 10.1016/j.cej.2016.09.046. URL: http://dx.doi.org/10.1016/j.cej.2016.09.046.

[307] J. Lefevere, S. Mullens and V. Meynen. "The impact of formulation and 3D-printing on the catalytic properties of ZSM-5 zeolite". In: *Chemical Engineering Journal* 349.November 2017 (2018), pp. 260–268. ISSN: 13858947. DOI: 10.1016/j.cej.2018.05.058. URL: https://doi.org/10.1016/j.cej.2018.05.058.

[308] Muxina Konarova, Waqas Aslam, Lei Ge et al. "Enabling Process Intensification by 3 D Printing of Catalytic Structures". In: *ChemCatChem* 9.21 (2017), pp. 4132–4138. ISSN: 18673899. DOI: 10.1002/cctc.201700829.

[309] Vesna Middelkoop, Antonis Vamvakeros, Dieter De Wit et al. "3D printed Ni/Al2O3 based catalysts for CO2 methanation-a comparative and operando XRD-CT study". In: *Journal of CO2 Utilization* 33.June (2019), pp. 478–487. ISSN: 22129820. DOI: 10.1016/j.jcou.2019.07.013. URL: https://doi.org/10.1016/j.jcou.2019.07.013.

[310] Jordan E. Katz, Todd R. Gingrich, Elizabeth A. Santori et al. "Combinatorial synthesis and high-throughput photopotential and photocurrent screening of mixed-metal oxides for photoelectrochemical water splitting". In: *Energy and Environmental Science* 2.1 (2009), pp. 103–112. ISSN: 17545692. DOI: 10.1039/b812177j.

[311] J. M. Gregoire, C. Xiang, S. Mitrovic et al. "Combined Catalysis and Optical Screening for High Throughput Discovery of Solar Fuels Catalysts". In: *Journal of The Electrochemical Society* 160.4 (2013), F337–F342. ISSN: 0013-4651. DOI: 10.1149/2.035304jes.

[312] Chengxiang Xiang, Santosh K. Suram, Joel A. Haber et al. "High-throughput bubble screening method for combinatorial discovery of electrocatalysts for water splitting". In: *ACS Combinatorial Science* 16.2 (2014), pp. 47–52. ISSN: 21568952. DOI: 10.1021/co400151h.

[313] John M. Gregoire, Chengxiang Xiang, Xiaonao Liu et al. "Scanning droplet cell for high throughput electrochemical and photoelectrochemical measurements". In: *Review of Scientific Instruments* 84.2 (2013), pp. 1–7. ISSN: 00346748. DOI: 10.1063/1.4790419.

[314] Xiaonao Liu, Yi Shen, Ruoting Yang et al. "Inkjet printing assisted synthesis of multicomponent mesoporous metal oxides for ultrafast catalyst exploration". In: *Nano Letters* 12.11 (2012), pp. 5733–5739. ISSN: 15306984. DOI: 10.1021/nl302992q.

[315] Michael Woodhouse, G. S. Herman and B. A. Parkinson. "Combinatorial approach to identification of catalysts for the photoelectrolysis of water". In: *Chemistry of Materials* 17.17 (2005), pp. 4318–4324. ISSN: 08974756. DOI: 10.1021/cm050546q.

[316] Michael Woodhouse and B. A. Parkinson. "Combinatorial discovery and optimization of a complex oxide with water photoelectrolysis activity". In: *Chemistry of Materials* 20.7 (2008), pp. 2495–2502. ISSN: 08974756. DOI: 10.1021/cm703099j.

[317] Michelle Kramer, Millie McKelvie and Matthew Watson. "Additive Manufacturing of Catalyst Substrates for Steam–Methane Reforming". In: *Journal of Materials Engineering and Performance* 27.1 (2018), pp. 21–31. ISSN: 15441024. DOI: 10.1007/s11665-017-2859-4.

[318] Yunhua Li, Sijing Chen, Xiaohu Cai et al. "Rational design and preparation of hierarchical monoliths through 3D printing for syngas methanation". In: *Journal of Materials Chemistry A* 6.14 (2018), pp. 5695–5702. ISSN: 20507496. DOI: 10.1039/c8ta01597j.

[319] Regina Knitter and Marcel A. Liauw. "Ceramic microreactors for heterogeneously catalysed gas-phase reactions". In: *Lab on a Chip* 4.4 (2004), pp. 378–383. ISSN: 14730197. DOI: 10.1039/b403361b.

[320] Niloufar Raeis Hosseini, Nigel Mark Sammes and Jong Shik Chung. "Manganese-doped lanthanum calcium titanate as an interconnect for flat-tubular solid oxide fuel cells". In: *Journal of Power Sources* 245 (2014). ISSN: 03787753. DOI: 10.1016/j.jpowsour.2013.07.010.

[321] Donald C Aduba, Keyton D Feller and Christopher B Williams. "an Investigation of Build Orientation on Shrinkage in Sintered Bioceramic Parts Fabricated By Vat Photopolymerization". In: *Solid Freeform Fabrication* (2017), pp. 2326–2340.

[322] P. Jacobs. *Rapid prototyping and manufacturing: Fundamentals of Stereolithography*. Society of Manufacturing Engineers, New York, NY, 1992, p. 434. ISBN: 0872634256. DOI: 10.1016/0278-6125(93)90311-g.

[323] Xuan Song, Yong Chen, Tae Woo Lee et al. "Ceramic fabrication using Mask-Image-Projection-based Stereolithography integrated with tape-casting". In: *Journal of Manufacturing Processes* 20 (2015). ISSN: 15266125. DOI: 10.1016/j.jmapro.2015.06.022.

[324] T. Chartier, C. Hinczewski and S. Corbel. "UV Curable Systems for Tape Casting". In: *Journal of the European Ceramic Society* 19.1 (1999), pp. 67–74. ISSN: 09552219. DOI: 10.1016/S0955-2219(98)00177-0.

[325] C. Pagnoux, T. Chartier, M. de F. Granja et al. "Aqueous suspensions for tape-casting based on acrylic binders". In: *Journal of the European Ceramic Society* 18.97 (1998), pp. 241–247. ISSN: 09552219. DOI: 10.1016/S0955-2219(97)00115-5.

[326] Maciej Wozniak, Yoram de Hazan, Thomas Graule et al. "Rheology of UV curable colloidal silica dispersions for rapid prototyping applications". In: *Journal of the European Ceramic Society* 31.13 (2011), pp. 2221–2229. ISSN: 09552219. DOI: 10.1016/j.jeurceramsoc.2011.05.004. URL: http://dx.doi.org/10.1016/j.jeurceramsoc.2011.05.004.

[327] Bahman Amini Horri, Prabhakar Ranganathan, Cordelia Selomulya et al. "A new empirical viscosity model for ceramic suspensions". In: *Chemical Engineering Science* 66.12 (2011), pp. 2798–2806. ISSN: 00092509. DOI: 10.1016/j.ces.2011.03.040. URL: http://dx.doi.org/10.1016/j.ces.2011.03.040.

[328] Jiangping Zhou, Zhongliang Lu, Kai Miao et al. "Quick fabrication of aeronautical complicated structural parts based on stereolithography". In: *Propulsion and Power Research* 4.2 (2015). ISSN: 2212540X. DOI: 10.1016/j.jppr.2015.05.001.

[329] B. C.H. Steele. "Interfacial reactions associated with ceramic ion transport membranes". In: *Solid State Ionics* 75.C (1995), pp. 157–165. ISSN: 01672738. DOI: 10.1016/0167-2738(94)00182-R.

[330] Junya Onishi, Yukinori Kametani, Yosuke Hasegawa et al. "Topology Optimization of Electrolyte-Electrode Interfaces of Solid Oxide Fuel Cells based on the Adjoint Method". In: *Journal of The Electrochemical Society* 166.13 (2019), F876–F888. ISSN: 0013-4651. DOI: 10.1149/2.0031913jes.

[331] M. Geagea, J. Ouyang, B. Chi et al. "Architectured interfaces and electrochemical modelling in an anode supported SOFC". In: *ECS Transactions* 68.1 (2015), pp. 2961–2969. ISSN: 19386737. DOI: 10.1149/06801.2961ecst.

[332] J A Cebollero, R Lahoz and A Larrea. "Tailoring the electrode-electrolyte interface of Solid Oxide Fuel Cells (SOFC) by laser micro-patterning to improve their electrochemical performance". In: *Journal of Power Sources* 360 (2017), pp. 336–344. ISSN: 0378-7753. DOI: 10.1016/j.jpowsour.2017.05.106. URL: http://dx.doi.org/10.1016/j.jpowsour.2017.05.106.

[333] A. Larrea, V. M. Orera, J. A. Cebollero et al. "Characterization of laser-processed thin ceramic membranes for electrolyte-supported solid oxide fuel cells". In: *International Journal of Hydrogen Energy* 42.19 (2017), pp. 13939–13948. ISSN: 03603199. DOI: 10.1016/j.ijhydene.2016.12.112.

[334] Pei Chen Su, Cheng Chieh Chao, Joon Hyung Shim et al. "Solid oxide fuel cell with corrugated thin film electrolyte". In: *Nano Letters* 8.8 (2008), pp. 2289–2292. ISSN: 15306984. DOI: 10.1021/nl800977z.

[335] Cheng-Chieh Chao, Ching-Mei Hsu, Yi Cui et al. "Improved Solid Oxide Fuel Cell Performance with Nanostructured Electrolytes". In: *ACS Nano* 5.7 (2011), pp. 5692–5696.

[336] Ankur Goswami, Geetika Srivastava, A. M. Umarji et al. "Thermal degradation kinetics of poly(trimethylol propane triacrylate)/poly(hexane diol diacrylate) interpenetrating polymer network". In: *Thermochimica Acta* 547 (2012), pp. 53–61. ISSN: 00406031. DOI: 10.1016/j.tca.2012.08.006. URL: http://dx.doi.org/10.1016/j.tca.2012.08.006.

[337] Hongyu Xing, Bin Zou, Qingguo Lai et al. "Preparation and characterization of UV curable Al2O3 suspensions applying for stereolithography 3D printing ceramic microcomponent". In: *Powder Technology* 338 (2018). ISSN: 1873328X. DOI: 10.1016/j.powtec.2018.07.023.

[338] A. Badev, Y. Abouliatim, T. Chartier et al. "Photopolymerization kinetics of a polyether acrylate in the presence of ceramic fillers used in stereolithography". In: *Journal of Photochemistry and Photobiology A: Chemistry* 222.1 (2011), pp. 117–122. ISSN: 10106030. DOI: 10.1016/j.jphotochem.2011.05.010. URL: http://dx.doi.org/10.1016/j.jphotochem.2011.05.010.

[339] Kehang Li and Zhe Zhao. "The effect of the surfactants on the formulation of UV-curable SLA alumina suspension". In: *Ceramics International* 43.6 (2017). ISSN: 02728842. DOI: 10.1016/j.ceramint.2016.11.143.

[340] R. D. Farahani, K. Chizari and D. Therriault. "Three-dimensional printing of freeform helical microstructures: A review". In: *Nanoscale* 6.18 (2014), pp. 10470–10485. ISSN: 20403372. DOI: 10.1039/c4nr02041c.

[341] Andrea V. Bordoni, M. Verónica Lombardo and Alejandro Wolosiuk. "Photochemical radical thiol-ene click-based methodologies for silica and transition metal oxides materials chemical modification: A mini-review". In: *RSC Advances* 6.81 (2016), pp. 77410–77426. ISSN: 20462069. DOI: 10.1039/c6ra10388j.

[342] Duo Sun, Faisal Mohamed Khan and David S.A. Simakov. "Heat removal and catalyst deactivation in a Sabatier reactor for chemical fixation of CO2: Simulation-based analysis". In: *Chemical Engineering Journal* 329.January 2019 (2017), pp. 165–177. ISSN: 13858947. DOI: 10.1016/j.cej.2017.06.160. URL: http://dx.doi.org/10.1016/j.cej.2017.06.160.

[343] Stefan Neuberg, Helmut Pennemann, Vetrivel Shanmugam et al. "CO2 Methanation in Microstructured Reactors – Catalyst Development and Process Design". In: *Chemical Engineering and Technology* 42.10 (2019), pp. 2076–2084. ISSN: 15214125. DOI: 10.1002/ceat.201900132.

[344] M. A.A. Aziz, A. A. Jalil, S. Triwahyono et al. "CO2 methanation over heterogeneous catalysts: Recent progress and future prospects". In: *Green Chemistry* 17.5 (2015), pp. 2647–2663. ISSN: 14639270. DOI: 10.1039/c5gc00119f. URL: http://dx.doi.org/10.1039/c5gc00119f.

[345] C. Suryanarayana, M. Grant Norton, C. Suryanarayana et al. "X-Rays and Diffraction". In: *X-Ray Diffraction*. 1998, pp. 3–19. DOI: 10.1007/978-1-4899-0148-4{_}1.

[346] Yoshio Waseda, Eiichiro Matsubara and Kozo Shinoda. "X-Ray Diffraction Crystallography". In: *X-Ray Diffraction Crystallography*. 2011. ISBN: 9783642166341. DOI: 10.1007/978-3-642-16635-8.

[347] T Chartier, R Penarroya, C Pagnoux et al. "Tape casting using {UV} curable binders". In: *Journal of the European Ceramic Society* 17.April (1997), pp. 765–771. ISSN: 0955-2219. DOI: http://dx.doi.org/10.1016/S0955-2219(96)00137-9. URL: http://www.sciencedirect.com/science/article/pii/S0955221996001379.

[348] K. Walters and W. M. Jones. "Measurement of Viscosity". In: *Instrumentation Reference Book*. 4th ed. Elsevier, 2010, pp. 69–75. ISBN: 9780750683081. DOI: 10.1016/B978-0-7506-8308-1.00007-3. URL: http://dx.doi.org/10.1016/B978-0-7506-8308-1.00007-3.

[349] Cintil Jose Chirayil, Jiji Abraham, Raghvendra Kumar Mishra et al. "Chapter 1 - Instrumental Techniques for the Characterization of Nanoparticles". In: *Micro and Nano Technologies*. Ed. by Sabu Thomas, Raju Thomas, Ajesh K Zachariah et al. Elsevier, 2017, pp. 1–36. ISBN: 978-0-323-46139-9. DOI: https://doi.org/10.1016/B978-0-323-46139-9.00001-3. URL: http://www.sciencedirect.com/science/article/pii/B9780323461399000013.

[350] "Chapter 3 - Methods for Assessing Surface Cleanliness". In: ed. by Rajiv Kohli, K L B T - Developments in Surface Contamination Mittal Volume 12 and Cleaning. Elsevier, 2019, pp. 23–105. ISBN: 978-0-12-816081-7. DOI: https://doi.org/10.1016/B978-0-12-816081-7.00003-6. URL: http://www.sciencedirect.com/science/article/pii/B9780128160817000036.

[351] Gurram Giridhar, R.R.K.N. Manepalli and Gudimamilla Apparao. "Chapter 7 - Confocal Raman Spectroscopy". In: *Micro and Nano Technologies*. Ed. by Sabu Thomas, Raju Thomas, Ajesh K Zachariah et al. Elsevier, 2017, pp. 141–161. ISBN: 978-0-323-46140-5. DOI: https://doi.org/10.1016/B978-0-323-46140-5.00007-8. URL: http://www.sciencedirect.com/science/article/pii/B9780323461405000078.

[352] D. G. Lamas and N. E. Walsöe De Reca. "X-ray diffraction study of compositionally homogeneous, nanocrystalline yttria-doped zirconia powders". In: *Journal of Materials Science* 35.22 (2000), pp. 5563–5567. ISSN: 00222461. DOI: 10.1023/A:1004896727413.

[353] Yannick Hemberger, Nadja Wichtner, Christoph Berthold et al. "Quantification of yttria in stabilized zirconia by Raman spectroscopy". In: *International Journal of Applied Ceramic Technology* 13.1 (2016), pp. 116–124. ISSN: 17447402. DOI: 10.1111/ijac.12434.

[354] Masatomo Yashima, Katsuya Ohtake, Masato Kakihana et al. "Determination of tetragonal-cubic phase boundary of BY Raman scattering". In: *Journal of Physics and Chemistry of Solids* 57.1 (1996), pp. 17–24. ISSN: 00223697. DOI: 10.1016/0022-3697(95)00085-2.

[355] J. Müller, W. Ibach, K. Weishaupt et al. *Confocal Raman Microscopy*. Vol. 9. S02. 2003, pp. 1084–1085. ISBN: 9783319753782. DOI: 10.1017/s143192760344542x.

[356] Ludwig Reimer. *Scanning Electron Microscopy Physics of Image Formation and Microanalysis*. 2nd. Springer-Verlag Berlin Heidelberg, 1998, p. 529. ISBN: 978-3-540-63976-3. DOI: 10.1007/978-3-540-38967-5.

[357] Joseph I. Goldstein, Dale E. Newbury, Joseph R. Michael et al. *Microscopy and X-Ray Microanalysis*. Ed. by Springer. 4th. 2018, pp. VII–XIV. ISBN: 9781493966745. DOI: 10.1007/978-1-4939-6676-9.

[358] B. J. Inkson. "Scanning Electron Microscopy (SEM) and Transmission Electron Microscopy (TEM) for Materials Characterization". In: *Materials Characterization Using Nondestructive Evaluation (NDE) Methods*. Elsevier Ltd, 2016, pp. 17–43. ISBN: 9780081000571. DOI: 10.1016/B978-0-08-100040-3.00002-X. URL: http://dx.doi.org/10.1016/B978-0-08-100040-3.00002-X.

[359] Mathias Uller Rothmann, Wei Li, Joanne Etheridge et al. "Microstructural characterisations of perovskite solar cells – From grains to interfaces: Techniques, features, and challenges". In: *Advanced Energy Materials* 7.23 (2017). ISSN: 16146840. DOI: 10.1002/aenm.201700912.

[360] Harold M. McNair, James M. Miller and Nicholas H. Snow. "Introduction, chapter 1". In: *Basic Gas Chromatography*. Ed. by Wiley. 2019. Chap. 1, pp. 1–14. ISBN: 9781119450757. DOI: 10.1002/9781119450795.

[361] Guha Manogharan, Meshack Kioko and Clovis Linkous. "Binder Jetting: A Novel Solid Oxide Fuel-Cell Fabrication Process and Evaluation". In: *JOM: the journal of the Minerals, Metals & Materials Society* 67.3 (2015), pp. 660–667. ISSN: 15431851. DOI: 10.1007/s11837-015-1296-9.

[362] Mark E. Orazem and Bernard Tribollet. *Electrochemical Impedance Spectroscopy*. Ed. by a John Wiley. 2008, p. 523. ISBN: 9780470041406.

[363] Zdravko Stoynov and Daria Vladikova. *Differential impedance analysis*. Marin Drinov Academic Publishing House, 2005, p. 227. ISBN: 9543220573 9789543220571.

[364] Bernard A. Boukamp. "Electrochemical impedance spectroscopy in solid state ionics: Recent advances". In: *Solid State Ionics* 169.1-4 SPEC. ISS. (2004), pp. 65–73. ISSN: 01672738. DOI: 10.1016/j.ssi.2003.07.002.

[365] Qiu An Huang, Rob Hui, Bingwen Wang et al. "A review of AC impedance modeling and validation in SOFC diagnosis". In: *Electrochimica Acta* 52.28 (2007), pp. 8144–8164. ISSN: 00134686. DOI: 10.1016/j.electacta.2007.05.071.

[366] A. Hornés, M. Torrell, A. Morata et al. "Towards a high fuel utilization and low degradation of micro-tubular solid oxide fuel cells". In: *International Journal of Hydrogen Energy* 42.19 (2017), pp. 13889–13901. ISSN: 03603199. DOI: 10.1016/j.ijhydene.2016.12.106.

[367] Thien An Le, Min Sik Kim, Sae Ha Lee et al. "CO and CO2 methanation over supported Ni catalysts". In: *Catalysis Today* 293-294 (2017), pp. 89–96. ISSN: 09205861. DOI: 10.1016/j.cattod.2016.12.036. URL: http://dx.doi.org/10.1016/j.cattod.2016.12.036.

[368] D W Dees, T D Claar and D C Fee. "Conductivity of Porous Ni / ZrO2-Y203 Cermets". In: *J. Electrochem. Soc.* 134.9 (1987), pp. 2141–2146.

[369] Y Ji, J A Kilner and M F Carolan. "Electrical properties and oxygen diffusion in yttria-stabilised zirconia (YSZ)– La 0 . 8 Sr 0 . 2 MnO 3 F d (LSM) composites". In: 176 (2005), pp. 937–943. DOI: 10.1016/j.ssi.2004.11.019.

[370] Chih-chung T Yang, Wen-cheng J Wei and Andreas Roosen. "Electrical conductivity and microstructures ofLa0.65Sr0.3MnO3–8 mol% yttria-stabilized zirconia". In: 81 (2003), pp. 134–142. DOI: 10.1016/S0254-0584(03)00158-5.

[371] Jae-dong Kim, Goo-dae Kim, Ji-woong Moon et al. "Characterization of LSM – YSZ composite electrode by ac impedance spectroscopy". In: (2001).

[372] Beata Jedrzejewska. "Factors affecting the TMPTA radical polymerization photoinitiated by phenyltrialkylborates paired with tri-cationic hemicyanine dye . Kinetic studies". In: *Colloid and Polymer Science* 291 (2013), pp. 2225–2236. DOI: 10.1007/s00396-013-2964-3.

[373] James E. Smay, Sarosh S. Nadkarni and Jian Xu. "Direct writing of dielectric ceramics and base metal electrodes". In: *International Journal of Applied Ceramic Technology* 4.1 (2007), pp. 47–52. ISSN: 1546542X. DOI: 10.1111/j.1744-7402.2007.02118.x.

[374] *Griffith_ Freeform fabrication of ceramics via stereolithography_ 1996.pdf*.

[375] Ranga Komanduri. "Machining fiber-reinforced composites". In: *Mechanical Engineering* 115.4 (1993), pp. 58–64.

[376] P. J. Bartolo and G. Mitchell. "Stereo-thermal-lithography: A new principle for rapid prototyping". In: *Rapid Prototyping Journal* 9.3 (2003), pp. 150–156. ISSN: 13552546. DOI: 10.1108/13552540310477454.

[377] Amir Rashid. *Additive Manufacturing Technologies*. 2019, pp. 39–46. ISBN: 9781441911193. DOI: 10.1007/978-3-662-53120-4{_}16866.

[378] Guido Busca. *Structural, Surface, and Catalytic Properties of Aluminas*. 1st ed. Vol. 57. Elsevier Inc., 2014, pp. 319–404. ISBN: 9780128001271. DOI: 10.1016/B978-0-12-800127-1.00003-5. URL: http://dx.doi.org/10.1016/B978-0-12-800127-1.00003-5.

[379] M. Marturano, E. F. Aglietti and O. Ferretti. "α-Al2O3 catalyst supports for synthesis gas production: Influence of different alumina bonding agents on support and catalyst properties". In: *Materials Chemistry and Physics* 47.2-3 (1997), pp. 252–256. ISSN: 02540584. DOI: 10.1016/S0254-0584(97)80060-0.

[380] Grégoire Witz, Valery Shklover, Walter Steurer et al. "Phase evolution in yttria-stabilized zirconia thermal barrier coatings studied by rietveld refinement of X-ray powder diffraction patterns". In: *Journal of the American Ceramic Society* 90.9 (2007), pp. 2935–2940. ISSN: 00027820. DOI: 10.1111/j.1551-2916.2007.01785.x.

[381] Chao Zhang, Chang Jiu Li, Ga Zhang et al. "Ionic conductivity and its temperature dependence of atmospheric plasma-sprayed yttria stabilized zirconia electrolyte". In: *Materials Science and Engineering B: Solid-State Materials for Advanced Technology* 137.1-3 (2007), pp. 24–30. ISSN: 09215107. DOI: 10.1016/j.mseb.2006.10.005.

[382] Steven Weingarten, Uwe Scheithauer, Robert Johne et al. "Multi-material ceramic-based components - additive manufacturing of blackand- white zirconia components by thermoplastic 3D-printing (CerAM - T3DP)". In: *Journal of Visualized Experiments* 2019.143 (2019), e57538. ISSN: 1940087X. DOI: 10.3791/57538.

[383] Tsepin Tsai and Scott A. Barnett. "Effect of LSM-YSZ cathode on thin-electrolyte solid oxide fuel cell performance". In: *Solid State Ionics* 93.3-4 (1997), pp. 207–217. ISSN: 01672738. DOI: 10.1016/s0167-2738(96)00524-3.

[384] Choji Fukuhara, Kotaro Hayakawa, Yuji Suzuki et al. "A novel nickel-based structured catalyst for CO2methanation: A honeycomb-type Ni/CeO2catalyst to transform greenhouse gas into useful resources". In: *Applied Catalysis A: General* 532 (2017), pp. 12–18. ISSN: 0926860X. DOI: 10.1016/j.apcata.2016.11.036. URL: http://dx.doi.org/10.1016/j.apcata.2016.11.036.

[385] C. Ahamer, A. K. Opitz, G. M. Rupp et al. "Revisiting the temperature dependent ionic conductivity of yttria stabilized zirconia (YSZ)". In: *Journal of the Electrochemical Society* 164.7 (2017), F790–F803. ISSN: 19457111. DOI: 10.1149/2.0641707jes.

[386] J. A. Kilner. "Fast oxygen transport in acceptor doped oxides". In: *Solid State Ionics* 129.1 (2000), pp. 13–23. ISSN: 01672738. DOI: 10.1016/S0167-2738(99)00313-6.

[387] Erica Perry Murray, Tsepin Tsai and Scott A. Barnett. "Oxygen transfer processes in (La,Sr)MnO3/Y2O3-stabilized ZrO2 cathodes: An impedance spectroscopy study". In: *Solid State Ionics* 110.3-4 (1998), pp. 235–243. ISSN: 01672738. DOI: 10.1016/s0167-2738(98)00142-8.

[388] Subhash C. Singhal and Kevin Kendall. *High-temperature Solid Oxide Fuel Cells: Fundamentals, Design and Applications*. 2003. ISBN: 9781856173872. DOI: 10.1016/B978-1-85617-387-2.X5016-8.

[389] Akio Konno, Hiroshi Iwai, Motohiro Saito et al. "A corrugated mesoscale structure on electrode-electrolyte interface for enhancing cell performance in anode-supported SOFC". In: *Journal of Power Sources* 196.18 (2011), pp. 7442–7449. ISSN: 03787753. DOI: 10.1016/j.jpowsour.2011.04.051.

[390] Anthony Chesnaud, Francesco Delloro, Maya Geagea et al. "Corrugated Electrode/Electrolyte Interfaces in SOFC: Theoretical and Experimental Development". In: *ECS Transactions* 78.1 (2017), pp. 1851–1863. ISSN: 1938-6737. DOI: 10.1149/07801.1851ecst.

[391] Ludger Blum, Wilhelm A. Meulenberg, Heinz Nabielek et al. "Worldwide SOFC technology overview and benchmark". In: *International Journal of Applied Ceramic Technology* 2.6 (2005), pp. 482–492. ISSN: 1546542X. DOI: 10.1111/j.1744-7402.2005.02049.x.

[392] A. Bertei, F. Tariq, V. Yufit et al. "Guidelines for the rational design and engineering of 3D manufactured solid oxide fuel cell composite electrodes". In: *Journal of the Electrochemical Society* 164.2 (2017), F89–F98. ISSN: 19457111. DOI: 10.1149/2.0501702jes.

[393] Ruth Knibbe, Johan Hjelm, Mohan Menon et al. "Cathode-electrolyte interfaces with CGO barrier layers in SOFC". In: *Journal of the American Ceramic Society* 93.9 (2010), pp. 2877–2883. ISSN: 00027820. DOI: 10.1111/j.1551-2916.2010.03763.x.

[394] N. Jordan, W. Assenmacher, S. Uhlenbruck et al. "Ce0.8Gd0.2O2 - δ protecting layers manufactured by physical vapor deposition for IT-SOFC". In: *Solid State Ionics* 179.21-26 (2008), pp. 919–923. ISSN: 01672738. DOI: 10.1016/j.ssi.2007.12.008.

[395] J. Malzbender, P. Batfalsky, R. Vaßen et al. "Component interactions after long-term operation of an SOFC stack with LSM cathode". In: *Journal of Power Sources* 201 (2012), pp. 196–203. ISSN: 03787753. DOI: 10.1016/j.jpowsour.2011.10.117. URL: http://dx.doi.org/10.1016/j.jpowsour.2011.10.117.

[396] Bin Hua, Meng Li, Bo Chi et al. "Enhanced electrochemical performance and carbon deposition resistance of Ni-YSZ anode of solid oxide fuel cells by in situ formed Ni-MnO layer for CH4 on-cell reforming". In: *Journal of Materials Chemistry A* 2.4 (2014), pp. 1150–1158. ISSN: 20507488. DOI: 10.1039/c3ta12766d.

[397] R. E. Williford, L. A. Chick, G. D. Maupin et al. "Diffusion Limitations in the Porous Anodes of SOFCs". In: *Journal of The Electrochemical Society* 150.8 (2003), A1067. ISSN: 00134651. DOI: 10.1149/1.1586300.

[398] M J Jørgensen, S Primdahl, C Bagger et al. "Effect of sintering temperature on microstructure and performance of LSM–YSZ composite cathodes". In: *Solid State Ionics* 139 (2001), pp. 1–11. ISSN: 0167-2738.

[399] Joëlle Aubin, David F. Fletcher, Joël Bertrand et al. "Characterization of the mixing quality in micromixers". In: *Chemical Engineering and Technology* 26.12 (2003), pp. 1262–1270. ISSN: 09307516. DOI: 10.1002/ceat.200301848.

[400] Alberto Cantu-Perez, Simon Barrass and Asterios Gavriilidis. "Residence time distributions in microchannels: Comparison between channels with herringbone structures and a rectangular channel". In: *Chemical Engineering Journal* 160.3 (2010), pp. 834–844. ISSN: 13858947. DOI: 10.1016/j.cej.2009.07.023. URL: http://dx.doi.org/10.1016/j.cej.2009.07.023.

[401] Antonio Vita, Cristina Italiano, Lidia Pino et al. "High-temperature CO2 methanation over structured Ni/GDC catalysts: Performance and scale-up for Power-to-Gas application". In: *Fuel Processing Technology* 202.September 2019 (2020), p. 106365. ISSN: 03783820. DOI: 10.1016/j.fuproc.2020.106365. URL: https://doi.org/10.1016/j.fuproc.2020.106365.

[402] Hideko Hayashi, Mariko Kanoh, Chang Ji Quan et al. "Thermal expansion of Gd-doped ceria and reduced ceria". In: *Solid State Ionics* 132.3 (2000), pp. 227–233. ISSN: 01672738. DOI: 10.1016/s0167-2738(00)00646-9.

[403] Mostafa Yakout, M. A. Elbestawi and Stephen C. Veldhuis. "A study of thermal expansion coefficients and microstructure during selective laser melting of Invar 36 and stainless steel 316L". In: *Additive Manufacturing* 24.September (2018), pp. 405–418. ISSN: 22148604. DOI: 10.1016/j.addma.2018.09.035. URL: https://doi.org/10.1016/j.addma.2018.09.035.

[404] A. M. Huntz, L. Maréchal, B. Lesage et al. "Thermal expansion coefficient of alumina films developed by oxidation of a FeCrAl alloy determined by a deflection technique". In: *Applied Surface Science* 252.22 (2006), pp. 7781–7787. ISSN: 01694332. DOI: 10.1016/j.apsusc.2005.08.116.

[405] Jose A.Hernandez Lalinde, Jing Si Jiang, Gabriel Jai et al. "Preparation and characterization of Ni/Al2O3 catalyst coatings on FeCrAl-loy plates used in a catalytic channel reactor with in-situ spatial profiling to study CO2 methanation". In: *Chemical Engineering Journal* 357.September 2018 (2019), pp. 435–446. ISSN: 13858947. DOI: 10.1016/j.cej.2018.09.161. URL: https://doi.org/10.1016/j.cej.2018.09.161.

[406] A. Muñoz-Murillo, L. M. Martínez T., M. I. Domínguez et al. "Selective CO methanation with structured RuO2/Al2O3 catalysts". In: *Applied Catalysis B: Environmental* 236.February (2018), pp. 420–427. ISSN: 09263373. DOI: 10.1016/j.apcatb.2018.05.020. URL: https://doi.org/10.1016/j.apcatb.2018.05.020.

[407] Calvin H. Bartholomew. "Mechanisms of catalyst deactivation Calvin". In: *Applied Catalysis A: General* 212 (2001), pp. 17–60. ISSN: 0926-860X. DOI: https://doi.org/10.1016/S0926-860X(00)00843-7.

[408] Rafael Barea, Manuel Belmonte, María Isabel Osendi et al. "Thermal conductivity of Al2O3/SiC platelet composites". In: *Journal of the European Ceramic Society* 23.11 (2003), pp. 1773–1778. ISSN: 09552219. DOI: 10.1016/S0955-2219(02)00449-1.

[409] P. Zielke, A. C. Wulff, X. Sun et al. "Investigation of a Spinel-forming Cu-Mn Foam as an Oxygen Electrode Contact Material in a Solid Oxide Cell Single Repeating Unit". In: *Fuel Cells* 17.5 (2017), pp. 730–734. ISSN: 16156854. DOI: 10.1002/fuce.201700005.

[410] M. Ghatee, M. H. Shariat and J. T.S. Irvine. "Investigation of electrical and mechanical properties of 3YSZ/8YSZ composite electrolytes". In: *Solid State Ionics* 180.1 (2009), pp. 57–62. ISSN: 01672738. DOI: 10.1016/j.ssi.2008.10.006. URL: http://dx.doi.org/10.1016/j.ssi.2008.10.006.

[411] Ana María Herrera, Amir Antônio Martins de Oliveira, Antonio Pedro Novaes de Oliveira et al. "Processing and Characterization of Yttria-Stabilized Zirconia Foams for High-Temperature Applications". In: *Journal of Ceramics* 2013 (2013), pp. 1–8. ISSN: 2090-8628. DOI: 10.1155/2013/785210.

[412] Mojtaba Ghatee, Mohammad Hossain Shariat and John Irvine. "Production of high conductivity composite zirconia solid oxide electrolytes with good mechanical strength through net-shape". In: *Journal of Materials Chemistry* 18.43 (2008), pp. 5237–5242. ISSN: 09599428. DOI: 10.1039/b811486b.

[413] Ashutosh Kumar, Abhishek Jaiswal, Mohit Sanbui et al. "Scandia stabilized zirconia-ceria solid electrolyte (xSc1CeSZ, $5 < x < 11$) for IT-SOFCs: Structure and conductivity studies". In: *Scripta Materialia* 121 (2016), pp. 10–13. ISSN: 13596462. DOI: 10.1016/j.scriptamat.2016.04.023. URL: http://dx.doi.org/10.1016/j.scriptamat.2016.04.023.

[414] Osamu Yamamoto, Yoshinori Arati, Yasuo Takeda et al. "Electrical conductivity of stabilized zirconia with ytterbia and scandia". In: *Solid State Ionics* 79.C (1995), pp. 137–142. ISSN: 01672738. DOI: 10.1016/0167-2738(95)00044-7.

[415] V. Vijaya Lakshmi and Ranjit Bauri. "Phase formation and ionic conductivity studies on ytterbia co-doped scandia stabilized zirconia (0.9ZrO2-0.09Sc2O3-0. 01Yb2O3) electrolyte for SOFCs". In: *Solid State Sciences* 13.8 (2011), pp. 1520–1525. ISSN: 12932558. DOI: 10.1016/j.solidstatesciences.2011.05.014. URL: http://dx.doi.org/10.1016/j.solidstatesciences.2011.05.014.

[416] M. Torrell, S. García-Rodríguez, A. Morata et al. "Co-electrolysis of steam and CO2 in full-ceramic symmetrical SOECs: a strategy for avoiding the use of hydrogen as a safe gas". In: *Faraday Discussions* 182 (2015), pp. 241–255. ISSN: 13645498. DOI: 10.1039/c5fd00018a.

Appendix A

Scale up of printed devices

In this appendix we present the efforts to scale-up the solutions proposed and investigated in the previous chapters. The achievements shown here are the results of studies in first steps of development. The aim of this section is to present the last advances, whilst non culminated, showing the potentiality and proving the possibility of using additive manufacturing for commercial and ready-to-use devices.
Section A.1 is dedicated to the production of large area electrolytes. The freedom of design associated with additive manufacturing enables the realization of a 70 cm^2 electrolyte, which mechanical properties are enhanced with the use of a honeycomb structure.
Section A.2 illustrates the design of an electrolyte with complex structure consisting on a double helix shape, realized with the purpose of maximizing the output current for unit of volume while increasing the compactness and robustness of the device.
A monolithic reactor with heat exchange was designed and realized by mean of additive manufacturing and presented in Section A.3.

A.1 3D printing of large area electrolyte

As proven in Section 4.1.2, stereolithography is a valid option to produce electrolytes for SOCs, giving, moreover, the possibility to improve the performance with the enhancement of the projected area. In this section, the freedom of design is used to produce large area self-sustaining electrolyte membranes. Previous similar attempts in this direction have been reported by NexTech (USA). In that work, an electrolyte was made by a thin sheet pressed in a double mesh with honeycomb shape in order to reduce the thickness of the membrane inside the hexagons and to improve the mechanical stability [97]. Following a similar idea we used a honeycomb net over a flat membrane to improve the mechanical stability of the electrolyte.
The mechanical properties of the printed piece is a critical aspect in the production steps in which handling is necessary, in particular during the cleaning. The complexity increases when the printed electrolyte is made of a membrane around 300 µm thick over an area of tens of square centimeters. In this case the use of a contour few millimeters thick is not enough to achieve good mechanical properties. For this reason a honeycomb structure is implemented as backbone to improve the robustness of the electrolyte and allow the procedure of cleaning and assembly in the test station.
The first successful design is reported in Figure A.1, as a comparison between the green piece (on the left) and the sintered one (on the right).

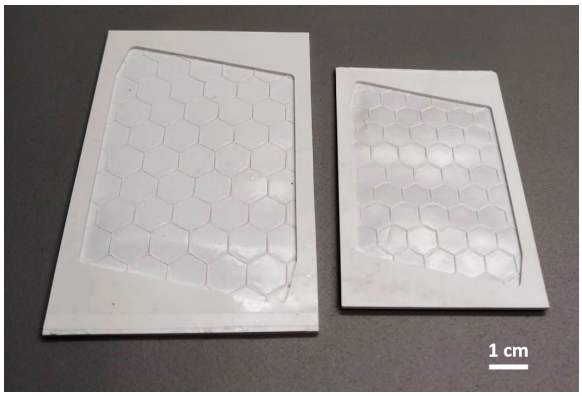

Figure A.1: *First large area electrolyte before (on the left) and after (on the right) the sintering.*

This design offered mechanical properties to the handling and cleaning of the pieces, although after the sintering the thinner part of the membrane appeared slightly bent due to thermal stresses.
Due to cracks in the electrolyte which invalidates the gas tightness, symmetric measurements are performed to evaluate the conductivity of the as-

fabricated electrolyte. The cell is functionalized with LSM-YSZ commercial electrodes (Fuelcell materials, USA) on both sides, to generate a symmetrical cell. A devoted test station was used for the characterization of the cells. Two stainless steel manifolds (Fuel Cell Store, USA) are used to supply air and apply the pressure to hold a CuMn sponge (Alantum, Germany) [409] and silver wires and paste are used to improve the contacts. The system is placed in a Lenton furnace and the EIS is recorded with a galvanostat frequency response analyser (Alpha-A, Novocontrol, Germany), in the temperature range 650°C-750°C.
When the obtained cell was assembled in the test station, the lack of flatness in the surface lead to the break of the cell. Other causes for this issue can be related with the stress generated when applying pressure to the more rigid elements like the conductive foam used for the test, or to the connection wires crossing the compressive seal. To overcome this problem, we implemented some changes in the design. First of all, the distance between the frame and the membrane is defined in such a way that it can perfectly allocate the contact foam, allowing a proper insertion without generating stresses. Following the same idea, notches were added to insert the contacting wires. To avoid the bending during the sintering, the contact of the hexagons membranes with the frame was optimized. In this way, the stresses should be released, generating a flat structure. Finally, 3YSZ is used instead of 8YSZ, in order to exploit its higher mechanical properties [410], [411]. The obtained cell is reported in Figure A.2.

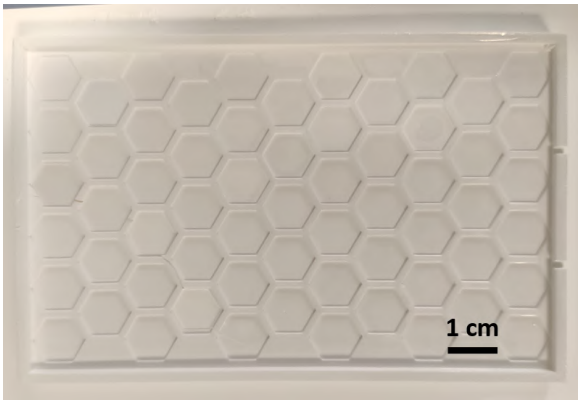

Figure A.2: *Improved large area electrolyte.*

Small cracks arise during the cleaning process, reason why the electrolyte is characterized as a symmetrical cell with LSM-YSZ electrodes as described before. The Nyquist plots are reported in Figure A.3. The ionic conductivity was calculated from the results of the fitting, as we have done for 8mol% yttria stabilized zirconia in Section 3.4.2. As can be observed in Figure A.4, the

reported values are comparable with the one previously obtained by other manufacturing techniques or by stereolithography on button cell size.

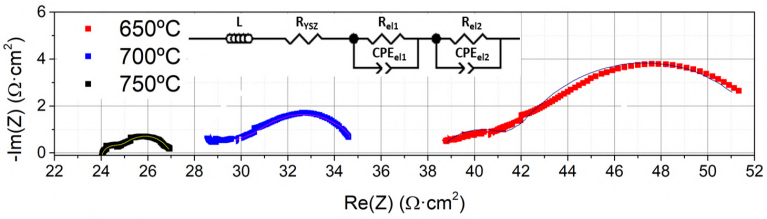

Figure A.3: *Nyquist plot of the impedance measured on the large area electrolyte as symmetrical cell.*

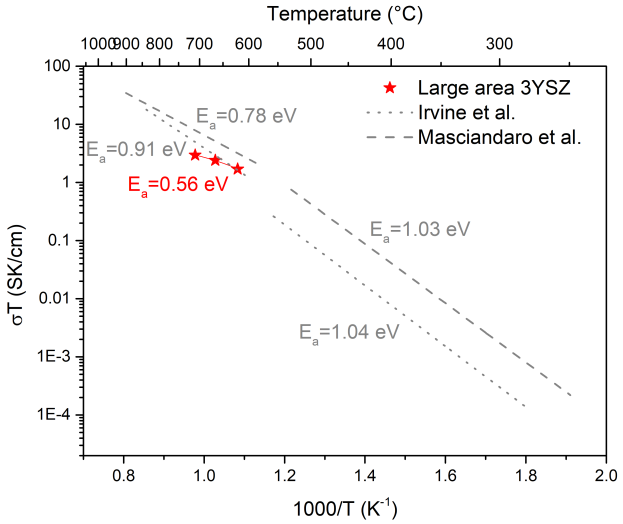

Figure A.4: *Ionic conductivity of the electrolyte realized in 3YSZ, compared with symmetrical button cell realized previously in the group (Masciandaro et al.) [267] and values reported in literature for manufacturing through isotactic pressing (Irvine et al.) [412].*

While the absolute values are close to the ones previously reported, the conductivity is not raising as expected at increased temperature. While further experiments are required to clarify the reasons of this behaviour, we can speculate here that it can be ascribed to a loose of electrical contact due to the poor connection between the noble metal and the electrode. Further developments will require the implementation of better contacts for these large area cells.

A.2 Monolithic SOC

Solid Oxide Cells require two chambers, one for the fuel and one for the air, separated by a gas-tight membrane capable to conduce oxygen ions. Due to the manufacturing constrains of the ceramic materials, on which these membranes are made of, these devices are in the practice limited to two designs: planar and tubular geometries. In Chapter 4 we proved the possibility of enhancing the performance through a structuration of the design. However, the cell were still characterized by a predominant dimension in the x and y plane and a lower grown in the z direction. Here we explore the use of additive manufacturing for the realization of complex and hierarchical structures, with embedded channels and manifolds. Pursuing the maximization of current output related with the volume of the device, we developed an electrolyte based on a double-helix structure.
The double-helix structure is generated as follows: a first hollow helix configured to act as fuel electrode, while a second one forms the air electrode. These two have a common axis and differ by a translation along the axis, so that the first fluid circulation channel is arranged adjacent to the second one, keeping a separation between the two gases. In this way, the common wall between the two electrode acts as electrolyte, since the entire device is produce in YSZ, proper to work as ionic conductor.
In the first attempts the generated double-helix was closed with a wall around, generating a cylinder with two inlets and two outlets, one for each chamber. Figure A.5 reports this design, as full piece and in cross section. To appreciate the two chambers, the fuel one is highlighted in green and the air one in grey.

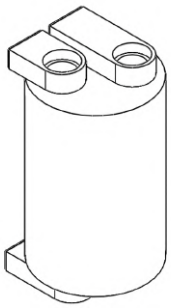

(a) Close double-helix

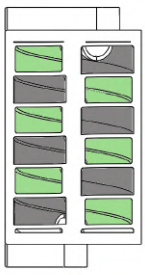

(b) Cross section of the close double-helix

Figure A.5: *CAD designs of the close double-helix electrolyte, fuel electrode highlighted in green, air electrode highlighted in grey.*

After first printing, it was observed that the cleaning of such close struc-

tures resulted difficult, and an open air electrode solution has been developed. As can be observed from the comparison between Figures A.6a and A.5a, the second case presents an easy access to one of the electrodes, facilitating the cleaning step. Due to the open nature of one of the electrode, a double inlet and double outlet are not necessary anymore, simplifying the removal of the uncured paste and the access to one of the path.

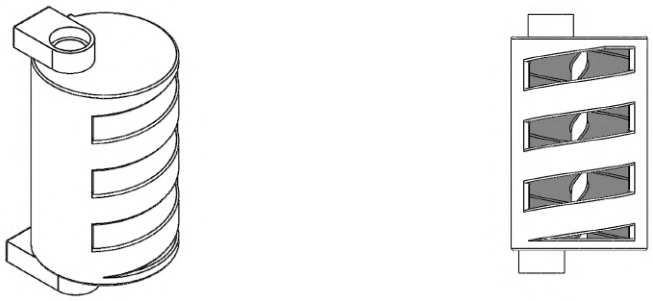

(a) Open double-helix *(b) Side view of the open double-helix*

Figure A.6: *CAD design of the open double-helix electrolyte, the grey highlighted the open air electrode.*

An example of a printed piece (in green) is reported in Figure A.7. Minor defects at the inlet and outlet are noticeable from the picture, these imperfection are not relevant to the functionality of the cell. While minor internal cracks are present, arisen during the cleaning of the membrane of 300 µm. This and other trials have been employed to adjust the electrode deposition and the set up to seal and characterize such devices, process currently under development in the group.

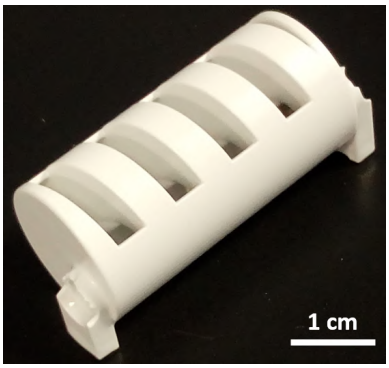

Figure A.7: *Printed double-helix electrolyte.*

Some designs have been devised (whilst not materialized) that combine possibility of implementing a previous enhancement strategies based on corrugation (as the ones demonstrated in Section 4.1.2), with the compact design of double-helix. Figure A.8 present the designs based on these concepts.

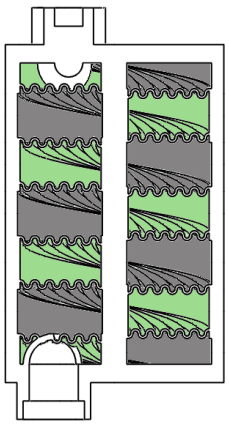

Figure A.8: *Cross section of the double-helix design implemented with a corrugation to improve the active area. The fuel electrode is highlighted in green, the air electrode in grey.*

A.3 Manufacturing of monolithic heat-exchange reactor

One of the many fields of application is the catalysis one, where the possibility of produce monolithic devices with integrated channels and manifolds are particular interesting. 3D printing technologies, once again, can provide complex geometries that are not reachable by any other manufacturing technique.
In this work we developed a heat exchanger reactor for Sabatier reaction in collaboration with the Fraunhofer Institute-IMM. The designed reactor, reported in Figure A.9, presents a reaction path, where the conversion of CO_2 and H_2 into methane takes place and two external heating circuits to heat up the reactor with a flow of hot gas. The design integrates cavities for allocating thermocoupes with the purpose of monitoring the temperature profile during the heating step and the reaction to detect eventual hot spots.

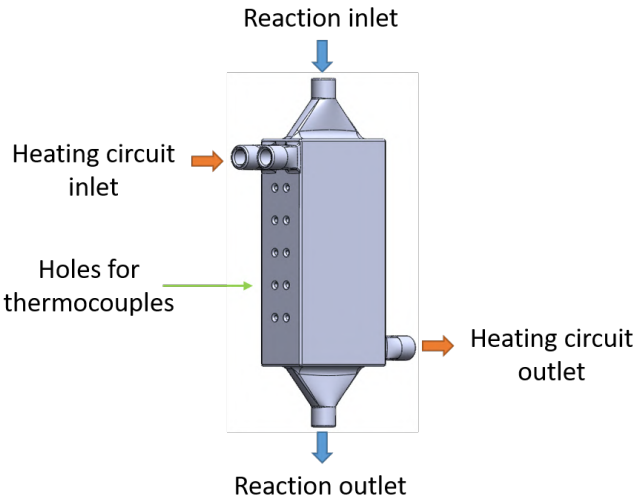

Figure A.9: *Design of the heat-exchange reactor.*

In detail, the reaction path consists in a straight micro-channel structure, similar to the one realized by test-plates in Chapter 5 (Figure A.10a). Two heating circuits (Figure A.10b) are placed outside the reaction channels to have a homogeneous temperature profile in the reactor.

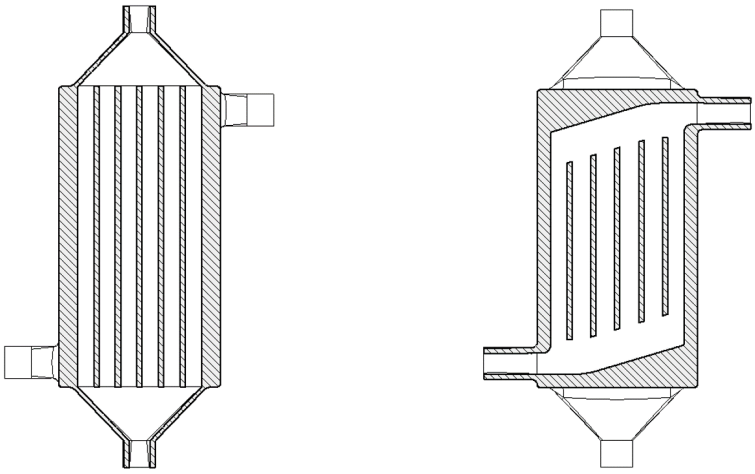

(a) Reaction channels *(b) Heating channels*

Figure A.10: *Cross section of the reaction and heating channels in the heat-exchange reactor.*

A cross section of the channels distribution is reported in Figure A.14. The structure is symmetrical with respect to a central plane, so from the external, the reactor is built with heating channels (3.5 mm by 2 mm) the holes for the thermocouples, and the reaction micro-channels where the reaction takes place (3 mm by 1 mm).

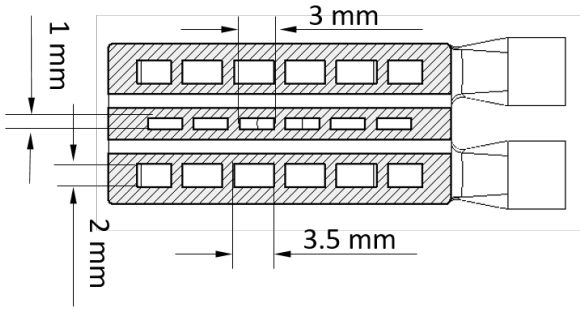

Figure A.11: *Size and disposition of the reaction and heating channels.*

The printed and sintered device is reported in Figure A.12.

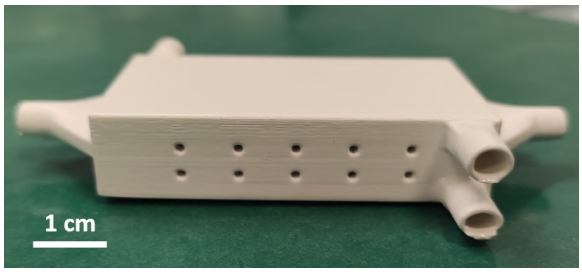

Figure A.12: *Printed heat-exchange reactor.*

The reactor has been assembled with an alumina sealant (Resbond 989F, Final Advance Material, France) to commercial ceramic tubes (Almath, UK) ending with Swagelock 1/8" connection to be assembled in the measurement station. The leak test reported in Figure A.13, shows the increase of the relative pressure under flow up to 3 bar, but at the removal of the flow the pressure drops up to 0.5 bar in 40 minutes. Visual analysis with leakage detector shows a leak from one of the thermocouple holes.

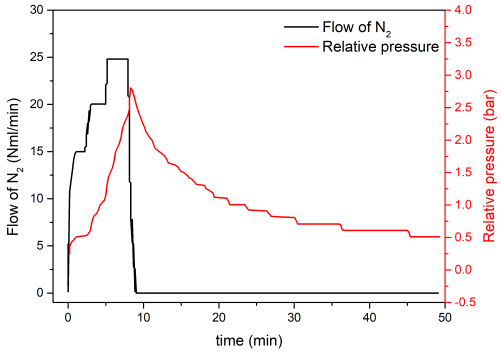

Figure A.13: *Printed heat-exchange reactor.*

The improvement of gas-tightness of the reactor is currently under development to generate a reactor able to perform under pressure.
Further developments include the production of a complex system (scheme presented in Figure A.14), in which the reaction channels are doubled around an external heater and the heating circuit is used to remove the heat generated during the methanation exothermic reaction.

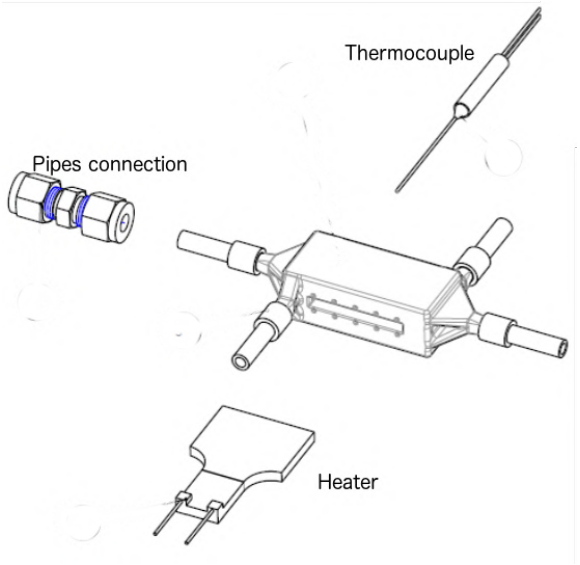

Figure A.14: *Printed heat-exchange reactor.*

A printed prototype realized during this work is reported in Figure A.15.

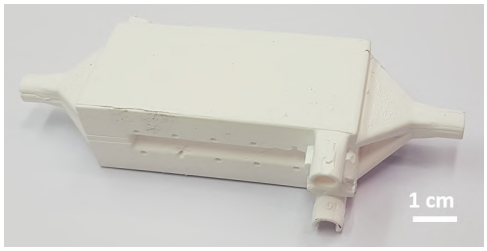

Figure A.15: *Printed heat-exchange reactor.*

Appendix B

Development of SLA pastes based on high ionic conductivity ceramic materials

In this appendix we present the development of slurries for stereolithography based on ceramic materials suitable for the production of SOC electrolytes. The attention of this study has been focused on zirconia based compounds materials which shows an higher ionic conductivity compared with the state-of-the-art yttria stabilized zirconia, namely ytterbia scandia stabilized zirconia ($(Yb_2O_3)_{0.06}\,(Sc_2O_3)_{0.04}\,(ZrO_2)_{0.9}$) and scandia ceria stabilized zirconia ($(Sc_2O_3)_{0.1}(CeO_2)_{0.01}\,(ZrO_2)_{0.89}$) [37], [413], [414].

B.1 Light absorbance electrolyte materials

Figure B.1 presents the absorbance of zirconia based powders suitable to produce SOCs electrolytes. In the plot, *8YSZ* refers to $(Y_2O_3)_{0.08}(ZrO_2)_{0.92}$, *6Yb4ScSZ* to $(Yb_2O_3)_{0.06}(Sc_2O_3)_{0.04}(ZrO_2)_{0.9}$ and *10Sc1CeSZ* to $(Sc_2O_3)_{0.1}(CeO_2)_{0.01}(ZrO_2)_{0.89}$. Powder of 8YSZ and 6Yb4ScSZ present comparable absorbance of light, which may reveal a similar behaviour during the printing. On the other hand, the presence of ceria in the compound increases the absorbance, especially in the region between 250 nm and 450 nm, where the frequency of laser user for polymerization falls (355nm). The absorbance of 10Sc1CeSZ is 62% in this range. In any case, from these outcomes it can be anticipated that the penetration of light on the material will be enough for allowing the SLA printing process.

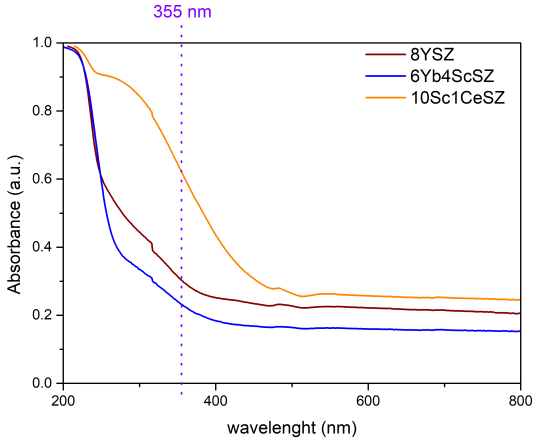

Figure B.1: *Spectrum of UV-Vis absorbance for the electrolyte materials, at 355 nm, the operation wavelength of the laser used in this work is reported.*

B.2 Developing of SLA pastes

The SLA pastes developed are based on the commercial mixture of monomers and photo-initiator called Spot-LV, used as comparison for the in-house developed vehicle in Section 3.1.2.
As a first step in the development, slurries based only on Spot-LV and ceramic powders, with a load of 70wt.% have been produced. The base ceramic materials are the powders discussed in the previous section: 10Sc1CeSZ and 6Yb4ScSZ. 8YSZ is also produced with the sake of comparing with the commercial product. The results of the polymerization tests are reported in the following table:

Ceramic powder	Cure depth (μm)
8YSZ	65 ± 3.5
6Yb4ScSZ	70 ± 3
10Sc1CeSZ	30 ± 2.5

Table B.1: *Polymerisation tests for the different electrolytes materials.*

Such results agree with the absorbance measurements, meaning that higher the absorbance, lower the cure depth. This is due to the fact that photons absorbed by the powders cannot reach the photo-initiator to start the reaction. Based on these values, we chose 6Yb4ScSZ as starting ceramic material for the slurries. However, for the initial sweep in resin composition, 8YSZ powders have been used, since the absorbance values for the two materials are close and the second is much more affordable.
In this frame, the effect of TMPTA on the polymerization has been studied, showing how this acrylate presents higher conversion in the current operation conditions than the one in the Spot-LV (indicated as a mixture of aliphatic acrylates from the producer). The realized slurries have been reported in Table B.2.

Test ID	Powder	Spot-LV	TMPTA
	wt.%	wt.%	wt.%
8YSZ+SpotLV30	70	30	0
8YSZ+SpotLV15	70	15	15
8YSZ+SpotLV05	70	5	25
8YSZ+SpotLV01	70	1	29

Table B.2: *Composition of the samples for the optimization of the ratio Spot-LV/TMPTA.*

In this way the commercial product has been used as source of photo-initiator, and such amount has been optimized according to the results shown in Figure B.2, establish a maximum in the polymerization for the ratio Spot-LV:TMPTA of 1:5.

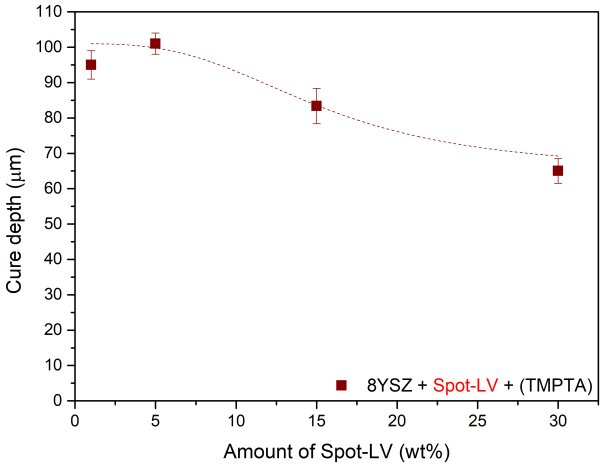

Figure B.2: *Cure depth as a function of Spot-LV content in 8YSZ SLA slurries. Dashed line as guide for the reader.*

After proving that the cure depth is not affected by the amount of Monofax up to 1wt%, a fixed percentage of dispersant is added to avoid the agglomeration of particles. Pursuing a high density of the electrolytes produced from these slurries, different ceramic load have been tested, keeping constant the ratio Spot-LV:TMPTA (Table B.3).

Test ID	**Powder**	**Spot-LV**	**TMPTA**	**Monofax**
	wt.%	wt.%	wt.%	wt.%
YbScSZ70	70	24.6	4.9	0.5
YbScSZ73	73	22.1	4.4	0.5
YbScSZ75	75	20.5	4.0	0.5
YbScSZ78	78	17.9	3.6	0.5
YbScSZ80	80	16.2	3.3	0.5

Table B.3: *Composition of the samples for the test for the dependence of the cure depth on the ceramic load.*

The thickness of the cured layer is slightly affected by the ceramic load in the range 70-80wt.%, showing a variation in the order of the experimental error. The composition showing the higher value, i.e. 75wt.% of ceramic powder, will be the one chosen for further studies.

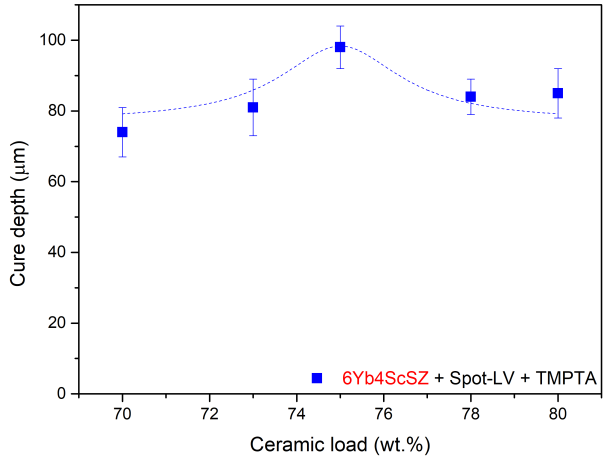

Figure B.3: *Cure depth as a function of ceramic load in YbScSZ SLA slurries. Dashed line as guide for the reader.*

The rheology of the final paste has been tested with a rheometer Brookfield RST-CPS available at the department of Materials Science and Chemical-Physics of the University of Barcelona (UB). The slurry presents a shear-thinning behaviour, necessary to be successfully printed by stereolithography.

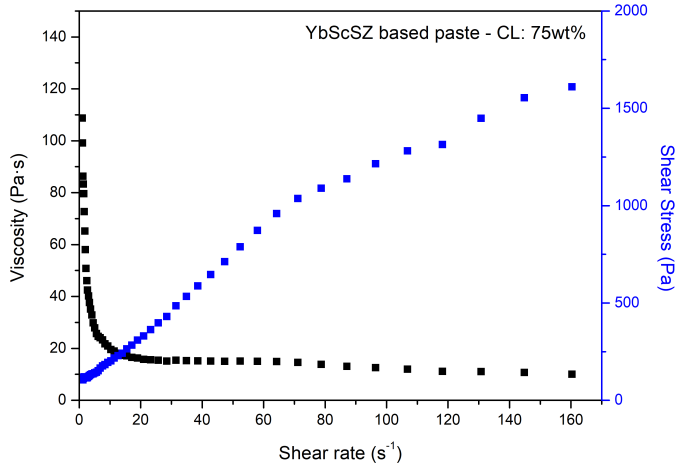

Figure B.4: *Rheological behaviour of the YbScSZ paste.*

The viscosity values are lower than the ones reported in the literature (which are in the order of hundreds of Pa·s) [221]. Despite this fact, the printing process has been run satisfactorily. The lower viscosity might, however, represent a problem in the case of printing high pieces (over 1 cm), since these are not going to be held in position by the paste underneath. In general, pastes with low viscosity are more prone to flow out of the platform, generating supply issues, local lacking of paste and consequently bad reproduction of the design.

B.3 3D printed electrolytes based on ytterbia scandia stabilized zirconia

Pellets of 400 µm thick have been produced, debinded and sintered up to 1300°C for four hours [415] (Figure B.5).

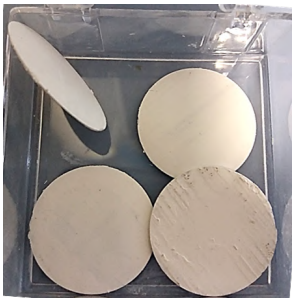

Figure B.5: *Printed electrolytes based on developed 6Yb4ScSZ paste*

The microstructure of the printed electrolytes has been evaluated by Scanning Electron Microscopy, showing residual porosity. As palliative measure for preventing this porosity, higher ceramic load or higher sintering temperature should be applied. The required optimization has not been conducted in the frame of this thesis.

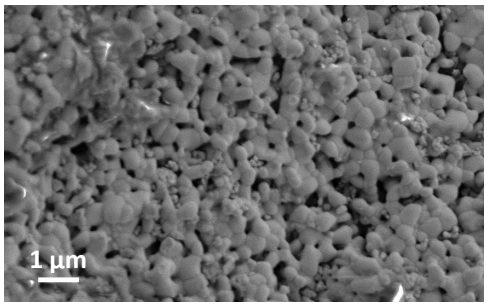

Figure B.6: *Microstructure of the electrolytes based on developed 6Yb4ScSZ paste*

To evaluate the ionic conductivity of the printed electrolytes, symmetrical cells have been produced using LSM ink (Fuelcell materials, USA) and attach at 1200°C. To ensure a proper adhesion, an attachment layer based on the same starting powder have been applied (as described in Section 2.2.1.2). Gold paint and wires have been used to connect the cell to the test station, following the procedure described in Section 2.4.2. The characterization has been performed by electrochemical impedance spectroscopy over the range of temperature between 700°-900°C and the obtained Nyquist plots are reported in Figure B.7.

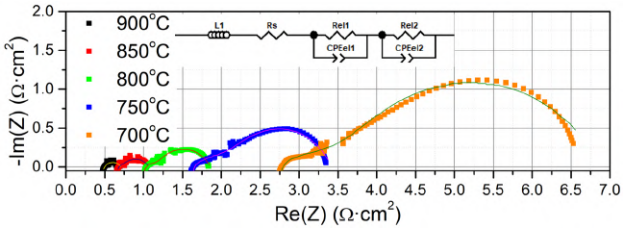

Figure B.7: *Nyquist plots of the LSM/6Yb4ScSZ/LSM symmetrical cell.*

The fitting has been performed using the equivalent circuit presented in the inset of Figure B.7 to evaluate the serial resistance and calculate the ionic conductivity applying the geometrical factors of the cell. The obtained results are reported in Figure B.8.

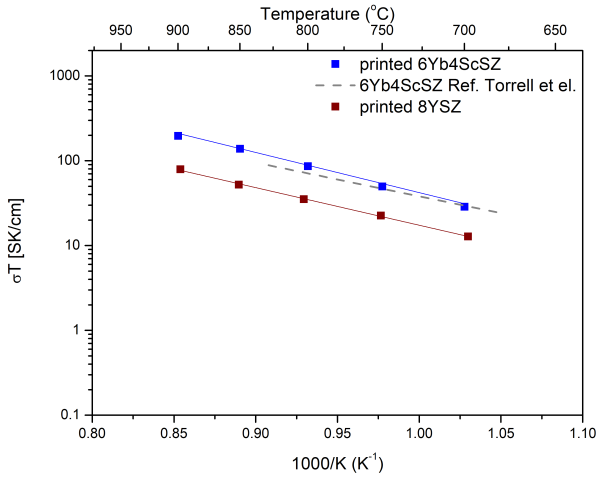

Figure B.8: *Arrhenius plot of the 6Yb4ScSZ ionic conductivity related with the values reported by Torrell et al. [416] and the printed 8YSZ, measured in this work.*

The conductivity values measured are in the range of the ones reported in the literature and significantly higher than the 8YSZ ones, making interesting the use of scandia based electrolyte for 3D printing. However, further optimizations of the printable feedstock is necessary, to improve the printability and the final density of the pieces. These improvements will lead to the development of a paste competitive with the commercial one based on 8YSZ, but showing higher ionic conductivity. These developments will enable the production of complex designs devoted to further enhance the performance of the cells.

Glossary

Abbreviations

AFC	Alkaline Fuel Cells
AJP	Aerosol Jet Printing
ASR	Area Specific Resistance
CHP	Combined Heat and Power
CODE	Ceramic On-Demand Extrusion
DC-SOFCs	Direct Carbon Solid Oxide Fuel Cells
DED	Direct Energy Deposition
DIJ	Direct Inkjet Printing
DLP	Digital Light Processing
EIS	Electrochemical Impedance Spectroscopy
FDM	Fused Deposition Modelling
GC	Gas-chromatography
IJ	Inkjet Printing
LOM	Laminated Object Manufacturing
MCFC	Molten Carbonate Fuel Cell
MIEC	Mixed Ionic-Electronic Conducting
MPD	Maximum Power Density
OCV	Open Circuit Voltage
PAFC	Phosporic Acid Fuel Cell

PEMFC	Proton-Exchange Membrane Fuel Cell
RE	Renewable Energy
SEM	Scanning Electron Microscope
SLA	Stereo-lithography
SLM	Selective Laser Melting
SLS	Selective Laser Sintering
SNG	Synthetic Natural Gas
SoA	State-of-the-art
SOC	Solid Oxide Cell
SOEC	Solid Oxide Electrolysis Cell
SOFC	Solid Oxide Fuel Cell
SRU	Single Repeating Unit
TEC	Thermal Expansion Coefficient
TIJ	Thermal Ink-Jet
TPB	Triple Phase Boundary
UV	Ultra-Violet
WHSV	Weight Hourly Space Velocity
XRD	X-Rays Diffraction

Chemical compounds

3YSZ	3mol% yttria stabilized zirconia, $(Y_2O_3)_{0.03}$ $(ZrO_2)_{0.97}$
8YSZ	mol% yttria stabilized zirconia, $(Y_2O_3)_{0.08}$ $(ZrO_2)_{0.92}$
BICUVOX	$Bi_2V_{0.9}Cu_{0.1}O_{5.35}$
BZY	$BaZr_{0.9}Y_{0.1}O_{3-\delta}$
CaSZ	Calcia stabilized zirconia, $CaZrO_3$
CDC	Calcium doped ceria, $Ce_{0.9}Ca_{0.1}O_{1.8}$
DMPA	2,2-Dimethoxy-2-phenylacetophenone
DWSB	$Dy_{0.08}W_{0.04}Bi_{0.88}O_{1.56}$

ESB	$Er_{0.4}Bi_{1.6}O_3$
GDC	Gadolinia doped Ceria, $Gd_{0.20}Ce_{0.80}O_{1.95}$
HDDA	1,6-Hexanediol diacrylate
LAMOX	$La_2Mo_2O_9$
LSC	Lanthanum strontium chromite, $La_xSr_{(1-x)}CoO_3$ (x∼0.6–0.8)
LSC	Lanthanum Strontium Cobaltite, $La_{0.6}Sr_{0.4}CoO_{3-\delta}$
LSCF	Lanthanum strontium cobalt ferrite, $La_{(1-x)}Sr_xFe_{(y)}Co_{(1-y)}O_{(3)}$ (x∼0.4, y∼0.2)
LSCF	Lanthanum Strontium Cobalt Ferrite, $(La_{0.6}Sr_{0.4})_{0.95}Co_{0.2}Fe_{0.8}O_{3-\delta}$
LSGM	Lanthanum Strontium Gallate Magnesite, $La_{0.8}Sr_{0.2}Ga_{0.8}Mg_{0.2}O_3$
LSGMC	$La_xSr_{1-x}Ga_yMg_{1-y-z}Co_zO_3$ (x∼0.8, y∼0.8, z∼0.085)
LSM	Lanthanum strontium manganite, $La_xSr_{(1-x)}MnO_3$ (x∼0.8)
NCAL	$Ni_{0.8}Co_{0.15}Al_{0.05}LiO_{2-\delta}$
SDC	Samaria doped Ceria, $Sm_{0.2}CeO_{0.8}O_{2-x}$
SSC	$Sm_xSr_{(1-x)}CoO_3$ (x∼0.5)
SSZ	Scandia stabilized zirconia, $(ZrO_2)_{0.8}(Sc_2O_3)_{0.2}$
TMPTA	Trimethylolpropane triacrylate
YDC	Yttria doped ceria, $Ce_{0.8}Y_{0.2}O_{1.96}$
YSB	Yttria stabilized bismuth oxide, $(Bi_2O_3)_{0.75}(Y_2O_3)_{0.25}$
YSZ	Yttria stabilized Zirconia

Symbols and Constants

η	Viscosity	[Pa · s]
λ	Wavelength	[nm]
ρ	Density	[g/cm^3]
σ	Conductivity	[S/cm]
C_d	Cure depth	[µm]
F	Faraday constant	[96485.33 C/mol]

j	Current density	[A/cm^2]
k	Boltzmann constant	[8.617×10_$_5$eV/K]
L_w	Cure width	[µm]
R	Resistance	[Ω]
T	Temperature	[°C]
V	Voltage	[V]

Scientific contribution

Publication

Peer-view journals

1. A. Pesce, A. Hornés, M. Núñez, A. Morata, M. Torrell, A. Tarancón; 3D printing the next generation of enhanced solid oxide fuel and electrolysis cells;Journal of Material Chemistry A; 2020, Volume 8, Issue 33, pp. 16926-16932; DOI: https://doi.org/10.1039/D0TA02803G

Patent

1. A. Tarancon, M. Torrell, A. Pesce, M. Nunez; ELECTROCHEMICAL CELL DEVICE FOR USE IN A SOFC AND/ OR A SOEC AND METHODS FOR OPERATING A SOFC OR A SOEC BY USING THEREOF, EP19382509, patent application

Proceedings

1. A. Pesce, C. Hernández, I. Sánchez, S. Masciandaro, A. Morata, M. Torrell, A. Tarancon; Improving performance of SOC through 3D printing of electrolytes; Proceeding of 13th European SOFC & SOEC Forum (2018); ISBN 978-3-905592-23-8; 6-15

2. A. Pesce, M. Lira Dos Santos, N. Kostretsova, A. Hornes, A. Morata, M. Torrell, A. Tarancon; New concepts for solid oxide cells manufacturing: The use of 3D printing technologies; Proceeding of 14th European SOFC & SOEC Forum (2020); ISBN: 978-3-905592-25-2; 403-412

Conferences[1]

1. E. Hernandez, M. Torrell, I. Sánchez, A. Pesce, S. Masciandaro, A. Morata, A. Tarancón; Ceramic 3D printed electrolytes for Solid Oxide Electrolyzers monolithic devices with complex hierarchical geometries; 23rd ICE/IEEE ITMC Conference, Madeira Island, Portugal, June 2017. Poster.

2. A. Pesce, M. Torrell, A. Morata, A. Tarancón; Developing of 3D printing of complex ceramic devices for energy application; 3rd scientific meeting BNC-b PhD students in Nanoscience, Barcelona, Spain, November 2017. Poster.

[1] In this section the underline indicates the presenting author.

3. A. Pesce, C. Hernández, I. Sánchez, S. Masciandaro, A. Morata, M. Torrell, A. Tarancon; Improving performance of SOC through 3D printing of electrolytes; 13th European SOFC & SOE Forum, Luzern, Switzerland, July 2018. Oral.

4. M.Torrell, A. Pesce, M. Nuñez, A. Hornés, A. Morata, A. Tarancón; 3D Printing of functional ceramics for Solid Oxide Cells; International Conference on High-Performance Ceramics (CICC), Kunming, China, May 2019. Invited talk

5. A. Pesce, M. Torrell, M. Nuñez, I. Sánchez, S. Anelli, A. Morata, A. Tarancon; Functional ceramic 3D printing of enhanced energy devices: High surface Solid Oxide Cells working as electrolysers; 2nd International Conference on Electrolysis (ICE), Louen, Sweden, June 2019. Poster.

6. A. Hornés, A. Pesce, M. Núñez, M. Torrell, A. Morata, A. Tarancón; 3D printing of solid oxide fuel cells: single step manufacturing: 9th International Conference on Electroceramics at F2CP2 Conference, Lousanne, Switzerland, July 2019. Oral.

7. A. Hornés, A. Pesce, M. Nuñez, M. Torrell, A. Morata, A. Tarancón; Multi-material 3D printing of technical ceramics for industrial fabrication of solid oxide fuel cells (SOFCs); Ceramitec Conference, Munich, Germany, September 2019. Invited keynote.

8. A. Pesce, M. Lira Dos Santos, N. Kostretsova, A. Hornes, A. Morata, M. Torrell, A. Tarancon; New concepts for solid oxide cells manufacturing: The use of 3D printing technologies; Proceeding of 14th European SOFC & SOEC Forum, Virtual, October 2020. Oral